CHALMERS

Assessment of Experimental, Computational, and Combined EFD/CFD Methods for Ship Performance Prediction

KADIR BURAK KORKMAZ

Department of Mechanics and Maritime Sciences
CHALMERS UNIVERSITY OF TECHNOLOGY
Göteborg, Sweden 2023

THESIS FOR THE DEGREE OF DOCTOR OF PHILOSOPHY IN SHIPPING AND MARINE TECHNOLOGY

Assessment of Experimental, Computational, and Combined EFD/CFD Methods for Ship Performance Prediction

KADIR BURAK KORKMAZ

Department of Mechanics and Maritime Sciences
CHALMERS UNIVERSITY OF TECHNOLOGY

Göteborg, Sweden 2023

Assessment of Experimental, Computational, and Combined EFD/CFD Methods for Ship Performance Prediction

KADIR BURAK KORKMAZ
ISBN 978-91-7905-931-6

Doktorsavhandlingar vid Chalmers tekniska högskola
Ny serie nr. 5397
ISSN 0346-718X
Department of Mechanics and Maritime Sciences
Chalmers University of Technology
SE-412 96 Göteborg
Sweden
Telephone: +46 (0)31-772 1000

Chalmers Reproservice
Göteborg, Sweden 2023

Assessment of Experimental, Computational, and Combined EFD/CFD Methods for Ship Performance Prediction

KADIR BURAK KORKMAZ
Department of Mechanics and Maritime Sciences
Chalmers University of Technology

Abstract

In today's highly competitive market, alongside increasingly stringent regulatory requirements, the precise prediction of ship performance has assumed paramount importance for both design verification and operational evaluations. This thesis addresses the need for a comprehensive assessment of Experimental Fluid Dynamics (EFD), Computational Fluid Dynamics (CFD), and their combination to enhance the accuracy of performance predictions. Moreover, it explores the potential of combined EFD/CFD methods in improving power predictions by either replacing or complementing certain aspects of the existing methodology, while also introducing novel methods.

The investigation identifies the Prohaska method as a prominent source of uncertainty in the ITTC-78 method. As an alternative, the CFD-based form factor method is meticulously examined, employing various codes and numerical approaches. The findings robustly establish the applicability and accuracy of the CFD-based form factor method, even when subjected to diverse numerical approaches and computational grids. Furthermore, best practice guidelines are derived for double-body RANS computations, ensuring compatibility with experimental form factors. Another debated issue within the ITTC-78 method is the very concept of form factor. This study conclusively affirms the Reynolds number dependence in form factors when the ITTC-57 line is employed. However, the numerical friction lines derived in this research, effectively eliminates these scale effects. Additionally, this study addresses conditions with flow separation, which renders the conventional form factor approach inadequate. A two form factor method ($2-k$ method) is proposed to address instances of separated flow, complemented by an empirical correction formula for vessels with deep transom submergence and wetted transom flow.

Furthermore, this thesis delves into the exploration of direct full-scale CFD computations for ship performance prediction. Extensive validation studies, encompassing numerous test cases and sea trials, are conducted to compare the accuracy of full-scale CFD computations with EFD based, and combined EFD/CFD methods. This thesis quantifies, for the first time in the literature, the difference in accuracy between fully computational and extrapolation-based methods using a large number of test cases and sea trials. The results indicate that while the prediction accuracy of full-scale CFD computations for power and RPM is lower than the other methods, the discrepancy is not substantial. Conversely, the investigations underscore that the combined EFD/CFD methods stand as the most accurate prediction method. Consequently, this thesis recommends incorporating combined EFD/CFD methods into the recommended procedures, as it offers immediate improvements to the existing ship performance prediction methods.

Keywords: EFD, CFD, Combined CFD/EFD Methods, form factor, numerical friction line, measurement uncertainty, verification and validation, power prediction

Acknowledgements

I am deeply grateful to my supervisors, Rickard Bensow and Sofia Werner, for their invaluable advice, continuous support, and patience during my PhD study. Their knowledge and extensive experience have been a constant source of encouragement throughout my academic journey. I greatly appreciate the freedom they granted me and the ample leeway provided whenever needed.

Sofia Werner deserves special mention, as this project was born from her vision and initiative. I extend my most sincere gratitude to her for her unwavering commitment to the project and her leadership and constructive engagement.

I owe a debt of gratitude to Professor Emeritus Lars Larsson for his support and encouragement throughout my graduate studies and for his pivotal role in my professional life. I acknowledge the significant contributions of my former manager, Lars Gustafsson, and my current manager, Christian Finnsgård, for creating and managing the harmonious working and research environment essential to my industrial PhD project.

I express my heartfelt thanks to my current and former colleagues, including Keunjae Kim, Alex Abolfazl Shiri, Da-Qing Li, Hans Liljenberg, Per Lindell, and Gheorghe Popa, for their invaluable support, guidance, and, at times, patience. Special thanks go to Gabriele Mazza for his cheerful disposition, enjoyable conversations at work, and beyond. I also extend my appreciation to Michal Orych at FLOWTECH International AB for his support, discussions, and dedication to assisting me.

Finally, I acknowledge SSPA and its impressive 83 years of institutional and intellectual knowledge accumulation. I am grateful for the valuable data, resources, support, and insightful discussions provided by all my colleagues. Without their contributions, this work would not have been possible.

I would like to extend my heartfelt appreciation to my dear friends for being a source of sanity and joy during the demanding times of my studies. Their company, shared experiences, and unwavering encouragement played a crucial role in making the time of my studies more enjoyable and less overwhelming.

I offer my thanks to my family for their unwavering support and belief in me. Last but not least, my deepest gratitude goes to my patient wife, Betül, for her steadfast support and tolerance during the ebbs and flows of my moods and involvement.

This research was supported by VINNOVA, the Swedish Governmental Agency for Innovation Systems (grant 2017-02953), Energimyndigheten, the Swedish Energy Agency (grant 2020-018759), and Hugo Hammars fond för internationell forskning inom sjöfarten. The computer resources at Chalmers Centre for Computational Science and Engineering (C3SE) provided by the Swedish National Infrastructure for Computing (SNIC), and RISE-SSPA are also greatly acknowledged.

Nomenclature

Acronyms

Symbol	Description
AGR	Adaptive Grid Refinement
ATTC	American Towing Tank Conference
BPG	Best Practice Guidelines
C3SE	Chalmers Centre for Computational Science and Engineering
CFD	Computational Fluid Dynamics
CII	Carbon Intensity Indicator
CSSRC	China Ship Scientific Research Centre
EASM	Explicit Algebraic Stress Model
EEDI	Energy Efficiency Design Index
EEXI	Energy Efficiency Existing Ship Index
EFD	Experimental Fluid Dynamics
GHG	Greenhouse Gas
IMO	International Maritime Organisation
ITTC	International Towing Tank Conference
ITTC-57	ITTC 1957 model-ship correlation
ITTC-78	1978 ITTC Power Prediction
KCS	KRISO Container Ship
KVLCC2	KRISO Very Large Crude Carrier version 2
L_{PP}	Length Between Perpendiculars
LCB	Longitudinal Centre of Buoyancy
NFL	Numerical Friction Line
NMRI	National Maritime Research Institute
OCRE	Ocean, Coastal and River Engineering
PDF	Probability Density Function
QA	Quality Assurance
RANS	Reynolds Averaged Navier-Stokes
RISE	Research Institudes of Sweden
RPM	Revolutions per Minute

SNIC	Swedish National Infrastructure for Computing
SSPA	Swedish Ship Testing Facility
SSSRI	Shanghai Ship and Shipping Research Institute
V&V	Verification and Validation
VINNOVA	Swedish Governmental Agency for Innovation Systems

Greek Symbols

Symbol	Description
σ	standard deviation

Roman Symbols

Symbol	Description
ΔC_{F}	Roughness allowance
a_j	Coefficients in the polynomial expression
C_{AAS}	Air resistance coefficient
C_{A}	Correlation allowance
C_{B}	Block coefficient
C_{FM}	Frictional resistance coefficient in model scale
C_{FS}	Frictional resistance coefficient in full scale
$C_{\mathrm{F}}^{'}$	Frictional resistance coefficient obtained from double-body CFD computation
C_{N}	Correlation factor for propeller turning rate
$C_{\mathrm{N}}^{'}$	Correlation factor for propeller turning rate of an individual speed trial
C_{PV}	Viscous pressure resistance coefficient
$C_{\mathrm{PV}}^{'}$	Viscous pressure resistance coefficient obtained from double-body CFD computation
C_{P}	Correlation factor for delivered power
$C_{\mathrm{P}}^{'}$	Correlation factor for delivered power of an individual speed trial
C_{R}	Residual resistance coefficient
C_{TM}	Total resistance coefficient in model scale
C_{TS}	Total resistance coefficient in full scale
C_{W}	Wave resistance coefficient
C_f	Local skin friction coefficient
C_{form}	Form resistance coefficient
D	Experimental measurement
$E\%D$	Comparison error

Fn	Froude Number
Fn_{tr}	Transom Froude number
k	Form Factor
k_{M}	Model scale form factor
k_{S}	Full scale form factor
k_{tr}	Transom form factor
n_{pred}	Predicted propeller turning rate
n_{trial}	Propeller turning rate measured in a sea trial
$P_{\mathrm{D}\ pred}$	Predicted power
$P_{\mathrm{D}\ trial}$	Power measured in a sea trial
P_{DM}	Delivered power in model scale
R_{TM}	Total resistance
Re	Reynolds Number
S	Computational result
tr_{ratio}	Ratio between the submerged transom area and the midship cross-section area
U_{bias}	Bias limit
y^{+}	Dimensionless parameter representing the distance from the first grid cell to the no-slip wall

"Yaşadım" diyebilmen için...

N.H.

List of Publications

This thesis consists of an extended summary and the following appended papers:

Paper I Korkmaz, K. B., Werner, S., & Bensow, R. (2019a). Numerical friction lines for CFD based form factor determination method. *VIII International Conference on Computational Methods in Marine Engineering MARINE 2019* (2019, May)

Paper II Korkmaz, K. B., Werner, S., & Bensow, R. (2019b). Investigations for CFD based form factor methods. *22nd Numerical Towing Tank Symposium, NuTTS 2019* (2019, October)

Paper III Korkmaz, K. B., Werner, S., Sakamoto, N., Queutey, P., Deng, G., Yuling, G., Guoxiang, D., Maki, K., Ye, H., Akinturk, A., Sayeed, T., Hino, T., Zhao, F., Tezdogan, T., Demirel, Y. K., & Bensow, R. (2021). CFD based form factor determination method. *Ocean Engineering* **220** (2021), 108451. https://doi.org/https://doi.org/10.1016/j.oceaneng.2020.108451

Paper IV Korkmaz, K. B., Werner, S., & Bensow, R. (2021). Verification and validation of CFD based form factors as a combined CFD/EFD method. *Journal of Marine Science and Engineering* **9**.(1) (2021). https://doi.org/10.3390/jmse9010075

Paper V Korkmaz, K. B., Werner, S., & Bensow, R. (2022). Scaling of wetted-transom resistance for improved full-scale ship performance predictions. *Ocean Engineering* **266** (2022, December), 112590. https://doi.org/10.1016/j.oceaneng.2022.112590

Paper VI Korkmaz, K. B., Werner, S., & Bensow, R. . "Investigations on experimental and computational trim optimisation methods". *Submitted to Ocean Engineering in 2023 June, under review*

Paper VII Korkmaz, K. B., Kim, K., Liefvendahl, M., Werner, S., & Orych, M. (2023). A validation study of full-scale CFD simulation for sea trial performance prediction of ships. *X International Conference on Computational Methods in Marine Engineering MARINE 2023* (2023, June)

Contents

1 Introduction

The accurate prediction of a ship's performance holds paramount significance during the design phase. As ship designs approach finalisation, the need for a higher level of confidence in predicting the speed-power-rpm relationships becomes increasingly critical. The final design must undergo verification employing the most precise prediction method available since the contractual speed, representing the speed achieved at a specified power consumption during a speed trial run, serves as a pivotal criterion in new ship orders. In the event that the projected speed-power relationship proves overly optimistic and fails to meet the stipulated specifications during the trial run, the shipyard incurs penalties in accordance with the contractual terms. Conversely, excessively conservative predictions can result in lost orders. Consequently, designers and shipyards face immense pressure to predict the vessel's performance with the utmost precision, aiming to minimise error margins (Larsson & Raven, 2010).

Furthermore, in addition to intensifying market competitiveness, legal authorities led by the International Maritime Organisation (IMO) have initiated measures to bolster the energy efficiency of ships, driven by growing environmental concerns. Given that shipping is responsible for approximately 3% of global greenhouse gas (GHG) emissions (IMO, 2021), it becomes imperative to reduce shipping emissions in accordance with the goals outlined by the IMO (2021). In pursuit of this vision, the IMO has introduced regulations, such as the Energy Efficiency Design Index (EEDI) (IMO, 2011), aimed at fostering energy-efficient ship designs and preventing the entry of inefficient ships into the market. The calculation of the EEDI index now represents a mandatory step, necessitating the conduction of towing tank tests during the design phase to verify applicable ships' compliance. Consequently, solutions aimed at enhancing efficiency during the design phase, such as hull form optimisation and the utilisation of energy-saving devices, have gained significant attention.

Recent IMO regulations introduced as of January 2023, namely the Energy Efficiency Existing Ship Index (EEXI) (IMO, 2022b) and the Carbon Intensity Indicator (CII) (IMO, 2022a), further emphasise the measurement of energy efficiency in existing ships and the monitoring of a ship's operational carbon intensity, respectively. Analogous to the previously implemented EEDI, the EEXI calculations are intended to assess the energy efficiency of existing ships. This new regulation mandates that all vessels, regardless of their construction date, undergo the calculation of the Energy Efficiency Existing Ship Index. As stated by the IMO (2022b), the calculated EEXI value for each individual ship must fall below the specified threshold, establishing a minimum energy efficiency standard for all ships. While towing tank tests can be employed to calculate the EEXI value based on extrapolated speed-power relations, such tests may not be feasible for all existing ships. Consequently, the IMO (2022b) has acknowledged Computational Fluid Dynamics (CFD) results as an acceptable alternative for EEXI calculation.

Additionally, the CII regulations also apply to existing ships, with the IMO setting goals to progressively reduce carbon intensity levels by 40% by 2030. Given that design-related solutions for increasing the energy efficiency of existing ships, such as hull form optimisation, are either inapplicable or impractical, the focus for CII regulations lies in improving operational factors. In this regard, the IMO's IMO-Norway GreenVoyage2050

Project (2023) has compiled a list of alternatives to enhance the carbon intensity rating of existing ships, encompassing measures such as speed and route optimisation, hull and propeller cleaning, reduction of power consumption by auxiliary systems, and trim optimisation. Notably, some operational applications, such as trim optimisation, require accurate ship performance prediction to provide decision support for the crew onboard.

In summary, the intensifying market competition and regulatory requirements have significantly heightened the demand for enhanced accuracy in ship performance prediction. The need for pre-verification of ship performance during the design phase has now expanded to encompass existing ships, which may undergo multiple evaluations throughout their lifespan as new solutions are implemented to comply with the increasingly stringent emission standards imposed by the IMO. Another critical aspect is related to the diversification of evaluation methods recognised and accepted by regulatory authorities, including the incorporation of CFD results into performance assessments. This thesis advocates for a comprehensive assessment of the strengths and weaknesses of Experimental Fluid Dynamics (EFD), CFD, and the combination of both approaches, as it holds the potential to yield more precise performance predictions and contribute to the achievement of the IMO's greenhouse gas reduction targets. The conclusions drawn from this assessment are expected to provide guidance to the shipping industry, shipyards, designers, and ship owners in selecting accurate, reliable, and feasible methods for evaluating ship performance.

This thesis is written in the format of compilation thesis. It consists of an extended summary (also referred as *kappa* in Sweden), and seven appended papers. The aim of the extended summary is to explain the research questions and objectives, and to provide an overarching theoretical background, a concise synthesis along with ample references to the appended papers and summary of the PhD project as a whole.

1.1 Experimental Methods

The development of methods for accurate ship performance prediction dates back over a century, originating from the pioneering work of William Froude and his experiments with scale models (Larsson & Raven, 2010). Froude's discovery of the Froude similarity and the subsequent formulation of scaling procedures paved the way for reasonably precise predictions of full-scale ship performance. A pivotal breakthrough in experimental and extrapolation methods occurred approximately four decades ago through the collaborative efforts of various institutions, led by the International Towing Tank Conference (ITTC). The introduction of the 1978 ITTC Power Prediction Method (ITTC, 1978) established standardised practices for towing tank testing and extrapolation procedures. While the ITTC-78 method has undergone some modifications since its inception, the fundamental assumptions and formulations have remained largely unchanged.

Despite the evolving commercial landscape observed among shipyards and ship owners, towing tank testing continues to be regarded as the final step in ship performance prediction. Legal authorities also emphasise the importance of towing tank testing, making it a mandatory requirement in evaluations such as the Energy Efficiency Design Index calculations mandated by the IMO (2011). Consequently, applicable ships must

undergo pre-verification through model testing during the design phase of new ships. However, it is essential to acknowledge the inherent limitations and well-known challenges associated with scale effects, as model tests are conducted based on Froude similarity, while simultaneously achieving Reynolds similarity remains elusive. To mitigate the impact of these limitations, towing tank facilities rely on experience and comprehensive databases encompassing both model tests and sea trials.

1.2 Computational Methods

Efforts to advance ship performance prediction methods have primarily concentrated on Computational Fluid Dynamics (CFD). This focus arises from the potential to replace model tests with CFD computations or directly simulate full-scale conditions once CFD methods demonstrate sufficient accuracy. Since the 1980s, when numerical methods first demonstrated their efficacy in ship design (Larsson, 1998, p. 2), the development of Reynolds Averaged Navier-Stokes (RANS) based methods has been ongoing. However, the verification and validation (V&V) of CFD methods have primarily been conducted at the model scale, primarily due to the limited availability of full-scale experimental data. Consequently, asserting the maturity of CFD computations for full-scale applications remains challenging, as the literature features limited studies that comprehensively verify and validate these computations for full-scale scenarios, unlike the extensive verification and validation efforts conducted for decades at the model scale (Hino et al., 2020; Larsson et al., 2014). Nonetheless, interest in and confidence regarding full-scale CFD computations have been growing, aided by initiatives such as the Joint Research Project (JoRes JRP), which aims to "collect and develop, through collaboration, a full set of ship performance data to better understand the potential for ship energy efficiency" (JoRes, 2019). Considering the acceptance of CFD computation results for calculating EEXI values and the increasing availability of public sea trial data, it is expected that the maturity and confidence in full-scale CFD computations will continue to improve in the future.

1.3 Combined EFD/CFD Methods

An alternative approach to performance prediction, distinct from purely EFD or CFD methods, involves leveraging the strengths of both CFD and EFD. As highlighted by the ITTC Specialist Committee on the Combined CFD/EFD Methods, if certain aspects of the extrapolation procedure or towing tank tests introduce higher uncertainty compared to the numerical uncertainty and modelling errors associated with CFD applications, the accuracy of power predictions can be expected to improve (ITTC, 2021e). In the 1978 ITTC Performance Prediction method, the form factor has been identified as a significant source of uncertainty by the Specialist Committee. This is due to the reliance on the EFD-based Prohaska method (Prohaska, 1966) for form factor determination and the influence of scale effects on form factors for estimating the full-scale resistance of ships. To address this, the use of double-body Reynolds Averaged Navier-Stokes (RANS) computations has been proposed as an alternative or supplementary method

to the Prohaska method (Raven et al., 2008). Double-body computations enable the replication of conditions described in the original form factor hypothesis (Hughes, 1954), while maintaining relative simplicity in numerical implementation.

Another aspect emphasised by the ITTC Specialist Committee on the Combined CFD/EFD Methods pertains to the presence of flow separation, which undermines the validity of the form factor concept. In cases involving flow separations, such as bubble-type separation around the stern of full-block vessels (Larsson & Raven, 2010) or substantially submerged transoms where the transom remains wet, double-body computations can be employed to modify the scaling of viscous resistance as advocated in this thesis.

As suggested by the ITTC Specialist Committee on the Combined CFD/EFD Methods, the combination of well-established, verified, and validated methods can yield immediate enhancements to the 1978 ITTC Performance Prediction Method.

1.4 Purpose

The purpose of this thesis is to investigate and advance ship performance prediction methodologies, with a focus on enhancing accuracy and applicability. The study is structured around the following objectives:

- To address the limitations and uncertainties associated with the current power prediction methodologies, particularly in relation to the form factor concept and its determination method.
- To examine the applicability and accuracy of CFD based form factor method as an alternative to conventional approaches.
- To address the challenges posed by the scale effects and flow separation in ship performance prediction, and propose alternative methods.
- To explore the utility of direct full-scale CFD computations in predicting ship performance and other operational characteristics.
- To quantify the differences in accuracy between fully computational methods and extrapolation-based methods by conducting an extensive analysis of numerous test cases and sea trials.

To achieve these objectives, the accuracy of each method, including EFD, CFD, and the suggested combined EFD/CFD approaches, was evaluated and compared against sea trial results. By identifying the strengths and weaknesses of each method, the research aims to provide valuable insights and recommendations for improving ship performance prediction methods.

The ultimate purpose of this thesis is to contribute to the advancement of power prediction methods and facilitate more accurate and reliable predictions for ship design and performance evaluation. By integrating EFD, CFD, and combined approaches, the research aims to improve the existing 1978 ITTC Performance Prediction Method and promote for more precise and efficient power predictions in the maritime industry.

The thesis thereby supports the industry's efforts to reduce greenhouse gas emissions by providing more precise prediction methods aligned with the International Maritime Organisation's targets toward more energy-efficient ships.

2 Extrapolation Methods

Experimental Fluid Dynamics (EFD) as applied in towing tanks plays a crucial role in ship design verification by generating a specific data set unique to a given hull form and its propulsive arrangement. This data set subsequently facilitates performance predictions for the ship in deep and calm waters. However, owing to the constraints of Froude and Reynolds similarities that cannot be simultaneously fulfilled in the towing tank environment, the extrapolation of this data becomes necessary to predict full-scale ship performance. In the 1870s, William Froude pioneered extrapolation procedures, incorporating a set of assumptions and testing techniques that led to reliable and, relatively speaking, accurate methods for power predictions for ships. Subsequently, in 1933, the International Towing Tank Committee (ITTC) was founded to standardise and improve model testing practices and extrapolation procedures.

Early prediction methods involved scaling self-propulsion tests using simple overall correction factors to predict power and propeller turning rate (Lindgren & Dyne, 1980). However, a survey conducted by ITTC (1969) in 1969 revealed significant variations in prediction methods among institutions. These variations included the implementation of emerging concepts and formulas such as form factor, friction lines, wake scaling, and roughness allowance (ITTC, 1969). Consequently, the Performance Committee recommended "compiling and comparing the various procedures and attempting to formulate a common method with a sound physical basis for future ship-model correlation studies" (ITTC, 1969). In 1973, as requested by the ITTC, SSPA created computer programs with different assumptions and extrapolation methods, which were evaluated by ten institutions within the ITTC through a comparison of power and propeller turning rate predictions with speed trials (ITTC, 1978; Lindgren & Dyne, 1980). This collaborative effort culminated in the development of the 1978 ITTC Performance Prediction Method, based on the comparison of approximately one thousand sea trials with model test predictions. Over the years, the originally recommended method underwent several revisions, including the replacement of the roughness allowance formulation by replacing the previous one with Townsin and Dey (1990), the introduction of a new correlation allowance formulation (ITTC, 1990), and modifications to the calculation of air resistance (ITTC, 2014). Nevertheless, the ITTC-78 method (ITTC, 2021a) remains in effect even after 45 years.

In this study, the ITTC-78 method (ITTC, 2021a) is used to extrapolate towing tank test results to full scale. The full-scale resistance of a ship is described by the equation

$$C_{\mathrm{TS}} = (1+k)C_{\mathrm{FS}} + \Delta C_{\mathrm{F}} + C_{\mathrm{A}} + C_{\mathrm{R}} + C_{\mathrm{AAS}}, \tag{2.1}$$

where k represents the form factor, C_{FS} denotes the frictional resistance coefficient in full scale (the subscript 'S' signifies the full-scale ship), C_{R} corresponds to the residual resistance coefficient, ΔC_{F} represents the roughness allowance, C_{A} accounts for the correlation allowance, and C_{AAS} characterises the air resistance coefficient. The determination of full-scale resistance hinges on two key components: the friction line and the form factor concept. These concepts, along with their historical backgrounds, will be reviewed in Section 2.1 and Section 2.2, respectively.

2.1 Friction Line

Frictional resistance coefficients have been a subject of extensive debate in early prediction methods, particularly those based on the Froude method, which calculates the residual resistance from,

$$C_{\mathrm{TM}} = C_{\mathrm{R}} + C_{\mathrm{FM}} \ . \tag{2.2}$$

Eq. 2.2 assumes that the frictional resistance of a ship is equivalent to that of a flat plate with the same surface area. The remaining part of total resistance coefficient, apart from C_{FM}, is referred to as the residual resistance coefficient (C_{R}), assumed to be same in both model and full-scale. Consequently, frictional resistance significantly influences final predictions. Before 1948, European towing tanks adhered to Froude's method and coefficients, while the American Towing Tank Conference (ATTC) adopted the Schoenherr formulation (Schoenherr, 1932).

The 5^{th} International Towing Tank Conference (ITTC) unanimously decided to leave Froude's coefficients, but no unanimous agreement was reached on any other particular line as the final choice. Instead, it was suggested that either the Froude or Schoenherr line could be used to facilitate the transition of results between the two systems once a consensus was reached. However, no alternative friction line proposals were put forth in subsequent conferences. The need for a new friction line was emphasised at the Scandinavian Conferences in 1954 ("Proceedings of the 7th ITTC", 1954). In the same year, the concept of the form factor, which was later adopted in the ITTC-78 method, was suggested by Hughes (1954) along with a new friction line. As the inclination to abandon the Froude coefficients grew and resistance to the universal use of the Schoenherr line persisted, the Madrid Conference (ITTC, 1957) was convened to establish a new "conference" line that met the following criteria:

1. "must produce, on the average, better correlation among geosim models of a variety of forms at different scales than does the Schoenherr line; and

2. must produce lower smooth-ship resistance in order to avoid the small or negative roughness allowances found for model all-welded hulls when the Schoenherr line is used for prediction of ship resistance" (ITTC, 1957, p.73).

The motivation behind the urgent need for a new line, as stated in item 2, was primarily driven by the transition from riveted hulls to all-welded hulls. The adoption of welding techniques and improved hull surface finish significantly reduced the full-scale resistance. Consequently, existing extrapolation methods had to apply small or negative roughness allowances to achieve correlation with sea trials. Item 1 indicates a shift toward three-dimensional flow analysis, specifically the form factor approach, as opposed to Froude's two-dimensional method.

The investigation by the ITTC on the existing flat plate and geosim test data did indicate a line that is somewhat steeper than the Schoenherr line (ITTC, 1957). However, the determination of the steepness of the curve at model scale Reynolds numbers was primarily influenced by item 2. The Skin Friction Committee decided to adopt the line given by the formula

$$C_{\mathrm{F}} = \frac{0.075}{(\log_{10}(Re) - 2)^2} \ . \tag{2.3}$$

The formulation in Equation 2.3 is denoted as the ITTC 1957 model-ship correlation line (alternatively referred as the ITTC-57 line). The ITTC-57 line was recommended by the ITTC with the statement "that this is to be regarded only as an interim solution to this problem for practical engineering purposes" (ITTC, 1957, p.324).

To illustrate the impact of adopting the ITTC-57 line in conjunction with the Froude method, a comparison can be made between C_{F} values obtained from the ITTC-57 and Schoenherr lines at a typical model scale Reynolds number of $\log_{10} Re = 6.0$. The ITTC-57 line yields a 2.78×10^{-4} higher C_{F} value compared to the Schoenherr line. Using Equation 2.2, the C_{R} would be 2.78×10^{-4} lower when the ITTC-57 line is employed. Since C_{R} depends solely on the Froude number, and the C_{F} values of the ITTC-57 and Schoenherr lines are nearly identical at Reynolds numbers larger than $\log_{10} Re = 8.0$, the full-scale total resistance would be 2.78×10^{-4} lower at the corresponding speed when the ITTC-57 line is used instead of the Schoenherr line. It should be noted that the commonly used roughness allowance coefficient during that period was constant and equal to 4.00×10^{-4}. Consequently, the adoption of the ITTC-57 line resulted in a reduction in full-scale smooth-ship resistance predictions by more than half the magnitude of the roughness allowance. In this way, the ITTC-57 line fulfilled the general requirement of the specification for a new engineering line (ITTC, 1957).

In the following decades, alternative formulations for C_{F} were proposed by Grigson (1999) and Katsui et al. (2005). These researchers criticised empirically derived lines, as they encompassed inevitable defects such as edge effects and measurement uncertainties. Instead, the Grigson and Katsui lines were analytically derived by calculating the frictional resistance of a flat plate using the integral form of the two-dimensional boundary layer equations under zero pressure gradient, similar to Coles (1956). Although the theoretical framework of the Grigson (Grigson, 1999) and Katsui (Katsui et al., 2005) lines is similar, the assumed behaviour of Coles' wake parameter (Coles, 1956) differs between the two lines across the range of Reynolds numbers. Consequently, the two lines result in significantly different friction lines.

Eça and Hoekstra (2008) and Wang et al. (2015) derived friction lines by numerically calculating the frictional resistance coefficients of an infinitely thin plate. A similar study is presented in Paper I, where the frictional resistance coefficients were computed using Reynolds-Averaged Navier-Stokes (RANS) equations and two turbulence models for Reynolds numbers ranging from typical model scale to full scale. Curve fits were applied to the computed data points at various Reynolds numbers, resulting in Numerical Friction Lines (NFL) for the $k-\omega$ SST and EASM turbulence models. These NFLs, obtained in Paper I, were compared with the ITTC-57 line (ITTC, 1957), Schoenherr line (Schoenherr, 1932), Hughes line (Hughes, 1954), Toki line (Toki, 2008), Katsui line (Katsui et al., 2005), Grigson line (Grigson, 1999), and the two numerical friction lines proposed by Eça and Hoekstra (2008) and Wang et al. (2015). Figure 2.1 presents the friction lines relative to the NFL of the $k-\omega$ SST turbulence model for improved visual clarity. It can be observed from Figure 2.1 that the $k-\omega$ SST lines by Eça and Hoekstra (2008) and Wang et al. (2015) are within $\pm 2\%$ of the C_{F} values obtained in Paper I for the same

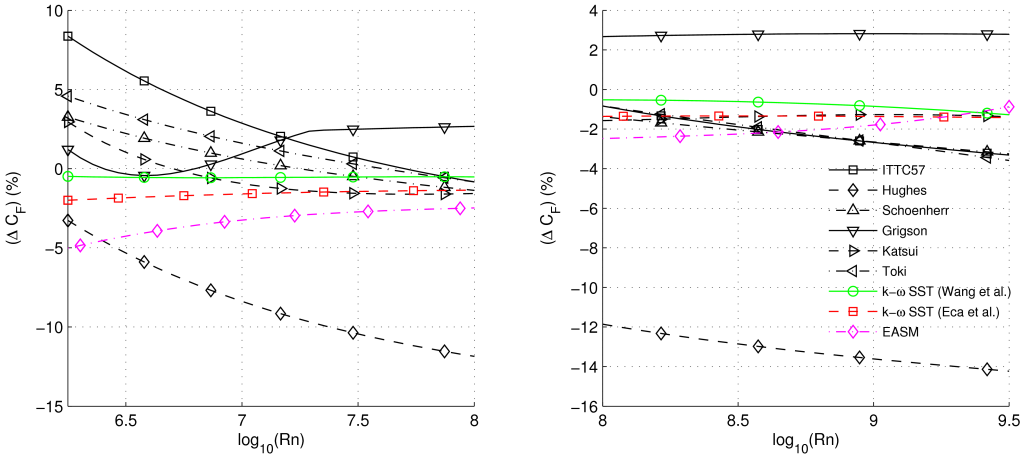

Figure 2.1: *Friction lines in comparison to numerical friction line of SHIPFLOW with $k-\omega$ SST turbulence model, from the study conducted in Paper I*

turbulence model across all Reynolds numbers. All numerical friction lines lead to lower C_F values compared to the other lines at the model scale Reynolds number. However, the discrepancy between all lines is considerably reduced in the full-scale Reynolds number range, except for the Hughes line, which consistently exhibits lower C_F values throughout the entire Reynolds number range.

Even though the ITTC-57 line was intended as an interim solution, it has remained in the extrapolation procedures, including the up-to-date recommended ITTC-78 Power Prediction Method (ITTC, 2021a). Investigations conducted by Toki (2008) showed that the expected gain by the revision of the ITTC-57 line in the ITTC-78 method is limited. Similar conclusions have been obtained from the study presented in Paper IV, where the accuracy of predictions using the ITTC-57 line and numerical frictional lines developed in Paper I were compared. Paper IV concluded that the roughness allowance (ΔC_F) coupled with the correlation allowance (C_A) and the form factor determination method have much a more profound effect on the end results compared to the choice of the friction line. Additionally, changing the friction line is likely to require changing the well-accustomed correlation factors of each institution, while only a marginal gain in accuracy can be expected.

2.2 Form Factor Concept

The concept of employing separate extrapolators, such as the form factor concept, for each hull, instead of relying on two-dimensional flow analysis, as in Froude's method, has been extensively discussed since the early 20th century. In 1954, the Skin Friction Committee emphasised that the extrapolation of resistance from model to ship scale should consider the effects of three-dimensional flow, which also necessitates the generation of a suitable smooth turbulent friction line ("Proceedings of the 7th ITTC", 1954). The

argument for three-dimensional flow stems from the fact that the frictional resistance of an actual curved hull surface generally differs from the two-dimensional frictional resistance of a flat plate. However, although Froude's assumption (Eq. 2.2) does not explicitly distinguish the contribution of the three-dimensional shape of the hull, it implicitly exists in the residual resistance, denoted as $C_{\mathrm{R}} = C_{\mathrm{PV}} + C_{\mathrm{W}}$, where C_{PV} is the viscous pressure resistance coefficient caused by the shape of the hull, and C_{W} represents the wave resistance coefficient. In Froude's method, as C_{R} is a function of the Froude number (Fn), it remains unchanged when the coefficient is scaled from model to ship using the same Froude number value. As stated in ITTC (1957), "some of the resistance represented by C_{PV} is undoubtedly of a skin friction nature scaling with Reynolds number". Therefore, addressing this point of view for the Froude's method was provided by Hughes (1954) who suggested separating C_{R} into two components, C_{PV} and C_{W}, and scaling the viscous pressure resistance with Reynolds number (Re), assuming that C_{PV} is a constant percentage of C_F for any given hull form. This approach leaves C_{W} to scale with the Froude number. The total resistance formulation proposed by Hughes (1954) is as follows:

$$\begin{aligned} C_{\mathrm{T}} &= C_{\mathrm{F}} + C_{form} + C_{\mathrm{W}} \ , \\ C_{form} &= k \ C_{\mathrm{F}} \ , \end{aligned} \tag{2.4}$$

where C_{F} is the resistance equivalent to a flat plate, the new term introduced by Hughes (1954), C_{form}, is form resistance due to the shape of the hull, C_{W} is wave resistance, and k is the form factor. In turbulent flow conditions, C_{form} is proportional to C_{F}, on the condition that the flow is smooth, free from separation, and the hull has a symmetrical form when towed at a zero incidence angle. The form resistance, C_{form}, consists of components arising from additional skin friction caused by curvature effects, eddy-making, and flow in transverse directions (Hughes, 1954).

The form factor concept proposed by Hughes (1954) was adopted by the ITTC 1978 Power Prediction Method as it showed better correlation with sea trials compared to the predictions obtained from two-dimensional analyses (ITTC, 1978). However, discussions regarding scale effects on the form factor have persisted, including during the 15th ITTC Conference when the ITTC-78 method was accepted (ITTC, 1978). Re-analysis of geosim test data conducted by García Gómez (2000) and Toki (2008) confirmed the presence of scale effects. Model tests performed on geosim families of KVLCC2 and KCS hulls indicated that scale effects were observed on the form factor for both hulls (Van et al., 2011). Additionally, CFD studies by Pereira et al. (2017) demonstrated a speed dependency of the form factor, which exceeded the level of numerical uncertainties. Terziev et al. (2019) pointed out that form factors are not only dependent on the Reynolds number but also vary with the Froude number. Further CFD investigations presented by Raven et al. (2008), Wang et al. (2015), and Dogrul et al. (2020) supported the existence of speed dependency on the form factor. They also indicated that the main cause of the scale effects lies in the "ITTC 57 model-ship correlation line" rather than the hypothesis of Hughes (1954).

The speed dependency of the form factors and scale effects were further explored in Papers II, III, IV, and V. The KVLCC2 and KCS hulls were computed at a low and the design speeds using both EASM and $k-\omega$ SST models in Paper II. The CFD based form factors with the ITTC-57 line showed significant variation between the two model scale

Reynolds numbers, while the form factors based on the numerical friction lines derived in Paper I remained nearly the same. Additionally, the form factors based on the ITTC-57 line were approximately 9.0% and 5.7% lower in the model scale compared to the full-scale for KVLCC2 and KCS hulls, respectively (calculated from the ratio $(1+k_S)/(1+k_M)$, where k_S and k_M are form factors in full and model scale). Conversely, the form factors with numerical frictional lines yielded consistently and nearly the same value for all Re, supporting the hypothesis of Hughes (1954). The speed dependency and scale effects on form factors were further investigated for the KVLCC2 and KCS hulls in Paper III utilising multiple CFD codes, and friction lines such as the ITTC-57 line, the Katsui line (Katsui et al., 2005) and the numerical friction lines derived from the same code and turbulence model used for the double-body computations. As concluded earlier in Paper I, the speed dependency of form factors with the ITTC-57 line was observed for both hulls. The speed dependencies were reduced considerably when the Katsui line was used for the form factors, and they were nearly eliminated with numerical friction lines for all test cases.

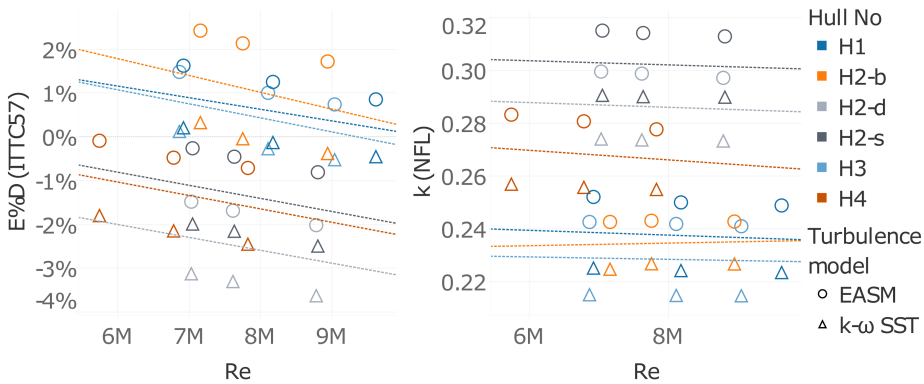

Figure 2.2: *Comparison error of form factors using the ITTC-57 line (left) and the form factors using the NFL (right) for all test cases at varying speeds, Paper IV*

Based on the conclusions from Papers II and III, the speed dependency of the form factors was further investigated in Paper IV where Best Practice Guidelines (BPG) were developed for CFD based form factor method using double-body computations. Six new test cases, including hulls at ballast, design, and scantling loading conditions, were computed at three different model scale Reynolds numbers. As presented in Figure 2.2 (plot on the left), the discrepancy between the CFD based form factors and experimentally determined form factors varied with a clear trend with Reynolds number when the ITTC-57 line was used. On the contrary, the CFD based form factors with the numerical friction lines remained fairly constant with varying Re, except for one test case. Further analysis of the local flow of this test case highlighted that the trend of decreasing form factor by the increasing Reynolds number observed for the H4 test case, seen in Figure 2.2 (plot on the right), was caused by mild bubble type (Larsson & Raven, 2010) flow separation at the stern. As Reynolds number increased, the separation diminished in intensity.

Consequently, the contribution of the form resistance relative to the viscous resistance, the form factor, was reduced. Note that, according to the form factor hypothesis of Hughes (1954), the existence of flow separation violates the preconditions of the form factor hypothesis, and as a consequence, the currently recommended extrapolation method (ITTC, 2021a, 2021d). However, the utilisation of numerical friction lines for the form factor determination can successfully test whether the resistance extrapolation will work or not.

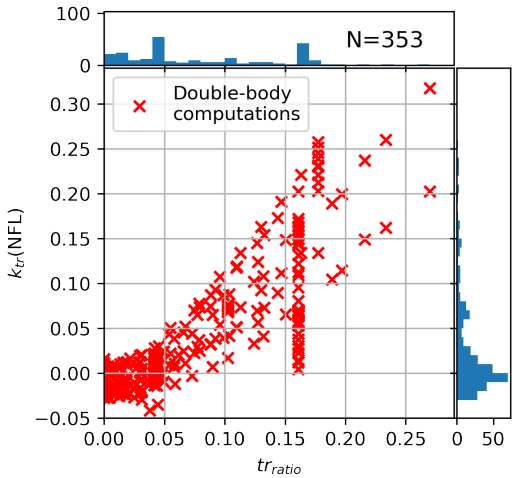

Figure 2.3: *The discrepancy between the model and full scale form factors with numerical friction lines versus the transom submergence, Paper V*

The scale effects on the form factor were investigated in the context of vessels with varying transom submergences in Paper V. Seven test cases, including KVLCC2 and KCS hull forms, were computed at varying draughts and trim angles where the transom submergence varies for each loading condition. Qualitative analysis of the flow field and quantitative conclusions demonstrated that flow separation does cause issues when the recommended resistance scaling (ITTC, 2021d) is applied even with the numerical friction lines. On the contrary, the scale effects on the form factors were not observed when numerical friction lines were employed and no flow separation occurred. This observation is demonstrated in Figure 2.3, where the x-axis represents the transom submergence through the ratio between the submerged transom area and the midship cross-section area (tr_{ratio}), and the transom form factor ($k_{tr} = k_S - k_M$) is plotted on the y-axis. According to Hughes (1954), a transom submergence that does not trigger a flow separation (typically $tr_{ratio} < 0.025$) should have the same model and full scale form factors ($k_{tr} \approx 0$). As presented in Figure 2.3, approximately 700 double body computations performed for seven test cases in model and full scale confirm the Hughes (1954) hypothesis as the k_{tr} values varied between $\pm 3\%$ which is approximately the combination of the numerical uncertainties from both scales. It is also observed in Figure 2.3 that the difference between the form factors between the model and full scale increases with the increasing transom

submergence, i.e. flow recirculation region. As concluded in Paper V and recognised by the ITTC (ITTC, 2021d), the current recommended procedures of the form factor approach for any vessel with a substantial transom stern for which the transom runs wet are not valid. It is demonstrated that the form factor is not independent of the Reynolds number when there is flow separation in the boundary layer. When the same model and full scale form factors are used to extrapolate the resistance, the full-scale viscous resistance is substantially under-predicted in the case of a wetted-transom flow as demonstrated in Paper V.

2.2.1 Experimental Determination of the Form Factor

Low-speed method

The low-speed method was proposed by Hughes (1954), who also introduced the form factor concept. This method involves conducting model tests at extremely low speeds, where the contribution of wave resistance becomes negligible. According to the formulation in Eq. 2.4, when the wave resistance term is eliminated, the total resistance coefficient consists solely of the frictional resistance coefficient and the form resistance. Since the form resistance is proportional to C_{F}, dividing the total resistance coefficient measured at a low-speed, where wave resistance is negligible, by the frictional resistance coefficient yields a value of $1+k$. Consequently, the form factor can be obtained. However, it is important to note that the low-speed method poses several challenges and impracticalities. Firstly, the speed range for the resistance tests must be significantly reduced to extremely low Froude numbers (Fn) and Reynolds numbers (Re), which may compromise the attainment of fully turbulent flow during the tests, even with the use of turbulence stimulators. Additionally, the accuracy of measurements tends to deteriorate at such low speeds, which can impede the accurate determination of the form factor according to Hughes' method (Lindgren & Dyne, 1980).

Prohaska Method

Alternatively, Prohaska (1966) proposed a simple method to derive the form factor based on Hughes' description (Hughes, 1954). In this method, the wave resistance coefficient, C_{W}, can be expressed as shown in Eq. 2.5, which is the asymptotic expansion formula for the wave-making resistance coefficient presented by Inui as cited in (Toki, 2008),

$$C_{\mathrm{W}} = a \times Fr^4 + b \times Fr^8 + c \times Fr^{12} + d \times Fr^{16} \ . \tag{2.5}$$

C_{T} at model scale as shown in Eq. 2.4, can be expressed along the Inui's asymptotic expansion formula, Eq 2.5, as

$$C_{\mathrm{TM}} = (1+k) \times C_{\mathrm{F}} + C_{\mathrm{W}} = (1+k) \times C_{\mathrm{F}} + a \times Fr^4 + b \times Fr^8 + c \times Fr^{12} + d \times Fr^{16} \ . \tag{2.6}$$

Neglecting the higher order terms of Eq. 2.6, as they are close to zero at low Froude numbers and dividing both sides by C_{F}, the following linear relationship is obtained,

$$C_{\mathrm{TM}}/C_{\mathrm{F}} \approx (1+k) + a \times Fr^4/C_{\mathrm{F}} \ . \tag{2.7}$$

Prohaska (1966) observed that when approximately 200 model tests were plotted using Eq. 2.7, the $C_{\mathrm{T}}/C_{\mathrm{F}}$ values for most models followed a linear trend within the recommended range of Froude numbers (Fn) between 0.1 and 0.2. However, some exceptions were identified for hull forms with $C_B > 0.75$, twin-screw models with appendages, and models with full aft body lines. These exceptions were attributed to significant changes in sinkage and trim during the tests, as well as flow separation (Prohaska, 1966). It is important to note that the Prohaska method, as discussed in the literature, has a primary limitation. It does not account for bulbous bows near the water surface or partly submerged bulbous bows under partial loading conditions. These limitations were not addressed by Prohaska (1966) as the model test data used by Prohaska dates back to 1966 and earlier, when bulbous bows were not a common design feature. Additionally, the detection of flow separation in the model tests and the treatment of deeply submerged transoms remain additional challenges associated with the Prohaska method.

In Paper III, the uncertainties in form factor determination caused by the Prohaska method were addressed. The first source of uncertainty arises from the applicability of the Prohaska method to ships with medium or large bulbous bows. As demonstrated in Paper III, the $C_{\mathrm{T}}/C_{\mathrm{F}}$ values of hulls with large protruding bulbous bows did not exhibit a linear trend within the recommended range of Fn due to the presence of steep waves generated by the bulb. The applicability of the Prohaska method is even less suitable for partially submerged bulbs, as even steeper waves are generated under ballast loading conditions, which is the condition for most sea trials. Considering that bulbous bows are now common in modern ship design, it is difficult to justify the validity and practicality of the Prohaska method for all hull designs and loading conditions.

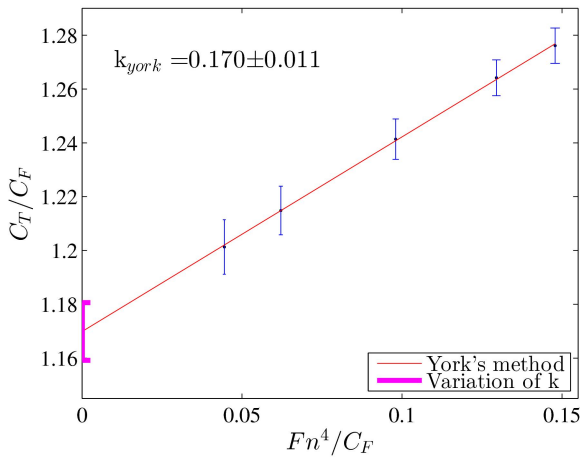

Figure 2.4: *Prohaska plot of KVLCC2 in ballast loading condition with measurement uncertainties, Paper III*

The second source of uncertainty associated with the Prohaska method originates from the experimental uncertainties in the resistance tests. In Figure 2.4, the Prohaska plot of KVLCC2 is presented for the ballast loading condition. The Prohaska plot illustrates

that the measured C_T/C_F values align linearly, as suggested by Prohaska (1966), due to the suitable forebody and bulb design of the KVLCC2 hull. Therefore, the applicability of the Prohaska method is not in question for the KVLCC2 hull under the ballast loading condition. As visualised in Figure 2.4, the combined measurement uncertainties and the uncertainty of the form factor determined by the Prohaska method are represented with error bars. The model test results of KVLCC2 in ballast condition in Paper III, along with six other test cases in various loading conditions in Paper IV, demonstrate that the experimental uncertainty is noticeably amplified for the form factor as a result of the regression analysis. This amplification of the uncertainty on the form factor can be much more severe if a hull with medium or large protruding bulbous bow was tested, as C_T/C_F values often cannot be used in the low speed range since they would not linearly align with the rest of the measurements. Therefore, the uncertainty of 0.011 on the form factor (0.022 within the 95% confidence interval) with the Prohaska method on KVLCC2 in ballast condition, as presented in Figure 2.4, can be considered merely as a best-case scenario.

Polynomial Approximation Method

The Prohaska method assumes a linear relationship between wave resistance and Fn^4 when the towing speed is low. However, the applicability of the Prohaska method is limited for vessels with bulbous bows, as the total resistance is nonlinear and cannot be expressed by Eq. 2.7. Therefore, Shirose and Hirono (1982) suggested approximating the wave resistance with a polynomial expression of Fn such as

$$C_{\mathrm{W}} = \sum_{j=N_1}^{N_2} a_j Fr^j \tag{2.8}$$

where a_j represents the coefficients in the polynomial expression. By substituting this polynomial expression into the total resistance coefficient equation (Eq. 2.4) and dividing both sides by C_{F},

$$C_{\mathrm{TM}}/C_{\mathrm{F}} = (1+k) + \sum_{j=N_1}^{N_2} a_j Fr^j \ . \tag{2.9}$$

The form factor k and the coefficients a_j can be determined using a least squares method to fit the polynomial to the experimental data. It is worth noting that when $N_1 = N_2 = 4$, the polynomial approximation method reduces to the Prohaska method, which assumes a linear relationship between the total resistance coefficient and Froude number.

The polynomial approximation method is particularly useful for cases where the total resistance coefficients are not linearly aligned, such as when bulbous bows are present or under specific loading conditions. It allows for a more flexible representation of wave resistance, capturing humps and hollows in the resistance curve. However, the drawback of this method is the need to cover a wide range of Froude numbers in the resistance tests, including low speeds where measurement uncertainties tend to increase, as shown in Papers III and VI. Additionally, a higher number of model test runs may be required to fit the polynomial accurately, given the use of a higher-degree polynomial.

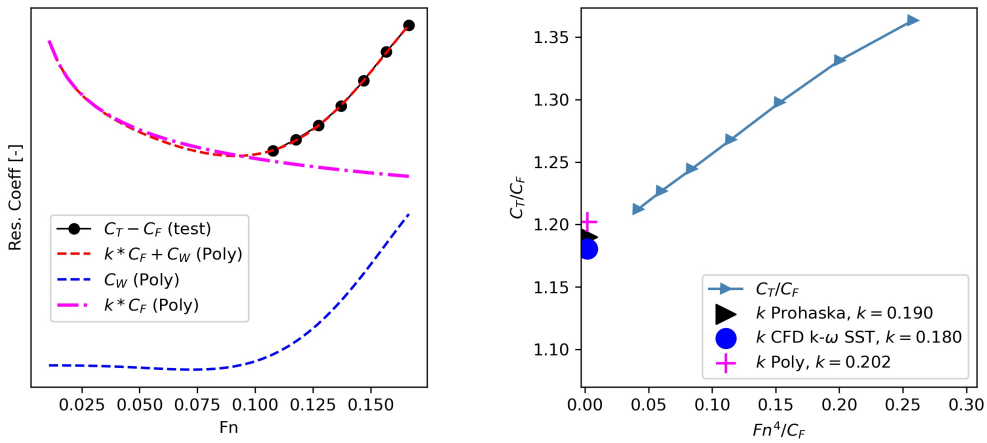

(a) *Resistance coefficients* (b) *Prohaska plot*

Figure 2.5: *Resistance test results of a full-block vessel at design loading condition*

The polynomial approximation method is used for the tests performed with a full block vessel at the design loading condition. As seen in Figure 2.5, the $C_{\mathrm{TM}}/C_{\mathrm{F}}$ values align linearly, as suggested by the Prohaska method. Since the vessel is a slow-steaming full block vessel, the bulb design does not cause humps and hollows in the design loading condition. Therefore, the assumption of the Prohaska method is fulfilled, and the form factor can be successfully determined. In addition to the Prohaska method, both the polynomial approximation method and the CFD based form factor (see Section 2.2.2) suggest similar form factors. The resistance coefficients, as approximated by the polynomial method (Shirose & Hirono, 1982), are presented in Figure 2.5a. The summation of measured wave resistance and the form resistance (denoted as $C_{\mathrm{T}} - C_{\mathrm{F}}$ (test)) is successfully approximated by the polynomial fit (denoted as $k * C_{\mathrm{F}} + C_{\mathrm{W}}$).

On the other hand, Figure 2.6 shows the resistance test results of a slender vessel with a partially submerged bulbous bow under ballast loading condition. In this case, the total resistance coefficients do not align linearly, rendering the Prohaska method inapplicable. However, both the polynomial approximation method and the CFD-based method provide consistent form factor predictions. As presented in Figure 2.6a, the polynomial approximation method successfully captures the test points (summation of measured wave resistance and the form resistance). The wave resistance approximation by the polynomial fit in Figure 2.6a indicates humps and hollows, hence, explaining why the Prohaska method fails for this test case.

It should be mentioned that the number of test points is limited for both examples presented in this section. Even though, the polynomial approximation method is applicable for these test cases, it failed to predict the form factors in some other test cases where the low-speed region was not tested. Therefore, it is important to note that the polynomial approximation method's applicability is constrained by the number of test runs, especially at low Froude numbers. If the low-speed region is not adequately covered in the resistance

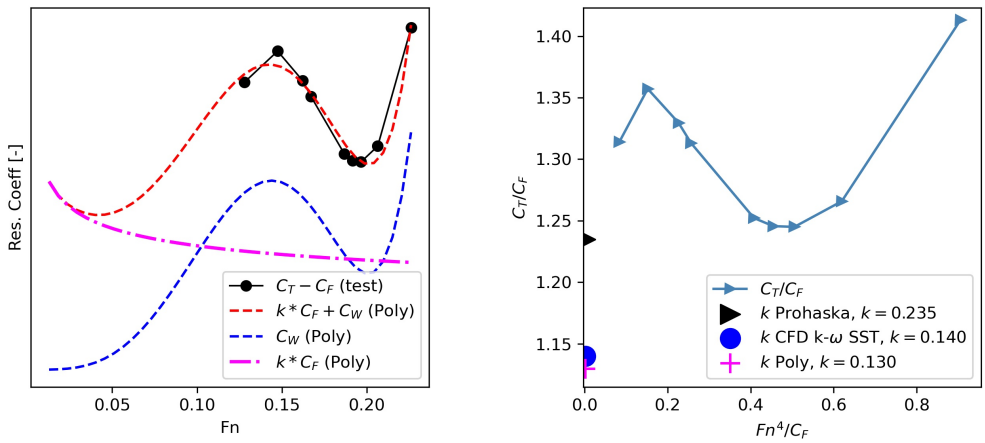

(a) *Resistance coefficients* (b) *Prohaska plot*

Figure 2.6: *Resistance test results of a slender vessel with a partially submerged bulbous bow*

tests, the accuracy of the polynomial fit and the resulting form factor estimation may be compromised.

2.2.2 Computational Determination of the Form Factor

The computational determination of the form factor using CFD follows a methodology similar to the low-speed approach proposed by Hughes (1954) since both methods involve obtaining the total resistance without the wave resistance. The advantage of the CFD-based approach lines in the double-body computation setup which can effectively neglect wave resistance, while any model scale speed can be computed as long as the flow is turbulent. The CFD based form factor is derived using the relation,

$$(1+k) = \frac{C_{\mathrm{F}}^{'} + C_{\mathrm{PV}}^{'}}{C_{\mathrm{F}}} = \frac{C_{\mathrm{V}}^{'}}{C_{\mathrm{F}}} \ , \tag{2.10}$$

where the frictional resistance coefficient ($C_{\mathrm{F}}^{'}$) and viscous pressure resistance coefficient ($C_{\mathrm{PV}}^{'}$) are obtained from a double-body CFD simulation, as explained in Section 3. C_{F} in the denominator of Eq. 2.10 represents the equivalent flat plate resistance in two-dimensional flow, obtained at the same Reynolds number as the computations. In Papers II, III, IV, V, and VI, the ITTC-57 model-ship correlation line (ITTC, 1957) and the numerical friction lines presented in Paper I were employed. Additionally, the Katsui line (Katsui et al., 2005) was incorporated into the analysis in Paper III.

Some of the limitations discussed in Section 2.2.1 for the Prohaska are also applicable to the CFD-based form factor method in similar contexts, particularly for hulls with prominent protruding bulbs. When such bulbs are positioned too closely to the still water surface (the mirror plane for the double-body simulations), the flow may become

excessively accelerated and, in some instances, even separated around the bulb. Raven et al. (2008) proposed a mitigation strategy involving submerging the bulb further by trimming the hull bow down. In Paper II, the loading condition of KVLCC2 and KCS hulls was systematically varied to assess the sensitivity of the form factor to changes in sinkage and trim, with results indicating limited form factor variation for both hulls. Furthermore, the discrepancy between form factors calculated from static and dynamic sinkage and trim was found to be smaller than the numerical uncertainties. Therefore, the suggestion of altering the loading condition to mitigate the issues arising from a large bulb near the water surface is feasible, as indicated in Paper II. However, Paper IV highlights that modifying static trim or sinkage may not always resolve flow separation around the bulb. In such cases, local modification of the bulb geometry, as performed for a test case in Paper IV, can effectively reduce steep pressure gradients, thereby preventing flow separation.

In contrast to the artificially induced flow separation around the bulb resulting from the double-body approximation, accurately modelling naturally occurring flow separation is crucial in both model and full-scale free-surface flow using computational fluid dynamics (CFD) simulations for form factor calculation. The conventional ITTC-78 method does not allow the us of the form factor method for the viscous resistance scaling (ITTC, 2021d) when flow separation is present. However, alternative methodologies, as proposed in Paper V, offer solutions to address this challenge. Therefore, it is imperative to accurately capture the bubble type flow separation observed at the stern of full block vessels and the flow separation occurring behind substantially submerged transoms accurately in both model and full-scale computations rather than attempting to prevent them.

A pivotal criterion for the widespread acceptance and utilisation of the CFD-based form factor method is its applicability across a majority of CFD codes and the consistency of predictions among different codes. This aspect was rigorously investigated in Paper III, which engaged contributions from nine organisations employing seven different codes. The study, initiated by the ITTC Specialist Committee of Combined CFD/EFD Methods, revealed that most codes, when configured with a specific CFD setup, exhibited consistent patterns of form factor predictions across various test cases. Nonetheless, it was observed that dependencies on CFD setups varied among different codes. Consequently, no general recommendations can be made regarding form factor determination for all CFD codes and setups. Instead, it is recommended for each CFD code to derive unique best practice guidelines for form factor calculations following the Quality Assurance Procedure of the ITTC (ITTC, 2021c), as demonstrated in Paper IV.

To further validate the trends observed in Paper III, additional studies involving a larger sample of hulls, as shown in Papers IV and V, are necessary. If these studies confirm the identified trends, the application of correlation factors (such as C_{P}-C_{N} or C_{A}) specific to each code and method can further mitigate disparities in full-scale predictions and enhance agreement among different codes. Thus, the incorporation of these correlation factors holds potential for improving the consistency of results in full-scale predictions.

2.3 Combined EFD/CFD Method: CFD Based Form Factor

The combination of computational fluid dynamics (CFD) and experimental fluid dynamics (EFD) offers alternative approaches to performance prediction. By leveraging the strengths of both methods, the accuracy of power predictions can be improved, specially when dealing with uncertainties and assumptions in the extrapolation procedure or towing tank tests that outweigh the numerical uncertainties and modelling errors associated with CFD applications.

As explained in Section 2.2, the form factor is a significant source of uncertainty in the 1978 ITTC Performance Prediction method. Relying on the EFD based Prohaska method for form factor determination and considering the impact of scale effects on form factor pose challenges in estimating full-scale ship resistance. To address these issues, double-body Reynolds Averaged Navier-Stokes (RANS) computations are proposed as an alternative or supplementary method to the Prohaska method. This approach allows for the replication of original form factor conditions while maintaining numerical simplicity.

Flow separation poses another concern, which undermines the validity of the viscous scaling, i.e., the form factor concept. Double-body computations can be employed to adjust the scaling of viscous resistance in cases involving flow separations, such as bubble-type separation around the stern of full-block vessels or substantially submerged transoms with a wet transom. This section elaborates on the suggested combined EFD/CFD combined methods.

2.3.1 One Form Factor Method

The one form factor method follows the same principles for scaling viscous resistance as the ITTC-78 method (ITTC, 2021d) but introduces the use of a CFD-based form factor as an alternative method for determining the form factor, as originally suggested by Raven et al. (2008). The extrapolation process involves the following steps:

1. C_{TM} is obtained from the towing tank tests.
2. The form factor, k is determined either by the Prohaska method (Prohaska, 1966) or by CFD in model scale (Korkmaz, Werner, & Bensow, 2021).
3. The residual resistance is calculated as $C_{\mathrm{R}} = C_{\mathrm{TM}} - (1 + k_{\mathrm{M}})C_{\mathrm{FM}}$
4. The full-scale form factor is assumed to be the same as the model scale
5. The full-scale total resistance coefficient is calculated as Eq. 2.1 where,
    - Residual resistance is obtained by using the model-scale form factor
    - Viscous resistance is obtained by using the same model-scale form factor.

The CFD-based form factor method was initially investigated in Paper II, as explained in Section 2.2.2. In a joint study (Paper III) conducted with the participants of the ITTC Specialist Committee on the Combined CFD/EFD Methods, various CFD methods were

evaluated. Subsequently, the CFD-based form factor method was verified and validated through multiple test cases following the Quality Assurance Procedure of ITTC (ITTC, 2021c) in Paper IV. The two studies presented in Papers III, and IV provided a solid basis and argumentation for the ITTC Specialist Committee on the Combined CFD/EFD Methods to recommend the CFD based form factor method as a supplementary method. Upon acceptance by the ITTC Resistance and Propulsion Committee, the form factor definition in the ITTC-78 method (ITTC, 2021a) was updated as follows:

> "k is the form factor determined from the resistance test, see ITTC standard procedure 7.5-02-02-01. Additionally, the determination can be supported by CFD calculation according to ITTC Guideline 7.5-03-02-04, "Practical Guidelines for Ship Resistance CFD", and following ITTC Recommended Procedure 7.5-03-01-02, "Quality Assurance in Ship CFD Application", using model scale benchmark data as well as full scale data for the demonstration." (ITTC, 2021a, p.5)

In summary, the one form factor method incorporates the CFD-based form factor as an alternative approach to enhance the accuracy of resistance prediction and broaden the applicability of the ITTC-78 method.

2.3.2 Two Form Factor Method ($2-k$ Method)

In situations where flow separation occurs either in the model or full-scale vessel, or in both scales, the conventional form factor approach, as described in ITTC (2021d), proves inadequate due to the violation of its preconditions caused by flow separation (Hughes, 1954). The use of a CFD-based form factor determination method, as employed in the one form factor method (see Section 2.3.1), fails to address the challenges associated with scaling viscous resistance. Therefore, an alternative method called the two form factor method or $2-k$ method is proposed in this section, based on the investigations presented in Papers IV and V.

The $2-k$ method is specifically tailored for cases involving flow separation. A common type of flow separation, known as the bubble type separation (Larsson & Raven, 2010), occurs at the stern of full block vessels. Bubble type separation typically arises from sudden increase in pressure after passing through a low-pressure region such as the bilge region. This type of separation is characterised by the interaction between the boundary layer and the pressure distribution. The pressure distribution around the hull plays a crucial role in boundary layer development, which, in turn, affects the pressure due to the displacement effect. As demonstrated in Paper V, an increase in Reynolds number (Re) diminishes the influence of viscosity and mitigates adverse pressure effects, leading to the dissipation of flow separation and a reduction in the form factor.

Another type of flow separation occurs in the region of recirculating flow behind a substantially submerged transom, similar to the flow over a backward-facing step. The mean velocities around the stern overhang of a vessel experience a sudden increase in cross-sectional area, resulting in flow separation because the mean velocities cannot follow the sharp turn at the transom edge. Consequently, a low-pressure region forms, giving rise to a recirculation flow region behind the transom. It is significant to note that flow

separation behind the transom differs from the bubble type separation (Larsson & Raven, 2010), as the root causes are not solely attributed to boundary layer effects and pressure gradients, as in the case of a largely submerged transom. Consequently, full-block vessels with significant transom submergence are more prone to experience wetted-transom flow in both model and full-scale, as highlighted in Paper V. Due to the persistent recirculating flow, using the same form factor in both model and full scale leads to underestimation full-scale viscous resistance. In Paper V, the viscous pressure resistance coefficient is decomposed into two components: one proportional to the frictional resistance coefficient of a friction line and the other that is *not* proportional. The findings in Paper V suggest that for vessels experiencing flow separation, the viscous resistance scaling in the one form factor method requires either correction or direct full-scale prediction using CFD, as the portion of the viscous pressure resistance coefficient that is not proportional to the frictional resistance coefficient is omitted. Similar to the application in Paper IV for hulls with mild flow separation at the stern (bubble type) and in Paper V for hulls with substantially submerged transoms, the $2-k$ method is employed by following these steps:

1. C_{TM} is obtained from the towing tank tests.
2. The model-scale form factor, k_{M}, is determined either by the Prohaska method (Prohaska, 1966) or by CFD (Korkmaz, Werner, & Bensow, 2021).
3. The residual resistance is calculated as $C_{\mathrm{R}} = C_{\mathrm{TM}} - (1 + k_{\mathrm{M}})C_{\mathrm{FM}}$
4. The full-scale form factor, k_{S}, is calculated using CFD based form factor method
5. The full-scale total resistance coefficient is calculated as

$$C_{\mathrm{TS}} = (1 + k_{\mathrm{S}})C_{\mathrm{FS}} + \Delta C_{\mathrm{F}} + C_{\mathrm{A}} + C_{\mathrm{R}} + C_{\mathrm{AAS}} \ , \tag{2.11}$$

   where,

   - Residual resistance is obtained by using the model-scale form factor
   - Viscous resistance is obtained by using the full-scale form factor.

In conclusion, the two form factor method ($2-k$ method) offers an alternative approach to address the challenges posed by flow separation in vessel resistance prediction. Traditional form factor methods and CFD-based form factor determination methods are inadequate in such cases. The $2-k$ method takes into account the specific characteristics of flow separation, such as bubble type separation and recirculation flow behind submerged transoms. By employing different form factors for the model and full-scale, it enables a more accurate prediction of viscous resistance in vessels experiencing flow separation. The proposed method, based on the findings presented in Papers IV and V, provides a valuable tool for researchers and towing tank practitioners in ship performance prediction.

2.3.3 Empirical Correction for Transom Submergence and Transom Form Factor

Instead of using the $2-k$ method, which necessitates double-body RANS computations and the demonstration of Quality Assurance for the CFD application, an alternative

correction method is proposed in Paper V. This correction method addresses the viscous resistance deficit caused by a wetted transom when using the ITTC-78 method for quantifying the transom form factor. An empirical correction formula has been developed to provide a quick and approximate estimation of the transom form factor, particularly for organisations without CFD capabilities and towing tank experiments involving tests at multiple loading conditions, such as trim optimisation tests (see Paper VI).

The resistance induced by a wetted transom can be analogised to the base drag observed in airfoil shapes with truncated trailing ends. It can be attributed to a reduction in hydrodynamic pressure on the base, caused by the entraining force exerted by the surrounding flow on the recirculation region behind the base, similar to the "jet-pump" effect described in Starke et al. (2007). The base drag phenomenon in projectiles and foil shapes with truncated trailing edges has been successfully modelled using relatively simple equations, as concluded in the investigations by Hoerner (1965). Motivated by this, an empirical correction formula has been derived through regression analysis of the results presented in Paper V.

The regression analysis aims to predict the transom form factor, denoted as k_{tr}, which represents the difference between the full-scale form factor k_{S} and the model-scale form factor k_{M},

$$k_{tr} = k_{\mathrm{S}} - k_{\mathrm{M}} \ . \tag{2.12}$$

The form factors in model and full scale are derived from the $k-\omega$ SST model using the numerical friction line. As argued earlier and presented in Papers II, III, IV, and V, the k_{tr} as in Eq. 2.12 from the ITTC-57 line include the scale effects introduced by the friction line itself; thus, they cannot be used to quantify the viscous resistance deficit in full scale.

The regression model was formulated with three independent variables: the ratio between the submerged transom area and the midship cross-section area (tr_{ratio}), the model-scale Reynolds number (Re_M), and the Longitudinal Centre of Buoyancy (LCB). By analysing the results of CFD computations for seven hull forms under various loading conditions and Reynolds numbers (as described in Paper V), the following empirical correction formula is obtained:

$$\begin{aligned} k_{tr} = \Big[-0.025 + tr_{ratio}\big(1.5 - 2.3tr_{ratio} - 0.07\mathrm{LCB}\big)\Big] \times \Big[-5.45 + \\ \log_{10}(\overline{Re_{\mathrm{M}}})\big(1.415 + 4.32tr_{ratio}\big) - \big(\log_{10}(\overline{Re_{\mathrm{M}}})\big)^2\big(0.081 + 0.55tr_{ratio}\big)\Big] \end{aligned} \tag{2.13}$$

where $\overline{Re_{\mathrm{M}}}$ is the average of Reynolds numbers in the model scale, and the LCB is relative to $\mathrm{L_{PP}}/2$ (in per cent of $\mathrm{L_{PP}}$). The suggested empirical correction method is applied through the following extrapolation procedure, similar to the $2-k$ method:

1. C_{TM} is obtained from the towing tank tests.
2. The model-scale form factor, k_{M} is determined either by the Prohaska method (Prohaska, 1966) or by model-scale CFD as described in the (ITTC, 2021b).
3. The residual resistance is calculated as $C_{\mathrm{R}} = C_{\mathrm{TM}} - (1 + k_{\mathrm{M}})C_{\mathrm{FM}}$

4. The full-scale form factor, k_S, as $k_S = k_M + k_{tr}$ where
   - if $tr_{ratio} \leq 0.025$, $k_{tr} = 0$
   - if $tr_{ratio} > 0.025$, k_{tr} is calculated from the Eq. 2.13
     - if the calculated $k_{tr} \leq 0$ then $k_{tr} = 0$
     - if the calculated $k_{tr} > 0$ then k_{tr} value can be used.
5. The full-scale total resistance coefficient is calculated as

$$C_{TS} = (1 + k_S)C_{FS} + \Delta C_F + C_A + C_R + C_{AAS} \ , \tag{2.14}$$

   where,
   - Residual resistance is obtained by using the model-scale form factor
   - Viscous resistance is obtained by using the full-scale form factor.

It is important to note that the correction proposed in Equation 2.13 includes a minimum transom area threshold, as small tr_{ratio} values may result in partially wetted transom or dry transom flow. The flow characteristics behind the transom depend on the overall vessel geometry and the wave pattern generated by the hull (Maki et al., 2006). Therefore, it is recommended to confirm the flow regime for cases with small transom submergence using free-surface RANS computations or model tests. If the flow behind the transom becomes dry or partially wetted, the assumptions of the double-body method are violated (either in the model or full-scale), rendering Equation 2.13 invalid regardless of the tr_{ratio} value.

In conclusion, the empirical correction method presented in this section offers an alternative approach to address the viscous resistance deficit caused by a wetted transom. This empirical correction formula provides a practical solution for organisations without CFD capabilities and enables a quick and approximate quantification of the transom form factor in various loading conditions.

3 Computational Methods

This section aims to summarise the key aspects of numerical methods employed for CFD applications, specifically double-body RANS resistance computations in model and full scale, as well as free-surface RANS resistance and self-propulsion computations in model and full scale. Throughout this project leading up to this thesis, two CFD codes, SHIPFLOW and FINE$^{\mathbf{TM}}$/Marine, have been utilised. The former code has been consistently applied in all papers included in this thesis, while the latter was specifically used in Papers I and VI.

3.1 Double-Body Computations

This section provides an overview of the double-body simulations conducted with the SHIPFLOW code in Papers II, III, IV, V and VI to obtain CFD-based form factors. While the double-body RANS simulation for viscous resistance of a smooth hull enjoys widespread use in industrial CFD applications (Larsson, 1998), the absence of a common Best Practice Guideline (BPG) is notable. This gap arises due to the diversity of numerical methods available within current CFD codes, as highlighted in Paper III.

Paper III presents a comparative analysis of CFD-based form factors computed by various organisations using different codes, turbulence models, and grid topologies, in comparison with model test data for the KVLCC2 and KCS test cases. Despite variations in methods and grids, the form factor predictions from the recommended CFD setups closely align with experimental results, exhibiting a standard deviation of 1.5% to 2.5% in terms of $(1 + \overline{k})$. This level of deviation is comparable to the experimental uncertainty reported in Papers III and IV and is consistent with the resistance computations conducted in the Tokyo 2015 Workshop (Hino et al., 2020). However, distinct code dependencies on specific CFD setups prevent the formulation of universal recommendations for form factor determination.

Expanding upon the findings of Paper III, Paper IV delves into Quality Assurance (QA) for the CFD-based form factor method at an organisational level. The QA procedure by ITTC (2021c) is rigorously followed in Paper IV, resulting in the development of Best Practice Guidelines (BPG) for determining CFD-based form factors using SHIPFLOW version 6.5. Systematic variations in grid density, non-dimensional cell height, grid refinement at the stern, domain size, and model scale speed are analysed across six test cases employing the $k - \omega$ SST and EASM turbulence models. The insights and recommendations emerging from this analysis are succinctly summarised in Paper IV, underscoring the necessity of updates in response to significant changes in numerical methods.

The best practice guidelines formulated in Paper IV are applied to the double-body computations conducted in Paper V, with one exception being the domain size. Investigations subsequent to the work in Paper IV revealed that the distance between the inlet and the forward perpendicular is insufficient, leading to blockage effects, particularly under design and scantling loading conditions. Consequently, the domain size in Paper V is extended to eliminate these blockage effects. The computations conducted at full scale

also adhere to the updated BPG, albeit with a 50% increase in the number of cells in the normal direction to the hull to maintain fine resolution near the wall.

Finally, the CFD-based form factor determination method is utilised in Paper VI where an open-shaft twin screw vessel was model tested for a trim optimisation study. Since the form factor determination needs to take place with the bare hull (without appendages except the rudder) at each loading condition, employing the Prohaska method increases the model test scope by at least 30%. In Paper VI, instead of employing experimental method of form factor determination for all loading conditions, the double-body computations have been used for most of the loading conditions. Consequently, the cost and time effort related to model tests were significantly reduced.

Grid Generation, Turbulence Modelling, and Verification & Validation Studies

Effective grid generation using the XGRID tool in SHIPFLOW plays a fundamental role in establishing best practices. Parametrically generated body-fitted structured grids ensure a nearly uniform distribution in both longitudinal and circumferential directions for most hull configurations. Achieving target y^+ values by adjusting the first cell size normal to the wall is essential for accurately calculating wall shear stresses, as extensively documented in Paper III. Sensitivity studies reveal that grid resolution significantly impacts form factor predictions in the aft body while having a lesser impact on other sections of the hull, as demonstrated in Paper II.

Turbulence modelling assumes a pivotal role in accurate force calculations and precise flow representation. Two-equation turbulence models exhibit superior predictive capabilities for resistance, whereas anisotropic non-linear statistical turbulence models offer greater accuracy in predicting local flow behaviours (Hino et al., 2020). Scrutinising the representation of local flow, especially at the stern where flow separation occurs, is imperative. The choice between combined EFD/CFD methods, such as the one form factor or two form factor approach, should depend on the presence or absence of flow separation. Notably, errors in turbulence modelling, including the transition from laminar to turbulent flow in wall-resolved approaches, have been identified as major sources of form factor prediction inaccuracies.

Verification and validation (V&V) studies play a pivotal role in refining CFD methods and ensuring the quality of CFD applications, including double-body computations for form factor determination. Grid dependence studies quantify numerical uncertainties in Papers III, IV, and V, revealing predicted uncertainties ranging from 0.6% to 1.6% for frictional resistance coefficients and 1.1% to 10.2% for viscous pressure resistance coefficients. Additionally, experimental uncertainties are determined, with validation consistently yielding comparison errors below the noise level. Exceptions occur in a few cases with exceptionally high numerical uncertainties attributed to the structured grid generation strategy, as detailed in Papers IV and V.

3.2 Free Surface

The free surface is a critical element in ship hydrodynamics, with its accurate prediction being vital for understanding the flow characteristics around a ship. This section briefly

introduces the two CFD codes, SHIPFLOW and FINE^{TM}/Marine, employed to perform computations with the free-surface Reynolds-Averaged Navier-Stokes (RANS) methods.

3.2.1 SHIPFLOW

In this study, SHIPFLOW version 7.0 is employed, utilizing a free surface Reynolds-Averaged Navier-Stokes (RANS) method. The same steady-state RANS solver used for double-body computations, discussed in Section 3.1, is also applied to free-surface RANS computations.

Resistance Computations

In Paper V, free-surface RANS resistance computations were conducted to investigate flow behind the transom. Ensuring reasonably similar flow behind the transom for both free-surface and double-body approaches is crucial, particularly when the transom is significantly submerged. This similarity is essential not only at the model scale but also at full scale, where the boundary layer plays a pivotal role in determining the flow regime behind the transom. Newly built ships undergoing sea trials cannot have hydrodynamically smooth hulls; they possess a certain hull roughness affecting the boundary layer. Therefore, the effect of hull roughness on the flow behind the transom must be assessed. Otherwise, a free-surface RANS computation with hydrodynamically smooth surfaces would predict a thinner boundary layer in full scale than the actual ship, resulting in discrepancies in the pressure distribution around the stern and the wave pattern aft of the transom. Hull roughness is particularly critical during the transitionary phase of the wetted-transom flow. Consequently, full-scale free-surface RANS computations incorporated the effect of hull roughness. As concluded in Paper V, the extent of the flow recirculation region and flow pattern were highly similar in double-body and free-surface computations, except for cases with small transom submergence, thus validating the double-body assumption. The critical threshold for similarity between free-surface and double-body computations was determined to be a transom Froude number (Fn_{tr}) of approximately 3.2 for a test case. However, it's important to note that the flow behind the transom depends on the overall vessel geometry and wave pattern generated by the hull, highlighting the necessity of confirming these findings through free-surface RANS computations or model tests, especially for small transom submergence.

Propulsion Computations

This section investigates the free-surface RANS method in self-propulsion mode, enabling the generation of a speed-power curve without relying on experimental data. Conducting simulations at full scale mitigates scale effects experienced by experimental methods, as both Froude and Reynolds number similarities can be simultaneously achieved. Consequently, research efforts in advancing ship performance prediction methods have primarily focused on Computational Fluid Dynamics (CFD). However, verification and validation of full-scale CFD computations are relatively recent and lag behind model-scale numerical methods, primarily due to limited access to publicly available full-scale data, such as sea trials. Nevertheless, growing interest and confidence in full-scale CFD computations are

evidenced by recent publications (Mikkelsen & Steffensen, 2016; Mikulec & Piehl, 2023; Niklas & Pruszko, 2019; Orych et al., 2021; Schouten et al., 2022; Sun et al., 2020), which indicate an acceptable level of accuracy in predicting sea trial conditions with full-scale CFD. However, most of the full-scale validation studies in the literature focus on a single ship or a limited number of sea trials.

To the best of the authors' knowledge, Paper VII represents the first comprehensive validation study in the literature, where full-scale CFD computations are performed for 14 common cargo ships. The power and propeller turning rate predictions obtained from the full-scale CFD computations are compared to 59 sea trials. The computational setup, grid generation, boundary conditions, domain size, and numerical methods remain consistent across all the computations, and they have been developed over several decades at SSPA and Flowtech, involving extensive verification, validation, and studies (Kim & Li, 2010; Korkmaz, 2015; Korkmaz, Werner, & Bensow, 2021; Korkmaz et al., 2015; Liefvendahl, 2023; Orych & Larsson, 2015; Orych & Regnström, 2023; Orych et al., 2021, 2022).

The numerical methods employed in this study differ significantly from the majority of state-of-the-art CFD codes, showcasing their potential for future applications in ship performance prediction. Thorough validation with a large number of sea trials is essential to establish confidence in CFD-based ship performance prediction methods.

3.2.2 FINE$^{\mathbf{TM}}$/Marine

In Paper VI, FINE$^{\mathbf{TM}}$/Marine computing suite version 10.2 was employed for conducting free-surface RANS computations (Queutey & Visonneau, 2007). All grids are generated with the HEXPRESS$^{\mathrm{TM}}$ module with Adaptive Grid Refinement (AGR) (Wackers et al., 2014) for further grid refinement and grid refinement studies.

The study described in Paper VI primarily investigates the trim trends of a RoPax vessel, utilising both experimental fluid dynamics (EFD) and computational fluid dynamics (CFD) methods, including free-surface RANS computations with the FINE$^{\mathbf{TM}}$/Marine code. These trim trends are analysed in resistance and self-propelled modes. The study includes uncertainty assessment for the experimental data and a verification and validation study for the free-surface RANS computations. Furthermore, predictions from EFD and CFD are compared with real operational data collected onboard, i.e., full-scale data.

Resistance computations

The trim optimisation study in Paper VI encompasses computations conducted under six different loading conditions: two displacements and three trims. Each loading condition is computed at three speeds in towing mode (i.e., resistance). The goal of these computations is to determine the minimum resistance for a given displacement and speed. Thus, obtaining the relative change in resistance between different trim angles at a given displacement and speed suffices for deriving the trim trends. The change in resistance between trimmed and even keel conditions for each displacement and speed is calculated as

$$\Delta R_{TM} = \frac{R_{TM}(trim) - R_{TM}(trim = 0)}{R_{TM}(trim = 0)} \times 100 \ , \tag{3.1}$$

where ΔR_{TM} is the relative change of resistance force in a given trim condition ($R_{TM}(trim)$) in per cent of the resistance of zero trim condition ($R_{TM}(trim = 0)$). Figure 3.1 illustrates the trim optimisation results for resistance based on towing tank measurements and free-surface RANS computations in Paper VI. The black markers represent the measured data from the tests, and the error bars indicate measurement uncertainties. The green triangle markers depict ΔR_{TM} values for the computations. Generally, it can be observed that ΔR_{TM} predictions closely match the towing tank measurements, with the mean absolute difference being only 1.82% (excluding zero trim conditions). However, the accuracy of ΔR_{TM} predictions varies significantly between trim by the bow (positive trim) and trim by the stern (negative trim). The accuracy is notably high for trim by the bow, where the flow behind the transom exhibits smooth and recirculation-free characteristics, closely resembling the towing tank tests. In contrast, trim by the stern involves more complex flow phenomena, including unsteady features like recirculation, spilling wave breakers, and eddies. While the computations successfully capture the main flow features, they exhibit limitations in replicating certain complex flow structures, suggesting modelling errors.

Besides capturing the relative change in total resistance between different trim conditions (e.g., ΔR_{TM}), accurately computing the absolute values of forces is relevant for various applications beyond trim optimization. Table 3.1 presents a comparison between model test measurements and free-surface RANS computations for eighteen combinations of displacement, speed, and trims, expressed as a comparison error, $E\%D$,

$$E\%D = (D - S)/D \times 100 \ , \tag{3.2}$$

where D is the experimental measurement, S represents the computational result.

Table 3.1: Comparison between the model tests and free-surface RANS computations in per cent of the measured resistance

	Light			Heavy		
trim	15 kn	17 kn	19 kn	15 kn	17 kn	19 kn
+1.5m	-1.23	-1.23	-0.74	-0.54	0.67	-0.34
0	0.77	0.16	-0.71	0.84	0.15	-1.62
-1.5m	0.57	1.55	1.68	3.51	3.43	1.96

As shown in Table 3.1, the free-surface RANS computations not only capture the relative change in total resistance with reasonable accuracy but also compute the absolute value of the total force with high precision. The mean absolute difference for the total resistance is only 1.2%. The measurement uncertainties for all test conditions were determined in the scope of Paper VI. The measurement uncertainties and $E\%D$ values exhibit close similarity when the loading conditions and speeds do not induce unsteady and complex flow structures such as recirculating separated flow, spill breakers, or breaking waves. However, prediction accuracy diminishes under loading conditions and speeds where wetted or partially dry transoms are observed, highlighting the limitations of the cost-efficient RANS approach with ordinary turbulence modelling.

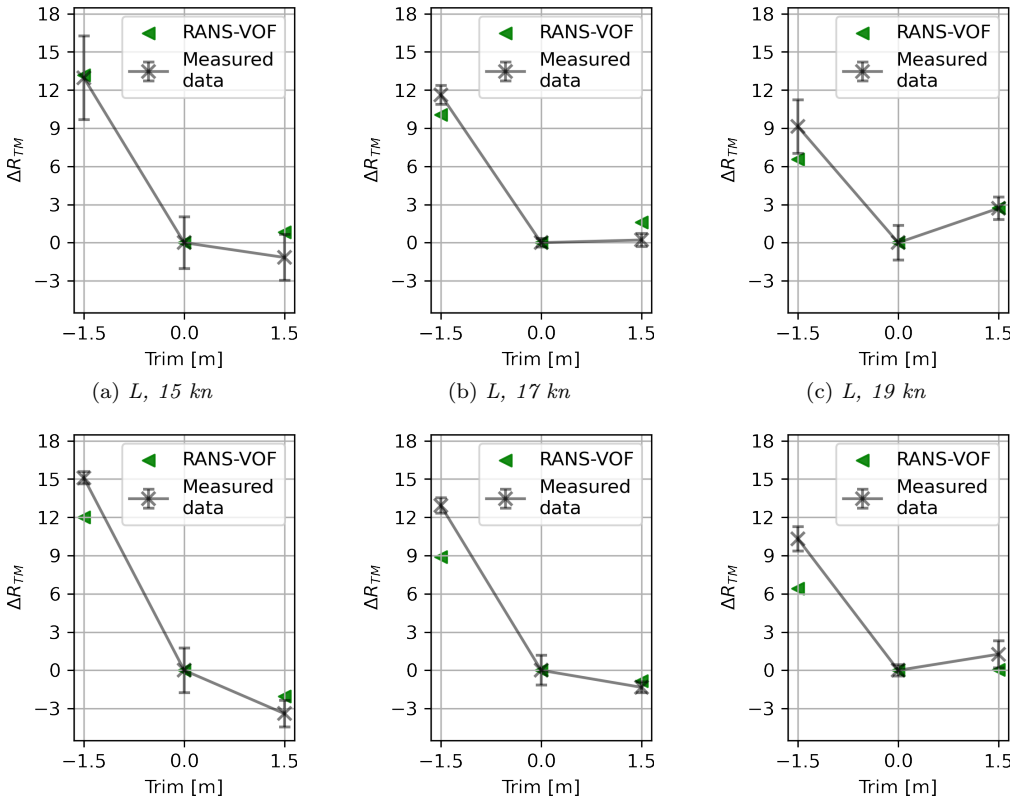

(a) *L, 15 kn* (b) *L, 17 kn* (c) *L, 19 kn*

(d) *H, 15 kn* (e) *H, 17 kn* (f) *H, 19 kn*

Figure 3.1: *Trim optimisation results of resistance from the towing tank measurements, and free-surface RANS computations. Paper VI*

Propulsion computations

In the context of Paper VI, trim optimisation tests were conducted under the same conditions as the resistance tests, as described in Section 3.2.2. These tests encompassed two displacements, three trims, and three speeds for the self-propulsion assessment. The changes in delivered power between the trimmed and even keel conditions, for each displacement and speed, were accurately captured by the free-surface RANS computations. The mean of the absolute discrepancies between the predictions of ΔP_{DM} (calculated similarly to Eq. 3.1) from the free-surface RANS propulsion computations and the model tests is 2.62%, excluding zero trim conditions. Despite the use of a simplified propeller model in the self-propulsion computations, the overall predictive precision of the trim trends closely matches that of the resistance computations. Therefore, it is reasonable to suggest that the actuator disc model effectively models the changes in thrust deduction, wake fraction, and propeller loading between the trim conditions. However, it is important to note that the accuracy in predicting the absolute power value is notably reduced in

Table 3.2: Comparison between the model tests and free-surface RANS computations in per cent of the measured power

	Light			Heavy		
trim	15 kn	17 kn	19 kn	15 kn	17 kn	19 kn
+1.5m	0.03	0.19	-1.38	-0.61	-2.68	-1.93
0	3.22	1.49	-0.51	3.45	0.76	-0.37
-1.5m	4.11	3.40	3.16	5.44	4.92	1.44

self-propulsion computations when compared to resistance mode computations.

In Paper VI, full-scale computations were also made with free-surface RANS method in self-propulsion mode using FINE$^{\mathbf{TM}}$/Marine code. There is no sea trial data available in full scale to compare the absolute values of the delivered power; however, the relative change of the trim trends are compared to the ship monitoring data collected onboard in Section 4.1.

4 Comparison of Full-Scale Predictions and Measurements

4.1 Comparison of Full-Scale Predictions with Ship Monitoring Data

This section discusses the investigations presented in Paper VI, where power predictions are compared with ship monitoring measurements. The focus of this discussion centres on the trim trends at three different speeds and two displacements. The analysis encompasses the utilisation of two distinct extrapolation methods: full-scale free-surface RANS computations and a combined EFD/CFD method for predicting delivered power at full scale. The comparison of these prediction methods yields several noteworthy conclusions.

Primarily, it becomes evident that the submergence of the transom plays a pivotal role in determining the agreement between predictions obtained from the various methods. Specifically, in scenarios of light displacement with an even keel and bow trim, as well as heavy displacement with bow trim, where transom submergence is minimal, power predictions using the extrapolation methods exhibit a high degree of similarity. However, under conditions of significant transom submergence, as observed in stern trim conditions, power predictions exhibit substantial variability.

Furthermore, it is observed that CFD-based predictions at full scale tend to overestimate power in bow trim conditions when compared to the extrapolation methods. This trend mirrors observations made at the model scale. Among the extrapolation methods employed, the combined EFD/CFD method, with the transom correction, demonstrates the highest degree of agreement in trim trends with the full-scale CFD predictions.

The findings in Paper VI reveal a close correspondence between ship monitoring data and predictions obtained from both the extrapolation methods (EFD-based and combined EFD/CFD methods) and full-scale CFD. The trim trends observed across a wide range of loading conditions and ship speeds remain consistent in all cases. While the optimum trim angle indicated by the ship monitoring data slightly differs from the predictions, the trim trends derived from all prediction methods fall within a 5% margin of the measured values.

Considering that trim trends are derived from the relative change of delivered power, full-scale CFD computations emerge as a cost-effective method. They provide a comprehensive representation of the flow field and hydrodynamic characteristics of the vessel without the influence of scale effects. On the other hand, full-scale free-surface RANS simulations are susceptible to numerical and modelling errors, which may potentially affect prediction accuracy, particularly in complex flow conditions.

4.2 Full-scale Predictions in Comparison to Sea Trials

A comprehensive validation study comparing sea trial measurements with full-scale free-surface RANS computations, the EFD-based ITTC-78 method, and combined EFD/CFD

methods is presented in this section. To adhere to the ITTC Quality Assurance Procedure (ITTC, 2021c), substantial number of test cases are required for validation. Furthermore, a large sample size is necessary for the comparisons with the sea trials since the combination of the precision and bias limits of a single speed trial result is approximately 10% of the total uncertainty, as indicated by Werner and Gustafsson (2020) and Insel (2008). Therefore, comparing the accuracy of the predictions from EFD, CFD, or combined EFD/CFD methods using a limited number of speed trials is unlikely to yield conclusive results. Instead, a large number of sea trials is required for a statistically significant comparison between different prediction methods since the uncertainty of each trial is substantial.

Correlation of power and propeller turning rate predictions with the speed trial measurements is quantified using the *correlation factors* based on the correlation scheme of C_{P} - C_{N} as described in (ITTC, 2017). To obtain these coefficients, the correlation factors of each individual speed trial, $C_{\mathrm{P}}^{'}$ and $C_{\mathrm{N}}^{'}$, are calculated as

$$C_{\mathrm{P}}^{'} = \frac{P_{\mathrm{D}\ trial}}{P_{\mathrm{D}\ pred}} \quad \text{and} \quad C_{\mathrm{N}}^{'} = \frac{n_{trial}}{n_{pred}} \tag{4.1}$$

where the $P_{\mathrm{D}\ trial}$ and n_{trial} are the power and propeller turning rate from a speed trial, while $P_{\mathrm{D}\ pred}$ and n_{pred} represent the corresponding predictions based on EFD, CFD, and combined EFD/CFD methods. The power, P_{D}, is derived from the faired speed-power curve at the design speed.

4.2.1 Comparison between combined EFD/CFD methods and the ITTC-78 method

In Paper IV, $C_{\mathrm{P}}^{'}$ and $C_{\mathrm{N}}^{'}$ are quantified using three different sources of form factors: the Prohaska method, CFD based form factors with EASM model using the ITTC-57 line and the numerical friction line. All predictions utilize the same model test data, with only the source of the form factor being varied. Probability Density Functions (PDFs) of the normalized correlation factors, $C_{\mathrm{P}}^{'}$ and $C_{\mathrm{N}}^{'}$, are calculated for 18 test cases and 78 speed trials.

In addition to the PDF curves, the standard deviations (σ) of $C_{\mathrm{P}}^{'}$ and $C_{\mathrm{N}}^{'}$ are also presented in Figure 4.1 as the standard deviation was the main measure used to rank different extrapolation methods when the original ITTC-78 method was decided. The comparison of the standard deviations for the power predictions (C_{P}) indicates that the scatter is significantly reduced when the CFD based form factors from the EASM turbulence model are used compared to the Prohaska method. However, for the propeller rate of revolution predictions, the standard deviations remain relatively consistent with CFD based form factors using the ITTC-57 line but slightly worsen when using CFD based form factors with NFL, considering the standard deviation.

It is noteworthy that the reduction of scatter in the power predictions holds more significance than for propeller turning rate predictions, as the scatter in power prediction is considerably larger than the prediction of propeller turning rate. Consequently, it was concluded in Paper IV that the utilisation of the CFD based form factors with the ITTC-57 line improves the predictions in general or, at the very least, does not deteriorate

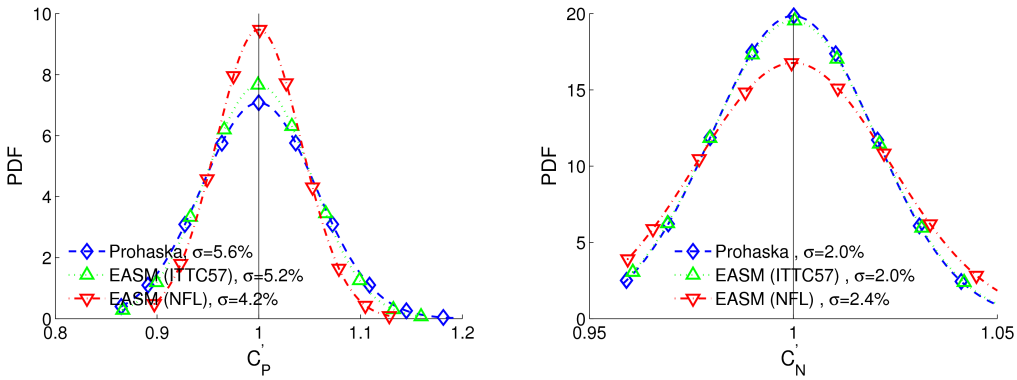

(a) *Correlation factor for power* (b) *Correlation factor for propeller turning rate*

Figure 4.1: *The probability density functions (PDFs) of the normalised correlation factors for the ITTC-78 method with Prohaska method, CFD-based form factors with the EASM model using the ITTC-57 line, and the numerical friction line, from the study conducted in Paper IV*

them. The improvement in predictions is even more substantial when CFD-based form factors with the numerical friction line are employed.

4.2.2 Comparison between extrapolation-based methods and full-scale free-surface RANS computations

In Paper VII, full-scale free-surface RANS computations (see Section 3.2.1) were employed to predict the performance of ships. In addition to the CFD computations performed in Paper VII, predictions from the EFD-based ITTC-78 method (using the Prohaska method) and the combined EFD/CFD method with empirical correction for transom submergence (see Section 2.3.3) were included in the comparison with the sea trials. The study comprised fourteen common cargo vessels that had previously undergone towing tank tests at RISE-SSPA. As some vessels underwent speed trials at multiple loading conditions, a total of twenty test cases were considered, one more than in Paper VII. The data set consisted of 60 sea trials in total, with most of the trials overlapping with those used in Paper IV.

$C_{\mathrm{P}}^{'}$ and $C_{\mathrm{N}}^{'}$ are quantified for each sea trial using Eq. 4.1 for each prediction method: full-scale free-surface RANS computations, EFD-based ITTC-78 method, and the combined EFD/CFD method with the empirical correction for transom submergence. Assembled correlation factors for each prediction method are determined for the power and propeller turning rate by taking the median of $C_{\mathrm{P}}^{'}$ and $C_{\mathrm{N}}^{'}$ of all trials of sufficient quality (Werner & Gustafsson, 2020). The assembled correlation factors are used in towing tank testing practice as a "correction for any systematic errors in model test and powering prediction procedure, including any facility bias" (ITTC, 2017). C_{P} and C_{N} corresponding to each method are used for correcting the predictions. The Probability Density Functions (PDFs)

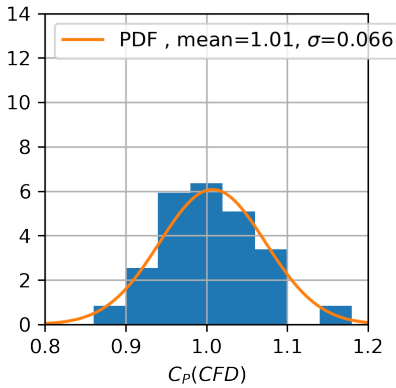

(a) *Full-scale free-surface RANS computations*

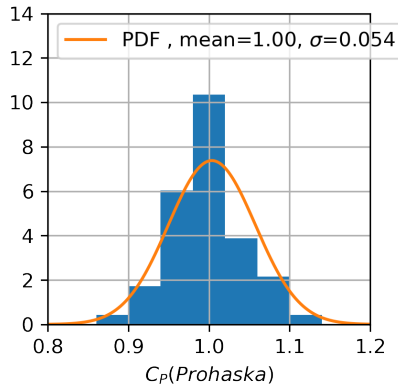

(b) *ITTC-78 method using the Prohaska method*

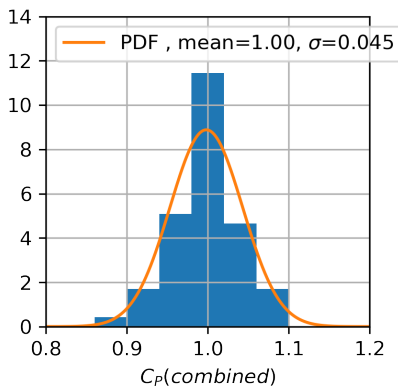

(c) *Combined EFD/CFD method with the empirical correction for transom submergence*

Figure 4.2: *Correlation factors with different performance prediction methods*

and the histograms of $C_{\mathrm{P}}^{'}$ and $C_{\mathrm{N}}^{'}$ are presented by shifting the median of PDFs to 1, i.e., multiplying individual correlation factors with the assembled C_{P} and C_{N}, respectively.

The histograms and the probability density functions of the normalised correlation factors for power prediction are shown in Figure 4.2 for the full-scale free-surface RANS computations (referred to as $C_{\mathrm{P}}(CFD)$ and $C_{\mathrm{N}}(CFD)$), EFD-based ITTC-78 method (referred to as $C_{\mathrm{P}}(Prohaska)$ and $C_{\mathrm{N}}(Prohaska)$), and the combined EFD/CFD method with the empirical correction for transom submergence (referred to as $C_{\mathrm{P}}(combined)$ and $C_{\mathrm{N}}(combined)$). The standard deviation, denoted as σ, of the correlation factors serves as the primary measure for ranking different extrapolation methods, as it signifies the difference between the predictions and the trial measurements for each method. As depicted in Figure 4.2, the combined EFD/CFD method with empirical correction for

transom submergence exhibits the smallest standard deviation, indicating its superior accuracy among the three methods. On the other hand, the full-scale free-surface RANS computations yield the least accurate predictions for delivered power. Nevertheless, it is worth noting that the standard deviations of all three methods are relatively similar, suggesting that the prediction accuracy does not significantly vary among them.

The histogram of the correlation factors and the approximated probability density function, derived from the normal distribution, exhibit a high degree of similarity. Consequently, the comparison errors for each method, e.g., $C_P(CFD)$-1, also follow a normal distribution, and no significant bias can be observed between the predictions and the trial measurements. Based on the assumption of a normal distribution of the comparison errors, it can be stated that 95% of the power measured in trials were predicted by full-scale CFD computations, EFD-based ITTC-78 method, and combined EFD/CFD method within ±13%, ±11%, and ±9% accuracy, respectively.

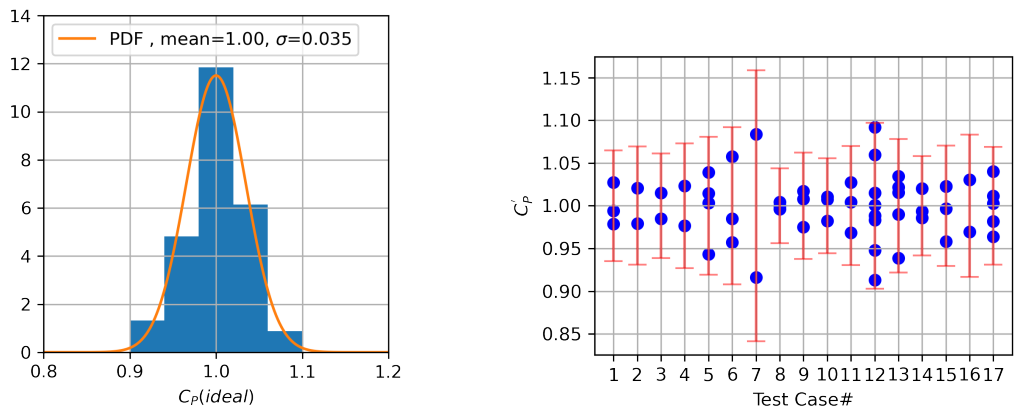

(a) *Ideal prediction case correlation factors*

(b) *Scatter among the test cases*

Figure 4.3: *Correlation factors from the ideal prediction case*

At first glance, the accuracy of the prediction methods may not appear highly impressive. However, a significant portion of the standard deviation arises from the precision of the trial measurements. This is visualised by the variation in speed trials among sister ships, as argued in Paper IV. To illustrate this, an ideal prediction scenario was created using cases with more than one speed trial. In the ideal case, the prediction is identical to the speed trial measurement. However, since the speed trial measurements between sister ships at each loading condition vary, the ideal case assumes that the mean $C_{\mathrm{P}}^{'}$ of a series of sisters at a given loading condition would be 1. The resulting $C_{\mathrm{P}}^{'}$ values for vessels with more than one speed trial are represented by blue markers in Figure 4.3b. To indicate the uncertainty of the speed trials for each test case, the standard deviation of the $C_{\mathrm{P}}^{'}$ values for a given hull at a certain loading condition is combined with the bias limit (U_{bias}) of 4% estimated by Insel (2008). The resulting total uncertainty estimations ($\sqrt{\sigma^2 + U_{bias}^2}$) are represented by error bars in Figure 4.3b for each hull. As observed in Figure 4.3b, the scatter among sister ships varies significantly for each test case, and the measured power

Table 4.1: The mean absolute comparison errors and standard deviations for each prediction method and the ideal test case

	Full-scale CFD		ITTC-78 (Prohaska)		Combined EFD/CFD		Ideal	
	$\overline{\lvert E\%D\rvert}$	σ	$\overline{\lvert E\%D\rvert}$	σ	$\overline{\lvert E\%D\rvert}$	σ	$\overline{\lvert E\%D\rvert}$	σ
$C_P^{'}$	5.15	0.066	3.96	0.054	3.52	0.045	2.64	0.035
$C_N^{'}$	2.72	0.033	2.27	0.026	2.27	0.026	0.87	0.012

at the trial can differ by up to 18% between sister ships at the same loading condition.

Similar to the previous plots, the histogram and the probability density functions of the ideal prediction case (including hulls with one speed trial) are presented in Figure 4.3a. The comparison between the predictions and the ideal case demonstrates that more than half of the scatter originates from the variation among sister ships. The standard deviation from the ideal prediction case is 0.035, indicating that within the best-case scenario, 95% of the speed trials can be predicted within ±7% accuracy, whereas the CFD predictions achieve ±13% accuracy. This comparison suggests that the accuracy of full-scale CFD is within acceptable levels considering that a significant portion of the scatter arises from the precision of measurements. However, the combined EFD/CFD method provides the most accurate power prediction, being only ±2% less accurate than the ideal condition within the 95% confidence interval.

Table 4.1 presents the mean absolute comparison errors ($\overline{|E\%D|}$) and standard deviations (σ) for the power and Revolutions per Minute (RPM) predictions obtained from the three prediction methods and the ideal prediction case. Comparing the standard deviations for power and RPM predictions reveals significantly lower scatter for the propeller turning rate in all prediction methods as also observed in Paper IV. This observation also holds true for the ideal prediction case, indicating much smaller scatter in the propeller turning rate measurements during trials. As shown in Table 4.1, the combined EFD/CFD method with empirical correction for transom submergence yields the smallest mean absolute comparison error and standard deviation for both power and RPM. This study quantifies, for the first time in the literature, the difference in accuracy between fully computational and extrapolation-based methods using a large number of test cases and sea trials. The results indicate that while the prediction accuracy of full-scale CFD computations for power and RPM is lower than that of the other methods, the difference is not substantial. However, the investigations carried out in Paper IV and Paper VII shows that the utilisation of CFD in combination with the experimental methods as in Paper I, II, III, IV, V, VI offers immediate improvements in the ship performance prediction.

5 Summary of Papers

5.1 Paper I

Korkmaz, K. B., Werner, S., & Bensow, R. (2019a). Numerical friction lines for CFD based form factor determination method. *VIII International Conference on Computational Methods in Marine Engineering MARINE 2019* (2019, May)

Motivation, Results and Conclusions

The primary objective of this study is to establish Numerical Friction Lines (NFL) that are suitable for the CFD based form factor determination and the extrapolation methods. The study involves the computation of frictional resistance coefficients for an infinitely thin 2D plate across 14 Reynolds numbers, spanning the typical model scale to full scale range. At each Reynolds number, simulations were conducted using five geometrically similar structured grids to ensure reliable grid dependency assessments. All computations adhered to the no-slip condition at the wall, employing two turbulence models: the $k-\omega$ SST and the EASM. The grid-independent frictional resistance coefficients, calculated using the SHIPFLOW code at these 14 Reynolds numbers, were subsequently transformed into separate numerical friction lines for the $k-\omega$ SST and the EASM turbulence models through curve fitting.

Furthermore, comprehensive grid dependency studies were performed at $\log_{10}(Re) = 6.25$ using both the SHIPFLOW and the FINE$^{\text{TM}}$/MARINE codes. Notably, differences in calculated C_{F} and predicted numerical uncertainties were observed between the two CFD codes, even though identical grids were employed for both solvers.

The investigation identified two primary modelling errors: turbulence modelling and the transition of flow from laminar to turbulent. Regarding the latter error source, it was revealed that the flow around the flat plate does not exhibit complete turbulence. However, the requirement for a fully turbulent friction line for the form factor method is largely met.

A comparison was made between the derived numerical friction lines and those available in the literature. The slope of the line derived from the $k-\omega$ SST model closely resembles numerical friction lines computed by others employing the same turbulence model, while the EASM model shows considerable difference from all other friction lines.

It is crucial to note that when utilising a numerical friction line for ship resistance extrapolation, results may be highly dependent on several factors, including non-dimensional wall distance (y^+), choice of turbulence model, boundary conditions such as turbulence intensity, and other numerical methods. Therefore, it is advisable to employ the NFL of the same code and the same turbulence model for CFD-based form factor determination.

All authors participated in the conceptualisation, the development of the methodology, and the review and editing of this paper. The literature study, CFD computations, post-processing, validation, data analysis, investigation, visualisation and writing of the original draft were performed by the first author.

5.2 Paper II

Korkmaz, K. B., Werner, S., & Bensow, R. (2019b). Investigations for CFD based form factor methods. *22nd Numerical Towing Tank Symposium, NuTTS 2019* (2019, October)

Motivation, Results and Conclusions

This study serves as a foundational investigation into CFD-based form factors, specifically testing the form factor hypothesis of Hughes (1954), which suggests that the same form factors apply to both model and full-scale hulls. The analysis is based on simulations conducted on the KVLCC2 and KCS hulls.

Following grid dependency assessments, various grid density distributions were simulated for the KVLCC2 model to determine acceptable grid densities and identify those that should be avoided. It has been concluded that unless the grid density in the longitudinal direction is too coarse, the sensitivity of the form factor to the grid resolution at the other parts of the hull is relatively low.

The study also explores the sensitivity of form factors under varying loading conditions for both the KVLCC2 and KCS. Double model simulations were conducted under dynamic sinkage and trim conditions, as well as draught and trim at rest. It was observed that the differences in calculated viscous resistance between these loading conditions were nearly one order of magnitude smaller than the numerical uncertainties for both the KVLCC2 and KCS.

Furthermore, the study investigates the speed dependency of form factors by performing double-body computations at both model and full scale. The results indicate that when using the ITTC-57 line, scale effects are unavoidable. However, when applying the numerical friction lines derived in Paper I, the speed dependency of form factors was virtually eliminated for both hulls.

All authors participated in the conceptualisation, the development of the methodology, and the review and editing of this paper. The CFD simulations, post-processing, validation, data analysis, investigation, visualisation and writing of the original draft were performed by the first author.

5.3 Paper III

Korkmaz, K. B., Werner, S., Sakamoto, N., Queutey, P., Deng, G., Yuling, G., Guoxiang, D., Maki, K., Ye, H., Akinturk, A., Sayeed, T., Hino, T., Zhao, F., Tezdogan, T., Demirel, Y. K., & Bensow, R. (2021). CFD based form factor determination method. *Ocean Engineering* **220** (2021), 108451. https://doi.org/https://doi.org/10.1016/j.oceaneng.2020.108451

Motivation, Results and Conclusions

This paper presents the outcome of a collaborative research effort initiated by the ITTC Specialist Committee of Combined CFD/EFD Methods. It involves contributions

from several institutions, including SSPA, Chalmers University of Technology, National Maritime Research Institute (NMRI), LHEEA CNRS Ecole Centrale de Nantes, Shanghai Ship and Shipping Research Institute (SSSRI), CSHL University of Michigan, Ocean, Coastal and River Engineering (OCRE), Yokohama National University, China Ship Scientific Research Centre (CSSRC), and University of Strathclyde.

This paper investigated the possibility to improve the power predictions by introducing the combined CFD/EFD Method where the experimental determination of form factor is replaced by double-body RANS computations. The research encompasses open cases KVLCC2 and KCS, including the publication of towing tank tests for KVLCC2 under ballast conditions, along with a detailed analysis of experimental uncertainties related to the form factor. The study compares CFD-based form factor predictions from nine organisations employing seven different CFD codes with experimental results.

In general, the CFD-based form factor predictions for KVLCC2 and KCS in design loading conditions closely match the experimental results. However, for KVLCC2 under ballast loading conditions, the CFD-based form factors tended to be slightly underestimated compared to the experiments. Nonetheless, most CFD-based form factors fell within the range of experimental uncertainty.

The computations conducted at the model scale encompassed not only CFD setups conforming to best practice guidelines but also those deviating from recommended standards. The analysis of non-standard CFD setups emphasised the critical role of describing the boundary layer with high grid quality, especially concerning grid resolution and the first cell size normal to the wall. Moreover, the choice of wall function proved significant when used in combination with certain turbulence models.

Further investigation of the form factor predictions aimed to highlight dependencies among CFD codes and methods. While no general trends were identified regarding turbulence modelling, the first cell size normal to the wall, and grid resolution near the wall, different codes exhibited varying tendencies in CFD setups. Consequently, specific recommendations for form factor determination across all CFD codes could not be generalised. However, it was observed that most codes with consistent CFD setups displayed coherent patterns in form factor predictions across different test cases. If these trends are corroborated through additional hulls and test cases, the application of unique correlation factors (C_{P}-C_{N} or C_A) for each code and method could further minimise disparities in full-scale predictions.

Model-scale computations were conducted at two different speeds to investigate the speed dependency of form factors. Speed dependency was observed with the ITTC-57 line but was reduced with the Katsui line and nearly eliminated by numerical friction lines. Comparing full-scale viscous resistance predictions obtained through extrapolation from model scale and direct full-scale computations revealed that the combined CFD/EFD method exhibited significantly less scatter, making it a preferable approach.

All authors participated in the CFD computations, review, and editing of this paper. The conceptualisation and the development of the methodology were conducted by the K. Burak Korkmaz, Sofia Werner and Rickard Bensow. The model test experiments, measurement uncertainty assessment for the Prohaska method, CFD simulations, coordination of the collaborative effort of nine participants, data analysis, validation, formal analysis, data curation, visualisation and writing of the original draft were performed by

the first author.

5.4 Paper IV

Korkmaz, K. B., Werner, S., & Bensow, R. (2021). Verification and validation of CFD based form factors as a combined CFD/EFD method. *Journal of Marine Science and Engineering* **9**.(1) (2021). https://doi.org/10.3390/jmse9010075

Motivation, Results and Conclusions

This paper demonstrates the application of a novel Quality Assurance (QA) procedure proposed by the ITTC Specialist Committee of Combined CFD/EFD Methods. The introduction of this QA procedure by the ITTC aims to address the need for a practical framework tailored to organisations regularly performing CFD predictions for similar cases. This study serves as a practical example of the procedure's implementation in the context of CFD-based form factors. The assurance of quality in addressing this practical problem unfolds in three main parts: the formulation and derivation of the Best Practice Guideline (BPG) within the SHIPFLOW code used in this study, the rigorous assessment of the BPG methodology through verification and validation studies, and, finally, the demonstration of quality through comprehensive comparisons of 78 speed trials with predictions derived from combined CFD/EFD methods.

To develop a best practice guideline for CFD-based form factors, systematic variations were applied to the CFD setups, including adjustments to non-dimensional cell height normal to the wall, varying grid refinements at the stern, domain size, and model scale speed.

The speed dependence of the form factors, following the ITTC-57 line, was consistently observed across all test cases. This phenomenon is expected, as the primary factor driving this dependence is the ITTC-57 line itself, rather than the numerical methodologies used. When applying the numerical friction lines from the same code and turbulence model to determine CFD-based form factors, the speed dependence of these factors was significantly reduced, particularly in cases with no flow separation.

The full scale speed-power-rpm relations between the speed trials and the full scale predictions were investigated for 18 test cases and 78 sea trials. Full-scale predictions relied on diverse extrapolation methods, yet all were based on identical model test data. Notably, integrating CFD-based form factors with the EASM turbulence model improved predictions, regardless of the friction line used. Among the investigated extrapolation methods, the most promising one involved using CFD-based form factors with the EASM turbulence model and the numerical friction line.

All authors participated in the conceptualisation, the development of the methodology, and the review and editing of this paper. The CFD computations, post-processing, validation, data analysis, investigation, visualisation and writing of the original draft were performed by the first author.

5.5 Paper V

Korkmaz, K. B., Werner, S., & Bensow, R. (2022). Scaling of wetted-transom resistance for improved full-scale ship performance predictions. *Ocean Engineering* **266** (2022, December), 112590. https://doi.org/10.1016/j.oceaneng.2022.112590

Motivation, Results and Conclusions

This study addresses challenges associated with predicting propulsive power of ships, focusing on flow characteristics behind the transom. The wetted-transom flow phenomenon and its implications on the 1978 ITTC Performance Prediction Method are investigated. According to the ITTC-78 method's extrapolation procedures, the Prohaska method for form factor determination should not be applied to vessels with substantial transom sterns exhibiting wet transoms, yet no alternative is suggested. To address this knowledge gap, wetted transom flow is investigated in both model and full scale using double-body and free-surface computations.

To enhance accuracy in speed-power predictions, two alternative methods are proposed: the two form factor method ($2-k$ method), which combines experimental and computational approaches to handle flow separation, and an empirical correction formula for hulls experiencing wetted-transom flow. The effectiveness of these methods is demonstrated by comparing full-scale speed-power relations obtained from sea trials with the standard ITTC-78 method. This study aims to provide valuable insights for improving the accuracy and reliability of speed-power predictions.

Initially, flow similarity between double-body and free-surface approaches is investigated in both model and full scale. The study reveals that the extent and shape of the recirculation region and the streamlines behind a substantially submerged transom are highly similar in double-body and free-surface computations at both scales, confirming the applicability of CFD-based form factors with double-body computations.

Further investigations into the flow field of a vessel with deep transom submergence show that the boundary layer is thinner at the stern outside the wake of the transom from model to full scale. However, the flow behind the transom remains relatively unchanged, even with a significant increase in Reynolds number from model to full scale. In addition to qualitative observations, quantitative analysis of form factors obtained from model and full scale using the numerical friction line derived in Paper I indicates that scaling of the viscous resistance needs modification not only for vessels with wetted transom flow but also for other types of flow separation. Consequently, the $2-k$ method is proposed.

In addition to the two form factor method, an empirical correction method is developed through regression analysis of form factors calculated for multiple vessels in model and full scale. This suggested correction method can be incorporated into the current ITTC-78 method as a second alternative and can accurately restore the deficit of extrapolated full-scale viscous resistance in the presence of wetted-transom flow.

Power predictions from the two proposed procedures are compared with predictions from the standard ITTC-78 method and speed trials. The improvement achieved by both suggested procedures aligns with the theory discussed in this study.

All authors participated in the conceptualisation, the development of the methodology,

and the review and editing of this paper. The literature study, CFD computations, post-processing, validation, data analysis, investigation, visualisation and writing of the original draft were performed by the first author.

5.6 Paper VI

Korkmaz, K. B., Werner, S., & Bensow, R. . Investigations on experimental and computational trim optimisation methods. *Submitted to Ocean Engineering in 2023 June, under review*

Motivation, Results and Conclusions

The paper aims to investigate the trim trends of a RoPax vessel using experimental, computational and combined EFD/CFD methods. The full-scale predictions from these methods are compared against operational data collected onboard. Trim optimisation, which involves operating the ship at hydrodynamically optimal forward and aft draughts for a given displacement and speed, is a measure to improve energy efficiency of ships. However, the trim trends are required to be determined by an accurate and cost-effective method. This study focuses on examining different CFD methods and extrapolation techniques for experimental results to determine trim trends. The main motivation of this study is to provide valuable insights into trim trend extraction methods and guide ship owners and operators in selecting the most appropriate method by investigating the prediction methods, and the comparing the real operational data with the predictions.

Grid dependency studies were conducted in model and full scale, concluding that grid adaptation based on metric tensors (adaptive grid refinement) can effectively generate suitable meshes for a verification study. Validation is achieved at a programmatic standpoint for the resistance computations. However, the comparison error for thrust from self-propulsion computations exceeds the validation uncertainty, indicating non-negligible modelling errors stemming from the simplistic approach of the actuator disc model used in this study.

Free-surface RANS computations provided overall better predictions than the other CFD approaches, but accuracy diminished as transom submergence increased, owing to modelling errors when complex and unsteady flow features were present. Decomposition of resistance components revealed that frictional resistance and viscous pressure resistance exhibited limited variation with trim, while wave resistance displayed significant variability. The design of the forebody, including the bulbous bow, also influenced optimum trim, underscoring the importance of considering wave patterns and resistance in trimmed states.

Self-propulsion model tests corroborated the trends observed in resistance tests, yet propulsive efficiency varied significantly with trim. The propeller jet exerted notable effects on dynamic sinkage, trim, and local flow. The free-surface RANS method effectively captured these changes in flow features during propulsion. A comparison of flow fields between resistance and self-propulsion tests and between model and full scale revealed significant scale effects in partially dry transom flow conditions.

Full-scale predictions for delivered power were made using various extrapolation methods. Transom submergence emerged as the most decisive factor affecting prediction agreement, with smaller submergence yielding similar predictions. Comparing ship monitoring data with predictions from extrapolation methods and full-scale CFD simulations, similar trim trends were evident across various loading conditions and ship speeds. While the optimum trim angle indications from the ship monitoring data were slightly smaller than the predictions, the trim trends from all prediction methods remained within 5% of the measurements. It is advisable to utilise ship monitoring data as a reference with a margin of 5% or more to account for artificial fluctuations observed in the data curve fits.

In conclusion, the full-scale self-propulsion CFD method demonstrated reasonable accuracy and cost-effectiveness for determining trim trends. However, modelling errors can be significant under certain conditions, necessitating thorough verification and validation. If experimental methods are preferred, extrapolation should incorporate techniques to account for submerged transoms.

All authors participated in the conceptualisation, the development of the methodology, and the review and editing of this paper. The literature study, CFD computations, post-processing, validation, data analysis, investigation, visualisation and writing of the original draft were performed by the first author.

5.7 Paper VII

Korkmaz, K. B., Kim, K., Liefvendahl, M., Werner, S., & Orych, M. (2023). A validation study of full-scale CFD simulation for sea trial performance prediction of ships. *X International Conference on Computational Methods in Marine Engineering MARINE 2023* (2023, June)

Motivation, Results and Conclusions

This paper addresses the utilisation of Computational Fluid Dynamics (CFD) for predicting ship performance, specifically focusing on the validation of the CFD-based method using SHIPFLOW version 7.0. The objective is to assess the accuracy of these predictions by comparing them with high-quality sea trials conducted on 14 cargo ships.

The validation study employing SHIPFLOW has demonstrated the accuracy of full-scale CFD computations in predicting ship performance. An analysis of 59 sea trials from these cargo ships was carried out, focusing on delivered power and propeller rotation rate. The comparison of standard deviations of the prediction errors indicates significantly lower scatter for propeller turning rate compared to delivered power. In other words, propeller turning rate predictions are more accurate than those for delivered power. Assuming a normal distribution of comparison errors holds, the standard deviations suggest that CFD can predict 95% of speed trials within $\pm 12\%$ accuracy for power and $\pm 7\%$ for RPM, respectively. It should be noted that a substantial portion of errors arises from the scatter in speed trials among sister ships, as discussed in this study, Paper IV, and Paper V.

Reliable simultaneous predictions of power and RPM are crucial for engine selection in achieving dependable full-scale performance predictions. This study successfully predicts

both power and propeller rotation rate with acceptable accuracy using the CFD-based method. Additionally, there is no noticeable bias observed in predicting specific loading conditions.

These findings underscore the reliability of CFD predictions in evaluating ship performance, offering valuable insights to ship operators and stakeholders. The CFD-based method effectively supports compliance with the Energy Efficiency Existing Ship Index (EEXI) requirements. The numerical techniques employed in this study, including structured and overlapping grids, no-slip wall treatment, free-surface treatment, and propeller modelling, exhibit their potential for future applications in ship performance prediction. These techniques differ significantly from many state-of-the-art CFD codes and provide valuable insights and experiences in their implementation.

All authors participated in the conceptualisation, and the review and editing of this paper. In addition, the second author performed the CFD computations. The literature study, post-processing, validation, data analysis, investigation, visualisation and writing of the original draft were performed by the first author.

6 Concluding Remarks

In today's competitive market and amidst the stringent regulatory requirements, the demand for accurate ship performance prediction has reached new heights. The verification of ship performance during the design phase and continuous evaluation of existing vessels throughout their operational life have become imperative, especially as the maritime industry strives to meet the increasingly rigorous emission standards set forth by the International Maritime Organisation (IMO). Furthermore, regulatory authorities now recognise and endorse various evaluation methods, including the integration of Computational Fluid Dynamics (CFD) results into performance assessments. This thesis underscores the necessity for a comprehensive evaluation of the strengths and limitations of Experimental Fluid Dynamics (EFD), CFD, and combination of both approaches. As advocated here, by leveraging the potential of these methods, more precise performance predictions can be achieved, ultimately contributing to the industry's endeavour to reduce greenhouse gas emissions in alignment with IMO targets.

In pursuit of improved ship performance prediction methodologies, the investigations commenced by identifying factors that introduce significant uncertainties into ship performance prediction, with a specific focus on model testing practices and extrapolation methods. One of the principal sources of uncertainty within the ITTC-78 method was found to be the determination of the experimental form factor using the Prohaska method. Consequently, this study initiated an investigation into a CFD based form factor method as an alternative to the Prohaska method.

A substantial contribution was made by demonstrating the applicability and accuracy of the CFD-based form factor method through a collaborative study involving nine organisations, as presented in Paper III. The study highlighted the limitations and lack of applicability of the Prohaska method, particularly for modern hull forms with bulbous bows. For the first time in the literature, Paper III determined the experimental uncertainty associated with the form factor. It revealed that the experimental uncertainty in resistance measurements is significantly amplified when determining the form factor using the Prohaska method, employing linear regression analysis. Taking into account the measurement uncertainty associated with the experimental form factor, the study showcased the applicability and accuracy of the CFD-based form factor method, utilising seven CFD codes with multiple numerical approaches and setups. Consequently, it was concluded that CFD-based form factors can serve as an alternative or supplementary method to the Prohaska method, as CFD predictions of form factors closely aligned with experimental values.

Another noteworthy contribution is the demonstration of the applicability and accuracy of the CFD-based form factor method across a diverse range of test cases involving varying ship types, sizes, and propulsive arrangements. Paper IV presented the first practical example in the literature illustrating the application of the ITTC Quality Assurance Procedure (ITTC, 2021c) to a specific problem: CFD-based form factors. The quality assurance of this practical problem was demonstrated in three components: (1) the content and derivation of the Best Practice Guideline (BPG) of the SHIPFLOW code used in the study, (2) the quality assessment of the BPG methodology through verification and validation studies, and (3) the demonstration of quality by comparing 78 speed trials to

predictions made by combined CFD/EFD methods. Paper IV demonstrated that the use of CFD-based form factors generally enhances predictions without compromising within the limits of the study. The studies conducted on the CFD based form factor in Papers I, III, and IV were part of the discussions in the final report of the ITTC Specialist Committee of Combined CFD and EFD Methods, which concluded that CFD can serve as a supportive method for determining the form factor (ITTC, 2021e). Consequently, this conclusion led to the acceptance of CFD-based form factors as a supplementary method for form factor determination in the currently recommended procedures of the ITTC-78 method (ITTC, 2021a).

Furthermore, the challenges posed by flow separation in both model tests and full-scale vessels were addressed. The conventional form factor approach used in the ITTC-78 method was found to be inadequate in the presence of flow separation, yet no alternative methods were previously proposed. Therefore, Paper V investigated vessels with significant transom submergence. By employing form factors based on numerical friction lines derived from computations performed at both model and full scale, the study demonstrated that conventional viscous resistance scaling fails when flow separation occurs. As an alternative, the paper proposed a two-form factor method ($2-k$ method) in the event of separated flow. Additionally, an empirical correction formula was proposed for vessels with deep transom submergence and wetted transom flow, which can be integrated into existing extrapolation procedures.

In addition to experimental and combined EFD/CFD methods, the use of direct full-scale CFD computations were explored for ship performance prediction, as presented in Paper VI. The trim optimisation study conducted in Paper VI revealed highly similar trends for full-scale trim predictions between the combined EFD/CFD method with transom correction and full-scale CFD computations, although there were slight differences in absolute values of power predictions. Given that trim trends are derived from relative changes in delivered power between the trimmed and even keel conditions, full-scale CFD computations emerge as a cost-effective method for predicting trim trends and providing a detailed representation of the flow field and hydrodynamic characteristics of a vessel, without being subject to scale effects. Through extensive investigations involving towing tank testing, CFD computations, and ship monitoring data, Paper VI contributed to assessing the most suitable and cost-effective method, i.e., full-scale self-propulsion CFD computations, for determining trim optimisation trends. The paper aims to offer valuable insights into trim trend extraction methods, assisting ship owners and operators in selecting the most appropriate approach.

The importance of a large sample size for evaluating ship performance prediction methods at full scale is demonstrated and emphasised. As discussed in Section 4.2, Papers IV, V, and VII, a large sample size is necessary for statistically evaluating prediction methods or comparing different approaches, given the substantial uncertainty associated with each trial. Accordingly, the full-scale speed-power-rpm relations between speed trials and predictions from EFD-based and combined EFD/CFD methods were investigated. The results presented in Papers IV and V demonstrated that the combined EFD/CFD methods reduce the scatter between speed trials and power predictions.

The thesis also delves into ship performance prediction using full-scale CFD computations in Paper VII, through a comprehensive validation study involving numerous test

cases and sea trials, as presented in Section 4.2. The study includes an EFD-based method and a combined EFD/CFD method with transom correction for comparison. This research quantifies, for the first time in the literature, the difference in accuracy between fully computational and extrapolation-based methods using numerous test cases and sea trials. The results indicate that while the prediction accuracy of full-scale CFD computations for power and RPM is slightly lower than that of other methods, the difference is not too significant. However, the investigations carried out in Papers IV and VII demonstrate that the utilisation of CFD in combination with experimental methods, as described in Papers I, II, III, IV, V, VI, offers immediate improvements to existing ship performance prediction methods.

In light of the results, the CFD based form factors, the two form factor method, the usage of numerical friction lines, and the empirical correction for transom submergence as combined CFD/EFD methods are expected to provide improvements to the 1978 ITTC Performance Prediction Method. Additionally, the suggested modifications from this study is currently revised and processed within ITTC for a possible inclusion in official recommended procedures. It is observed that the full-scale CFD computations can be used for the applications where the relative change of power and rps are relevant, such as a trim optimisation study. However, obtaining the absolute values of power and rpm from the full-scale CFD computations was less accurate then the existing methods and the proposed combined CFD/EFD methods; however, not by a large margin. Therefore, until further advancements in the numerical methods and computational setups for full-scale CFD, the combined CFD/EFD methods are recommended as they appear to be the the most accurate ship performance prediction method evaluated in this study.

The impact of this thesis extends to various stakeholders within the maritime industry. Ship designers and naval architects can benefit from the improved ship performance prediction methods, enabling them to verify and optimise ship designs more effectively. Ship operators and owners can use these methods to assess the performance of existing ships and optimise their operations for better fuel efficiency and reduced emissions. Regulatory authorities can find value in the findings, as it highlights alternative evaluation methods, such as CFD-based form factors, which can be considered as supplementary approaches to the traditional methods. Ultimately, the implementation of more accurate ship performance prediction methods can lead to increased efficiency, reduced environmental impact, and enhanced compliance with regulatory standards in the maritime sector.

It should be noted that the recommendations in this thesis should be interpreted with caution, as the number of test cases and speed trials evaluated within the scope of this study is limited compared to the joint effort involved in the creation of the original ITTC-78 method. Therefore, further studies are recommended, involving a larger number of test cases encompassing different ship types, sizes, and hull design characteristics for the comparison of speed trials and power predictions. Evaluating a significant number of speed trials is particularly crucial when comparing different full-scale prediction methods (EFD, CFD, or combined CFD/EFD methods) due to the substantial uncertainty often associated with sea trials.

References

Coles, D. (1956). The law of the wake in the turbulent boundary layer. *Journal of Fluid Dynamcics* **1 (2)** (1956), 191–226.

Dogrul, A., Song, S., & Demirel, Y. K. (2020). Scale effect on ship resistance components and form factor. *Ocean Engineering* **209** (2020), 107428. https://doi.org/https://doi.org/10.1016/j.oceaneng.2020.107428

Eça, L., & Hoekstra, M. (2008). The numerical friction line. *Journal of Marine Science and TechnologyJournal of Marine Science and Technology* **13** (2008, November), 328–345. https://doi.org/10.1007/s00773-008-0018-1

García Gómez, A. (2000). On the Form Factor Scale Effect. *Ocean Engineering* **26** (2000), 97–109.

Grigson, C. W. B. (1999). A planar algorithm and its use in analysing hull resistance. *Trans. RINA* (1999), 76–115.

Hino, T., Stern, F., Larsson, L., Visonneau, M., Hirata, N., & Kim, J. (2020). *Numerical Ship Hydrodynamics: An Assessment of the Tokyo 2015 Workshop*. Springer International Publishing. https://doi.org/10.1007/978-3-030-47572-7

Hoerner, S. (1965). *Fluid-Dynamic Drag*. Hoerner Fluid Dynamics, Bakersfield, California.

Hughes, G. (1954). Friction and Form Resistance in Turbulent Flow, and a Proposed Formulation for Use in Model and Ship Correlation. *R. I. N. A.* **96** (1954).

IMO. (2011). *Annex 19: Resolution MEPC.203(62)* (2011).

IMO. (2021). *Fourth IMO GHG Study 2020*. International Maritime Organisation.

IMO. (2022a). 2022 guidelines on operational carbon intensity indicators and the calculation methods (CII guidelines, G1). *Annex 14: Resolution MEPC.352(78)* (2022).

IMO. (2022b). 2022 guidelines on the method of calculation of the attained energy efficiency existing ship index (EEXI). *Annex 12: Resolution MEPC.350(78)* (2022).

IMO-Norway GreenVoyage2050 Project. (2023). *Definitions of maturity levels according to uptake across the maritime industry, and degree of proven technology/principle*. Retrieved March 15, 2023, from https://greenvoyage2050.imo.org/technology-groups/

Insel, M. (2008). Uncertainty in the analysis of speed and powering trials. *Ocean Engineering* **35**.(11) (2008), 1183–1193. https://doi.org/https://doi.org/10.1016/j.oceaneng.2008.04.009

ITTC. (1957). *Subjects 2 and 4 Skin Friction and Turbulence Stimulation* (1957).

ITTC. (1969). *Report of Performance Committee* (1969, September).

ITTC. (1978). *Report of Performance Committee* (1978, September).

ITTC. (1990). *Report of Power Performance Committee* (1990, September).

ITTC. (2014). 1978 ITTC performance prediction method. *ITTC – Recommended Procedures and Guidelines* **7.5-02-03-01.4** (Revision 03 2014).

ITTC. (2017). Guidelines on the determination of model-ship correlation factors. *ITTC – Recommended Procedures and Guidelines* **7.5-04-05-01** (Revision 00 2017).

ITTC. (2021a). 1978 ITTC performance prediction method. *ITTC – Recommended Procedures and Guidelines* **7.5-02-03-01.4** (Revision 05 2021).

ITTC. (2021b). Practical guidelines for ship resistance CFD. *ITTC – Recommended Procedures and Guidelines* **7.5–03–02–04** (Revision 01 2021).

ITTC. (2021c). Quality assurance in ship CFD application. *ITTC – Recommended Procedures and Guidelines* **7.5–03-01–02** (Revision 02 2021).

ITTC. (2021d). Resistance test. *ITTC – Recommended Procedures and Guidelines* **7.5-02-02-01** (Revision 05 2021).

ITTC. (2021e). The specialist committee on CFD and EFD combined methods final report and recommendations. *Committee Reports* (2021, June).

JoRes. (2019). *Joint research project*. Retrieved April 26, 2023, from https://jores.net

Katsui, T., Asai, H., Himeno, Y., & Tahara, Y. (2005). The proposal of a new friction line. *Fifth Osaka colloquium on advanced CFD applications to ship flow and hull form design, Osaka, Japan* (2005).

Kim, K., & Li, D.-Q. (2010). Estimation of numerical uncertainty of Shipflow in self-propulsion simulation of KCS. *Gothenburg 2010 workshop – CFD in ship hydrodynamics* (2010).

Korkmaz, K. B. (2015). *CFD predictions of resistance and propulsion for the JAPAN Bulk Carrier (JBC) with and without an energy saving device* [Master's thesis, Department of Shipping and Marine Technology, Chalmers University Technology, Gothenburg, Sweden].

Korkmaz, K. B., Kim, K., Liefvendahl, M., Werner, S., & Orych, M. (2023). A validation study of full-scale CFD simulation for sea trial performance prediction of ships. *X International Conference on Computational Methods in Marine Engineering MARINE 2023* (2023, June).

Korkmaz, K. B., Orych, M., & Larsson, L. (2015). CFD prediction including verification and validation of resistance, propulsion and local flow for the Japan bulk carrier (JBC) with and without an energy saving device. *Tokyo 2015 workshop – CFD in ship hydrodynamics* (2015).

Korkmaz, K. B., Werner, S., & Bensow, R. (2019a). Numerical friction lines for CFD based form factor determination method. *VIII International Conference on Computational Methods in Marine Engineering MARINE 2019* (2019, May).

Korkmaz, K. B., Werner, S., & Bensow, R. (2019b). Investigations for CFD based form factor methods. *22nd Numerical Towing Tank Symposium, NuTTS 2019* (2019, October).

Korkmaz, K. B., Werner, S., & Bensow, R. (2021). Verification and validation of CFD based form factors as a combined CFD/EFD method. *Journal of Marine Science and Engineering* **9**.(1) (2021). https://doi.org/10.3390/jmse9010075

Korkmaz, K. B., Werner, S., & Bensow, R. (2022). Scaling of wetted-transom resistance for improved full-scale ship performance predictions. *Ocean Engineering* **266** (2022, December), 112590. https://doi.org/10.1016/j.oceaneng.2022.112590

Korkmaz, K. B., Werner, S., Sakamoto, N., Queutey, P., Deng, G., Yuling, G., Guoxiang, D., Maki, K., Ye, H., Akinturk, A., Sayeed, T., Hino, T., Zhao, F., Tezdogan, T., Demirel, Y. K., & Bensow, R. (2021). CFD based form factor determination method. *Ocean Engineering* **220** (2021), 108451. https://doi.org/https://doi.org/10.1016/j.oceaneng.2020.108451

Larsson, L., Stern, F., & Visonneau, M. (2014). *Numerical Ship Hydrodynamics: An assessment of the Gothenburg 2010 Workshop*. Springer. https://doi.org/10.1007/978-94-007-7189-5

Larsson, L. (1998). Will Computational Fluid Dynamics Completely Take the Role of Model Testing? *11th WEMT International Conference: The West European Maritime Industry in the Global Challenge of the Next Century* (1998, May).

Larsson, L., & Raven, H. C. (2010). *Ship Resistance and Flow*. The Society of Naval Architects and Marine Engineers.

Liefvendahl, M. (2023, January). *Ship power prediction with cfd in full scale* (tech. rep. No. RE71221461-01-00-A). RISE Research Institutes of Sweden.

Lindgren, H., & Dyne, G. (1980). Ship performance prediction. *SSPA Publication* **No:85** (1980).

Maki, K., Doctors, L., Beck, R., & Troesch, A. (2006). Transom-stern flow for high-speed craft. *Aust. J. Mech. Eng.* **3** (2006, January), 191–199. https://doi.org/10.1080/14484846.2006.11464508

Mikkelsen, H., & Steffensen, M. L. (2016, June). *Full scale validation of CFD model of self-propelled ship* [Master's thesis, Technical University of Denmark].

Mikulec, M., & Piehl, H. (2023). Verification and validation of CFD simulations with full-scale ship speed/power trial data. *Brodogradnja* **74**.(1) (2023, March), 41–62. https://doi.org/10.21278/brod74103

Niklas, K., & Pruszko, H. (2019). Full-scale CFD simulations for the determination of ship resistance as a rational, alternative method to towing tank experiments. *Ocean Engineering* **190** (2019, October), 106435. https://doi.org/10.1016/j.oceaneng.2019.106435

Orych, M., & Larsson, L. (2015). Hydrodynamic aspects of transom stern optimization. *5th High Performance Yacht Design Conference* (2015, March), pp.247–256.

Orych, M., & Regnström, B. (2023). Verification and validation of volume-of-fluid functionality in Shipflow. *personal communication* (2023).

Orych, M., Werner, S., & Larsson, L. (2021). Validation of full-scale delivered power CFD simulations. *Ocean Engineering* **238** (2021, October), 109654. https://doi.org/10.1016/j.oceaneng.2021.109654

Orych, M., Werner, S., & Larsson, L. (2022). Roughness effect modelling for wall resolved RANS – Comparison of methods for marine hydrodynamics. *Ocean Engineering* **266** (2022, December), 112778. https://doi.org/10.1016/j.oceaneng.2022.112778

Pereira, F. S., Eça, L., & Vaz, G. (2017). Verification and Validation Exercises for the Flow around the KVLCC2 Tanker at Model and Full-Scale Reynolds Numbers. *Ocean Engineering* **129** (2017), 133–48. https://doi.org/10.1016/j.oceaneng.2016.11.005

Proceedings of the 7th ITTC. (1954). (1954).

Prohaska, C. W. (1966). A Simple Method for the Evaluation of the Form Factor and Low Speed Wave Resistance. *Proceeding of 11th ITTC* (1966).

Queutey, P., & Visonneau, M. (2007). An interface capturing method for free-surface hydrodynamic flows. *Computers and Fluids* **36** (2007), 1481–1510.

Raven, H. C., van der Ploeg, A., Starke, A. R., & Eça, L. (2008). Towards a cfd-based prediction of ship performance - progress in predicting full-scale resistance and

scale effects. *International Journal of Maritime Engineering* **Transactions of the Royal Institution of Naval Architects Part A** (2008).

Schoenherr, K. E. (1932). Resistance of flat surfaces. *Trans. SNAME* **40** (1932), 279–313.

Schouten, D. R., Drouet, A., Birvalski, M., & Morand, L. (2022). Full Scale CFD Validation Using Ship Performance and Wave Pattern Measurements of a Mega Cruise Ship. *Volume 7: CFD and FSI* (2022, June), V007T08A041. https://doi.org/10.1115/OMAE2022-79208

Shirose, Y., & Hirono, S. (1982). A Method to Determine Form Factor of Ship Models from Resistance Tests. *IHI Engineering Review* **15**.(3) (1982, July).

Starke, B., Raven, H., & van der Ploeg, A. (2007). Computation of transom-stern flows using a steady free-surface fitting RANS method. *9th International Conference on Numerical Ship Hydrodynamics* (2007, August), 18.

Sun, W., Hu, Q., Hu, S., Su, J., Xu, J., Wei, J., & Huang, G. (2020). Numerical Analysis of Full-Scale Ship Self-Propulsion Performance with Direct Comparison to Statistical Sea Trail Results. *Journal of Marine Science and Engineering* **8**.(1) (2020, January), 24. https://doi.org/10.3390/jmse8010024

Terziev, M., Tezdogan, T., & Incecik, A. (2019). A Geosim Analysis of Ship Resistance Decomposition and Scale Effects with the Aid of CFD. *Applied Ocean Research* **92** (2019). https://doi.org/10.1016/j.apor.2019.101930

Toki, N. (2008). Investigation on Correlation Lines through the Analyses of Geosim Model Test Results. *Journal of the Japan Society of Naval Architects and Ocean Engineers* **8** (2008), 71–79.

Townsin, R. L., & Dey, S. K. (1990). The Correction of Roughness Drag with Surface Characteristics. *Proc. Int. Workshop on Marine Roughness and Drag, RINA* (1990).

Van, S. .-., Ahn, H., Lee, Y. .-., Kim, C., Hwang, S., Kim, J., Kim, K. .-., & Park, I. .-. (2011). Resistance characteristics and form factor evaluation for geosim models of kvlcc2 and kcs. *Advanced Model Measurement Technology for EU Maritime Industry* (2011).

Wackers, J., Deng, G., Guilmineau, E., Leroyer, A., Queutey, P., & Visonneau, M. (2014). Combined refinement criteria for anisotropic grid refinement in free-surface flow simulation. *Computers & Fluids* **92** (2014), 209–222. https://doi.org/https://doi.org/10.1016/j.compfluid.2013.12.019

Wang, Z. .-., Xiong, Y., Shi, L. .-., & Liu, .-., Z. (2015). A Numerical Flat Plate Friction Line and Its Application. *Journal of Hydrodynamics* **23** (3 2015), 383–393.

Werner, S., & Gustafsson, L. (2020). Uncertainty of Speed Trials. *5th Hull Performance & Insight Conference* (2020, October).

Paper I

Numerical Friction Lines for CFD Based Form Factor Determination Method

VIII International Conference on Computational Methods in Marine Engineering
MARINE 2019
R. Bensow and J. Ringsberg (Eds)

NUMERICAL FRICTION LINES FOR CFD BASED FORM FACTOR DETERMINATION

Kadir B. Korkmaz[*†], Sofia Werner[†] and Rickard Bensow[*]

[*] Department of Mechanics and Maritime Sciences
Chalmers University of Technology
Chalmersplatsen 4, 412 96 Göteborg, Sweden
e-mail: korkmaz@chalmers.se
e-mail: rickard.bensow@chalmers.se

[†] SSPA Sweden AB
Chalmers Tvärgata 10, 412 58 Göteborg, Sweden
email: sofia.werner@sspa.se - Web page: www.sspa.se

Key words: Friction resistance coefficient, form factor, numerical uncertainty, flat plate

Abstract. In this study, frictional resistance coefficients of an infinitely thin 2D plate have been computed at 14 Reynolds numbers (between $log_{10}(Rn) = 6.25$ to 9.5) in sets of five geometrically similar structured grids in order to perform reliable grid dependence studies. Additional grid dependency studies have been performed by using 5 sets of grids which have the same number of cells in all directions but varying first cell sizes normal to the flat plate at $log_{10}(Rn) = 6.25$. Average y^+ values for each grid set for the finest grid varies between 0.0075 and 0.5 (from set 1 to 5 respectively) while none of the simulations exceeded average y^+ value of 1. All simulations were performed with the direct application of the no-slip condition at walls. Therefore, no wall functions were used. Two turbulence models have been used for the investigations: $k-\omega$ SST and EASM. Extensive grid dependence studies have been performed with two different CFD codes SHIPFLOW and FINE™/MARINE, using the same grids. Special attention was paid to the transition from laminar to turbulent flow at the lowest Reynolds number since laminar part can cover a significant part of the plate. At $log_{10}(Rn) = 6.25$ for both CFD codes, laminar flow and transition to turbulent flow was distinctive even though no transition models were applied. Significant dependency on y^+ has been observed with FINE™/MARINE on friction resistance coefficient. On the other hand, SHIPFLOW exhibited less sensitivity to the first cell size variation, hence, revealed smaller numerical uncertainties in general. To ensure a numerical uncertainty of frictional resistance component below 1%, average $y^+ < 0.016$ have been used for generating the data points of friction line with SHIPFLOW for each turbulence model. Data points of 14 Reynolds number have been transformed into numerical friction lines by applying curve fits. Obtained friction lines are compared with ITTC57 line, Schoenherr, Hughes, Toki, Katsui, Grigson lines and two numerical friction lines.

1 INTRODUCTION

The friction line, i.e. the dependency of flat plate frictional resistance coefficients on Reynolds number, is used in the 1978 ITTC method for scaling of ship resistance measured in a towing tank. The 1978 ITTC method adopted the form factor concept as described by Hughes

in [1], where the viscous resistance is expressed in relation to the "ITTC 57 model-ship correlation line" as shown in the following equation:

$$C_V = (1 + k)C_F \tag{1}$$

where k is the form factor and C_F is the friction resistance coefficient. The form factor concept, as well as the determination method proposed by Prohaska [2] has been questioned and investigated for many decades. The scale effects on form factor has been well demonstrated by García-Gómez [3], Toki [4] and Van et al. [5] using geosim test data analysis. In addition to the re-analysis of the geosim test data, CFD studies by Raven et al. [6] and Wang et al. [7] supported the existence of substantial scale effects on form factor and the main cause of the scale effects have been found to be the "ITTC 57 model-ship correlation line" rather than the original hypothesis of Hughes which suggested the form factor is independent of the Reynolds number. Additionally, when the growing disposition to leave the Prohaska's method of form factor determination and growing confidence in numerical resistance calculations are considered, CFD might be able to provide a new method of form factor determination, which can increase the accuracy of the full-scale resistance predictions.

In this study, numerical friction lines have been investigated and two numerical friction lines have been derived with k-ω SST and EASM turbulence models. Grid dependency studies have been performed with SHIPFLOW and FINE™/MARINE codes in order to highlight the aspects that influence the skin friction coefficient, such as the effect of non-dimensional wall distance (y^+), turbulence intensity and transition from laminar to turbulent flow. The study is part of a larger research scope with the goal of recommending suitable procedures for using CFD to derive the form factor and the full scale ship resistance based on towing tank test.

2 FLOW SOLVERS, COMPUTATIONAL DOMAIN, BOUNDARY CONDITIONS AND GRIDS

2.1 Flow Solvers

Two CFD codes have been used for this study: SHIPFLOW 6.3 and FINE™/MARINE 7.2. Starting with the former, XCHAP is the solver of SHIPFLOW which solves the Reynolds averaged Navier-Stokes (RANS) equations with a finite volume method. EASM, as described in [8], and $k-\omega$ SST, of [9], turbulence models are available. The convective terms are discretized with a Roe scheme which is first order accurate. Therefore, in order to increase the accuracy a flux correction is applied explicitly. The equations are solved with Krylov solver (adopted from PETSc) which implements the Generalized Minimal Residual method (KSPGMRES). Note that results from SHIPFLOW will be referred as "SF" in the plots in order to save space.

ISIS-CFD is the flow solver of FINE™/MARINE. The solver is based on Finite volume method and incompressible unsteady Reynolds-averaged Navier Stokes equations are solved. There is no specific requirements on the topology of cells since the face-based method is used. The discretisation of the convective fluxes in both the momentum equations and the equations for turbulence modelling have been performed with AVLSMART scheme for this study. Among many turbulence models available in FINE™/MARINE, EASM, described in [8], and $k-\omega$ SST, of [9], turbulence models have been selected. Note that results from FINE™/MARINE will be referred as "FM" in the plots.

2.2 Computational Domain

The computational domain size is based on the requirements of XCHAP and ISIS-CFD solvers. The domain is shaped as a rectangular prism since a 3D domain is required by the solvers. Size of the domain has been determined by the preliminary computations carried out at $log_{10}(Rn) = 6.25$ with two alternative domains. The flat plate have a length of *L*. The first domain has the inlet located *0.25L* upstream of the leading edge, the outlet is placed *0.25L* downstream of the trailing edge, side boundary located *0.25L* away from the flat plate in the normal direction. The second domain (Dm2) has been designed with double the distance of the inlet, outlet and side boundaries (*0.5L*). The height of the domain is *1L* for both domains since the flow is 2D and height has no effect on the results.

Table 1 Comparison of influence of domain size on the computed prediction of the friction resistance

	EASM (SHIPFLOW)		EASM (FINE™/MARINE)		$k-\omega$ SST (SHIPFLOW)		$k-\omega$ SST (FINE™/MARINE)	
	g1	g5	g1	g5	g1	g5	g1	g5
$\Delta C_F(\%)$	-0.6	-0.6	-0.6	-0.7	-0.6	-0.6	-0.6	-0.6
$U(C_F)(\%)$								
Dm1	0.08	0.29	0.13	0.37	0.18	0.69	0.09	0.32
Dm2	0.08	0.28	0.10	0.36	0.17	0.63	0.10	0.35

The differences between the frictional resistance coefficients for the two domain sizes, $\Delta C_F(\%) = 100 \times (C_F(Dm2) - C_F(Dm1))/C_F(D1)$, together with obtained numerical uncertainties, $U(C_F)$, for the finest grid are presented in Table 1. The differences in C_F between the two domains are larger than the numerical uncertainties (presented in Section 3), opposed to what was observed by Eça and Hoekstra [10]. The investigations have indicated that the difference might originate from the dissipated turbulent kinetic energy between the inlet boundary and the flat plate. As it will be more thoroughly discussed in the Section 2.4, larger domain (Dm2) seems to act as a flow with lower turbulence intensity which results in slightly delayed transition from laminar to turbulent flow and lower friction resistance in the turbulent region. In order to confirm this argument, additional simulations have been performed with Dm2 domain at $log_{10}(Rn) = 8.00$. The difference of C_F has been reduced to the numerical uncertainty levels as at such high Reynolds numbers turbulence intensity is not expected to have substantial impact. In the light of these findings the initial domain, Dm1, has been chosen for the further computations.

2.3 Boundary Conditions

The inlet boundary conditions are fixed uniform velocity (U_∞) and specific turbulent dissipation rate, ω, at the inlet is calculated by $(\omega)_{inlet} = \lambda U_\infty/L$. The default values of the factor of proportionality, λ, are set to $\lambda = 1$ for FINE™/MARINE and $\lambda = 10$ for SHIPFLOW. The turbulent kinetic energy at the inlet is defined as $(k)_{inlet} = \mu\omega_{inlet}C_i/\rho$ where μ and ρ are dynamic viscosity and density respectively. FINE™/MARINE assumes the value of the constant $C_i = 1 \times 10^{-3}$ while SHIPFLOW adopted $C_i = 1 \times 10^{-4}$. As a result, both codes have the same turbulence intensity at the inlet. The outlet boundary condition of both codes consists of Neumann boundary condition that sets the gradient of velocity, k and pressure to zero,

normal to the outflow plane. Slip condition simulates a symmetry condition by setting the normal velocity and normal gradient of other variables to zero. Noslip condition specifies the velocities components, k and normal pressure component as zero at the wall. ω on the wall is specified differently by both codes. For FINE™/MARINE, $\omega_w = 10 \times (6\mu/0.075\rho d^2)$ where d is the distance of the first cell away from the wall. SHIPFLOW defines the wall value of ω of a smooth surface as $\omega_w = (u_\tau^2/\nu) \times \left(50/4.3y^{+0.85}\right)^2$ as introduced in [11] where $u_\tau$is he frictional resistance and ν is the kinematic viscosity. All simulations have been performed with the direct application of the no-slip condition at walls. Therefore, no wall functions were used.

2.4 Local skin friction coefficient and transition from laminar to turbulent flow

Local skin friction coefficients of have been investigated in order to assess the behaviour of turbulence models in transition from laminar to turbulent flow. The local skin friction coefficient has been defined as:

$$C_f = \frac{\mu\left(\frac{\partial u_x}{\partial y}\right)_{y=0}}{\frac{1}{2}\rho U_\infty L} \tag{2}$$

At the typical *Rn* that towing tank model tests are normally performed, transition is considered to be important. As indicated by Eça et al. [10], the natural transition in the boundary layer of a flat plate occurs approximately at $Re_x = 10^6$. However, the transition can occur earlier if the turbulence intensity is increased. In this study, no transition models have been used as the aim is to determine the behaviour of the regular turbulence models readily available in both SHIPFLOW and FINE™/MARINE.

The calculated skin friction coefficients from SHIPFLOW and FINE™/MARINE at $log_{10}(Rn) = 6.25$ are presented in Figure 1 together with the ERCOFTAC Classic Database [12] where flat plate experiments with three different free-stream turbulence intensity ($0.009U_\infty^2$, $0.03U_\infty^2$ and $0.06U_\infty^2$) were performed. The turbulence intensity at the inlet boundary with SHIPFLOW and FINE™/MARINE are the same, $k_\infty \cong 5.6 \times 10^{-10}U_\infty^2$ for $log_{10}(Rn) = 6.25$. The first significant observation is the laminar flow region where C_f of both turbulence models and CFD codes follow Blasius line until the transition to turbulent flow occurs. If laminar flow covers a significant part of the plate, the calculated skin friction coefficient will be smaller than a fully turbulent flow. However, both turbulence models and CFD solvers predicted the transition location approximately where the turbulence stimulators are usually fitted to towing tank ship models (5% of L_{pp} from fore perpendicular). The position of the transition is similar to ERCOFTAC experiments with 3% and 6% even though turbulence intensity in the computations are extremely smaller than the experiments. It is also significant that the transition shows qualitatively similar behaviour to the experiments with both $k-\omega$ SST and EASM turbulence models with both solvers. The laminar flow can be observed even at *Rn* numbers as high as $log_{10}(Rn) = 9.5$ as presented in Figure 1 even though only a fraction of the flat plate (~0.003%) is covered with laminar flow. As can be seen from the Figure 1 (on the right), simulations at different Reynolds numbers show consistency in skin friction coefficient not only at the laminar region but also at the turbulent region. It should be noted that, the vertical lines occurs due to local increase of C_f at the trailing edge of the flat plate.

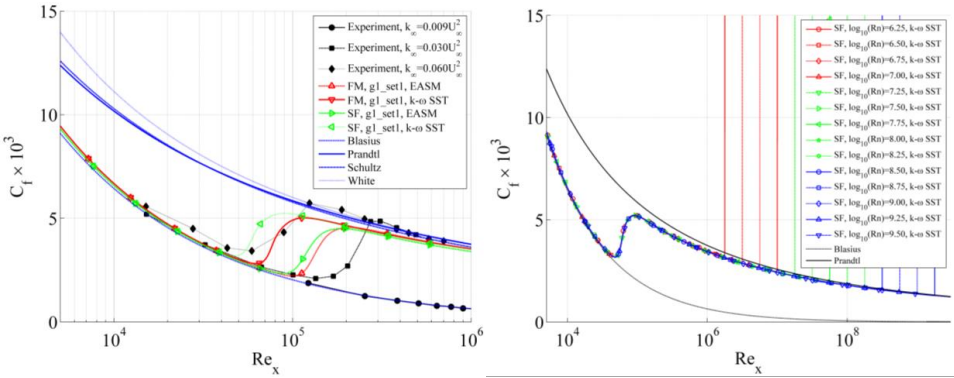

Figure 1 Skin friction coefficient C_f along the flat plate at $log_{10}(Rn) = 6.25$ (on the left) and C_f along the flat plate at $log_{10}(Rn) = 6.25$ to 9.5

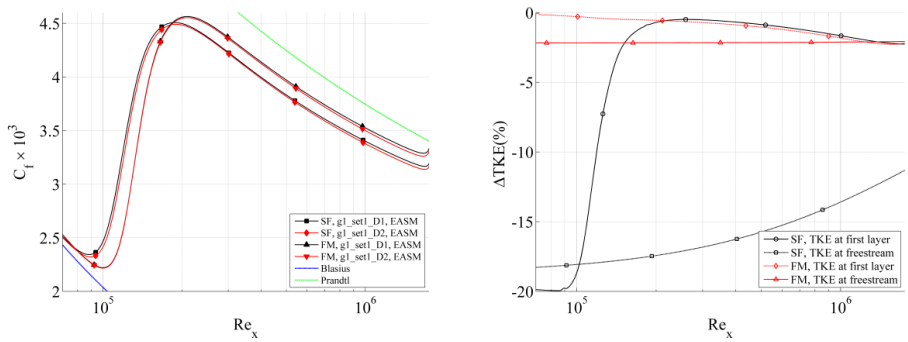

Figure 2 Influence of domain size on TKE and on the skin friction coefficient along the flat plate at $log_{10}(Rn) = 6.25$. $\Delta TKE(\%) = 100 \times (TKE(Dm2) - TKE(Dm1))/TKE(D1)$

As mentioned previously, the increase of the domain size resulted in a reduction of C_F approximately 0.6% which is significantly larger than the numerical error for both codes. The investigations have shown that with a larger domain size (Dm2), the turbulent kinetic energy (TKE) dissipates more than with the smaller domain (Dm1). The difference of TKE between the domains has been calculated as $\Delta TKE(\%) = 100 \times (TKE(Dm2) - TKE(Dm1))/TKE(Dm1)$. As shown in Figure 2 (on the right), the freestream TKE levels are approximately -18.8% and -2.1% lower in Dm2 compared to Dm1 domain at the alignment in x-direction of the leading edge of the plate for SHIPFLOW and FINE™/MARINE respectively. The reason of such difference in TKE dissipation levels is explained by the different boundary condition of $(\omega)_{inlet}$ which is ten times larger in SHIPFLOW than FINE™/MARINE. TKE at the first layer away from the plate with Dm2 are also lower than Dm1 all over the Re_x range. As shown in Figure 2, the transition has been slightly delayed in SHIPFLOW simulation and the C_f values are lower with an increasing rate from the transition location (where TKE levels are similar in both domains around $Re_x = 2 \times 10^5$) to the trailing edge where C_f is approximately 0.8% lower in Dm2 than Dm1 case for both codes. This means that the domain size has an effect on the TKE that gives a non-negligible impact on the total skin friction.

2.5 Grid Sets

The discretization of the computational domain has been done by five sets (sets 1 to 5) of orthogonal stretched grids. Each set consists of five geometrically similar grids. Grid sets have the same number of cells along the x-direction and y-direction but differing in the first cell size perpendicular to the flat plate for the corresponding Reynolds number. The smallest first cell sizes in y-direction (yielding lowest y^+ values) are denoted as set1 and first cell sizes are gradually increased from set1 to set5 having the largest y^+ values. In all the grids, the number of cells along the plate makes *4/6* of all the cells in x-direction, leaving 1/6 of cells for upstream and downstream of the plate. The cells in the normal direction has been stretched with a one sided stretching function. The leading edge and trailing edges are also stretched in a similar fashion. The five geometrically similar grids of each set have been refined with grid refinement ratio of $h_i/h_1 = \sqrt{N_{cells_1}/N_{cells_i}}$. The number of cells corresponding to each grid and flow speed are presented in Table 2. In order to assure growth rate of the cells in y-direction (normal to the plate) remain in similar levels throughout the Rn range, three different mesh density have been used.

Table 2 Number of cells in each direction

	g1		g2		g3		g4		g5	
lo10Rn	Nx	Ny	Nx	Ny	Nx	Ny	Nx	Ny	Nx	Ny
6.25-7.0	1440	240	1260	210	1080	180	900	150	720	120
7.25-8.25	2160	360	1890	315	1620	270	1350	225	1080	180
8.5-9.5	2880	480	2520	420	2160	360	1800	300	1440	240

Table 3 Calculated $(y^+)_{mean}$ and $(y^+)_{max}$ values from SHIPFLOW at the first layer away from the flat plate for EASM turbulence model at $log_{10}(Rn) = 6.25$

	$(y^+)_{mean}$					$(y^+)_{max}$				
	set1	set2	set3	set4	set5	set1	set2	set3	set4	set5
g1	0.008	0.057	0.105	0.238	0.448	0.09	0.53	0.90	1.73	2.66
g2	0.009	0.065	0.120	0.272	0.512	0.10	0.59	1.00	1.88	2.88
g3	0.010	0.076	0.140	0.318	0.598	0.11	0.66	1.12	2.08	3.15
g4	0.012	0.091	0.167	0.381	0.719	0.13	0.76	1.27	2.33	3.50
g5	0.016	0.113	0.209	0.477	0.900	0.15	0.90	1.48	2.66	3.96

The first layer cell size is varied with the same ratio (h_i/h_1) for each grid set. In Table 3, mean and maximum y^+values for computations from SHIPFLOW at $log_{10}(Rn) = 6.25$ have been presented. The y^+ values from FINE™/MARINE were almost identical to Table 3. All simulations have been performed with $(y^+)_{mean} < 1$ which is the widespread rule of thumb. The $(y^+)_{max}$ values exceeds the non-dimensional height of $y^+ = 1$ for set3 to set5, however, it is observed only at the very ends of leading and trailing edges of the plate. For a given Reynolds number (the speeds other than $log_{10}(Rn) = 6.25$), first cells sizes has been adjusted so that similar $(y^+)_{mean}$ values are obtained as presented in Table 3.

It is important to note that SHIPFLOW solver does not have 2D flow option therefore 3 cells are added in the z-direction which is the only way they differ from the meshes used for FINE™/MARINE. To ensure FINE™/MARINE solver provides the same results for 2D and

3D meshes, several computations have been performed and no significant difference has been found. Therefore, 2D grids have been calculated with ISIS-CFD solver in order to save time and reduce the computational demand.

3 GRID DEPENDENCE STUDY

In order to assess the numerical uncertainty, grid dependence studies have been performed. All computations have been performed in double precision in order to eliminate the round-off errors. Additionally, iterative uncertainties have been predicted from the standard deviation of the force in percent of the average force over the last 10% iterations. Iterative uncertainty was kept below 0.01% for all simulations. Simulations at $log_{10}(Rn) < 8$ exhibited even lower standard deviations of force (typically lower than 1×10^{-4}). Therefore, both iterative errors and round-off errors are assumed to be small enough to be neglected and numerical errors are dominated by the discretization errors. The procedure proposed in [13] have been adopted to predict the numerical uncertainties.

Table 4 Observed order of accuracy, p, for the flat plate at $log_{10}(Rn) = 6.25$

	SHIPFLOW					FINE™/MARINE				
	set1	set2	set3	set4	set5	set1	set2	set3	set4	set5
EASM	1.9	1.9	1.6	1.1	1.5	1.5	1.4	1.2	0.9	0.6
$k-\omega$ SST	2	2	1.8	1.1	0.9	1.8	1.4	1.1	0.8	0.5

Table 5 Predicted numerical uncertainties, $U(C_F)$, for EASM turbulence model, in percentage

	SHIPFLOW						FINE™/MARINE				
	set1	set2	set3	set4	set5		set1	set2	set3	set4	set5
g1	0.08	0.10	0.18	0.55	0.62	g1	0.13	0.41	0.86	2.48	6.15
g2	0.10	0.13	0.22	0.64	0.76	g2	0.16	0.50	1.01	2.79	6.65
g3	0.14	0.17	0.29	0.76	0.94	g3	0.20	0.62	1.21	3.19	7.28
g4	0.19	0.24	0.39	0.93	1.24	g4	0.26	0.79	1.50	3.74	8.12
g5	0.29	0.36	0.55	1.19	1.71	g5	0.37	1.08	1.95	4.55	9.26

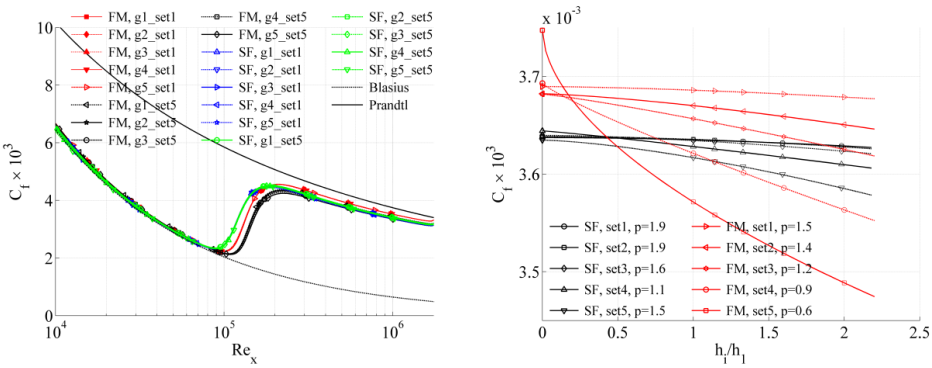

Figure 3 Influence of first cell size (set1 and set5) on the skin friction coefficient along the flat plate and convergence of friction coefficient C_F for SHIPFLOW and FINE™/MARINE at $log_{10}(Rn) = 6.25$

The observed order of accuracies and numerical uncertainties for SHIPFLOW and FINE™/MARINE are presented in Table 4 and Table 5. The numerical uncertainties from *k-ω* SST model is slightly higher than EASM for all grid sets with FINE™/MARINE. However, predicted uncertainties on set 1 and set2 with k-ω SST are almost two times higher with SHIPFLOW. The ISIS-CFD solver have been found to be sensitive to near wall cell height compared to XCHAP solver since numerical uncertainties on the skin friction coefficient can be as high as 9% with $(y^+)_{\mathrm{mean}}$ values around 0.9.

In order to explain the difference of $U(C_F)$ between the two solvers, the skin friction coefficient along the flat plate has been investigated. As presented in Figure 3, the grids belong to set1 and set5 has been plotted for SHIPFLOW and FINE™/MARINE. It is important to notice that C_f values from SHIPFLOW are consistent in set1 and set5 grids in the laminar region and transition location but differing marginally in the turbulent region. However, for FINE™/MARINE the C_f values are consistent in the laminar region but differing significantly between set1 and set 5 for the transition location also in the fully turbulent region (up to 5% difference in C_f). Sensitivity to y^+ can also be observed with convergence of C_f with the grid refinement presented for EASM model for both solvers in Figure 3. It is worth to recall that the number of cells corresponding to each h_i/h_1 value ($h_i/h_1 = 1$ being the finest grid) are identical. Considering the numerical uncertainties presented, it can be concluded that $(y^+)_{\mathrm{mean}} \cong 1$ is not acceptable for any of the solvers and in order to attain $U(C_F)$lower than 1%, $y^+ \cong 0.1$ should be used for *k-ω* SST and EASM turbulence models, as also concluded by Eça et all. [14].

Considering the outcomes of the grid dependence study performed at $log_{10}(Rn) = 6.25$, the rest of the simulations have been performed with 5 geometrically similar grids per speed with y^+ values similar to the set1 presented in Table 3 .Observed order of accuracies and predicted numerical uncertainties for the finest grids are presented in Table 6 and Table 7.

Table 6 Observed order of accuracy,p, of the friction resistance for SHIPFLOW

	$\log_{10}(Rn)$													
	6.25	6.5	6.75	7	7.25	7.5	7.75	8	8.25	8.5	8.75	9	9.25	9.5
EASM	1.9	1.8	1.7	1.7	1.8	1.9	1.8	1.7	1.7	2	1.8	1.7		
$k-\omega$ SST	2	2	2	2	2	2	1.2	2	2	2	2	2	2	2

Table 7 Predicted numerical uncertainties of the finest girds (g1), of the friction resistance, $U(C_F)$, for SHIPFLOW, in percentage

	$\log_{10}(Rn)$													
	6.25	6.5	6.75	7	7.25	7.5	7.75	8	8.25	8.5	8.75	9	9.25	9.5
EASM	0.08	0.10	0.12	0.13	0.06	0.06	0.07	0.09	0.08	0.04	0.05	0.05		
$k-\omega$ SST	0.18	0.21	0.25	0.29	0.10	0.11	0.14	0.14	0.15	0.04	0.09	0.08	0.08	0.05

4 NUMERICAL FRICTION LINE

The friction resistance coefficient C_F is obtained from the integration of the C_f along the flat plate. As explained earlier, C_F of 5 geometrically similar grids for 14 Reynolds number has been calculated with $k-\omega$ SST and EASM turbulence models with SHIPFLOW. The last two

speeds with EASM are omitted due to difficulties with convergence issues. As a result of performing the grid dependence study as explained by Eça and Hoekstra [13], the exact numerical solution of friction resistance coefficient at each Reynolds number have been calculated. The exact solutions or in other words grid independent results, are then used for the generation of numerical friction lines. Curve fits have been applied to data generated using the two alternative formulations. The first alternative is based on the ITTC 57 analytical formula

$$C_F^a = \frac{a_1^a}{(\log_{10}(Rn) - a_2^a)^{a_3^a}} \tag{3}$$

The second alternative as adopted from [10] assumes that C_F can be expressed as a cubic polynomial in logarithmic scales

$$\log(C_F^c) = \log(a_1^c) + a_2^c \log(Rn) + a_3^c (\log Rn)^2 + a_4^c (\log Rn)^3 \tag{4}$$

Eq. 4 can be re-formulated as the following

$$C_F^c = a_1^c (Rn)^{(a_2^c + a_3^c \log(Rn) + a_4^c (\log Rn)^2)} \tag{5}$$

The three constants a_1^a, a_2^a and a_3^a of Eq. 3 and the four constants a_1^c, a_2^c, a_3^c and a_4^c of Eq. 5 have been determined with a non-linear least squares approach. In order to assess the quality of the fit, root-mean-square error (denoted as *S*) has been calculated by determining the degree of freedom by the difference between the number of data points and number of constraints. The constants and the standard deviations of the two equations have been presented in Table 8.

Table 8 Constants of the curve fits for of Eq. 3 and Eq. 5 to the friction coefficients of EASM and k-ω STT turbulence models

	C_F^a				C_F^c				
	a_1^a	a_2^a	a_3^a	$S^a \times 10^6$	$a_1^c \times 10^2$	$a_2^c \times 10^2$	$a_3^c \times 10^3$	$a_4^c \times 10^5$	$S^c \times 10^6$
EASM	11.300	-3.617	3.512	5.329	1.792	-2.400	-9.40	23.40	2.796
$k-\omega$ SST	0.612	-0.592	2.638	2.383	10.810	-30.75	5.81	-3.96	1.627

The curve fits of Eq.3 and Eq.5 shows both very good agreement with the data. The differences between the two fits are graphically hard to assess since they are almost coinciding throughout the Rn range. However, the root-mean-square error indicates that Eq.5 is the better fit for both turbulence models. Therefore, Eq. 5 is adopted and compared to the other friction lines. Obtained numerical frictional lines for *k- ω* SST and EASM turbulence models have been compared with ITTC57 line [15], Schoenherr [16], Hughes [1], Toki [4], Katsui [17], Grigson [18] and two numerical friction lines proposed by Eça et al. [10] and Wang et al. [7]. Figure 4 presents the friction lines in a relative way because the visual judgement over the friction lines is difficult when presented many lines at a time. The differences between the friction lines are presented with respect to numerical friction derived from *k- ω* SST model of SHIPFLOW and calculated, i.e. $\Delta C_F(ITTC57)\ (\%) = 100 \times (C_F(ITTC57) - C_F(\mathrm{k}-w\ SST))/C_F(\mathrm{k}-w\ SST)$. As can be seen from Figure 4, *k-ω* SST lines of Eça et al. [10] and Wang et al. [7] are very similar to *k-ω* SST line derived by SHIPFLOW in all Reynolds numbers. The spread among the numerical friction lines is much smaller than analytical friction lines in general. All numerical friction lines lead to lower C_F values than the analytical correlations (except Hughes line) at the lower Rn range but the gap is reduced around $log_{10}(Rn) = 8.0$ and onwards. Existence of

laminar flow in the lowest Reynolds numbers for the numerical friction lines can be responsible for such behavior which should be investigated further.

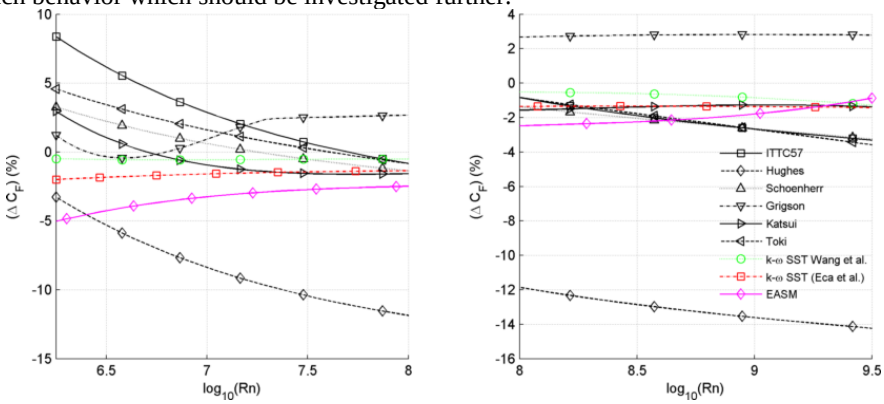

Figure 4 Friction lines in comparison to SHIPFLOW $k-\omega$ SST, in percentage

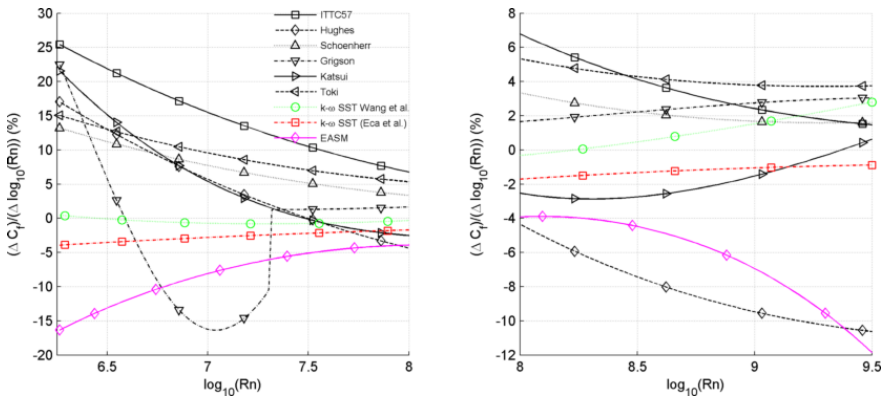

Figure 5 Derivative of the friction lines in comparison to SHIPFLOW $k-\omega$ SST, in percentage

The slope of the friction line is more important than the absolute values for the purpose of extrapolation. Therefore, the derivatives of the lines have been calculated and presented in Figure 5, again with respect to k-ω SST line of SHIPFLOW. The similarity of k-ω SST lines of Eça and Hoekstra [10] and Wang et al. [7] to the k-ω SST line derived from SHIPFLOW is remarkable. All numerical friction lines possess significantly lower slope at the lower range of Reynolds numbers, but this difference is reduced significantly at $Rn < 10^8$ except Hughes lines and the friction line derived from EASM turbulence model. The slope obtained with EASM is distinctively smaller at the both ends of the Reynolds numbers.

5 CONLUSIONS

This paper presents a study on the numerically calculated friction resistance coefficient of an infinitely-thin flat plate as a function Reynolds number in the range of $6.25 < log_{10}(Rn) < 9.5$. EASM and k-ω SST turbulence models have been used and investigated. Comprehensive

grid dependence studies have been performed with SHIPFLOW and FINE™/MARINE codes. Two numerical friction lines are derived from the SHIPFLOW and compared to the lines available in open literature.

The grid dependence studies at $log_{10}(Rn) = 6.25$ indicated that numerical uncertainty on the friction resistance coefficient is highly dependent on the first cell size. In order to achieve numerical uncertainty of frictional resistance coefficients below 1%, SHIPFLOW requires approximately $y^+ \leq 0.4$ for both EASM and *k-ω* SST models. However, the requirement to achieve numerical uncertainties below 1% for FINE™/MARINE is $y^+ \leq 0.1$ for both EASM and *k-ω* SST models which was also the conclusion of [14] for the latter turbulence model.

Two main modelling errors have been investigated: transition of flow from laminar to turbulent and turbulence models. Laminar to turbulent transition has been observed in both turbulence models and CFD solvers. Even though, transition location was predicted differently by the two CFD codes, transition behavior was qualitatively correct compared to ERCOFTAC experiments. Comparing the turbulence intensity levels at ERCOFTAC experiments to the very low turbulence intensity levels in CFD, transition occurs at too low Reynolds numbers with CFD. When the location of the transition is analyzed, only around 5% of the plate featuring the laminar flow at the lowest *Rn*. Considering that the turbulence stimulators in model testing are usually placed at 5% of L_{pp} from the fore perpendicular, amount of wetted surface covered by laminar flow in a model test is comparable to the numerical conditions.

The numerical calculations with two different domain sizes indicated that the effect of turbulence intensity at the leading edge affects the calculated friction resistance. Obviously, the slope of the friction line at the lower Reynolds number will change depending on which turbulence intensity have been chosen. Its implications are not investigated within the context of this study.

Numerical friction lines have been obtained for EASM and *k-ω* SST turbulence models using SHIPFLOW. The expression based on cubic polynomial in the logarithmic scales (Eq.5) provided the best fit for both turbulence models. The derived numerical friction lines were compared to the friction lines available in open literature. The slope of the line derived from k-ω SST is similar to other the numerical friction lines of Eça and Hoekstra [10] and Wang et al. [7] of the same turbulence model. EASM line exhibits significantly less slope at the both ends of the *Rn* range and differing from all other friction lines in the high Rn range except the Hughes line to some extent.

When using a numerical friction line for ship resistance extrapolation it should be considered that the result could be highly dependent on several factors: non-dimensional wall distance (y^+), choice of turbulence model, boundary conditions such as turbulence intensity and the CFD code. Since numerical approaches differ for each code, the effect of these factors can be different as well. Hence, it may not be advisable to use a general friction line for CFD based form factor determination method. The next step in our research is to study the previously mentioned factors that may affect the ship resistance extrapolation.

REFERENCES

[1] G. Hughes, “Friction and Form Resistance in Turbulent Flow, and a Proposed Formulation for Use in Model and Ship Correlation”. *Trans. RINA*, Vol. 96, (1954) p.314-376

[2] C. W. Prohaska, “A Simple Method for the Evaluation of the Form Factor and Low Speed

Wave Resistance", *Proceeding of 11th ITTC*, (1966).

[3] A. García-Gómez, "On the Form Factor Scale Effect", *Ocean Engineering*, Vol 26, (2000) pp.97-109.

[4] N. Toki, "Investigation on Correlation Lines through the Analyses of Geosim Model Test Results", *Journal of the Japan Society of Naval Architects and Ocean Engineers*, Vol 8, (2008). pp.71-79

[5] S.-H.Van, H. Ahn, Y.-Y. Lee, C. Kim, Hwang, S. Hwang, J. Kim, K.-S. Kim, I.-R. Park, "Resistance Characteristics and Form Factor Evaluation for Geosim Models of KVLCC2 and KCS", *Advanced Model Measurement Technology for EU Maritime Industry*, (2011) pp.282-293.

[6] H. C. Raven, A. van der Ploeg, A.R. Starke, L. Eça, "Towards a CFD-based prediction of ship performance --- progress in predicting full-scale resistance and scale effects", *International Journal of Maritime Engineering*, Vol. 135, (2009).

[7] Z.-z. Wang, Y. Xiong, L.-p. Shi, Z,-h, Liu, "A Numerical Flat Plate Friction Line and Its Application", *Journal of Hydrodynamics*, Vol 23 (3), (2015) pp.383-393.

[8] G. B. Deng and M. Visonneau, "Evaluation of eddy- viscosity and second- moment turbulence closures for steady flows around ships,", *21st ONR Symposium on Naval Hydrodynamics*, (1996) pp. 453–469.

[9] F. Menter, "Two-equation Eddy-viscosity turbulence models for engineering applications", *AIAA Journal* Vol.32 no. 8 (1994) pp.1598-1605

[10] L. Eça and M. Hoekstra, "The numerical friction line", *Journal of Marine Science and Technology*, Vol 13, (2008) pp. 328-345.

[11] A. Hellsten Some improvements in Menter's k-omega SST turbulence model, *29th AIAA, Fluid Dynamics Conference*, Fluid Dynamics and Co-located Conferences, (1998)

[12] ECOFTAC Classic Collection Database -http://cfd.mace.manchester.ac.uk/ercoftac

[13] L. Eça and M. Hoekstra, "A Procedure for the Estimation of the Numerical Uncertainty of CFD Calculations Based on Grid Refinement Studies", *Journal of Computational Physics*, Vol 262, (2014) pp. 104-130.

[14] L. Eça, F.S. Pereira, G. Vaz, "Viscous flow simulations at high Reynolds numbers without wall functions: Is y+ ≅ 1 enough for the near-wall cells?", *Computers and Fluids*, Vol. 170, (2018) pp.157-175

[15] Proceedings of the 8th ITTC, Madrid, 1957

[16] Karl E. Schoenherr, "Resistance of flat plate surfaces", *Trans. SNAME* (1932) 40:279-313

[17] T. Katsui, H. Asai, Y. Himeno, Y. Tahara, "The Proposal of a New Friction Line" *Fifth Osaka Colloquium on Advanced CFD Applications to Ship Flow and Hull Form Design*, Osaka, Japan, (2005).

[18] C.W.B. Grigson, "A planar algorithm and its use in analysing hull resistance". *Trans. RINA*, Vol 142, (1999) pp. 76-115.

Paper II

Investigations for CFD Based Form Factor Methods

Investigations for CFD Based Form Factor Methods

Kadir Burak Korkmaz[*] [†], **Sofia Werner**[†], **and Rickard Bensow**[*]
[*]Chalmers University of Technology, Gothenburg/Sweden, [†]SSPA Sweden AB, Gothenburg/Sweden
korkmaz@chalmers.se

1 Introduction

Performance prediction of full-scale ship is one of the most important tasks in the design stage. Depending on the design phase, required accuracy of the prediction varies as well as the prediction methods. Often towing tank tests are carried out at the last stage of the design process. The procedures of the towing tank tests are regulated by the International Towing Tank Committee (ITTC) and the prediction is based on the 1978 ITTC Performance Prediction Method. The form factor concept was adopted by this method as described by Hughes (1954), where the viscous resistance is expressed in relation to the 'ITTC 57 model-ship correlation line' as shown in the Eq. (1).

$$C_V = (1 + k)\, C_F. \tag{1}$$

The concept of Hughes (1954) and the determination method of Prohaska (1966) of form factor have been questioned and investigated for many decades. By analyzing the geosim test data, García-Gómez (2000), Toki (2008) and Van et al. (2011) demonstrated the scale effects on form factor. Additionally, CFD studies presented by Raven et al. (2009) and Wang et al. (2015) supported the existence of substantial scale effects on form factor. The main cause of the scale effects has been found to be the 'ITTC 57 model-ship correlation line' rather than the original hypothesis of Hughes (1954) which suggested that form factor is independent of the Reynolds number. As explained by Raven et al. (2009), scale effects on the form factor depends on several aspects:

1. The assumption that the form factor is not dependent on the Reynolds number. As Raven et al. (2009) and Wang et al. (2015) presented, viscous resistance was nearly proportional for bare hull when modern friction lines, i.e. Grigson (1999) and Katsui (2005), or numerical friction of the same turbulence model is used for extrapolation.

2. The friction line used for the extrapolation method

3. If form factor is determined by CFD, choice of turbulence model might play a significant role

Additionally, when the growing disposition to leave the Prohaska's method of form factor determination and growing confidence in numerical resistance calculations considered, CFD might be able to provide a new method of form factor determination, which can increase the accuracy of the full-scale resistance predictions.

In this study, the form factor concept has been investigated by analyzing the results obtained from the simulations performed on KVLCC2 and KCS hulls. Grid dependence studies, sensitivity analysis of loading conditions and varying grid setups have been performed with SHIPFLOW code. Extrapolation of viscous resistance to full scale has been performed with ITTC57 line and numerical friction lines.

2 Flow Solver, Computational Domain, Grid Generation

Two of the flow solvers and the structured grid generator of SHIPFLOW 6.3 has been used for this study. Potential flow solver, XPAN, is used for obtaining sinkage and trim for the bare hull. Viscous flow is solved with the XCHAP module which solves the Reynolds Averaged Navier-Stokes equations with a finite volume method. XCHAP is a steady state solver which requires structured grids but overlapping grids can be used to introduce refinement regions or appendages.

Viscous flow computations for all cases were carried as double model. The computational domain consists of six boundaries. The distance between inlet and fore-perpendicular (FP) is $0.5L_{PP}$. Outlet plane is located at $0.8L_{PP}$ behind the aft-perpendicular and the radius of the cylindrical outer boundary is $3L_{PP}$ in order to eliminate the blockage effect as much as possible. EASM and $k-\omega$ SST turbulence

models have been used for this study. All simulations performed as wall resolved, i.e. no wall functions used. The computational conditions are presented in Table 1.

Table 1: Computational conditions for the KVLCC2 and KCS hulls

Ship	L (m)	Scale	T (m)	S/L^2	Speed	Rn model	Rn ship	Vm (m/s)	Vs (kts)
KLVCC2 with rudder	320	58	20.8	0.2682	Low	4.1×10^6	1.80×10^9	0.88	13
					Design	4.9×10^6	2.14×10^9	1.05	15.5
KCS with rudder	230	31.6	10.8	0.1803	Low	7.33×10^6	1.39×10^9	1.281	14
					Design	1.26×10^7	2.39×10^9	2.196	24

3 Grid Dependence Study

Grid dependence studies have been performed for KVLCC2 and KCS hulls at two speeds and two grid configurations (with rudder and without rudder). Each grid dependence study has been performed with 5 geometrically similar grids. The finest grid is named as g1 while the coarsest grid denoted as g5. Considering the sensitivity of frictional resistance coefficient to the first layer thickness as highlighted in Korkmaz et al. (2019), average y^+ values are kept below the recommended value of 0.4 which was observed from the flat plate simulations.

All CFD calculations have been performed in double precision in order to eliminate the round-off errors. The iterative uncertainties have been determined from the standard deviation of the force in percent of the average force over the last 10% iterations. Iterative uncertainty for C_F and C_{PV} was kept below 0.01% and 0.15% for all simulations in model scale. Hence, it is assumed that the numerical errors are dominated by the discretization errors and both iterative errors and round-off errors are neglected.

There has been issues with the grids of the KCS hull around and behind the bulb. Close inspection has shown that the first layer thickness was varying irregularly due to difficulties of grid generation around the large protruding bulb at the forebody. Unfortunately, the issue hasn't been resolved completely but only a slight improvement was possible. The grid dependence analysis has shown that the calculated resistance components varied unexpectedly due to the meshing issue. Even though the variations were very limited (for example maximum variation of C_V is approximately 0.4% between 5 geometrically similar grids), it still caused rather high numerical uncertainties in bare hull cases. On the other hand, when the KCS hull is appended with rudder, numerical uncertainties are dropped significantly as presented in Table 2. In contrast to KCS hull, the simulations with KVLCC2 indicates similar uncertainty levels for different speed, turbulence model and existence of the rudder. The $k-\omega$ SST model gave slightly lower uncertainties compared to EASM. As it was the case for the KCS hull, existence of rudder reduced the uncertainties. The numerical uncertainties for KVLCC2 with rudder are presented in Table 2. Below 1% uncertainty was only achieved when the rudder was included in the simulations.

Table 2: Numerical uncertainties of KVLCC2 and KCS hulls, both with rudder and EASM turbulence model

KVLCC2						**KCS**					
$U_{SN}\%S$	g1	g2	g3	g4	g5	$U_{SN}\%S$	g1	g2	g3	g4	g5
C_F	1,3%	1,7%	2,3%	3,2%	4,8%	C_F	1,7%	1,8%	2,3%	3,0%	4,5%
C_{PV}	0,5%	1,6%	0,9%	1,2%	3,1%	C_{PV}	14,0%	17,0%	19,1%	24,7%	34,1%
C_V	0,8%	1,0%	1,0%	1,3%	1,4%	C_V	0,20 %	0,31 %	0,34 %	0,65 %	0,48 %

The first cell size have been varied with KCS and KVLCC2 hulls. The calculated C_F and C_V varies only marginally with the first cell size variation. It is significant to note that the maximum difference of C_F is around 0.1% at KCS hull case. The grid density of KCS hull g1 corresponds to g5 of the numerical flat plate investigations explained in Korkmaz et al. (2019). Such y+ variation caused 0.5% difference in C_F which is significantly larger than of the hull. Therefore it can be concluded that the effect of y^+ variation with a hull from is smaller than the flat plate case.

4 Sensitivity of form factor for varying loading conditions (different draughts and trims)

The loading condition varies during the operation of the ship. Typically, design and ballast loading conditions are tested in towing tanks. However, sea trials are often performed in ballast condition and sea trial at design condition is calculated via an extrapolation. Since the extrapolation is based on the model tests, it is critical to have the correct form factors. Due to the modern forebody designs or bows with bulbs, Prohaska method for obtaining the form factor at ballast condition is often not easy because of the significant wave patterns even at low Froude numbers. The same issue is also common at the design or other loading conditions. Therefore, CFD based form factor has potential improve the form factor determination. In this case, the first question is whether to perform the double model simulation with dynamic sinkage and trim or draught and trim at rest. The loading condition variation has also been suggested by Raven et al. (2009) as a solution to the large protruding bulbs for CFD based methods since the flow is accelerated or in some cases separated around the bulb. It is suggested that if the bulb the submerged more by trimming the hull (bow down) this issue can be prevented. The other issue of the form factor determination is the large submerged transoms which causes large separations behind the ship wake. It is worth to remember that the assumption of Hughes (1954) that form factor is the same in model and full scale is only valid if there is no flow separation. In order to reduce or eliminate the effect of a large submerged transom, the loading condition can be altered with reduced draught.

The loading condition (sinkage&trim) variation has been applied to KVLCC2 and KCS hulls. The form factor has been calculated based on the ITTC57 line and full scale viscous resistance (C_{V_S}) is calculated using the Eq. (1). As presented in Table 3, KVLCC2 and KCS hulls differ 0.24% and 0.10% in C_{V_S} between dynamic sinkage&trim and the draught&trim at rest for the design speed of each hull. This difference is significantly smaller for the lower speeds since the dynamic sinkage and trim is smaller compared to higher speeds. The trim variation is also applied to both hull forms in a way that the draught at the aft perpendicular is equal to the draught at rest (the pivot point) and the hull is trimmed bow up (- sign) or bow down (+ sign). The variation of C_{V_S} due to trim is shown as percentage with respect to the draught&trim at rest and presented in Table 3. Both hull forms indicated that form factor would increase when the hull is trimmed bow down (bow is submerged more) and vice versa for the bow down condition. Having in mind the slight variation in the grids between the trimmed hulls compared to dynamic sinkage and trim, it should be noted that the variation in C_{V_S} due to trim is smaller than the numerical uncertainties of each hull presented in Table 2.

Table 3: Form factor and viscous resistance variations as a result of different loading condition variation with EASM model, g2 with rudder at model scale design speed

KVLCC2					KCS			
Trim	Sinkage	k	C_{V_S}		Trim	Sinkage	k	C_{V_S}
dynamic	dynamic	0,230	0,24 %		dynamic	dynamic	0,106	0,10 %
0°	rest	0,227	ref.		0°	rest	0,105	ref.
0°	-2.5%	0,222	-0,37 %		0°	-2.5%	0,106	0,11 %
0°	2.5%	0,233	0,48 %		0°	2.5%	0,099	-0,55 %
0,25°	rest	0,233	0,46 %		0,25°	rest	0,107	0,19 %
-0,25°	rest	0,221	-0,49 %		-0,25°	rest	0,104	-0,04 %

Increasing the sinkage (with zero trim) for the KVLCC2 hull raises the form factor as expected since the transom is submerged even more compared to the original draught. Similarly, the form factor is decreasing with decreasing draught for the KVLCC2 hull. However, KCS hull indicated opposite trends for the sinkage variation compared to KCS hull. It should be noted that the transom of the KCS hull is not submerged even when the draught is increased 2.5%. On the other hand, the large part of the stern overhang is submerged when the draught is increased since buttocks are rather flat (a common feature for the container ships). As a result of large change in the submerged part of the aftbody due to increased draught, the C_{V_S} change is rather larger than other loading variations applied to the KCS hull.

5 Sensitivity of form factor for varying grid distributions

In addition to the grid dependence studies, several other grid setups have also been tested. The aim of this analysis is to determine the best grid distribution but also to figure out which grid distribution is not acceptable for the purpose of form factor determination. For this exercise, *g2* and *g5* of the grid dependence study has been selected as a starting point. The number of cells and longitudinal grid distribution of g2 has been selected based on the previous experiences. The coarsest grid g5 has only 1.69×10^6 cells. The new grid distributions are created by decreasing the number of cells in one region at a time and keeping all other regions the same. The flow domain and hull is divided into different regions longitudinally as can be seen in Figure 1. In Table 4, each grid is distinguished by it's parent grid (g2 or g5) and the modified region where the number of cells are changed. As an example, g2 grid with coarse bow and medium bow modification has 1/3 (35 cells) and 2/3 (70 cells) of number of cells in longitudinal direction at the bow region (see Figure 1) compared to original g2 grid (105 cells), respectively.

Fig. 1: Longitudinal divisions for grid generation

In Table 4, calculated form factors based ITTC57 line and extrapolated C_{V_S} values of KVLCC2 are presented for EASM and $k-\omega$ SST turbulence models. The coarsest grid with original grid distribution, g5, provides remarkably close C_{V_S} prediction (0.53% smaller) compared to g2 grid. As expected, the grids based on the parent grid of g2 is much less sensitive than g5. However, grids with coarser aft modification is more sensitive than coarser bow. The from factor obtained from the coarse aft grid based on the g5 is abnormally high for both turbulence models. It should be noted that this grid has only 20 cells in the longitudinal direction from aft shoulder to transom. The absolute values of C_{V_S} values are different but the relative changes between the grids are almost the same for both turbulence models.

Table 4: Grid variation, rudder appended at model scale design speed

Parent grid	Modification	Cells	EASM		$k-\omega$ SST	
			k	C_{V_S}	k	C_{V_S}
g2	Original	$8{,}39\times10^6$	0,227	ref.	0,245	ref.
g2	Coarse Bow	$7{,}66\times10^6$	0,233	0,49 %	0,251	0,45 %
g2	Medium Bow	$8{,}02\times10^6$	0,228	0,07 %	0,248	0,18 %
g2	Coarse Aft	$7{,}66\times10^6$	0,236	0,76 %	0,254	0,70 %
g2	Medium Aft	$8{,}02\times10^6$	0,228	0,07 %	0,248	0,18 %
g5	Original	$1{,}69\times10^6$	0,220	-0,53 %	0,240	-0,47 %
g5	Coarse Bow	$1{,}55\times10^6$	0,233	0,49 %	0,250	0,36 %
g5	Medium Bow	$1{,}62\times10^6$	0,223	-0,34 %	0,241	-0,34 %
g5	Coarse Aft	$1{,}55\times10^6$	0,318	7,42 %	0,337	7,32 %
g5	Medium Aft	$1{,}62\times10^6$	0,223	-0,34 %	0,241	-0,34 %

6 Speed dependency of form factor

The scale effects on the form factor has been previously mentioned. In this section, scale effects have been demonstrated by varying the speed of the KVLCC2 and KCS hulls. Since the simulations are performed as double model, the form factors obtained from different speeds should be the same since form factor should be independent of the Reynolds number. The form factor and the full scale viscous resistance (extrapolated) figures are presented in Table 5 and Table 6 for KCS and KVLCC2, respectively. The

same grid density, g2, were used and both hulls are appended with rudders. The form factor and the C_{V_S} values are calculated using both ITTC57 line and numerical friction lines of the corresponding turbulence model used for the calculations. The numerical friction lines for EASM and $k-\omega$ SST turbulence model were derived using SHIPFLOW and used for this study as recommended in Korkmaz et al. (2019). As can be seen in Table 5 and Table 6, the form factors based on the ITTC57 line differs significantly with the varying speed for both hulls and turbulence models. However, when the numerical friction lines are applied, form factors are almost the same at different speeds for the same turbulence model. The form factors differ for the different turbulence models because calculated C_{V_M} is different and also the numerical friction line for EASM and $k-\omega$ SST models are different when numerical friction line is used. However, the difference between extrapolated C_{V_S} values from different turbulent models are significantly smaller when numerical friction lines are applied instead of the ITTC57 line. In Table 7, results of the full scale simulations are presented for the KCS hull. It should be noted that when ITTC57 line is used, extrapolated C_{V_S} values are significantly smaller compared to computed C_{V_S} values.

Table 5: Calculated form factor and extrapolated C_{V_M} values of KCS with rudder

		ITTC57 line			numerical friction line		
Turbulence model	Speed	k	C_{V_S}(14kts)	C_{V_S}(24kts)	k	C_{V_S}(14kts)	C_{V_S}(24kts)
EASM	design	0,106	$1{,}626\times10^{-3}$	$1{,}524\times10^{-3}$	0,169	$1{,}740\times10^{-3}$	$1{,}644\times10^{-3}$
EASM	low	0,088	$1{,}600\times10^{-3}$	$1{,}499\times10^{-3}$	0,169	$1{,}740\times10^{-3}$	$1{,}643\times10^{-3}$
$k-\omega$ SST	design	0,132	$1{,}664\times10^{-3}$	$1{,}559\times10^{-3}$	0,159	$1{,}754\times10^{-3}$	$1{,}649\times10^{-3}$
$k-\omega$ SST	low	0,117	$1{,}642\times10^{-3}$	$1{,}539\times10^{-3}$	0,158	$1{,}753\times10^{-3}$	$1{,}648\times10^{-3}$

Table 6: Calculated form factor and extrapolated C_{V_M} values of KVLCC2 with rudder

		ITTC57 line			numerical friction line		
Turbulence model	Speed	k	C_{V_S}(13kts)	C_{V_S}(15.5kts)	k	C_{V_S}(13kts)	C_{V_S}(15.5kts)
EASM	design	0,230	$1{,}752\times10^{-3}$	$1{,}717\times10^{-3}$	0,340	$1{,}940\times10^{-3}$	$1{,}905\times10^{-3}$
EASM	low	0,219	$1{,}737\times10^{-3}$	$1{,}701\times10^{-3}$	0,337	$1{,}936\times10^{-3}$	$1{,}901\times10^{-3}$
$k-\omega$ SST	design	0,249	$1{,}779\times10^{-3}$	$1{,}743\times10^{-3}$	0,308	$1{,}923\times10^{-3}$	$1{,}885\times10^{-3}$
$k-\omega$ SST	low	0,238	$1{,}764\times10^{-3}$	$1{,}728\times10^{-3}$	0,304	$1{,}917\times10^{-3}$	$1{,}880\times10^{-3}$

Table 7: Full scale simulations of KCS

speed	EASM	$k-\omega$ SST
C_{V_S}(14kts)	1.747×10^{-3}	1.772×10^{-3}
C_{V_S}(24kts)	1.603×10^{-3}	1.665×10^{-3}

7 Conclusions

In this study, CFD based form factor determination method have been investigated by analyzing the calculations performed on KVLCC2 and KCS hulls. The following observations have been made:

- Grid dependence studies indicated that numerical uncertainties around 1% is achievable with KVLCC2 hull regardless of existence of rudder and the choice of turbulence model (EASM and $k-\omega$ SST). On the other hand, there has been meshing issues with KCS at the forebody due to large protruding bulb. The numerical uncertainties around 1% was only possible when the rudder appended to the KCS hull.

- Frictional resistance component was less sensitive to the first layer thickness with KCS and KVLCC2 hulls compared to flat plate simulations.

- The loading condition (sinkage&trim) variation had limited effect on the calculated form factor for both KCS and KVLCC2 hulls. The difference in the extrapolated C_{V_S} values due to varying sinkage&trim were often smaller than the numerical uncertainties.

- Different grid density distributions have been simulated in order to find out which grid density is acceptable and which grids should be avoided. The sensitivity of form factor to the grid density at the aft body is bigger than the forebody. It can be argued that unless the grid resolution at the aftbody is very coarse, sensitivity of form factor to the grid resolution at the other parts of the hull is rather low.

- The scale effects on form factor have been one of the most important discussion topic. It has been showed that when ITTC57 line is used, the scale effects are in-avoidable. However, when the numerical friction line that of the same CFD code and same turbulence model is applied scale effects are reduced significantly. The computations with EASM turbulence model with the numerical friction line of the same turbulence model eliminated the scale effects almost completely.

- The EASM and $k-\omega$ SST turbulence models gives different form factors regardless of the friction line used. However, when the numerical friction line is used, the variation of the extrapolated C_{V_S} values between turbulence models are reduced compared to ITTC57 line.

- The C_{V_S} obtained from the full scale simulations with KCS is significantly closer to the extrapolated C_{V_S} when the numerical friction lines are used.

Acknowledgements

This project has been funded by *Vinnova* and the computational resources were provided by the Chalmers Center for Computational Science and Engineering (C3SE).

References

A. García-Gómez (2000). On the Form Factor Scale Effect. *Ocean Engineering*, **Vol. 26**, p.97-109.

C. W. Prohaska (1966). A Simple Method for the Evaluation of the Form Factor and Low Speed Wave Resistance. *Proceeding of 11th ITTC*.

C.W.B. Grigson (1999). A planar algorithm and its use in analysing hull resistance. *Trans. RINA*, **Vol. 142** p.76-115.

G. Hughes (1954). Friction and Form Resistance in Turbulent Flow, and a Proposed Formulation for Use in Model and Ship Correlation. *Trans. RINA*, **Vol. 96**, p.314-376.

H. C. Raven, A. van der Ploeg, A.R. Starke and L. Eça (2009). Towards a CFD-based prediction of ship performance — progress in predicting full-scale resistance and scale effects. *International Journal of Maritime Engineering*, **Vol. 135**.

K.B. Korkmaz, S. Werner, R. Bensow (2019). *Numerical Friction Lines For CFD Based Form Factor Determination. VIII International Conference on Computational Methods in Marine Engineering (Marine 2019).*

L. Eça and M. Hoekstra (2014). A Procedure for the Estimation of the Numerical Uncertainty of CFD Calculations Based on Grid Refinement Studies. *Journal of Computational Physics*, **Vol. 262** p.104-130.

N. Toki (2008). Investigation on Correlation Lines through the Analyses of Geosim Model Test Results. *Journal of the Japan Society of Naval Architects and Ocean Engineers*, **Vol. 8**, p.71-79.

Proceedings of the 8th ITTC (1957).

S.-H. Van, H. Ahn, Y.-Y Lee, C. Kim, S. Hwang, J. Kim, K.-S Kim, and I.-R Park (2011). Resistance Characteristics and Form Factor Evaluation for Geosim Models of KVLCC2 and KCS. *Advanced Model Measurement Technology for EU Maritime Industry*.

T. Katsui, H. Asai, Y. Himeno and Y. Tahara, (2005). The Proposal of a New Friction Line. *Fifth Osaka Colloquium on Advanced CFD Applications to Ship Flow and Hull Form Design, Osaka, Japan*.

Z.-z. Wang, Y. Xiong, L.-p Shi and Z,-h Liu (2015). A Numerical Flat Plate Friction Line and Its Application. *Journal of Hydrodynamics*, **Vol. 23**(3) p.383-393.

Paper III

CFD based form factor determination method

Ocean Engineering 220 (2021) 108451

Contents lists available at ScienceDirect

Ocean Engineering

journal homepage: www.elsevier.com/locate/oceaneng

CFD based form factor determination method

Kadir Burak Korkmaz [a,b,*], Sofia Werner [a], Nobuaki Sakamoto [c], Patrick Queutey [d], Ganbo Deng [d], Gao Yuling [e], Dong Guoxiang [e], Kevin Maki [f], Haixuan Ye [f], Ayhan Akinturk [g], Tanvir Sayeed [g], Takanori Hino [h], Feng Zhao [i], Tahsin Tezdogan [j], Yigit Kemal Demirel [j], Rickard Bensow [b]

[a] SSPA Sweden AB, Chalmers Tvärgata 10, Box 24001, Se-400 22, Göteborg, Sweden
[b] Chalmers University of Technology, Sweden
[c] National Maritime Research Institute (NMRI), Japan
[d] LHEEA, CNRS Ecole Centrale de Nantes, France
[e] Shanghai Ship and Shipping Research Institute (SSSRI), China
[f] CSHL University of Michigan, USA
[g] Ocean, Coastal and River Engineering (OCRE), NRC, Canada
[h] Yokohama National University, Japan
[i] China Ship Scientific Research Centre (CSSRC), China
[j] University of Strathclyde, United Kingdom

ARTICLE INFO

Keywords:
Ship resistance
Form factor
CFD
Scale effects
Combined CFD/EFD Methods
Experimental uncertainty analysis

ABSTRACT

The 1978 ITTC Power Prediction method is used to predict the propulsive power of ships through towing tank testing. The form factor approach and its determination in this method have been questioned. This paper investigates the possibility to improve the power predictions by introducing Combined CFD/EFD Method where the experimental determination of form factor is replaced by double body RANS computations applied for open cases KVLCC2 and KCS, including first-time published towing tank tests of KVLCC2 at ballast condition including an experimental uncertainty analysis specifically derived for the form factor. Computations from nine organisations and seven CFD codes are compared to the experiments. The form factor predictions for both hulls in design loading condition compared well with the experimental results in general. For the KVLCC2 ballast condition, majority of the form factors were under-predicted while staying within the experimental uncertainty. Speed dependency is observed with the application of ITTC57 line but it is reduced with the Katsui line and nearly eliminated by numerical friction lines. Comparison of the full-scale viscous resistance predictions obtained by the extrapolations from model scale and direct full-scale computations show that the Combined CFD/EFD Method show significantly less scatter and may thus be a preferred approach.

1. Introduction

Performance prediction of a ship is one of the most important tasks during the design phase. As a ship design progresses from beginning to end, the required confidence interval for the prediction method increases. According to the majority of commercial tendencies presented by shipyards and ship owners, towing tank tests are still considered as the last step of the performance prediction. Additionally, legal authorities consider towing tank testing as a mandatory step in their evaluations such as EEDI calculations as enforced by IMO (2011) where the applicable ships must go through the pre-verification by model testing during the design phase of a new ship.

Towing tank testing has remained as the only practice for more than a century with high accuracy to predict the performance of a ship in deep and calm water since William Froude introduced the extrapolation procedures in the 1870s. The foundation of the International Towing Tank Committee (ITTC) in 1933, lead to improved and standardized procedures in nearly all aspects of performance prediction. An important step towards a common prediction method was taken in 1973 when computer programs with different assumptions and extrapolation methods were created by SSPA as requested by the ITTC (Lindgren and Dyne, 1980). Ten institutions known to have access to sea trials for

* Corresponding author. SSPA Sweden AB, Sweden.
E-mail address: burak.korkmaz@sspa.se (K.B. Korkmaz).

https://doi.org/10.1016/j.oceaneng.2020.108451
Received 16 September 2020; Received in revised form 27 November 2020; Accepted 28 November 2020

different types of ships evaluated each method by starting from their model test results to calculate the shaft power and propeller rate of revolution (ITTC, 1978). The 1978 ITTC Performance Prediction Method emerged as a result of comparing approximately one thousand sea trials to model test predictions and it is still in effect after going through several revisions.

Even though towing tank testing and extrapolation methods have been debated, discussed and improved over decades, there are inherent and well known shortcomings due to scale effects since model tests are carried out at Froude similarity while Reynolds similarity cannot be fulfilled simultaneously. In order to limit the effects of the shortcomings, towing tank facilities must rely on experience and large databases of both model tests and sea trials. Computational Fluid Dynamics (CFD) has been seen as an alternative to towing tank testing because of CFD's ability to fulfill both Froude and Reynolds similarities while providing a great deal of detail about the flow. However, the accuracy of CFD on prediction of full scale performance is still under concern. Even though several studies presented by Sun et al. (2020) and Niklas and Pruszko (2019) demonstrated that full-scale simulations can provide similar or better power predictions than towing tank experiments, the results from Reynolds Averaged Navier-Stokes (RANS) solvers in full scale is highly dependent on the computational set-up, e.g., the choice of turbulence model and modelling of hull roughness. The results of Lloyd's Register workshop on ship scale hydrodynamics (Ponkratov, 2016) also confirmed that differences between the numerical setups can lead to very diverse predictions on both power and propeller turning rate. Unlike the limited full scale verification and validation (V&V) studies mainly due to lack of full scale test data, assessment of state of the art in CFD methods in model scale has been a well established practice since 1980 Larsson et al. (2014). According to the resistance statistics of Larsson et al. (2014), the mean comparison error in per cent of the measured data value is −1.7% and −1.3% for KVLCC2 and KCS in fixed trim and sinkage condition while the standard deviations are 1.3% and 1.2% of the data value, respectively. It was also noted that the mean comparison error and standard deviation in self-propelled cases are considerably higher than those in the resistance cases (Larsson et al., 2014).

As identified by the Combined CFD/EFD Methods ITTC Specialist Committee, combination of EFD and CFD could be a feasible solution to increase the accuracy of power predictions instead of choosing EFD or CFD for the time being. If a part of the model testing or extrapolation procedure causes higher uncertainty than the numerical uncertainty and physical modelling errors of the CFD applications, accuracy will be increased. In the 1978 ITTC Performance Prediction method, the form factor has been identified by the Specialist Committee as one of the major causes of uncertainties, due to the Prohaska method (Prohaska, 1966) and scale effects on form factor for the determination of full scale resistance of ships. Form factor determination method suggested by Prohaska (1966) was recommended by 14th ITTC meeting (ITTC, 1975) when standardized performance prediction procedures were formulated and debated. During the formulation of the 1978 ITTC Power Prediction method, the form factor concept was found superior to 2-D methods such as the 1957 Power Prediction Method as it led to a better ship-model correlation (ITTC, 1978). The form factor determination method remained as the Prohaska method. However, the main issue with the Prohaska method was described by the ITTC as stated below:

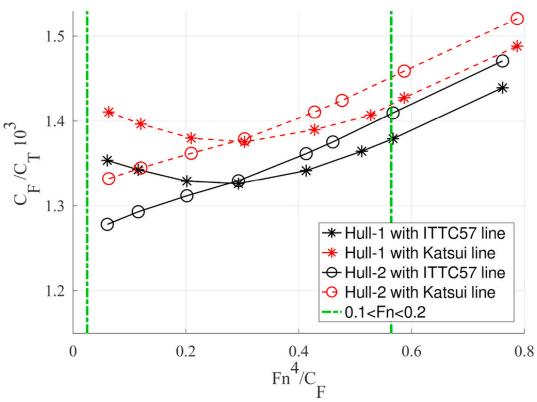

Fig. 1. Example of Prohaska plot in design loading condition.

> "The problems of ships with partly submerged bulbous bows and the effects of wave breaking resistance for blunt bow forms need further consideration; in both cases it is probably advisable to lower the … speed limits. Future developments for the determination of form factors on a more scientific basis is expected from the Resistance Committee" (ITTC, 1978)

In the 1978 ITTC Power Prediction method, the form factor concept of Hughes (1954) was adopted. It suggests that viscous resistance of a ship can be expressed in relation to a two-dimensional turbulent friction line and the form factor is independent of Reynolds number. As it will be explained in more detail in Section 2, the Prohaska method can be replaced by model scale double body CFD computations which is one of the least numerically complicated CFD applications since modelling of propulsors, free surface and roughness are omitted.

After the form factor determination method, the second error source was identified as the scale effects or speed dependency on form factor. When the 1978 ITTC method was accepted there has been substantial evidence on the scale effects on form factor with ITTC-57 line ITTC (1978). Further re-analysis of geosim test data performed by García Gómez (2000) and Toki (2008) confirmed the scale effects. Additionally, CFD studies performed by Pereira et al. (2017) showed that the speed dependency of form factors with the ITTC-57 line were larger than the numerical uncertainties. Terziev, Tezdogan and Incecik (2019) also showed that form factor is Reynolds number dependent and additionally suggested that the form factor varies with Froude number. The CFD investigations presented by Raven et al., 2008; Wang et al. (2015); Dogrul et al. (2020) and Korkmaz, Werner and Bensow (2019a) supported the existence of scale effects or speed dependency on form factor and indicated that the main cause of the scale effects are due to the 'ITTC 57 model-ship correlation line' rather than the hypothesis of Hughes (1954). CFD based form factor methods were investigated by Korkmaz et al. (2019a) and Wang et al. (2019) in further detail for sensitivity of form factor to grid density and type, speed dependency, presence of rudder, sinkage and trim. The latter investigation also demonstrated that CFD based form factors correlated better with the sea trials compared to the Prohaska method.

As a continuation of the initial study started by the Combined CFD/EFD Methods Specialist Committee, in this paper CFD based form factor methods have been investigated as an alternative method to the Prohaska method. KVLCC2 in design and ballast loading condition; KCS in design loading condition are computed at two speeds at both model and full scale. The model tests of KVLCC2 in ballast loading condition performed at SSPA's towing tank and the resistance data together with the measurement uncertainty analysis is presented for the first time in the literature. Wide range of CFD methods and setups are compared with the contribution from 9 different organisations and 7 different CFD codes. In order to quantify the sensitivity of different CFD approaches on form factor, non-ideal CFD setups are also computed and discussed. The scale effects on the form factor are presented by using the friction line proposed by Katsui et al. (2005) and numerical friction lines suggested by Korkmaz et al., 2019b in comparison to form factor based on the ITTC 57 model-ship correlation line.

The following research questions are aimed to be answered by this study.

Table 1
Participants and methods.

Organisation	Acronym	Code	ID	Turbulence model	Wall model	Discretization		Grid Type
						Type	Order	
CSHL University of Michigan	UM	OpenFOAM	1	Spalart-Allmaras, $k-\omega$ SST	WF	FV	2	U
China Ship Scientific Research Center	CSSRC	NaViiX	2	RNG $k-\varepsilon$	WF	FV	2	S
Ecole Centrale de Nantes	ECN/CNRS	ISIS-CFD	3	EASM, $k-\omega$ SST	WF, WR	FV	2	U
National Maritime Research Institute	NMRI	NAGISA	4	EASM, $k-\omega$ SST	WF, WR	FV	3	OS
Ocean, Coastal and River Engineering	NRC-OCRE	OpenFOAM	5	$k-\omega$ SST	WF	FV	2	U
SSPA/Chalmers University of Technology	SSPA/CTU	SHIPFLOW	6	EASM, $k-\omega$ SST	WR	FV	2	OS
Shanghai Ship and Shipping Research Institute	SSSRI	Star-CCM+	7	$k-\omega$ SST, RSTM, Realizable $k-\varepsilon$	WF	FV	2	U
Strathclyde University	Strathclyde	Star-CCM+	8	$k-\omega$ SST	WF	FV	2	U
Yokohama National University	YNU	SURF	9	EASM, $k-\omega$ SST	WR	FV	2	S

FV Finite Volume; WR wall resolved; OS Overlapping Structured; S Single Block Structured; U Unstructured; WF wall functions.

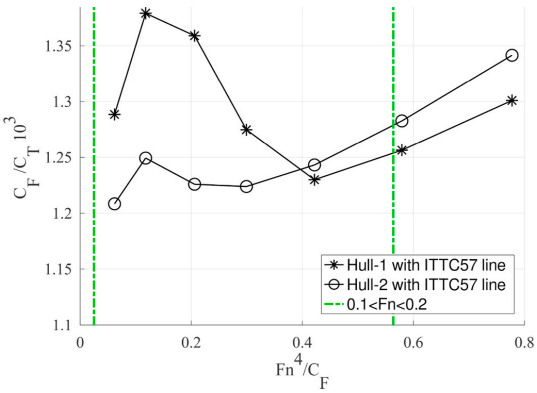

Fig. 2. Example of Prohaska plot in design ballast condition.

- Can CFD based form factors with state-of-the-art CFD codes be an alternative or supplement to the Prohaska method?
- Which CFD methods and setups are not fit for reliable CFD based form factor predictions?
- Can the scale effects on form factor be prevented?
- Should the full scale simulations replace the extrapolation methods for full scale resistance predictions?

This paper is structured as follows: Section 2 describes the background of the form factor concept and its determination by experimental methods. The flow solvers, numerical methods, computational domain and boundary conditions, procedure of CFD based form factor calculation are presented in Section 3. The computational conditions and details of the KVLCC2 towing tank tests in ballast condition are presented in Section 4. In Section 5, results and discussions are presented and conclusions are summarized in Section 6.

2. Background of the form factor concept and experimental determination methods

The form factor concept has been long discussed since the early 20^{th} century. ITTC (1957) stated that ship resistance extrapolation based on three dimensional analysis (such as form factor approach) has been considered when the ITTC 1957 line was selected. In fact, some researchers believed that a two dimensional flow line is not sufficient for the extrapolation problem ITTC (1957), but rather that each hull form requires a separate extrapolator such as Hughes (1954).

The definition of form factor as described by Hughes was adopted by the ITTC (1972) and it is still in practice. The wave-making resistance depends on the Froude number and at low speeds it becomes negligible for most hulls. Thus in carefully conducted experiments where care is taken with regard to turbulence stimulation, measurement accuracy at low speeds and good surface finish, a point in the C_T curve can be found. From this point towards smaller Froude numbers, the curve of C_T is 'sensibly' parallel to the two dimensional turbulent friction line. This is called by Hughes the 'low Froude number run-in' point (Hughes, 1954). The total resistance curve is formulated as,

$$\begin{aligned} C_T &= C_F + C_{form} + C_W, \\ C_{form} &= k\, C_F, \end{aligned} \tag{1}$$

where C_F is the resistance equivalent to a flat plate in two dimensional flow, C_{form} is form resistance due to the shape of the hull, C_W is wave resistance and k is the form factor. C_{form} is proportional to C_F when the flow is turbulent and the given hull is smooth, streamlined (without separation) and in symmetrical form when towed in zero incidence angle. C_{form} is made up of components due to additional skin friction caused by curvature effects, flow in transverse directions and eddy-making (Hughes, 1954).

As Hughes (1954) described, form factor for a hull can be determined by the ratio C_T/C_F at the "run-in point" since the C_W is small enough be

Table 2
Computational conditions.

Computational conditions	L_{pp} (m)	Scale factor	Draught at FP(m)	Draught at AP(m)	S/L^2	V_m (m/s)	V_s (kn)	Re_m	Re_s	Fn
KVLCC2 (design)	320	58	20.8	20.8	0.2682	0.878	13	4.11×10^6	1.80×10^9	0.119
						1.047	15.5	4.90×10^6	2.14×10^9	0.142
KVLCC2 (ballast)	320	45.714	8.6	11.4	0.1921	0.989	13	6.24×10^6	1.80×10^9	0.119
						1.179	15.5	7.44×10^6	2.14×10^9	0.142
KCS (design)	230	31.6	10.8	10.8	0.1803	1.281	14	7.33×10^6	1.39×10^9	0.152
						2.196	24	1.26×10^7	2.39×10^9	0.260

Table 3
Combination of uncertainty in measurement for resistance at $Fn = 0.119$ and $Fn = 0.142$.

Uncertainty Components	Uncertainty at 16.0 °C	
	$Fn = 0.119$	$Fn = 0.142$
Wetted area	0.080%	0.080%
Speed	0.067%	0.057%
Water temp.	0.002%	0.002%
Dynamometer	0.705%	0.492%
Repeat test, Deviation	0.470%	0.344%
Combined for single test	0.854%	0.609%
Repeat test, Deviation of mean	0.210%	0.154%
Combined for repeat mean	0.743%	0.525%
Expanded for repeat mean	1.487%	1.050%

neglected in Eq. (1). However, in order to find the run-in point, the speed range for the resistance test must be extended to very low *Fn* and *Re* numbers which is rather challenging as the *Re* at such low speeds might be too low for turbulence stimulators to make sure the flow around the hull is turbulent. Additionally, certain scatter in resistance measurements at low speeds due to worsening measurement accuracy for small forces can hinder the form factor determination, as Lindgren and Dyne (1980) indicated.

As an alternative, Prohaska (1966) suggested a simple method to derive the form factor from resistance tests. When no separation is present, the form factor is expressed as

$$C_T = C_W + (1 + k)C_F. \tag{2}$$

The wave resistance coefficient, C_W, can be expressed as Eq. (3) which is the asymptotic expansion formula of wave-making resistance coefficient presented by Inui as cited in Toki (2008),

$$C_W = a \times Fr^4 + b \times Fr^8 + c \times Fr^{12} + d \times Fr^{16}. \tag{3}$$

C_T at model scale is then expressed together with the Inui's asymptotic expansion formula, Eq (3), as

$$C_{Tm} = (1 + k) \times C_F + C_W = (1 + k) \times C_F + a \times Fr^4 + b \times Fr^8 + c \times Fr^{12} + d \times Fr^{16}. \tag{4}$$

Neglecting the higher order terms of Eq. (4) as they are close to zero at low Froude numbers and dividing each sides by C_F, the following linear relationship is obtained,

$$C_{Tm} / C_F \approx (1 + k) + a \times Fr^4 / C_F. \tag{5}$$

Prohaska (1966) noted that when results of approximately 200 model tests have been plotted with Eq. (5), for *Fn* between 0.1 and 0.2, the C_T/C_F values for a great majority of the models plot on straight lines. One of the exceptions when the C_T/C_F values deviated from the straight line and points correlate with concave curves is with hull forms with $C_B > 0.75$. It was suspected that $1 + k$ may be speed dependent, or as Prohaska (1966) stated "can be easily explained by as resulting from increasing trim on the bow." The other hull form Prohaska observed where C_T/C_F values plot on convex curves was twin-screw models with appendages and for some models with full aft body lines, which was explained by a certain separation (Prohaska, 1966). It should be noted that detection of flow separation and treatment of deeply submerged transoms remain as challenges of the Prohaska method. However, the main weakness of the Prohaska method discussed in modern literature is the bulbous bow near the water surface and partly submerged bulbous bow in partial loaded conditions which is not mentioned by Prohaska (1966) since the model test data used by Prohaska dates back to 1966 and earlier when bulbous bows were not a popular design concept.

Table 4
Total resistance coefficient, C_T, combined mean measurement uncertainty, U_D, number of repeat tests, N, at.16.0°C.

Fn	$C_T \times 10^3$	U_D	N
0.110	3.981	0.84%	4
0.119	3.968	0.74%	5
0.133	3.976	0.60%	4
0.142	4.001	0.52%	5
0.147	4.016	0.51%	4

In order to illustrate this aspect of the uncertainty of form factor determination caused by the Prohaska method, the model test results of the resistance curves of two hulls are plotted as in Eq. (5) and presented in Fig. 1 and Fig. 2. In order to protect the confidentiality of the test results, C_T/C_F curves shown in Figs. 1 and 2 are slightly tilted without changing neither the general shape of the curves nor the relative position of each measurement point at the same Froude number. Hull-1 and Hull-2 are only different in bulbous bow and they are geometrically similar for the rest of the hull (95% identical hulls). The bulbous bow of Hull-1 features a mild goose-neck design (distinctly convex upper stem profile of the bulb) and has significantly more volume close to water surface at design loading condition compared to Hull-2. As can be seen from Fig. 1, not all C_T/C_F values of Hull-1 in design loading condition follow a straight line within the recommended *Fn* range, which is between 0.1 and 0.2 as indicated by the green vertical lines. The concave shape of C_T/C_F values for Hull-1 can be explained by the presence of significant and often steep waves that are generated by the bulb. The waves generated at significantly lower Froude numbers than the design speed are too short in wave length to favourably interact with the bow waves of the hull. On the other hand, C_T/C_F values of Hull-2 reasonably follow a straight line which suits the description of Prohaska (1966) since the waves are much smaller at low *Fn* as a result of reduced the pressure gradient and moving the bulb volume away from the water surface. Considering that the two hulls are 95% identical, large differences are observed in C_T/C_F curves.

The uncertainly with the Prohaska method further increases in the ballast loading conditions as shown in Fig. 2. The C_T/C_F values of Hull-1 within the recommended range shows a large hump which cannot be used for a line fit. In other words, the wave making resistance cannot be described by Eq. (4) and the linear relationship proposed by Prohaska in Eq. (5) is not valid. In ballast condition at the low speeds, Hull-2 also shows a hump in C_T/C_F values which was not existent in the design condition. In order to demonstrate that a different friction line would not have helped, the C_T/C_F values are also calculated with the Katsui friction line (Katsui et al., 2005) instead of the 1957 ITTC model-ship correlation line. As seen in Fig. 1, the convex shape of the C_T/C_F values persists. As shown in this example, quantifying the uncertainty or error of Prohaska form factor determination method is difficult since it is very sensitive to the hull design. Considering that the bulbous bows are now a common feature of modern ship design, it is hard to advocate the validity and practicality of the Prohaska method for all hull designs and loading conditions.

One further aspect of uncertainty of form factor determination with the Prohaska method originates from the experimental uncertainty, U_D. The uncertainty on form factor can be significantly higher than the experimental uncertainty since it is not directly measured but obtained as a result of data reduction, i.e. regression analysis. This will be discussed thoroughly in Section 4 when the towing tank tests for KVLCC2 in ballast loading condition are presented.

3. Participants and methods

In total 9 different organisations with 7 different CFD codes contributed to the current study. The organisations are listed in Table 1 together with the main features of their methods. The results will be discussed and presented with the ID numbers of the organisations in the

Fig. 3. KVLCC2 in ballast loading condition at.$Fn = 0.142$

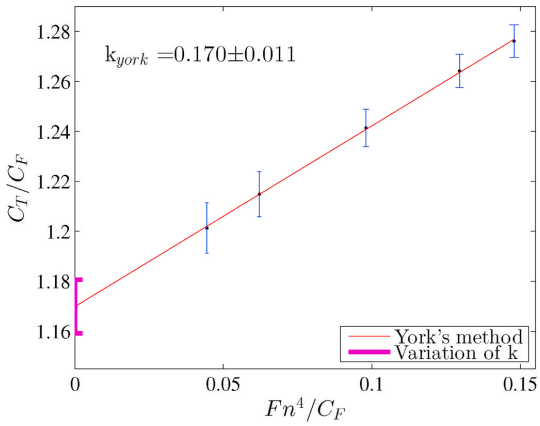

Fig. 4. Prohaska plot of KVLCC2 in ballast loading condition.

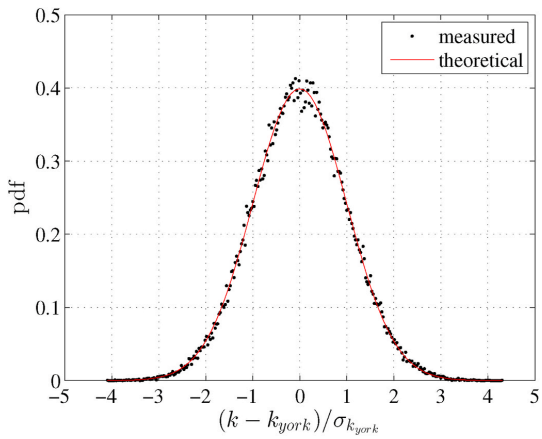

Fig. 5. Probability density function of the form factor of KVLCC2 in ballast loading condition.

paper.

Two-equation turbulence models $k-\omega$ SST, RNG $k-\varepsilon$, Realizable $k-\varepsilon$ are used by the majority of the computations. Anisotropic models, EASM and RSTM, are not used by all organisations but EASM model is still covering a large portion of the calculations. Only one organisation used the one-equation Spalart-Allmaras model.

Simulations were performed using finite volume codes with 2nd order accurate schemes except one code with 3rd order accurate scheme. The grids used were single or multi-block structured grids (butt-joined, curvilinear or overlapping techniques) and unstructured ones.

Computational domain shape and size varies with each code. Majority of the upstream boundaries are located between 1L_{PP} and 1.5L_{PP} from the fore perpendicular (FP), but ECN/CNRS and SSPA/CTU are differing from others by using the distance of 5L_{PP} and 0.5L_{PP}, respectively. The downstream extent of the domains varied between 8L_{PP} and 0.8L_{PP} from the aft perpendicular (AP) while the common distance of downstream extent is between 2L_{PP} and 3L_{PP}. Lateral (both sidewards and downwards) extend is commonly located between 1.5L_{PP} and 2.5L_{PP} away from the ship center-plane and free surface plane but two notable exceptions are 1L_{PP} and 4L_{PP} from UM and ECN/CNRS, respectively.

All computations were performed as double model with a symmetry boundary condition at the ship center-plane and free surface plane. Most popular upstream boundary condition is uniform in all variables with the exception of one participant with prescribed pressure. The downstream conditions are usually zero gradient in the streamwise direction except the pressure quantity that is specified. The lateral boundaries are dominated by far field boundary conditions but slip and zero gradient boundaries are also used. Majority of the computations (approximately 60%) are performed with wall resolved condition and the remaining simulations were performed with wall functions.

The CFD based form factor method considered for this study follows the assumptions of Hughes (1954) and is derived using the relation,

$$(1+k) = \frac{C_F + C_{PV}}{C_{F0}} = \frac{C_V}{C_{F0}}, \tag{6}$$

where the frictional resistance coefficient (C_F) and viscous pressure coefficient (C_{PV}) are obtained by the double body CFD simulation. C_{F0} in the denominator of Eq. (6) is the equivalent flat plate resistance in two dimensional flow obtained from the same Reynolds number as the computations. In this study, three friction lines are considered: the ITTC-57 model-ship correlation line (ITTC, 1957), the Katsui line (Katsui et al., 2005) and numerical friction lines proposed by Korkmaz et al. (2019b). It is worth mentioning that the ITTC-57 line is not a pure friction line but it contains a component of form resistance (11.94% of the friction line of Hughes (1954)). It is included in the scope of the study because it is still the model to ship correlation line recommended by ITTC (2014a).

The shortcomings of the Prohaska method for the hulls with a pronounced bulbous bow have been mentioned in Section 2. In a case when there is just a small gap between the top of the bulb and the still-water surface, a flow separation may be generated around the top of the bulb for the double body simulations. Such flow separation would not occur in free-surface flow; therefore, the form factor obtained from the double

body computation will be affected. Raven et al. (2008) suggested that if the bulb is submerged more by trimming the hull bow down, this issue can be prevented. Another drawback that is shared between CFD and EFD based form factor determination methods is the large submerged transom which may cause flow separation in the wake. The test cases used in this study do not possess the hull form features that may cause aforementioned issues for the CFD based form factor method. Therefore, no corrections have been applied to the double-body flow computations.

4. Test cases and computational conditions

The two hulls used for the current study are:

- KVLCC2 with rudder
- KCS with rudder

The KVLCC2 and KCS hulls are designed at the Korea Research Institute for Ships and Ocean Engineering (KRISO) to be used as open test cases for CFD predictions. Extensive towing tank tests and CFD investigations were carried out in the last two decades. Therefore, hull lines and detailed hydrostatics are not presented. The hull and rudder geometries are obtained from Tokyo (2015) and SIMMAN (2008) workshops for KCS and KVLCC2, respectively.

The computational conditions for the study is presented in Table 2. Non-dimensional quantities, *Re* and *Fn*, are based on L_{PP}. The force coefficients are non-dimensionalized with the corresponding wetted surface coefficients, S/L^2PP, to the loading conditions. For each hull and loading condition, two different speeds were used for the computations in order to investigate the importance and the effect of selecting a speed for the form factor determination. The first speed is chosen in the low side of the regular model testing speed range where C_T/C_F is close to the form factor (see Fig. 1) determined by the Prohaska method. The second speed is the design speed of each vessel. Data for resistance tests of KVLCC2 and KCS at design draught are adopted from Van et al. (2011). The resistance test data of the KVLCC2 in ballast loading condition has never been published. Therefore, SSPA determined a typical ballast loading condition for Very Large Crude Carriers (VLCC). Towing tank tests were performed at SSPA's towing tank including an uncertainty analysis of the resistance tests.

4.1. Uncertainty analysis of KVLCC2 resistance tests in ballast draught

A KVLCC2 model with a scale factor of 45.714, made of the plastic foam material Divinycell, was manufactured with 5-axis CNC milling machine at SSPA. After the surface finishing and painting, the model was scanned with a 3D scanner to check the tolerances described in ITTC (2014c). A trip wire is mounted at 5% of L_{PP} aft from the fore perpendicular for the turbulence stimulation. The hull model is equipped with a dummy propeller hub and a rudder. The geometry of the rudder is obtained from SIMMAN (2008) and the dummy hub is a simple cylinder with the diameter of the boss end of the hull.

The model tests were performed in SSPA's towing tank which is 260 m long, 10 m wide and 5 m deep. The model tests were carried out in mid-May 2020. The total resistance, sinkage and trim were measured at Froude numbers varying between 0.110 and 0.147. The mid-sectional area of the KVLCC2 model in ballast loading condition is 0.155% of the towing tank section area. Therefore, no blockage correction is applied. The tests were started by performing one run per $Fn = 0.119$ and $Fn = 0.142$ speeds, respectively. It was followed by starting from the lowest *Fn* and the speed is increased successively at each run after 20 min of waiting time. There was a total of five repeat tests for $Fn = 0.119$ and $Fn = 0.142$, while the rest of the speeds were repeated four times.

The uncertainty regarding the wetted surface area are quantified by measuring the model ballasting. The model and weights (calibrated 25 separate pieces) used for ballasting the model were weighted by two digital scales (ITTC, 2014b). Resulting uncertainties on the wetted surface are presented in Table 3 for $Fn = 0.119$ and $Fn = 0.142$ speeds.

The relative uncertainty of the towing speed is assessed by the bias limit of the towing carriage and they are presented in Table 3.

The water temperature during the tests showed less than 0.1°C variation. As described in ITTC (2014b), the measured resistance is converted to 16.0°C which was used for the CFD computations prior to the tests. The corresponding component of uncertainties in resistance due to temperature variation are presented in Table 3. The model was scanned and checked at the model workshop. The thermal deformation of the model is expected to be limited as the temperature difference between the model workshop and the towing tank is less than 5°C.

An in-house design dynamometer with a sampling rate of 10 Hz was used for measuring the resistance. The measurement at each speed is obtained by averaging the time history of the signal as described in ITTC (2014b). The standard uncertainty of average of the sampling history varied between 0.0008% and 0.0015%, while the average of all repetitions is 0.0011%. Therefore, the uncertainty of one reading from the Data Acquisition System (DAS) is negligible. The dynamometer available at the time of the towing tank tests were calibrated to a much greater range than the maximum model resistance. As a result, the uncertainty regarding to the dynamometer is the dominant source as can be seen in Table 3. The dynamometer calibration was checked after the tests. Additionally, a calibration with a range that was approximately 3 times the maximum model resistance was performed. The uncertainty due to the dynamometer dropped nearly three times with the smaller range which would have halved the total uncertainty in Table 3.

Based on the analysis described in ITTC (2014b), the significant components of uncertainties are combined through RSS (Root-Sum-Square). As seen in Table 3, major sources of the uncertainties are originating from the dynamometer (with the large calibration range) and the precision of measurement in the repeat tests. The uncertainty of resistance measurements for $Fn = 0.119$ and $Fn = 0.142$ are 0.74% and 0.53%, respectively. The expanded uncertainties in Table 3 correspond to the confidence level of 95%.

In Table 4, combined measurement uncertainties are presented in per cent of the measured data value which is the mean total resistance of all repeat tests at each speed. The uncertainties are between 0.51% and 0.84%. As seen in Table 4, it is decreasing with increasing speed because at the high speeds the contribution from the dynamometer decreases.

As mentioned before, one aspect of uncertainty of form factor determination with Prohaska method originates from the experimental uncertainty, U_D. In order to illustrate that the uncertainty on form factor is significantly higher than the experimental uncertainty, the Prohaska plot is presented in Fig. 4 with the error bars representing the experimental uncertainties presented in Table 4. Unlike the main discussion point in Section 2, the C_T/C_F values can be sensibly aligned to a line as the waves generated at the ballast loading condition were not too substantial as can be seen in Fig. 3.

The regression line in Fig. 4 is obtained by applying the method explained by York et al. (2004). This method considers the experimental uncertainties in the regression progress and predicts the uncertainties in the form factor as well. The resulting regression line is indicated as the York's method in Fig. 4 where the uncertainty on the form factor is illustrated with an error bar at $Fn^4/C_F = 0$. The uncertainty of form factor is calculated as 0.011.

Additionally a Monte Carlo simulation is performed to illustrate the variation on form factor due to measurement uncertainty. For each iteration, all measured point are varied as

$$C_T^{'} = C_T + U_{SD} \times R \tag{7}$$

where C_T is measured point presented in Table 4, U_{SD} is the measurement uncertainty and R is normally distributed random number. In every iteration, a new regression line and form factor are calculated with the York et al. (2004) method. The error, $k - k_{york}$, obtained from the Monte Carlo simulation is normalized by the uncertainty obtained from

the York et al. (2004) method (σ_{york}) and the probability density function (pdf) is calculated. As can be seen in Fig. 5, the Monte Carlo simulation indicates a normal distribution for the normalized error of the form factor and the standard deviation of the error is equal to the uncertainty obtained from the York et al. (2004) method. As a result of using both methods, the uncertainty of the form factor is calculated as 0.022 corresponding to 1.9% of $1 + k$ for the 95% confidence interval.

5. Results

The analysis of approximately 300 double body simulations of the two hulls under the conditions stated in Table 2 is discussed in this section.

5.1. Friction and viscous pressure resistance in model scale

Firstly, friction and viscous pressure resistance coefficients are investigated since only these quantities are directly computed by CFD codes. Instead, form factor is a combination of the two computed values and a friction line. Therefore, detecting the tendencies between different CFD methods might be hindered due to errors cancelling each other.

5.1.1. Uncertainty analysis

Uncertainty analysis is performed to quantify the grid uncertainty (U_G) by SHIPFLOW and NAGISA codes. For the grid dependence study, five geometrically similar grids were used with the former code and systematically refined grid triplets are prepared for latter. Both SHIPFLOW and NAGISA performs the simulations in double precision in order to eliminate the round-off errors. The iterative uncertainties were quantified by the standard deviation of the force in percent of the average force over the last 10% of the iterations. Iterative uncertainty for C_F and C_{PV} were kept below 0.01% and 0.15% for SHIPFLOW, while iterative uncertainty for C_F, C_{PV} and C_T for NAGISA were kept below 0.1% of their mean values for all simulations in model scale. Therefore, it was assumed that the numerical errors are dominated by the discretization errors and both iterative errors and round-off errors are neglected.

For SHIPFLOW, the procedure proposed by Eça and Hoekstra, 2014 was used to predict the grid uncertainties which are presented for the finest grid as a ratio of the computed value ($U_G\%S_1$) in Table 5. In order to quantify the grid uncertainty for NAGISA, three criteria are adopted, e.g. Factor of Safety (FS) method proposed by Xing and Stern (2009), Correction Factor (CF) method and Grid Convergence Index (GCI) method shown in ITTC (2017). Table 6 summarizes the results for KVLCC2 in design and ballast loading condition and KCS. In the cases where monotonic convergence is not obtained, the solution change is less than 1% of S_1 ($\varepsilon_{21}\varepsilon_{32}$). Therefore, U_G is omitted and noted with a " - " symbol in Table 6.

Table 5
Estimated grid uncertainties of SHIPFLOW for KVLCC2 and KCS in model scale for EASM and $k-\omega$ SST turbulence models, in percentage of the computed result of the finest grid S_1.$U_{C_T} = U_{C_F} + U_{C_{PV}}$.

U_G	Turbulence model	KVLCC2 (design)		KVLCC2 (ballast)		KCS (design)	
		Fn 0.119	Fn 0.142	Fn 0.119	Fn 0.142	Fn 0.152	Fn 0.26
C_F	EASM	1.0	1.2	1.3	1.2	3.5	3.2
	$k-\omega$ SST	1.1	1.4	0.9	1.0	5.9	9.6
C_{PV}	EASM	1.0	3.0	17.9	5.1	32.5	19.4
	$k-\omega$ SST	1.1	3.0	23.0	10.8	30.2	21.0
C_T	EASM	1.0	1.6	3.6	1.8	6.7	5.0
	$k-\omega$ SST	1.1	1.7	3.7	2.3	8.4	10.7

Table 6
Estimated grid uncertainties (U_G) of NAGISA for KVLCC2 and KCS in model scale for EASM turbulence model, in percentage of the computed result of the finest grid S_1.

U_G	Method	KVLCC2 (design)	KVLCC2 (ballast)		KCS (design)
		Fn 0.142	Fn 0.119	Fn 0.142	Fn 0.26
C_F	FS	3.1	2.1	2.0	–
	CF	3.8	2.4	2.3	–
	GCI	0.3	1.2	1.2	–
C_{PV}	FS	0.1	–	–	4.7
	CF	0.1	–	–	5.1
	GCI	0.1	–	–	3.0
C_T	FS	–	0.3	0.3	–
	CF	–	0.2	0.2	–
	GCI	–	0.2	0.2	–

5.1.2. Statistics of C_F and C_{PV}

The simulations in model scale comprise computations from seven different codes and six different turbulence models with wall functions and wall resolved approaches. These computations include not only the CFD setups according to the best practice guidelines (BPG) or standard settings but also setups that deviated from recommended guidelines since one of the aim of this study is to identify the methods that are not well suited for the form factor determination. In order to differentiate the contribution of the computations with deliberately made undesired settings, two different populations are considered when the statistics, such as mean and standard deviation, are calculated. The first population (denoted as P1) includes all simulations and the second population (denoted as P2) is the computations performed with best practices or standard settings of each code. It was deemed necessary to add one more population as a sub-population of the latter because of concerns on the statistics being biased by a code significantly outnumbering others in some test cases. Therefore, the third population (denoted as P3) is obtained by selecting the computations from the two finest grids of each code per CFD approach such as turbulence model, wall treatment. This selection is based on the number of cells under the assumption that fine grids have less discretization uncertainty.

The mean and standard deviation of C_F and C_{PV} for each condition is calculated with the three previously mentioned populations. As presented in Table 7 and Table 8, it is observed that statistics of different populations of the same condition showed limited variation except KVLCC2 in design condition which is the condition many of the deliberate variations were applied to CFD setups. In Fig. 6, the Population 2 and simulations with non-desired CFD set-ups are visualised by dividing all the computations for KVLCC2 in design condition into two groups: computations with non-standard CFD set-ups, and simulations with the best practice guidelines (BPG) or standard CFD set-ups. The small difference in statistics between the Population 2 and 3 shows that the statistics are not biased even though some test cases are overcrowded with simulations from one code. The computations performed with the best practices or the standard settings of each code (Population 2) will be used for the rest of the analysis, except when the results of deliberate variations of CFD setups are discussed.

Friction and viscous pressure resistance coefficients. C_F and C_{PV}

Table 7
The mean and standard deviation of C_F for KVLCC2 and KCS in model scale.

Quantity	KVLCC2 (design)		KVLCC2 (ballast)		KCS (design)	
	Fn 0.119	Fn 0.142	Fn 0.119	Fn 0.142	Fn 0.152	Fn 0.26
Mean (P1)	3.462	3.381	3.298	3.21	3.112	2.893
Mean (P2)	3.47	3.394	3.298	3.215	3.105	2.892
Mean (P3)	3.455	3.376	3.298	3.215	3.095	2.885
σ (P1)	2.7%	2.5%	2.5%	2.4%	2.0%	1.6%
σ (P2)	2.5%	2.6%	2.5%	2.5%	2.0%	1.6%
σ (P3)	2.9%	2.8%	2.5%	2.6%	1.9%	1.8%

P1 Population 1; P2 Population 2; P3 Population 3.

Table 8
The mean and standard deviation of C_{PV} for KVLCC2 and KCS in model scale.

Quantity	KVLCC2 (design)		KVLCC2 (ballast)		KCS (design)	
	Fn 0.119	Fn 0.142	Fn 0.119	Fn 0.142	Fn 0.152	Fn 0.26
Mean (P1)	0.793	0.777	0.504	0.494	0.387	0.33
Mean (P2)	0.789	0.739	0.501	0.49	0.387	0.326
Mean (P3)	0.794	0.745	0.499	0.488	0.393	0.335
σ (P1)	9.2%	13.1%	6.6%	6.2%	7.6%	13.6%
σ (P2)	9.7%	9.8%	7.3%	6.9%	9.0%	14.4%
σ (P3)	10.2%	10.3%	7.9%	7.5%	9.2%	15.0%

in model scale for KVLCC2 in both loading conditions and KCS in design condition are presented versus grid size (in logarithmic scale) in Fig. 7 and Fig. 8. In order to have references for the friction resistance coefficient, the ITTC-57 line and the Katsui line are plotted in Fig. 7.

As can be seen in Figs. 7 and 8, there is no distinct dependence of results on the grid size. Note that this is a comparison of unsystematically varied methods and grids. However, other dependencies such as the turbulence modelling and the wall treatment were found both on C_F and C_{PV}. The frictional resistance coefficients from UM (Participant 1) and SSPA/CTU (Participant 6) indicate a strong dependence on turbulence model while this effect is rather limited on the results of ECN/CNRS (Participant 3), NMRI (Participant 4) and YNU (Participant 9). The viscous pressure coefficients from ECN/CNRS and SSPA/CTU show larger dependence on turbulence models than the others. ECN/CNRS and NMRI performed simulations both with wall resolved and wall function. Both codes indicate a significant dependence on wall treatment especially for C_F but also for C_{PV} which is less sensitive to the wall treatment than the frictional resistance component.

Variations of CFD setups. The previously mentioned CFD setups that varied from recommended guidelines on KVLCC2 in design condition have been applied by UM, ECN/CNRS, SSPA/CTU and SSSRI. UM (Participant 1) varied grids focusing specifically to the grid resolution near the wall using two turbulent models. As can be seen in Fig. 9, where all computations on KVLCC2 in design condition are presented, $k-\omega$ SST and Spalart-Allmaras turbulence models shows high sensitivity on C_F to both grid refinement and y^+ variation. However, the variation on C_{PV} is limited except for the coarsest grid set.

ECN/CNRS (Participant 3) performed grid variations also with adaptive grid refinement. When wall functions were used, C_F and C_{PV} showed small variation even for the very coarse grids. However, wall resolved simulations of ECN/CNRS are more grid dependent compared

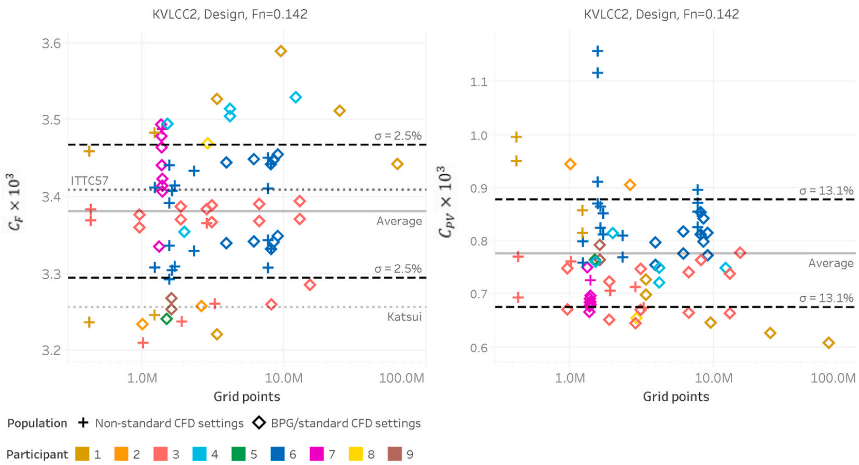

Fig. 6. Frictional coefficient (left) and viscous pressure coefficient (right) in model scale for KVLCC2 hull in design loading condition at Fn. = 0.142

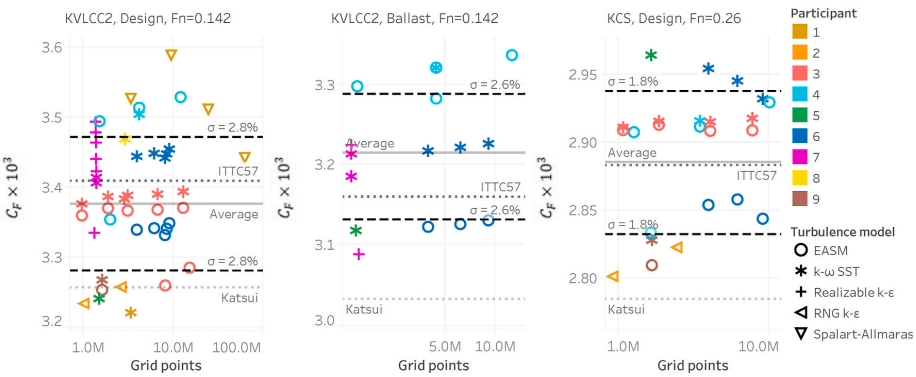

Fig. 7. Frictional coefficient, C_F, in model scale for KVLCC2 hull in design loading condition at Fn= 0.142 (left), KVLCC2 in ballast loading condition Fn= 0.142 (center) and KCS hull in design loading condition at Fn= 0.26 (right).

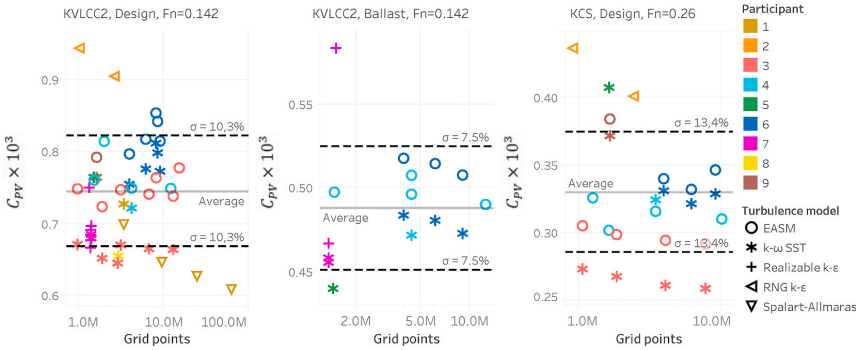

Fig. 8. Viscous pressure coefficient, C_{PV}, in model scale for KVLCC2 hull in design loading condition at Fn= 0.142 (left), KVLCC2 in ballast loading condition Fn= 0.142 (center) and KCS hull in design loading condition at Fn= 0.26 (right).

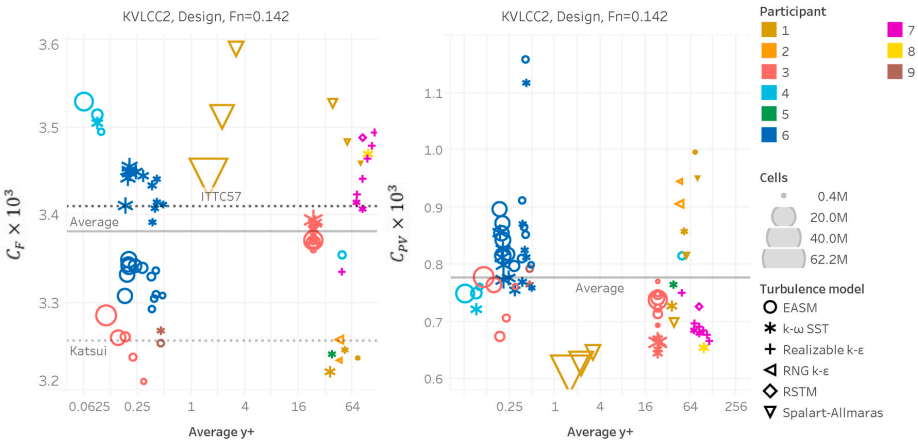

Fig. 9. C_F (left) and C_{PV} (right) in model scale for KVLCC2 hull in design loading condition at Fn= 0.142 against mean y^+. $y^+ < 1$: wall resolved, $y^+ > 1$: wall function.

to wall functions. This is explained by the increasing grid resolution near the wall rather than the increase in grid size for the wall resolved computations.

In addition to the systematic grid variations for the grid dependence studies, SSPA/CTU (Participant 6) performed grid variations by coarsening the grid of the bow and the stern region of the KVLCC2 hull in the longitudinal direction while keeping the rest of the grid the same. For this exercise, the second finest grid and the coarsest grid of the grid dependence study was selected as a starting point. Coarsening the bow and stern regions up to grid density of one third of the starting grids did not show a significant variation on C_F but some variation in C_{PV} for the same turbulence model except for one case. When the coarsest grid was further coarsened in the aft, the C_{PV} was calculated extremely high as seen in Fig. 6 (highest two values from Participant 6) while the variation of C_F was limited. The grid variations of SSPA/CTU on KVLCC2 showed that when the grid resolution normal to the wall is kept similar, C_F and C_{PV} are more sensitive to the grid density in aftbody than forebody.

Simulations of SSSRI (Participant 7) was performed with three different turbulence models. As can be seen from Fig. 9, both C_F and C_{PV} obtained from Reynolds Stress Turbulence Model (RSTM) were significantly higher than the realizable $k-\varepsilon$ and $k-\omega$ SST models with similar grids and average y^+ values. Additionally, different types of wall functions were used with realizable $k-\varepsilon$ and $k-\omega$ SST models while keeping the grids similar. C_F and C_{PV} showed only marginal change due to different wall function type for the $k-\omega$ SST model. However, the realizable $k-\varepsilon$ model showed a substantial variation in both C_F and C_{PV} due to different wall function treatment. Finally, y^+ is varied with the realizable $k-\varepsilon$ model. It is observed that when the average y^+ increases (from 71 to 112 in steps of 11), C_F also increases up to 2% while C_{PV} decreases up to 4.5% as shown in Fig. 9. Therefore, a significant dependence of y^+ and wall function treatment on viscous resistance is observed with the realizable $k-\varepsilon$ model.

5.2. CFD based form factors with the ITTC-57 line

CFD based form factors are calculated using Eq. (6) and presented versus the number of grid points in Fig. 10. Note that only the simulations performed according to the best practice guidelines or standard settings of each code are presented and logarithmic scale is used in the grid points axis for better clarity. In addition to standard deviation in percentage of $(1+\overline{k})$ and mean of the CFD based form factors ($\overline{k}$), form factors determined by model tests of Van et al. (2011) for KVLCC2 and KCS in design condition and KVLCC2 in ballast loading condition of SSPA are plotted in Fig. 10.

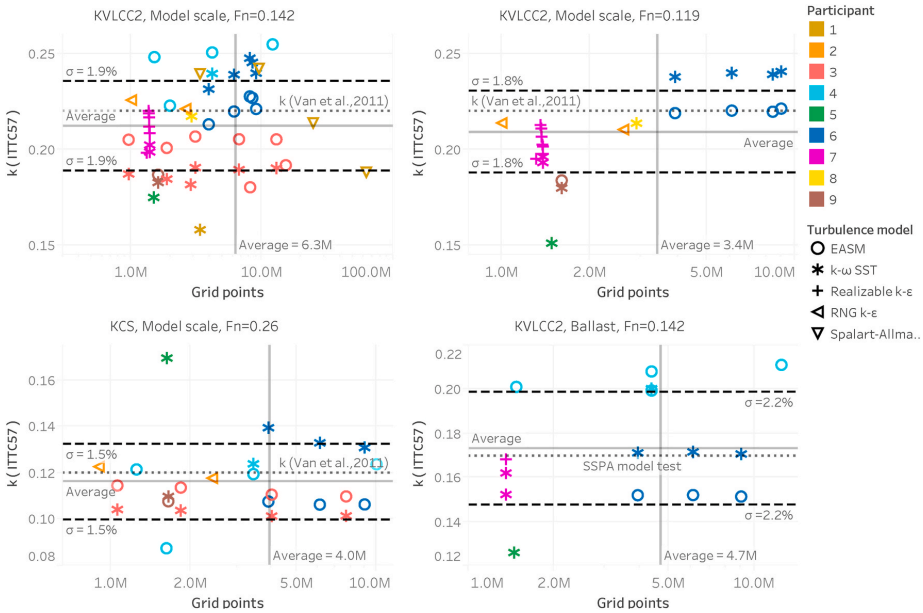

Fig. 10. Form factor, k, based on ITTC-57 line versus grid size for KVLCC2 hull in design loading condition at Fn = 0.142 (top left) and Fn = 0.119 (top right), KCS hull in design loading condition at Fn = 0.26 (bottom left) and KVLCC2 in ballast loading condition Fn = 0.142 (bottom right).

Mean of the form factor predictions for the KVLCC2 in design condition at $Fn = 0.119$ and $Fn = 0.142$ are both close to the form factor determined experimentally. The standard deviation of the form factors obtained from the unsystematically varied methods and grids at both speeds is around 1.9%. If the form factor is used in extrapolation of the model resistance value for this KVLCC2 case, this would cause approximately 3% spread in the predicted full-scale resistance (roughness, correlation allowance and air resistance excluded). Number of grid cells among the computations varied between one million to 62 million, However, form factor predictions do not indicate dependence on the number of grid cells.

Mean of the form factor predictions for the KCS in design condition at $Fn = 0.26$ is very close to the experimental value. However, at $Fn = 0.152$, the mean value of form factor is 0.015 smaller than the mean form factor at $Fn = 0.26$ as shown in Table 9 in Section 5.3. This difference was not as large for the KVLCC2 because the Re difference between the speeds were small (19%). However, Re difference between the speeds for the KCS hull is 71% which is big enough to reveal the speed dependency of the form factor as it is discussed in further detail in Section 5.3. The standard deviation of 1.5% translates to approximately 1% in full scale resistance excluding the contribution of roughness, correlation allowance and air resistance. Note that this is a remarkable result even though such a wide range methods and grids were used since KCS like hulls are the ones that suffers the most from the Prohaska method because of the prominent bulb designs.

All the computations for KVLCC2 in ballast case had to be performed prior to the model tests. The slight discrepancy in water temperature between computations and tests were corrected using ITTC (2014b) procedures for form factor determination. Form factor predictions for the KVLCC2 in ballast loading condition showed a similar standard deviation to the other cases. However, the mean value of the form factor is not as close to the experimentally determined form factor as the other cases. As explained in Section 4, uncertainty analysis was performed for the form factor. When the uncertainty of the Prohaska method on the experimentally determined form factor is considered, majority of the simulations are still within the uncertainty range.

It is observed in Fig. 10 that some form factor predictions are relatively far from the experimentally derived form factor. However, it is encouraging to observe that there are some consistent patterns for most of the codes. The form factor was under-predicted similarly by YNU (Participant 9) and ECN/CNRS (Participant 3) for both KVLCC2 and KCS hulls in design condition. Results of SSSRI (Participant 7) are also under-predictions for all the cases. It should be noted that as long as one code with a certain set-up consistently predicts the form factor with the same tendency, application of correlation factors (C_P or C_A) in the 1978 ITTC Power Prediction method will help to reduce the discrepancies.

CFD Code Dependency. The dependencies and tendencies of each code for the form factor predictions are plotted in Fig. 11 and Fig. 12. Computations from each code are stacked in separate columns where box-and-whisker plots are placed with markers. The box plot can be identified with the gray color and sized with the lower and upper quartiles. Lines extending from the boxes (whiskers) extend to the data within 1.5 times the interquartile range (IQR). The markers are colored with the turbulence models, shaped according to the wall treatment type and sized according to the number of cells.

Turbulence Model Dependency. The choice of turbulence model stands out as a decisive element of the CFD based form factors when the results of UM, ECN/CNRS, NMRI and SSPA/CTU are considered. Even if the same code and similar CFD set-ups are used, a significant dependence on turbulence models are observed. However, a general trend for each turbulence model cannot be maintained either. For example, ECN/CNRS (Participant 3), NMRI (Participant 4) and YNU (Participant 9) predicted higher form factors with EASM turbulence model than with $k-\omega$ SST, while this is the opposite with SSPA/CTU (Participant 6). It should be also noted that the form factor predictions from the same turbulence model with different CFD codes are largely scattered. Therefore, the dependence of form factors to the CFD codes surpasses the choice of the turbulence model.

Wall Treatment Dependency. The type of wall treatment and y^+ can be considered as significant dependencies of form factor as it was the

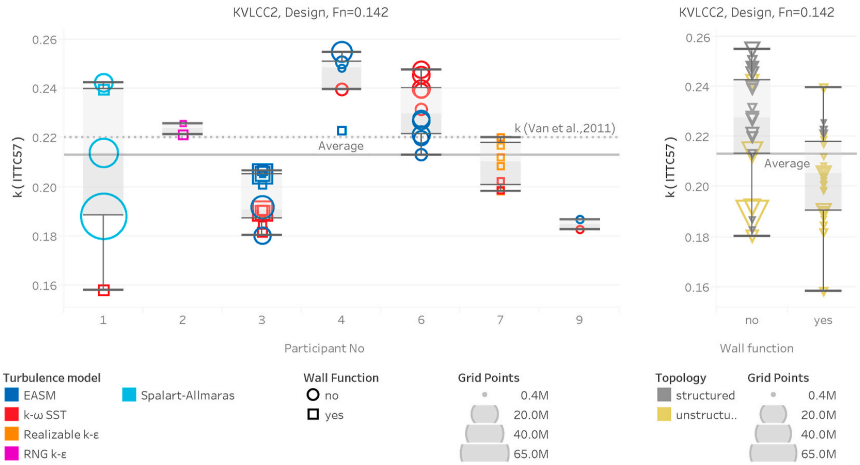

Fig. 11. Tendency of CFD codes and methods for form factors, k, based on ITTC-57 line for KVLCC2 hull in design loading condition at Fn = 0.142.

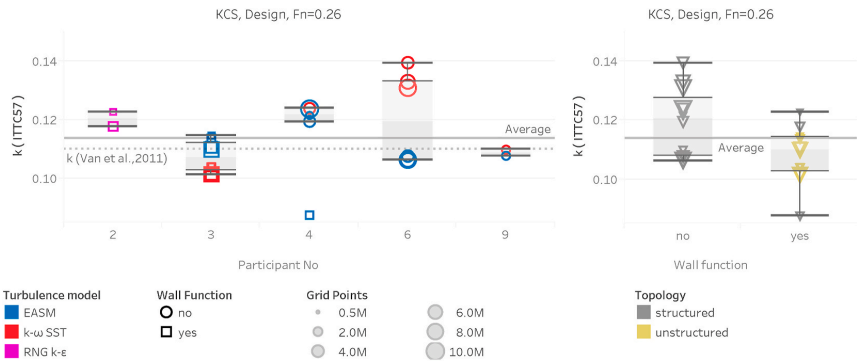

Fig. 12. Tendency of CFD codes and methods for form factors, k, based on ITTC-57 line for KCS hull in design loading condition at Fn = 0.26.

case for C_F and C_{PV} investigated earlier. ECN/CNRS and NMRI performed computations with the same turbulence models of $k-\omega$ SST and EASM and also both participants had simulations with and without wall functions. As can be seen from Figs. 11 and 12, form factor dependence on the wall treatment is observed with both ECN/CNRS (Participant 3) and NMRI (Participant 4), while a significant dependence on y^+ was observed with the realizable $k-\varepsilon$ model for SSSRI.

On the right side of Figs. 11 and 12, simulations from all codes are sorted with the type of wall treatment. The markers are colored with the type of the grid. The box plots of both KVLCC2 and KCS indicate that interquartile range (IQR) of simulations with wall functions are smaller than wall resolved. However, the distance between the whiskers are similar for both approaches. Although the CFD results as a whole are a product of unsystematically varied methods and grids, the comparison of median values of different wall modelling indicates that simulations with wall functions predict considerably smaller form factors compared to wall resolved approach.

5.3. Form factors with alternative friction lines

As mentioned earlier in Section 1, speed dependency or scale effects have been found on the form factor by the previous investigations. However, it should be noted that the form factors should always be considered with the friction line used as the physical meaning of speed dependency or scale effects on the form factor is that the viscous resistance of a ship is not proportional to the selected friction line. Even if the concept of Hughes (1954) (see Section 2) is true, different sizes of geosim models and double body simulations at different Reynolds numbers will result in different form factors as a result of using an 'improper' friction line. The currently recommended fiction line, the ITTC-57 line (ITTC, 1957), is in fact not a pure friction line as Hughes (1954) hypothesis requires but a model-ship correlation line. Therefore, speed dependency of the form factors with ITTC-57 line is not extraordinary but expected.

Instead of the ITTC-57 line, C_{F0} in Eq. (6) can be replaced by other friction lines such as Katsui et al. (2005) or numerical friction lines (NFL) that are derived by using the same code as the double body simulations. Prior to this study, only SSPA/CTU obtained a NFL with the SHIPFLOW code for EASM and $k-\omega$ SST turbulence models (Korkmaz et al., 2019b). Since other participants did not have numerical friction lines, frictional resistance coefficients of infinitely thin 2D plates were computed by NMRI, SSSRI, Strathclyde and YNU with the same turbulence models, wall treatment and Reynolds number as the corresponding double body simulations. These C_F values obtained from the flat plate simulations were then used as C_{F0} in Eq. (6) for the form factor determination.

Table 9
Statistics of the form factor predictions with ITTC-57 line (I), Katsui line (K) and numerical friction lines (N).

Quantity	KVLCC2 (design)		KVLCC2 (ballast)		KCS (design)	
	Fn	Fn	Fn	Fn	Fn	Fn
	0.119	0.142	0.119	0.142	0.152	0.260
Mean (I)	0.212	0.223	0.175	0.181	0.102	0.117
Mean (K)	0.271	0.280	0.227	0.231	0.149	0.156
Mean (N)	0.296	0.296	0.242	0.243	0.163	0.165
σ (I)	1.5%	1.6%	2.1%	2.0%	1.3%	1.2%
σ (K)	1.5%	1.6%	2.1%	2.0%	1.3%	1.2%
σ (N)	2.4%	2.1%	1.8%	1.9%	0.7%	0.8%

Form factors based on the ITTC-57 line and the Katsui line are also calculated using the same simulations where NFL data is available. The mean values and the standard deviations of the form factors based on different friction lines are presented in Table 9. The speed dependency can be identified by comparing the mean of the form factor predictions of different Reynolds numbers at the same loading condition. As expected, speed dependency of form factors with the ITTC-57 line is observed for the both hulls and the loading conditions. The largest speed dependency, however, is observed for the form factors of the KCS hull with the ITTC-57 line as the difference between the Reynolds numbers is the greatest among other cases. The speed dependencies are reduced considerably when the Katsui line is used and they are almost completely eliminated with numerical friction lines for all test cases.

Regardless of an existence of speed dependency of form factors, the choice of speed from which the form factor will be determined is a relevant issue for CFD computation. The extrapolated full scale viscous resistance predictions will be influenced by the choice of the model scale speed when the speed dependency exists. Therefore, the speeds that correlates better with the experimentally determined form factors should be preferred. Based on the form factor predictions presented in Table 9, design speeds of KVLCC2 and KCS are suggested if the ITTC-57 line is used for the form factor determination. Another point of concern is choosing the speed that provides the smaller numerical uncertainties and modelling errors. The grid uncertainties presented in Tables 5 and 6 for SHIPFLOW and NAGISA codes showed limited change of grid uncertainties with the speed while the change of U_G were not systematically increasing or decreasing. In terms of modelling errors, numerical transition from laminar to turbulent flow can be concerning when the *Re* is too low as this phenomenon occurs even without the use of transition turbulent models as shown in Eça and Hoekstra, 2008 and Korkmaz et al. (2019b).

As presented in Table 9, the mean of form factors with ITTC-57 line greatly differs from Katsui line and NFL. The physical explanation of this observation is that when ITTC-57 line is used, the form resistance (see Section 2) is significantly under-predicted due to too large frictional resistance component in model scale. The effect of the under-prediction of form resistance to the full scale viscous resistance will be discussed in Section 5.4.2.

Form factors with numerical friction lines for KVLCC2 are presented in Fig. 13. Opposing to the results from the ITTC-57 line, the mean value of the form factors with NFL are almost identical for both speeds. Close investigation on the individual simulation points between the different speeds also support this suggestion except the simulations from Strathclyde (Participant 8) and the coarse grids of SSPA/CTU (Participant 6). KVLCC2 in both loading conditions shows smaller speed dependency with ITTC-57 line compared to KCS as the Reynolds number difference between the two speeds is smaller. It is worth noticing that the speed dependency is larger in design condition than the ballast loading condition with the ITTC-57 line. This is a consequence of the "artificial" steepness of the ITTC-57 line which increases as the *Re* decreases. Therefore, as any other model with big scale factor (the ratio of ship to model length) would, KVLCC2 model in design condition suffers more from the scale effects with the ITTC-57 line.

The standard deviations of the form factor in percentage of $(1+\bar{k})$ predictions for all cases are presented in Table 9. Using the Katsui line, the standard deviation of the form factor are the same in all cases compared to using the ITTC-57 line as the same computations were used. Form factors with NFL showed an increase in the standard deviation for the KVLCC2 in design condition. However, the standard deviation is reduced significantly for KVLCC2 in ballast loading condition and especially for KCS due to a decrease in variation of form factors obtained from different turbulence models. Even though the dependence of turbulence models on form factor seems to decrease by the adoption the NFL of the same code and turbulence model as the double body simulation, the form factors are not expected to be the same for different turbulence models. Application of NFL for different turbulence models arranges the quantity of form resistance with respect to the friction line of the respective turbulence model. As a result, nearly the same full scale viscous resistance values can be obtained by the different turbulence models as shown in Section 5.4.2.

As an alternative to the CFD based form factor determination method used in this study, Wang et al. (2016) and Terziev et al. (2019) calculated the form factors simply by dividing the viscous pressure coefficient to friction coefficient ($k = C_{PV}/C_F$) obtained from the double body simulation with the hull. Therefore, the need of any friction line is removed for form factor determination. This method of form factor determination is dismissed in this study because of the deviation from the approach of Hughes (1954) as C_F from double body computation already includes the additional skin friction caused by the curvature effects which should have been included the form resistance as explained in Section 2.

5.4. Full scale predictions

5.4.1. Statics of computed C_F and C_{PV} in full scale

Full scale double body simulations are performed according to the conditions described in Table 2. The friction and viscous pressure resistance coefficients are presented in Fig. 14 and Fig. 15, respectively.

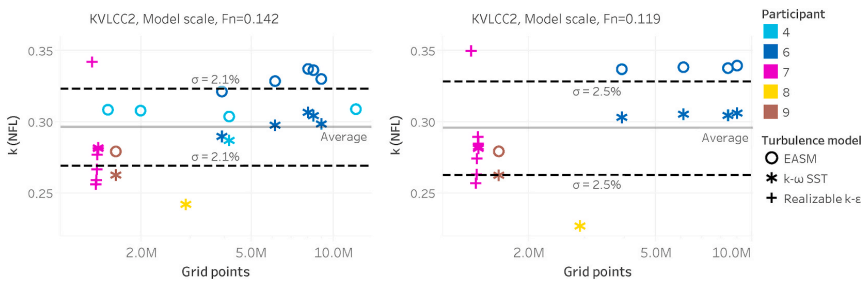

Fig. 13. Form factor, *k*, based on numerical friction lines versus grid size for KVLCC2 hull in design loading condition at Fn = 0.142 (left) and Fn = 0.119 (right).

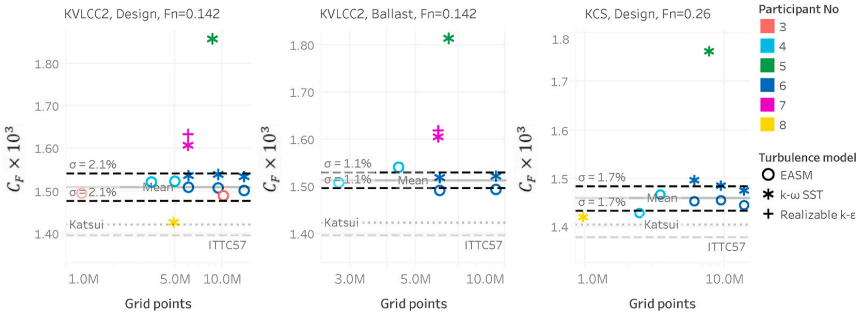

Fig. 14. Full scale CFD simulations. Computed frictional coefficient, C_F, for KVLCC2 hull in design loading condition at Fn = 0.142 (left), KVLCC2 in ballast loading condition Fn = 0.142 (center) and KCS hull in design loading condition at Fn = 0.26 (right).

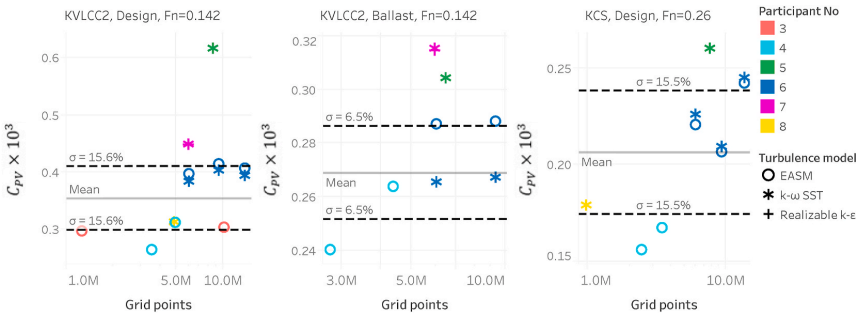

Fig. 15. Full scale CFD simulations. Computed viscous pressure coefficient, C_F, for KVLCC2 hull in design loading condition at Fn = 0.142 (left), KVLCC2 in ballast loading condition Fn = 0.142 (center) and KCS hull in design loading condition at Fn = 0.26 (right).

The mean and standard deviation of the computed resistance coefficients are calculated excluding the results from NRC-OCREand SSSRI who encountered difficulties with grid generation. The mean of C_F is by approximately 6% and 3% higher than the Katsui line due to additional skin friction caused by the curvature effects for KVLCC2 and KCS, respectively. The standard deviation of C_F in full scale is reduced considerably compared to model scale for KVLCC2 at both loading conditions mainly because of the reduction of dependence on turbulence models. The standard deviation of C_F is similar both in model and full scale for the KCS hull. However, the standard deviation of C_{PV} is increased for KCS and KVLCC2 in design condition compared to model scale while the variation of C_{PV} is similar in model and full scale for KVLCC2 in ballast condition. Considering the standard deviation and the quantity of C_F and C_{PV} observed in full scale simulations, the viscous pressure resistance component is the dominant source of variation in C_V.

As mentioned earlier, the difficulties in the grid generation for NRC-OCRE and SSSRI can be observed through the average y^+ values varied between 450 and 750 for NRC-OCRE and 8300 to 15,000 for SSSRI. As a result, mainly the predicted C_F values are significantly higher than the mean of the rest of the computations. A strong dependence on

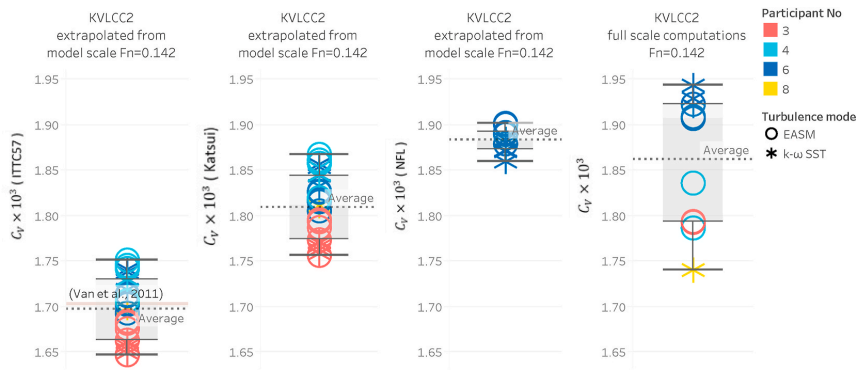

Fig. 16. Extrapolated and directly computed full scale viscous resistance coefficients, C_V, for KVLCC2 hull in design loading condition at Fn = 0.142.

turbulence model was observed with the computations of SSPA/CTU in model scale. However, this dependence is reduced by half for SSPA/CTU except the KVLCC2 in ballast loading condition. NMRI performed two simulations per case where one with wall resolved (higher number of grid cells) and the other with wall function where the latter under-predicted both friction and viscous pressure resistance coefficients compared to wall resolved approach.

5.4.2. Full scale viscous resistance extrapolation

Full scale viscous resistance predictions of KVLCC2 and KCS hulls are performed via extrapolation from model scale and compared with full scale computations in Fig. 16 and Fig. 17. The extrapolation to full scale is performed using the CFD based form factors and the ITTC-57, Katsui and numerical friction lines. In Figs. 16 and 17, full scale viscous resistance predictions are presented as box-and-whisker plots with the markers. The participants without full scale computations are excluded for clarity and fair comparison between extrapolated values and full scale computations. The friction line used for the extrapolation and form factor determination is indicated within brackets on the y-axis label.

The extrapolations based on the model tests data of Van et al. (2011) with the ITTC-57 line is represented by a horizontal line that is almost coinciding with the mean C_V values of the predictions from CFD based form factors for both KVLCC2 and KCS. When the ITTC-57 line is used, full scale viscous resistance of KVLCC2 and KCS are approximately 6.6% and 5.5% lower on average compared to extrapolation based on Katsui line. The mean of the extrapolations based on the ITTC-57 line is 9.7% and 8.0% lower than the full scale computations for KVLCC2 and KCS, respectively. Similar conclusions were obtained by the investigations performed by Raven et al. (2008) on a containership which showed that C_V from direct full scale computations are 7.4% higher than the extrapolation method with the ITTC-57 line. This difference is mainly due to too steep the ITTC-57 line which causes an underestimated C_V at full scale. Raven et al. (2008) suggested that the underestimation of C_V due to the ITTC-57 line is mainly compensated by the correlation allowance (C_a) in the ITTC scaling procedures.

Using the same model scale simulations but form factors and extrapolation with the Katsui line, the full scale viscous resistance values are similar to the predictions of full scale simulations. The C_V predictions with numerical friction lines are only performed with SSPA/CTU as others did not have numerical friction lines. The mean of extrapolated full scale viscous resistance with NFL are in agreement with the mean of full scale computation results. However, the extrapolated values are slightly under-predicted compared to direct full scale computations for both hulls. Agreement between the extrapolations with the Katsui line and NFL is also noticeable.

As can be seen in Figs. 16 and 17, the standard deviation of full scale computations are twice as large as the standard deviation of model to full scale extrapolations with the ITTC-57 and Katsui lines for both hulls. This means that full scale simulations are still less reliable than the model scale computations as the agreement on the CFD predictions are higher in model scale. The standard deviations of extrapolations with the ITTC-57 and Katsui lines are almost identical. But as discussed in Section 5.3, the speed dependency on the form factor was noticeably reduced with the Katsui line compared to the ITTC-57 line. When numerical friction lines are considered, only the results from the SSPA/CTU are considered for the comparison of the standard deviations for a fair comparison. For KVLCC2 and KCS, the smallest standard deviations are observed with extrapolation with the numerical friction lines which also eliminated the speed dependency of the form factors almost completely.

The extrapolated full scale viscous resistance values presented in Figs. 16 and 17 were based on the model scale computations performed at $Fn = 0.142$ and $Fn = 0.26$ for KVLCC2 in design loading condition and KCS, respectively. As presented in Table 9, the form factors were speed dependent when ITTC-57 and Katsui lines were used. Therefore, the extrapolated C_V values would be approximately 1.2% and 0.7% lower than the C_V values presented in Figs. 16 and 17 when the model scale computations at $Fn = 0.119$ and $Fn = 0.152$ are used with ITTC-57 and Katsui lines, respectively. On the other hand, the application of NFL eliminated the speed dependency of the form factors almost completely as shown in Table 9.

The standard deviation is perhaps a more essential measure for improving the power predictions compared to the absolute values of C_V predictions. As long as C_V is predicted with the same tendency, correlation factors (C_P or C_A) based on the experience of each institution can be used effectively to adjust the final predictions in terms of absolute values.

6. Conclusions

This paper presents an investigation on CFD based form factor methods which was initiated by the ITTC Specialist Committee Combined CFD/EFD Methods. The assumptions underlying the form factor approach and the Prohaska method is discussed and model test data is compared to the RANS simulations performed by 7 different CFD codes.

The disposition to leave the Prohaska method of form factor determination is explained through two types of uncertainty.

- The linear relationship proposed by Prohaska in Eq. (5) is not valid for the hulls with prominent bulb designs at fully or partially submerged conditions. Since a substantial portion of the merchant and naval fleet are equipped with bulbous bows, the validity of the

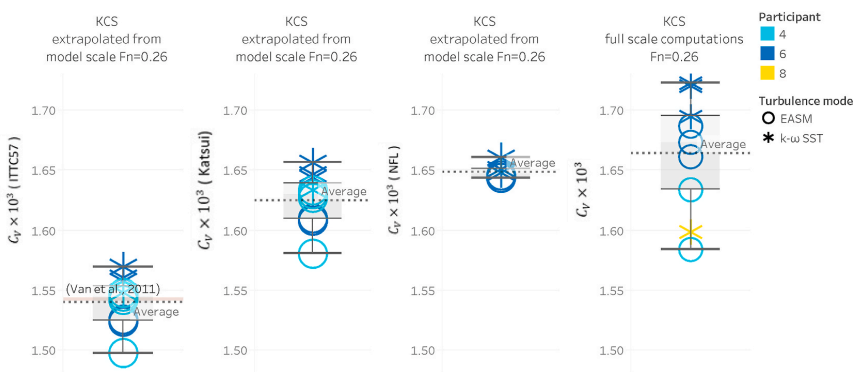

Fig. 17. Extrapolated and directly computed full scale viscous resistance coefficients, C_V, for KCS hull in design loading condition at Fn = 0.26.

Prohaska method as a common tool for all hull forms is under question. As discussed in Section 2, it is difficult to quantify this uncertainty as the case sensitivity is very high.

- The second uncertainty source of the Prohaska method originates from the experimental uncertainty. As demonstrated with the model tests results of KVLCC2 in ballast condition, the experimental uncertainty is noticeably amplified for the form factor as a result of the regression analysis. This amplification of the uncertainty on the form factor can be much more severe if a hull with voluminous bulb is tested where the C_T/C_F values often cannot be used in low speed range. Therefore, uncertainty of 0.022 (within 95% confidence interval) on the form factor with Prohaska method on KVLCC2 in ballast condition can be considered merely as a best case scenario.

Model scale simulations are performed with seven different codes and six different turbulence models with wall functions and wall resolved approaches. The resulting form factor predictions with the ITTC-57 line from the computations with recommended or standard CFD setups compared well with the experimentally determined form factors for KVLCC2 and KCS in design loading condition at design speeds. The CFD based form factors are mostly under-predicted for KVLCC2 in ballast loading condition compared to experiments. However, the majority of the CFD based form factors were within the experimental uncertainty. The form factors showed 1.5–2.5% standard deviation in percentage of $(1+\overline{k})$ even though the abundance of unsystematically varied methods and grids. It should be noted that the experimental uncertainty of the form factor will be of similar levels even for the cases when the linear relationship proposed by Prohaska holds.

Model scale computations include not only the CFD setups according to the best practice guidelines or standard settings but also setups that deviated from the recommended guidelines as one of the goal of this study is to identify the methods that are not well suited for the form factor determination. The resulting form factor predictions with the ITTC-57 line from the computations with non-standard CFD setups.

- indicated that describing the boundary layer with a good quality grid in terms of the grid resolution and the first cell size normal to the wall is essential for both wall treatment types;
- are considerably more sensitive to the grid density in aftbody than forebody and
- can be sensitive to the different types of wall functions with certain turbulence models such as realizable $k-\varepsilon$.

As mentioned before, different codes indicated varying dependencies on CFD setups, and therefore general recommendations for all CFD setups cannot be made specifically for the sake of form factor determination. Instead, it is observed that most of the codes with a certain CFD setup showed consistent patterns of form factor predictions among different test cases. If these trends are confirmed with more hulls and test cases, application of correlation factors (C_P or C_A) unique for each code and method will be able to reduce the differences in full scale predictions further.

Speed dependency of the form factors are confirmed with the application of the ITTC-57 line for all test cases. The question of which model scale speed should be chosen for the CFD based form factors with the ITTC-57 line cannot be answered within the scope of this study because of the differing trends of each code. However, the mean values of form factors with ITTC-57 line are closer to the experimental values in design speeds of KVLCC2 and KCS hulls. If another friction line is preferred such as the Katsui or numerical friction lines, the speed dependency on the form factor is reduced significantly, and therefore decreasing the importance of the choice of the speed for the model scale simulations.

Full scale viscous resistance is calculated by extrapolating the model-scale results with different friction/correlation lines and direct full scale simulations. The scatter among the full scale computations are substantially higher than the extrapolations from the model scale for both KVLCC2 and KCS hulls. Even though the standard deviation of C_F in full scale computations is reduced considerably compared to model scale computations for KVLCC2 at both loading conditions as a result of reduced dependence on turbulence models, the increased discrepancy on full scale C_{PV} predictions lead to a larger scatter of C_V for full scale simulations. Hence, the full scale simulations should not to be preferred over the form factor approach yet.

Finally, CFD based form factors can be considered as an alternative or supplementary method to the Prohaska method. It is considered as a step towards answering the request of ITTC Performance Committee of 1978: "Future developments for the determination of form factors on a more scientific basis is expected" (ITTC, 1978). The selection of friction lines would also have an impact on reducing the scatter between the full scale predictions and sea trials due to elimination of scale effects. However, the improvements expected from a change of friction line are minor compared to the implementation of a CFD based form factor method.

Although there are still shortcomings with full scale resistance predictions, combination of EFD and CFD is expected to provide immediate improvements to the 1978 ITTC Performance Prediction Method. Further studies should be performed with many more test cases and CFD codes to establish a better understanding for the dependencies of CFD methods on the form factor prediction. As a final step, comparison of sea trials and the power predictions with CFD based form factors should be performed for different types of ships.

CRediT authorship contribution statement

Kadir Burak Korkmaz: Conceptualization, Methodology, Validation, Formal analysis, Investigation, Data curation, Writing - original draft, preparation, Writing - review & editing, Visualization. **Sofia Werner:** Conceptualization, Methodology, Investigation, Writing - review & editing, Supervision, Project administration, Funding acquisition. **Nobuaki Sakamoto:** Investigation, Writing - review & editing. **Patrick Queutey:** Investigation, Writing - review & editing. **Ganbo Deng:** Investigation, Writing - review & editing. **Gao Yuling:** Investigation, Writing - review & editing. **Dong Guoxiang:** Investigation, Writing - review & editing. **Kevin Maki:** Investigation, Writing - review & editing. **Haixuan Ye:** Investigation, Writing - review & editing. **Ayhan Akinturk:** Investigation, Writing - review & editing. **Tanvir Sayeed:** Investigation, Writing - review & editing. **Takanori Hino:** Investigation, Writing - review & editing. **Feng Zhao:** Investigation, Writing - review & editing. **Tahsin Tezdogan:** Writing - review & editing. **Yigit Kemal Demirel:** Investigation, Writing - review & editing. **Rickard Bensow:** Conceptualization, Methodology, Investigation, Writing - review & editing, Supervision.

Declaration of competing interest

The authors declare that they have no known competing financial interests or personal relationships that could have appeared to influence the work reported in this paper.

Acknowledgments

The contribution by SSPA/CTU was funded by VINNOVA, the Swedish Governmental Agency for Innovation Systems, grant 2017–02953, and the computational resources provided by Chalmers Center for Computational Science and Engineering (C3SE).

The contribution by NMRI was partially funded by JSPS Grant-in-Aid for Scientific Research (C) #19k04872.

The contribution by ECN/CNRS was granted access to the HPC resources of CINES and IDRIS computing centres under the allocations 2019-A0052A01308 and 2020-A0072A01308 made by GENCI (Grand

Équipement National de Calcul Intensif).

The contribution by UM was supported by the US Office of Naval Research and the computational resources and services provided by Advanced Research Computing at the University of Michigan, Ann Arbor.

The contribution by YNU was supported by JSPS (Japan Society for the Promotion of Science) KAKENHI grant number JP18H01638.

References

Dogrul, A., Song, S., Demirel, Y.K., 2020. Scale effect on ship resistance components and form factor. Ocean. Eng. 209, 107428. https://doi.org/10.1016/j.oceaneng.2020.107428. http://www.sciencedirect.com/science/article/pii/S0029801820304534.

Eça, L., Hoekstra, M., 2008. The numerical friction line. Journal of Marine Science and TechnologyJournal of Marine Science and Technology 13, 328–345. https://doi.org/10.1007/s00773-008-0018-1.

Eça, L., Hoekstra, M., 2014. A procedure for the estimation of the numerical uncertainty of cfd calculations based on grid refinement studies. J. Comput. Phys. 262, 104–130. https://doi.org/10.1016/j.jcp.2014.01.006.

García Gómez, A., 2000. On the form factor scale effect. Ocean. Eng. 26, 97–109.

Hughes, G., 1954. Friction and form resistance in turbulent flow, and a proposed formulation for use in model and ship correlation. R. I. N. A. 96.

IMO, 2011. Annex 19: Resolution MEPC, vol. 203, 62.

ITTC, 1957. Subjects 2 and 4 Skin Friction and Turbulence Stimulation.

ITTC, 1972. Report of Performance Committee.

ITTC, 1975. Report of Performance Committee.

ITTC, 1978. Report of Performance Committee.

ITTC, 2014a. 1978 ittc performance prediction method. ITTC – Recommended Procedures and Guidelines 7, 5-02-03-01.4.

ITTC, 2014b. General guideline for uncertainty analysis in resistance tests. ITTC – Recommended Procedures and Guidelines 7, 5-02-02-02.

ITTC, 2014c. Ship models. ITTC – Recommended Procedures and Guidelines 7, 5-01-01-01.

ITTC, 2017. Uncertainty analysis in cfd verification and validation, methodology and procedures. ITTC - Quality System Manual Recommended Procedures and Guidelines 7, 5-03-01-01.

Katsui, T., Asai, H., Himeno, Y., Tahara, Y., 2005. The proposal of a new friction line. In: Fifth Osaka Colloquium on Advanced CFD Applications to Ship Flow and Hull Form Design, Osaka, Japan.

Korkmaz, K.B., Werner, S., Bensow, R., 2019a. Investigations for cfd based form factor methods. In: Numerical Towing Tank Symposium (NuTTS 2019).

Korkmaz, K.B., Werner, S., Bensow, R., 2019b. Numerical friction lines for cfd based form factor determination method. In: VIII International Conference on Computational Methods in Marine Engineering MARINE 2019.

Larsson, L., Stern, F., Visonneau, M., 2014. Numerical Ship Hydrodynamics: an Assessment of the Gothenburg 2010 Workshop. Springer. https://doi.org/10.1007/978-94-007-7189-5.

Lindgren, H., Dyne, G., 1980. Ship Performance Prediction. SSPA Publication No, p. 85.

Niklas, K., Pruszko, H., 2019. Full-Scale CFD Simulations for the Determination of Ship Resistance as a Rational, Alternative Method to Towing Tank Experiments. Ocean Engineering 190. https://doi.org/10.1016/j.oceaneng.2019.10643.

Pereira, F.S., Eça, L., Vaz, G., 2017. Verification and validation exercises for the flow around the KVLCC2 tanker at model and full-scale Reynolds numbers. Ocean. Eng. 129, 133–148. https://doi.org/10.1016/j.oceaneng.2016.11.005.

Ponkratov, D., 2016. 2016 workshop on ship scale hydrodynamic computer simulation. In: Ponkratov, D. (Ed.), loyd's Register Workshop on Ship Scale Hydrodynamics. https://doi.org/10.1016/j.oceaneng.2019.10643.

Prohaska, C.W., 1966. A Simple Method for the Evaluation of the Form Factor and Low Speed Wave Resistance. Proceeding of 11th ITTC.

Raven, H.C., van der Ploeg, A., Starke, A.R., Eça, L., 2008. Towards a cfd-based prediction of ship performance - progress in predicting full-scale resistance and scale effects. International Journal of Maritime Engineering Transactions of the Royal Institution of Naval Architects Part A.

SIMMAN, 2008. Simman 2008 Workshop Verification and Validation of Ship Manoeuvring Simulation Methods. http://www.simman2008.dk/KVLCC/KVLCC2/kvlcc2_geometry.html.

Sun, W., Qiong, H., Jia, S., Jie, X., Jinfang, W., Guofu, H., 2020. Numerical analysis of full-scale ship self-propulsion performance with direct comparison to statistical sea trail results. J. Mar. Sci. Eng. 8 https://doi.org/10.3390/jmse8010024. https://www.mdpi.com/2077-1312/8/1/24.

Terziev, M., Tezdogan, T., Incecik, A., 2019. A geosim analysis of ship resistance decomposition and scale effects with the aid of CFD. Appl. Ocean Res. 92 https://doi.org/10.1016/j.apor.2019.101930.

Toki, N., 2008. Investigation on correlation lines through the analyses of geosim model test results. J. Jpn. Soc. Nav. Archit. Ocean Eng. 8, 71–79.

Tokyo, 2015. Tokyo 2015 a Workshop on Cfd in Ship Hydrodynamics. https://t2015.nmri.go.jp/kcs.html.

Van, S.H., Ahn, H., Lee, Y.Y., Kim, C., Hwang, S., Kim, J., Kim, K.S., Park, I.R., 2011. Resistance characteristics and form factor evaluation for geosim models of KVLCC2and KCS. In: Advanced Model Measurement Technology for EU Maritime Industry.

Wang, J., Yu, H., Zhang, Y., Xiong, X., 2016. CFD-based method of determining form factor k for different ship types and different drafts. J. Mar. Sci. Appl. 15, 236–241.

Wang, J.B., Yu, H., Feng, Y., 2019. Feasible study on full-scale delivered power prediction using CFD/EFD combination method. J. Hydrodyn. 31 https://doi.org/10.1007/s42241-019-0075-4.

Wang, Z.Z., Xiong, Y., Shi, L.P., Liu, Z.H., 2015. A numerical flat plate friction line and its application. J. Hydrodyn. 23, 383–393.

Xing, T., Stern, F., 2009. Factors of safety for richardson extrapolation. Journal of Fluids Engineering-transactions of The Asme - J FLUID ENG 132, 65. https://doi.org/10.1115/1.4001771.

York, D., Evensen, N., Ló, M., Nez, M., De, J., Delgado, B., 2004. Unified equations for the slope, intercept, and standard errors of the best straight line. American Journal of Physics - AMER J PHYS 72. https://doi.org/10.1119/1.1632486.

Paper IV

Verification and Validation of CFD Based Form Factors as a Combined CFD/EFD Method

Journal of
Marine Science and Engineering

MDPI

Article

Verification and Validation of CFD Based Form Factors as a Combined CFD/EFD Method

Kadir Burak Korkmaz [1,2,*], Sofia Werner [1] and Rickard Bensow [2]

[1] SSPA SWEDEN AB, Chalmers Tvärgata 10, Box 24001, SE 400 22 Göteborg, Sweden; sofia.werner@sspa.se
[2] Department of Mechanics and Maritime Sciences, Chalmers University of Technology, SE 412 96 Göteborg, Sweden; rickard.bensow@chalmers.se
* Correspondence: burak.korkmaz@sspa.se

Abstract: Predicting the propulsive power of ships with high accuracy still remains a challenge. Well established practices in the 1978 ITTC Power Prediction method have been questioned such as the form factor approach and its determination method. This paper investigates the possibility to improve the power predictions by the introduction of a combined CFD/EFD Method where the experimental determination of form factor is replaced by double body RANS computations. Following the Quality Assurance Procedure proposed by ITTC, a best practice guideline has been derived for the CFD based form factor determination method by applying systematic variations to the CFD set-ups. Following the verification and validation of the CFD based form factor method in model scale, the full scale speed-power-rpm relations between large number of speed trials and full scale predictions using the CFD based form factors in combination with ITTC-57 line and numerical friction lines are investigated. It is observed that the usage of CFD based form factors improves the predictions in general and no deterioration is noted within the limits of this study. Therefore, the combination of EFD and CFD is expected to provide immediate improvements to the 1978 ITTC Performance Prediction Method.

Keywords: ship resistance; form factor; best practice guidelines; numerical friction line; combined CFD/EFD methods

Citation: Korkmaz, K.B.; Werner, S.; Bensow, R. Verification and Validation of CFD Based Form Factors as a Combined CFD/EFD Method. *J. Mar. Sci. Eng.* **2021**, *9*, 75. https://doi.org/10.3390/jmse9010075

Received: 27 December 2020
Accepted: 8 January 2021
Published: 13 January 2021

1. Introduction

During the design process of ships, power predictions are of utmost importance because the speed attained at a certain power consumption in a trial run, so called the contract speed, is specified at the contract of a new ship order. If the speed does not meet the specifications, the yard is forced to pay a penalty depending on the terms in the contract. Therefore, designers are under a pressure of being just in the limits. The dilemma for the designer and the yard as stated by Larsson and Raven [1] is that too optimistic predictions might end up in a big burden for the yard while too conservative predictions will be a lost order. In addition to increasing competitiveness of the market, legal authorities have also been taking steps towards further improvement of the energy efficiency of ships due to environmental concerns IMO [2]. Therefore, the importance of the power predictions and the required accuracy are increasing ever more.

The towing tank testing and extrapolation procedures have been used for more than a century to predict the performance of a ship in deep and calm water. The efforts to standardize and improve the early towing tank testing and extrapolation practices resulted in the foundation of the International Towing Tank Committee (ITTC) in 1933. The extrapolation of full scale ship resistance evolved in time, starting from a rather simple William Froude's method and going through several major revisions: adoption of using both Froude and Schoenherr lines in ITTC [3]; adoption of ITTC 1957 model to ship correlation lines [4]; recommendation of the Prohaska method [5] following the introduction of the form factor concept of Hughes [6]; adoption of the Bowden and Davison [7] formula in ITTC [8]; and

confirmation and integration of the previous concepts and formulas [4–7] via comparison of approximately one thousand sea trials to model test predictions in the formulation of the ITTC 1978 Power Prediction Method [9]. The roughness allowance was updated by replacing the previous formulation with Townsin and Dey [10] and introducing a new correlation allowance formulation in the ITTC Report of Power Performance Committee [11], and the calculation of air resistance was modified in the Revision 03 of the 1978 ITTC Performance Prediction Method [12]. The extrapolation procedures and towing tank tests are still considered as the last step of the performance prediction considering the current commercial tendencies and the evaluations such as EEDI calculations as enforced by IMO [2] where the applicable ships must go through the pre-verification by model testing during the design phase of a new ship.

Even though towing tank testing and extrapolation methods have been improved over many decades, there are inherent and well known shortcomings mainly because the Froude and Reynolds similarities cannot be fulfilled simultaneously, i.e., scale effects. Therefore, towing tank facilities must rely on experience obtained from large databases of model tests and sea trials. Computational fluid dynamics (CFD), however, can handle these scale effects and have been under development for more than a century as the advent of computational hydrodynamics dates back to 1898 by the work of Michell [13]. However, it was in 1980s when the "numerical methods to started to become really useful in ship design" Larsson [14] (p. 2). The development of the Reynolds Averaged Navier–Stokes (RANS) methods have been evaluated since 1980 [15] and the verification and validation (V&V) of CFD methods in model scale is now a well established practice. According to the statistics presented in Hino et al. [16], the mean absolute comparison error of JBC is around 2% for the towed cases (resistance) and 3% for the self-propulsion, while the standard deviation is approximately 2% and 4%, respectively. It is noticeable that no further reductions neither in comparison error nor in scatter were obtained at the 2015 Workshop [16] compared to the 2010 Workshop [15]. Unlike in model scale, the accuracy of CFD on prediction of full scale performance is still under concern mainly due to scarcity of the full scale validation data in the literature and limited CFD studies. Recently, studies presented by Sun et al. [17] and Niklas and Pruszko [18] showed that full scale simulations can predict the power similar to or better than the towing tank tests. On the other hand, the results of Lloyd's Register workshop on ship scale hydrodynamics [19] indicated that differences between the numerical setups can lead to very diverse predictions on both power and propeller turning rate.

Instead of choosing between towing tank testing (EFD) and computational hydrodynamics (CFD), a combination of the two methods can be a feasible solution to increase the accuracy of the power predictions. As identified by the ITTC Specialist Committee on the Combined CFD/EFD Methods, if a part of the model testing or extrapolation procedure causes higher uncertainty than the numerical uncertainty and modeling errors of the CFD applications, the accuracy is expected to increase. In the 1978 ITTC Performance Prediction method [20], the form factor approach is identified as a major uncertainty source due to its determination method, i.e., the Prohaska Method [5], and the scale effects when the ITTC-57 model to ship correlation line is used [21–28]. The study performed by Wang et al. [29] showed that when the Prohaska Method is replaced by CFD based form factors in the ITTC-78 Power Prediction Method, the sea trials correlated better for a ship. As it is the case for the direct full scale CFD predictions, the CFD/EFD combined methods were applied to only a limited number of cases. Therefore, this paper aims to address this issue by investigating the verification and validation of the CFD based form factor approach in model scale and by comparing large number predictions using combined CFD/EFD methods to sea trials.

Verification and validation of CFD codes and methods are essential measures not only for the improvement of the CFD methods, but also the quality assurance of the CFD applications. It requires significant computational resources and validation data with an experimental uncertainty at hand. Since the derived uncertainty levels are only valid for a

unique case and condition, each test case should be subjected to V&V studies in order to ensure the quality of the CFD application. However, thorough verification studies cannot be performed for each commercial application for practical reasons and experimental uncertainty analysis is not available in advance. This raises the question on whether a V&V result is valid for a similar case and also if it is required to be done only once. Therefore, a practical procedure is needed for the organizations that regularly perform CFD predictions for similar cases. To respond to this need, two ITTC committees jointly proposed a new procedure for the quality assurance comprised of the following parts: (1) requirement of an organization's Best Practice Guideline (BPG), (2) Quality Assessment (QA) of the BPG methodology, and (3) demonstration of quality. This paper will follow the proposed Quality Assurance Recommended Procedures when demonstrating the application of the CFD based form factors. For the first time in the literature, the practicality and usefulness of the proposed QA procedure will be tested for the quality assurance of CFD based form factor method and are presented in the following steps:

1. Detailed explanation of the flow solver, numerical methods, boundary conditions, grid generation, and computational conditions are presented in Section 3 and the derivation of the BPG for the SHIPFLOW code by systematically varying the CFD set-up such as grid dependence studies in Section 5.1, y^+ in Section 5.1.1, additional grid refinements in Section 5.1.2, domain size in Section 5.1.3, model scale speed in Section 5.1.4, and turbulence models in Section 5.1.5.
2. Verification and validation of the CFD based form factors of six test cases in model scale is presented in Section 5.1.6.
3. Comparison of up to 78 sea trials to the predictions made by combined CFD/EFD methods is presented in Section 6.

Through these steps, the following research questions are aimed to be answered by this study:

- Can the proposed quality assurance procedure be used to to ensure the predicted form factors are suitable for full scale predictions?
- Can CFD based form factors introduce immediate improvements to the existing ITTC-78 method?
- Can there be further improvements to the full scale predictions by further modification of ITTC-78 method such as the change of the friction line in combination with CFD based form factors?

2. Extrapolation of Model Tests to Full Scale

In this study, the procedure recommended by ITTC [20] is used to extrapolate the towing tank test results to full scale. According to the 1978 ITTC Performance Prediction Method [20], the resistance of the full scale ship is calculated as

$$C_T = (1+k)C_{FS} + \Delta C_F + C_A + C_R + C_{AAS}, \quad (1)$$

where k is the form factor, C_{FS} is the frictional resistance coefficient in full scale (the subscript 'S' signifies the full scale ship), C_R is the residual resistance coefficient, ΔC_F represents the roughness allowance, C_A is the correlation allowance, and C_{AAS} is the air resistance coefficient.

According to the recommended procedure [20], the form factor is obtained by the Prohaska method [5] in model scale. The residual resistance, which is assumed to be the same in model and full scale, is then obtained as

$$C_R = C_{TM} - (1+k)C_{FM}, \quad (2)$$

where C_{TM} is the total resistance coefficient (the subscript 'M' signifies the model). C_{TM} is measured at each speed in the towing tank, and C_{FM} is obtained from the friction lines. In the study, two form factors were obtained from the Prohaska method and CFD based

form factor determination methods. The latter method follows the assumptions of [6] and is derived using the relation:

$$(1+k) = \frac{C_F + C_{PV}}{C_{FM}} = \frac{C_V}{C_{FM}}, \quad (3)$$

where the frictional resistance coefficient (C_F) and viscous pressure coefficient (C_{PV}) are obtained by the double body CFD simulation. C_{FM} in the denominator of Equation (3) is the equivalent flat plate resistance in two-dimensional flow obtained from the same Reynolds number as the computations. When the CFD based form factor determination is used, C_{FM} in Equation (3), C_{FM} in Equation (2) and C_{FS} in Equation (1) are derived from the same friction line.

The frictional resistance coefficients of the ship, C_{FM} and C_{FS}, are obtained by using three different friction lines: the ITTC-57 model-ship correlation line [4], and two numerical friction lines for EASM and $k-\omega$ SST turbulence models, respectively, proposed by Korkmaz et al. [30].

Correlation factors for the extrapolation were separated from the roughness allowance by ITTC [11] and the formulation of Bowden and Davison [7] is replaced by Townsin and Dey [10]. The correlation allowance recommended by the 19th ITTC is

$$C_A \approx (\Delta C_F)_{\text{Bowden}} - (\Delta C_F)_{\text{Townsin}} = 5.68 - 0.6\log(Re) \times 10^{-3}, \quad (4)$$

where $(\Delta C_F)_{\text{Bowden}}$ is the roughness allowance proposed by Bowden and Davison [7], and $(\Delta C_F)_{\text{Townsin}}$ [10] is the recommended roughness allowance in the present recommended procedures [20]. Note that, if the recommended C_A in Equation (4) is used for the extrapolation, summation of $(\Delta C_F)_{\text{Townsin}}$ and C_A is essentially the same as using the old formulation of roughness allowance proposed by Bowden and Davison [7], i.e., the original 1978 ITTC method. As an option, it was recommended in the ITTC Report of Power Performance Committee [11] that each institution maintains their own C_A formulations. However, a certain reluctance can be expected from towing tanks to change the C_A value since it would require a substantial amount of work and risk-taking to derive new model-full scale correlations that are derived from a consistent model testing and extrapolation practices. Therefore, in the context of this study, C_A used for the extrapolations is the recommended correlation factor in Equation (4). As explained in Section 6, C_A is omitted in calculation of the full scale resistance when the numerical friction lines are used as $(\Delta C_F)_{\text{Bowden}}$ "is suitable when extrapolating resistance using the 1957 ITTC line on a form factor basis..." Bowden and Davison [7].

For the cases when a flow separation is observed in model scale CFD computations, an additional computation has been performed also in full scale. The extrapolation method is slightly altered to mitigate the adverse effect of the flow separation which causes an overestimation of the full scale viscous resistance. In the altered method, the residual resistance is obtained by using the model scale form factor as in Equation 2, but the viscous resistance of the full scale ship ($(1+k) \times C_{FS}$) is calculated by the form factor obtained from the full scale double body computations.

3. Flow Solver, Grid Generation, Computational Domain, and Boundary Conditions

The XCHAP module of SHIPFLOW 6.5 is used for solving the steady state viscous flow [31]. Reynolds Averaged Navier–Stokes (RANS) equations are solved with a finite volume method. The first order accurate Roe scheme is used for discretization of the convective terms and a flux correction is applied explicitly in order to increase the order of accuracy. The equations are solved with a Krylov solver (adopted from PETSc) which implements the Generalized Minimal Residual method (KSPGMRES). Two turbulence models are available in XCHAP solver: EASM as described by Deng and Visonneau [32] and $k-\omega$ SST as described by Menter [33]. Both turbulence models are used in this study.

The viscous flow solver XCHAP can only handle structured grids, which can be in H-H, H-O, or O-O topologies. Although it is possible to import external grids to the

solver, the grid generator of SHIPFLOW, XGRID, is used for the study. The coarsest body fitted grid used for the study is presented in Figure 1. The parametrized nature of grid generation with XGRID ensures almost identical grid distribution in the longitudinal and circumferential directions for the most conventional hulls simulated. However, the grid distribution in the normal direction to the hull varies between different hulls as the *Re* differs; therefore, different first cell sizes in the normal direction to the wall and cell growth ratios are obtained to achieve (nearly) the same y^+ values. The overlapping grid technique is used to model the flow around the rudders [34] and to apply refinement on the single block of structured grid. As can be seen in Figure 1b, a refinement is applied to the region within the black line boundaries. The refinement does not improve the geometry resolution but only divides the existing cells into two or more pieces in desired directions [31]. In this study, the refinements are applied in all directions and the cells are divided in two. All simulations in this study were performed as double body computations with rudders that are integrated into the flow domain with an overlapping grid technique as seen in Figure 1b.

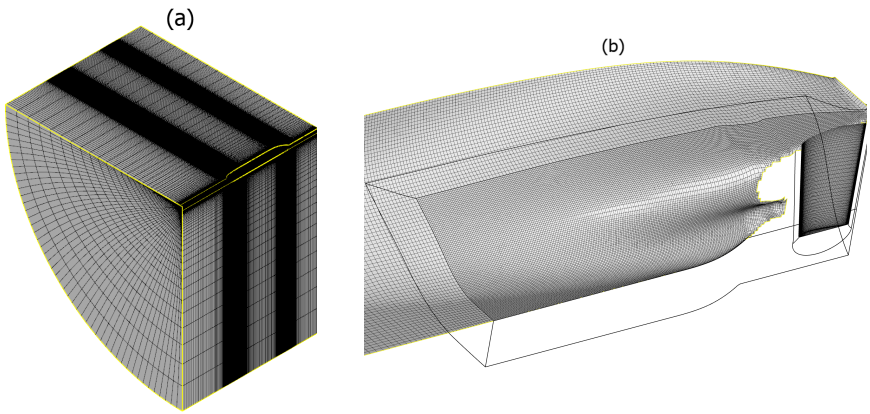

Figure 1. (**a**) Grid distribution of the coarsest grid, (**b**) grid refinement at the stern and the rudder as overlapping grids.

The computational domain is shaped as a quarter of a cylinder that consists of six boundaries where the center plane of the ship is set as the symmetry boundary condition. By default, the distance between inlet and fore-perpendicular (FP) is $0.5L_{PP}$, outlet plane is located at $0.8L_{PP}$ behind the aft-perpendicular, and the radius of the cylindrical outer boundary is $3L_{PP}$.

Two boundary conditions are used: Dirichlet and Neumann conditions. Boundary types employed in XCHAP are noslip, slip, inflow, outflow, and interior. Inlet boundary condition sets a fixed uniform velocity (U_∞), the estimated turbulent quantities and a zero pressure gradient normal to the inlet boundary. The turbulent quantities, specific turbulent dissipation rate, and turbulent kinetic energy at the inlet are estimated as

$$\omega_{inlet} = \lambda U_\infty / L \,, \tag{5}$$

$$k_{inlet} = \mu \omega_{inlet} C_i / \rho \,, \tag{6}$$

where the factor of proportionality, λ, is set to $\lambda = 10$, L is the reference length, μ represents the dynamic viscosity, and ρ is the water density and constant $C_i = 1 \times 10^{-4}$. Outflow condition only consists of a Neumann boundary condition that sets the gradient of velocity, turbulent kinetic energy, and pressure to zero, normal to the outflow plane. Slip condition is similar to a symmetry condition where the normal velocity and normal gradient of other variables are set to zero. No-slip condition specifies the velocities components, turbulent

kinetic energy, and normal pressure component as zero at the wall. The ω on the wall for a smooth surface is specified as described by Hellsten [35]:

$$\omega_w = \frac{u_\tau^2}{\nu} \times \left(\frac{50}{4.3(y^+)^{0.85}} \right)^2, \quad (7)$$

where u_τ is the friction velocity and ν is the kinematic viscosity. Since no wall-functions are used in XCHAP, all simulations were performed with the wall resolved approach.

4. Test Cases and Computational Conditions

Fourteen common cargo vessels having a model test and full scale speed trial results are used as test cases. As the speed trials of some vessels were carried out at more than one loading condition, the total number of tests cases are 18. The L_{PP} of the vessels are ranging from 200 m to 355 m, block coefficients (C_B) vary between 0.5 and 0.84, and the Froude numbers (the achieved speed at 75% MCR) are covering the range of 0.14 to 0.23. The vessels are built in series and speed trials were performed for each sister ship. The data set consists of 78 sea trials in total. The trial measurements were conducted by the yards and analyzed by SSPA with an in-house software according to ITTC Recommended Procedures and Guidelines for Preparation, Conduct and Analysis of Speed/Power Trials [36] and ISO Ships and marine technology—Guidelines for the assessment of speed and power performance by analysis of speed trial data [37]. The trials fulfill the ISO 15016/ITTC limits on weather condition. The corresponding model tests were conducted at SSPA.

The model tests corresponding to the speed trials were performed at SSPA's towing tank (260 m long, 10 m wide and 5 m deep). The models were made of the plastic foam material Divinycell, and they were manufactured with a 5-axis CNC milling machine at SSPA. A trip wire is mounted at 5% of L_{PP} aft from the fore perpendicular for the turbulence stimulation. All hull models are equipped with a dummy propeller hub and a rudder (two rudders for twin skeg hulls) for the resistance tests. The computational conditions for each test case are replicating the same conditions as in the corresponding towing tank tests such as the non-dimensional quantities, Re and Fn, loading condition, and geometrical features.

5. Best Practice Guidelines and the Quality Assurance of the CFD Based Form Factor Methodology

The proposed ITTC QA procedure consists of three steps, the first one being derivation of a Best Practice Guideline. In this section, the derivation of a best practice guideline for the CFD based form factors will be presented. Considering the plethora of numerical methods and possible CFD set-ups, it is not possible to formulate a general standard procedure for CFD-work that is generally applicable to all codes and cases [28]. Instead, each organization is required to formulate their own process (BPG) and assess its suitability for a specific application.

In order to derive the best practice guidelines for the determination of form factor using the SHIPFLOW code, CFD setups were varied systematically and verification and validation of the predicted form factors were performed. Since the validation is a key factor for the evaluations, the hulls were selected on the basis that experimentally determined form factors are suitable for the Prohaska method (i.e., C_T/C_{FM} values are fairly linear as presented in Section 5.1.6). The analysis is based on 300 double body simulations of the six test cases consisting of four hulls (H1, H2, H3, and H4) out of which one is in three different loading conditions (indicated as H2-b, H2-d, H2-s). The variations applied to the CFD set-ups are explained in Sections 5.1.1–5.1.6.

5.1. Grid Dependence Study

Grid dependence studies were performed to quantify the numerical uncertainty (U_{SN}). Four geometrically similar grids were generated for each test case. The simulations were performed in double precision in order to eliminate the round-off errors. The iterative uncertainties were quantified by the standard deviation of the force in percent of the

average force over the last 10% of the iterations. Iterative uncertainty for C_F and C_{PV} were kept below 0.01% and 0.20% for all simulations except two computations where mild separation is observed at the stern, and standard deviations are 3 to 4 times higher than the rest of the simulations. Considering the small standard deviations in both resistance components, it was assumed that the numerical errors are dominated by the discretization errors and both iterative errors and round-off errors are neglected. The procedure proposed by Eça and Hoekstra [38] was used to predict the grid uncertainties which are presented for the finest grid as a ratio of the computed value ($U_{SN}\%S_1$) in Table 1.

Table 1. Estimated numerical uncertainties of SHIPFLOW in model scale for EASM and $k-\omega$ SST turbulence models, in a percentage of the computed result of the finest grid, S_1.

$U_{SN}\%S_1$	Turb. Model	H1	H2-b	H2-d	H2-s	H3	H4
C_F	EASM	1.2	0.6	1.3	1.1	1.1	4.5
	$k-\omega$ SST	1.5	0.7	0.5	1.2	1.3	1.0
C_{PV}	EASM	37.2	4.1	52.6	20.1	7.8	13.2
	$k-\omega$ SST	61.2	4.1	52.9	20.7	9.1	8.2
C_V	EASM	6.9	1.1	10.6	4.7	2.2	6.0
	$k-\omega$ SST	10.2	1.1	9.5	4.8	2.5	2.2

Numerical uncertainty of the viscous resistance is predicted by a combination of the frictional and viscous pressure resistance components ($U_{C_V} = U_{C_F} + U_{C_{PV}}$) as C_V is not directly computed. As seen in Table 1, grid uncertainties on C_F mostly vary between 0.6 to 1.5 percent of the computed result of S_1. The grid uncertainty on C_{PV} varies greatly between different hulls. As a result of the large fluctuations in the C_{PV}, the grid uncertainty on the viscous resistance coefficient varies between 1.1% and 10.2%. The reason for the large fluctuation in the grid uncertainties is explained by the scatter in the computed values which strongly penalizes the estimated uncertainties [38]. Computed values for C_F, C_{PV} and C_V are presented in Figure 2 in a percentage of the result of the finest grid which has approximately 10M cells (N_{grid}). As seen in Figure 2, a majority of the C_F and C_{PV} values shows somewhat oscillatory behavior, which is observed significantly more for the latter. The fluctuations stems mostly from the grid generation strategy, which is a structured grid with a stair-step profile in the stem and stern profiles. As the curvature around the bulb changes rapidly, the structured grid that captures the profile of the bulb changes abruptly with changing grid. As a result, the computed quantities are influenced by the such variations. Considering the tip of the bulb where the stagnation point is often situated and followed by a steep pressure gradient, it is expected that C_{PV} will be influenced more than C_F as observed in Figure 2.

The estimated numerical uncertainties shown in Table 1 do not indicate a particular trend for a specific ship type or loading condition. Even though U_{SN} varies significantly between the test cases due to the drawbacks of the grid generation, its reflection on C_V is limited and the variation on the predicted form factors is rather small, especially between the finest two grids. Therefore, the g_2 grid settings have been chosen as a baseline for the rest of the BPG investigation since the grid cell count were reduced to approximately 7 million, and computational time was shortened compared to the finest grid.

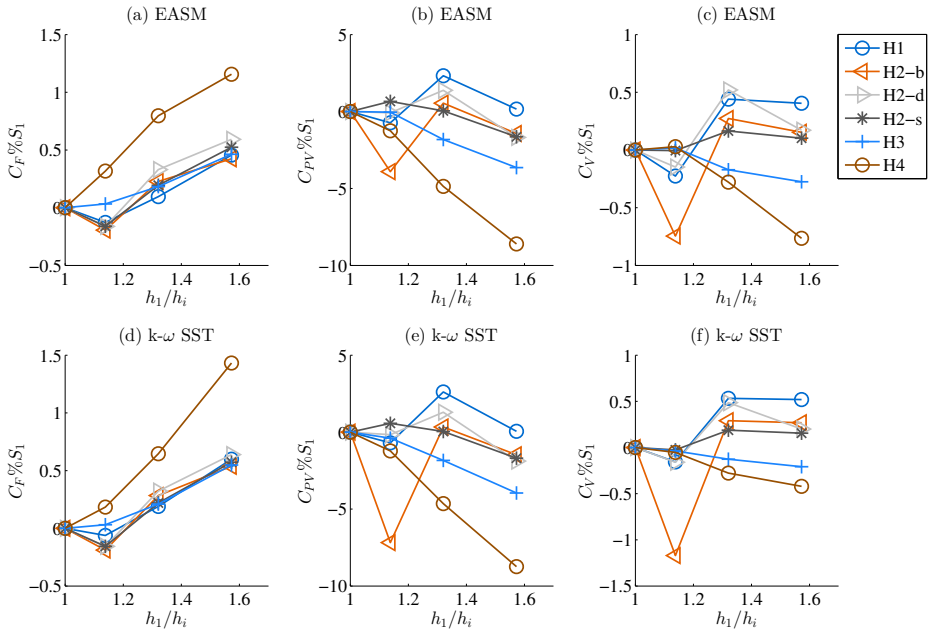

Figure 2. Computed values for (**a**) C_F, (**b**) C_{PV} and (**c**) C_V with the EASM model and (**d**) C_F, (**e**) C_{PV} and (**f**) C_V with the $k-\omega$ SST model vs. grid refinement ratio, $h_1/h_i = \sqrt[3]{N_{grid_1}/N_{grid_i}}$.

5.1.1. Variation of the First Cell Size Normal to the Wall, i.e., y^+ Variation

It is essential to calculate the wall shear stresses accurately as the resistance of a ship at model scale is often dominated by the frictional resistance component. Previous studies performed with SHIPFLOW and other codes [28,39,40] showed that computation of the frictional resistance component is rather sensitive to the turbulence model, and the first cell size normal to the wall. In order to investigate both of them, the second finest grid (g_2) is selected as a reference point since the differences between the g_1 (finest grid) and g_2 in C_V were less than 0.2% (except for one hull). Keeping the same number of cells as g_2 in all directions and the position of no-slip grid points identical in longitudinal and circumferential directions, the height of the first cell in the normal direction to the wall was varied. These variations were performed for all test cases using EASM and $k-\omega$ SST turbulence models.

The height of the first cell normal to the wall is non-dimensionalized as $y^+ = (u_* y)/\nu$, where y is the height of the first cell and ν is the kinematic viscosity. In SHIPFLOW, the average y^+ is calculated by arithmetic mean

$$(y^+)_{avg} = \frac{1}{N_{grid}} \sum_{i=1}^{N_{grid}} y_i^+ \,. \tag{8}$$

The height of the first cells for all test cases are adjusted to cover a wide range of $(y^+)_{avg}$ including the values exceeding the recommended $y^+ < 1$ for the wall resolved approach. The results of the y^+ variations are presented in Figure 3 as the comparison error of form factors

$$E\%D = (D - S)/(D + 1) \times 100 \tag{9}$$

where D is the experimentally determined form factor (using the Prohaska method), and S denotes the CFD based form factor based on the ITTC-57 line. The comparison error

shows a consistent ±2.5% of spread throughout the $(y^+)_{avg}$ range of 0.1 to 1.5. When the fitted curve to all the computed results (dashed black line) is considered, the average $E\%D$ converges to zero as the $(y^+)_{avg}$ gets smaller, and it is nearly constant for the simulations performed where $(y^+)_{avg} < 0.5$. The mean comparison error for the computations where $(y^+)_{avg} \approx 1.5$ is the largest, as expected, since the non-dimensional height y^+ is required to be lower than 1 for the wall resolved approach. However, the $E\%D$ of the simulations with $(y^+)_{avg} \approx 0.75$ and $(y^+)_{avg} \approx 1$ are also in an increasing trend. As presented in Figure 4, the histogram of the acquired y^+ values for the six different first cell heights for the H3 hull reveals that achieving $(y^+)_{avg} < 1$ does not guarantee that all (or most) of the y^+ values will be also below 1. As seen in Figure 4, 3%, 35% and 60% of the no-slip cells have y^+ values are higher than 1 for the simulations that resulted in $(y^+)_{avg}$ of 0.5, 0.73, and 0.95, respectively. Considering the histogram plots of y^+ values of the other test cases as well, it is recommended that the target $(y^+)_{avg}$ should be smaller than 0.5 in order make sure that nearly all the y^+ values will be smaller than 1.

As observed in Figure 3, CFD based form factors are heavily dependent on the choice of the turbulence model. The form factors obtained by the $k-\omega$ SST model are consistently 1.5 to 2.5 percent higher than what is achieved with EASM, mainly as a result of the calculated C_F being approximately 3% higher with the $k-\omega$ SST model than the EASM for the same grid. These trends are noticeably consistent within the range of $0.1 < (y^+)_{avg} < 1$. Therefore, if the $(y^+)_{avg}$ is smaller than 0.5, the modeling error is dominated by the choice of turbulence model.

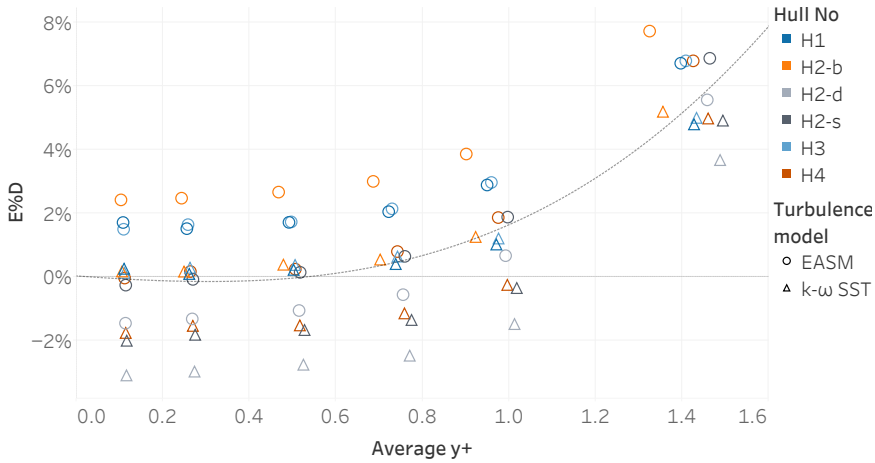

Figure 3. Comparison error of all test cases for average y^+ variation.

5.1.2. Variation of Refinement Region

Using the overlapping grid technique, the single block grid describing the flow domain can be effectively refined as explained in Section 3. As shown in Figure 5, three geometrically similar refinement regions (R1, R2, and R3) are determined for all test cases. The refinements are applied to the g_2 grid of each test case presented in Section 5.1. The starting and ending boundaries of the refinement regions are positioned at the same longitudinal position (with respect to L_{PP} of each hull) relative to the aft perpendicular. The smallest refinement limits in the circumferential and normal directions are determined with respect to the propeller diameter to be able to encapsulate the *nominal wake*, i.e., flow field at the propeller plane without the presence of the propeller.

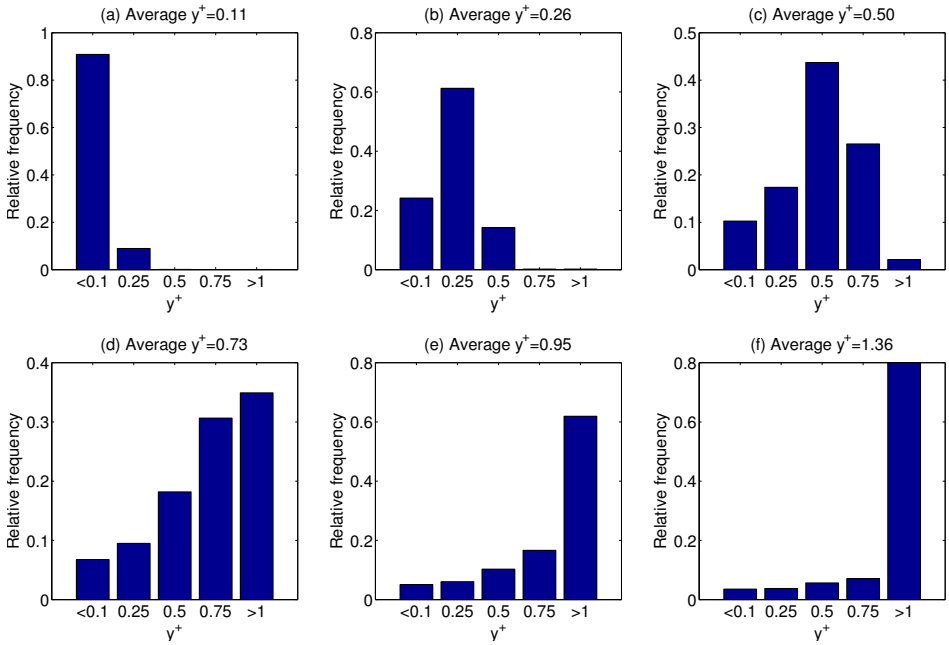

Figure 4. The histogram of the acquired y^+ values for the H3 hull for the average (**a**) $y^+ = 0.11$, (**b**) $y^+ = 0.26$, (**c**) $y^+ = 0.50$, (**d**) $y^+ = 0.73$, (**e**) $y^+ = 0.95$ and (**f**) $y^+ = 1.36$.

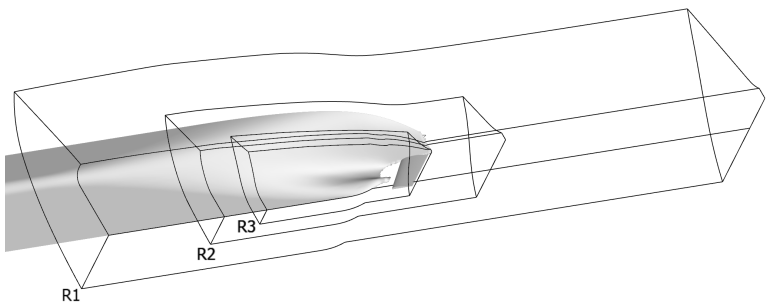

Figure 5. Systematic refinement variation in three steps for R1, R2, and R3 regions.

As observed in Figure 6, the comparison error of the form factor remains relatively unchanged between the grids without refinement (computations with 7M grid cells) and the grids with different refinement regions (shown in Figure 5). The regression lines are fitted to computations of each test case. As seen in Figure 6, the steepest line belongs to the H4 hull where a mild flow separation at the bilge of the gondola (i.e., lower part of the stern bulb) is observed. In this case, the varying refinement regions had a somewhat noticeable effect on the local flow as well as the computed resistance components. However, the variations in C_F, C_{PV} and C_V are well within the grid uncertainties reported in Table 1 for all hulls. Therefore, it is concluded that, for the purpose of obtaining CFD based form factors, g_2 (the baseline) is fine enough for all test cases, and no further grid refinements are required.

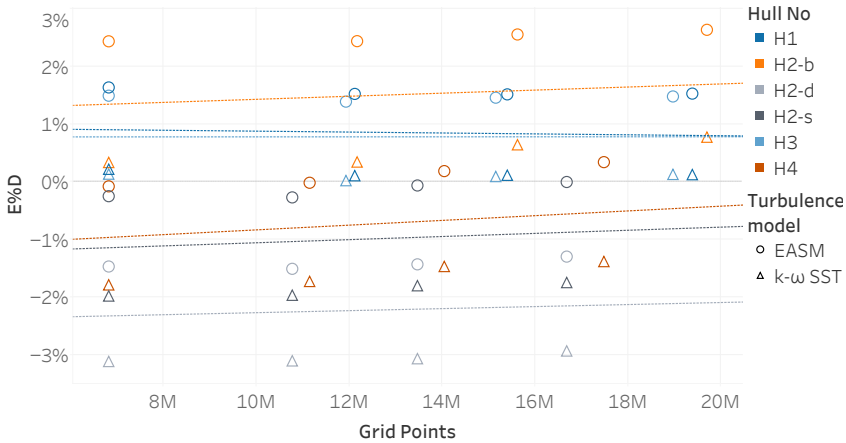

Figure 6. Comparison error of all test cases for the refinement region variation.

5.1.3. Domain Size Variation

The size of the domain was varied from the default settings where the distance between inlet and fore-perpendicular (FP) is $0.5L_{PP}$ (denoted as U/L_{PP}), outlet plane is located at $0.8L_{PP}$ behind the aft-perpendicular (denoted as W/L_{PP}), and the radius of the cylindrical outer boundary is $3L_{PP}$ (denoted as N/L_{PP}). The default domain size is increased in two steps by changing the distance of only one part (either U/L_{PP}, W/L_{PP} or N/L_{PP}) and keeping the rest the same. When a part of the domain is changed (for example U/L_{PP}), the number of cells are also changed with the same ratio in that region (e.g., number of cells are doubled when the distance is doubled), while the rest of the domain (in this example W/L_{PP} or N/L_{PP}) parameters and the grid cells within the coverage of the unchanged domain are kept identical. In this way, errors due to the discretization is aimed to be kept similar to the baseline grid (g_2).

The distance between the outlet plane and the aft-perpendicular (W/L_{PP}) is varied between 0.8 and 2.4. The variations of C_F due to changing W/L_{PP} are smaller than 0.03% which is more than one order smaller than the numerical uncertainties shown in Table 1. The calculated viscous pressure resistance component increased up to 2% with respect to the base line. Investigations in the modified part of the flow domain showed that the traces of the wake of the hulls are reaching the outlet boundary in most of the test cases. However, when the outlet boundary moved further away from the hull (W/L_{PP} = 1.6 and 2.4), the wake almost completely dissipated and diffused into the free stream. The difference in C_V for all test cases varied between 0.1 to 0.4%, and, therefore, it is concluded that the Neumann boundary condition at the outlet boundary worked satisfactorily to handle the wake reaching the outlet plane. The resulting changes can be seen in Figure 7b where the predicted form factors are rather insensitive to the W/L_{PP} change regardless of the turbulence model used.

The radius of the cylindrical domain varied between $N/L_{PP} = 3$ to 5. Similar to the W/L_{PP} variations, the change in the frictional resistance component is limited (up to 0.2%) and approximately one order smaller than the numerical uncertainties on Cf. The change in the C_{PV} and C_V is also comparable for N/L_{PP} and W/L_{PP} variations. Considering the insignificant variation in form factor predictions as seen in Figure 7c and already having much smaller blockage effect (ratio between mid-sectional area of the hulls and the towing tank section area) in CFD compared to towing tank, the domain size of the baseline grid (N/L_{PP} = 3) is found to be large enough.

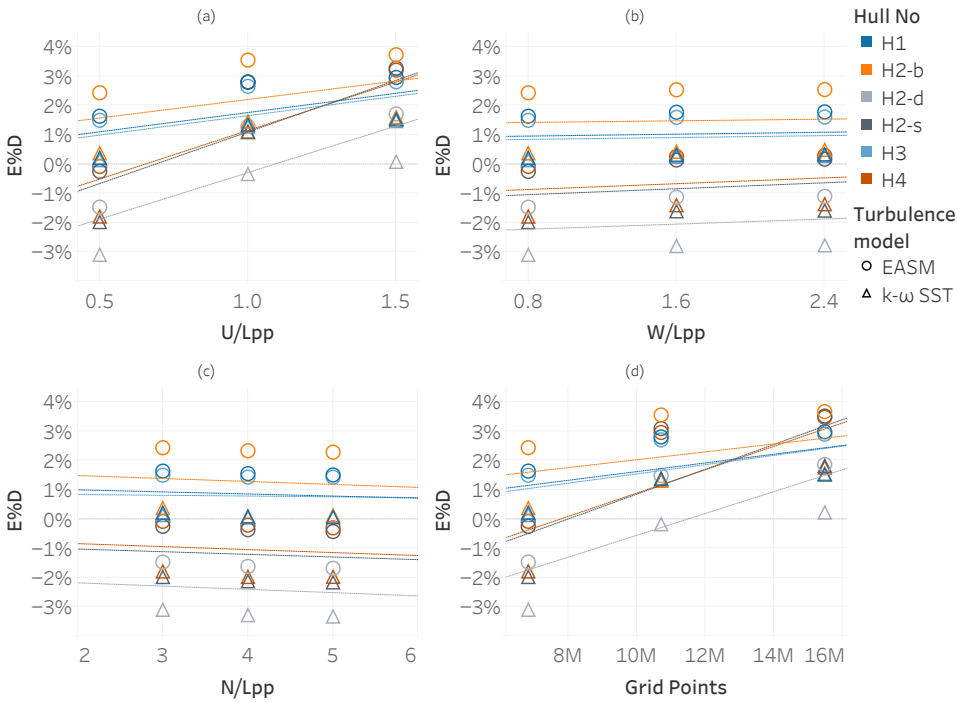

Figure 7. Comparison error of all test cases for the domain size variations: (**a**) U/L_{PP}, (**b**) W/L_{PP}, (**c**) N/L_{PP}, (**d**) in all directions.

The distance between the inlet and the fore-perpendicular (U/L_{PP}) is varied between 0.5 and 1.5. Contrary to the previously mentioned parts of the domain (N/L_{PP} and W/L_{PP}), the choice of the inlet plane location had prominent implications both on the local flow and the resistance components. The analysis performed on all test cases indicated that the significant changes between different U/L_{PP} values are mainly due to the differing turbulence intensity reaching the hull. As explained in Section 3, the specific turbulent dissipation rate and turbulent kinetic energy (TKE) are set at the inlet plane for each hull regardless of the distance between inlet boundary and the FP (see Equations (6) and (7)). As a result, the TKE reaching the hulls decreased since the TKE is dissipated more by traveling greater distances with the increasing U/L_{PP}. The reduced turbulence intensity in the free stream arriving to the hulls caused a significant drop in C_V varying between 1.3% to 3.5%. The contribution of the frictional and viscous pressure resistance to the reduced viscous resistance is nearly equal for all cases. As seen in Figure 7a, the comparison errors in form factors are highly dependent on the U/L_{PP}.

In addition to commonly known modeling errors such as turbulence modeling, the transition from laminar to turbulent flow is also considered for this study. Contrary to the common perception, the flow in a typical model scale RANS computation with a wall resolved approach is *not* fully turbulent in the boundary layer even with the commonly used turbulence models (i.e., without transition models). The analysis performed on infinitely thin 2D flat plates by Eça and Hoekstra [39] and Korkmaz et al. [30] indicated that, even though the correct position of the transition could not be predicted using ordinary turbulence models such as k-omega SST [33] and EASM [32], the transition occurs qualitatively rather accurately. In order to show if this is the case also for the hulls, local skin friction coefficient, C_f is calculated for baseline grid of each test case as

$$C_f = \frac{\mu\left(\frac{\partial u_x}{\partial y}\right)_{y=0}}{\frac{1}{2}\rho U_\infty A}, \tag{10}$$

where $\left(\frac{\partial u_x}{\partial y}\right)_{y=0}$ is the velocity gradient at the wall and A is the wetted surface of the hull. The velocity gradients of the cells in the same x-position were summed, and all no-slip cells are included in the calculation of the local skin friction coefficient.

In Figure 8, the local skin friction coefficient of all test cases are presented together with the Blasius solution [41] for the reference of the friction coefficient of the laminar flow, Prandtl–Schlichting formula [41] for the fully turbulent flat plate skin friction coefficient, and the numerical friction line [30] for the EASM turbulence model derived using SHIPFLOW.

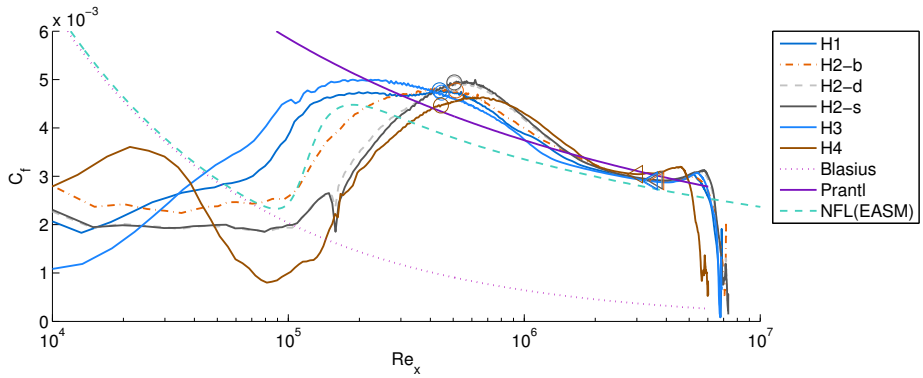

Figure 8. Local skin friction resistance coefficients for all hulls versus Reynolds number.

As seen in Figure 8, C_f of all test cases are even below the Blasius line before $Re < 4 \times 10^4$. However, C_f values are steeply increasing approximately between $Re = 7 \times 10^4$ and $Re = 1.5 \times 10^5$ where the numerical friction line is also showing remarkably similar increase from laminar regime towards turbulent. The C_f values of each test case are expected to have some quantitatively and qualitatively differences both among themselves and the friction lines (Blasius, Prandtl–Schlichting, and NFL) since each hull shape is unique and the flow is not under zero-pressure-gradient. However, it can be argued that the flow is not fully turbulent in all parts of the hull in the computations as it may be also the case for the towing tank tests. To make sure that turbulent flow is achieved in the model tests, turbulence simulators are attached to the hull. The model tests used for all the test cases in this study also utilized turbulence stimulators placed at 5% of the L_{PP} from the fore perpendicular. In Figure 8, these locations are marked with circles. It is ensuring to observe that the flow in CFD transitioned into turbulent flow before the position of the turbulence stimulators. In the previous studies with flat plates [30,39], the Reynolds number where transition occurred was found to be dependent on the choice of turbulence model and turbulence intensities. Additionally, different CFD solvers (SHIPFLOW and FINEMARINE) using the same grid also led to not only different transition behaviors but also significantly different C_f values in the turbulent region [30]. Therefore, it is recommended to adjust the turbulence intensities for each code and the turbulence model when the wall resolved approach is used for making sure the flow characteristics are similar in CFD to the experiments.

In order to investigate the effect of varying turbulence intensities, the local skin fiction coefficient of the H1 hull is presented in Figure 9a for U/L_{PP} = 0.5, 1 and 1.5. C_f of all U/L_{PP} values seem to be nearly identical in Figure 9a except where the C_f is steeply increasing, i.e., transition of the flow. In order to visualize the differences in more detail,

C_f of the U/L_{PP} = 1 and 1.5 are plotted relative to C_f of the baseline domain. As seen in Figure 9b, the C_f[%] values are differing the most at the position where transition from laminar to turbulent flow occurs. In the laminar and turbulent regions, C_f values are nearly uniformly 0.7% and 0.8% less for U/L_{PP} = 1 and 1.5 compared to U/L_{PP}=0.5. The local viscous pressure resistance component also decreased with the lower turbulence intensity but not as uniformly as is the case for C_f. The local viscous pressure resistance coefficient, C_{pv}, of U/L_{PP} = 1 and 1.5 was predominantly lower in the laminar parts of the hull and at the stern region that is covered by the boundary layer.

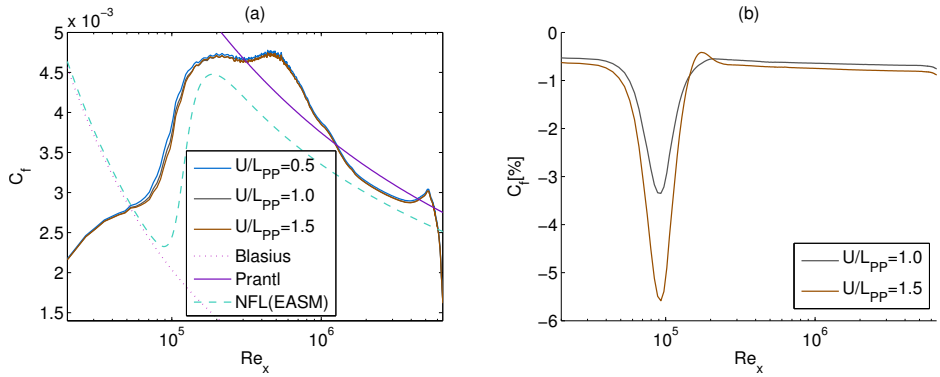

Figure 9. (**a**) Comparison of the local frictional resistance coefficients of H1 hull for the domain size variation in U/L_{PP} and (**b**) comparison of C_f of H1 hull relative to U/L_{PP} = 1.

In the final step, the domain size is varied in all directions (U/L_{PP}, N/L_{PP} and W/L_{PP}) at the same time in two steps. Starting from the baseline grid (U/L_{PP} = 0.5, W/L_{PP} = 0.8 and N/L_{PP} = 3), the boundaries in all directions are first moved to U/L_{PP} = 1.0, W/L_{PP} = 1.6 and N/L_{PP} = 4 and then U/L_{PP} = 1.5, W/L_{PP} = 2.4 and N/L_{PP} = 5 for all test cases. The number of cells are also increased proportionally in the region where the domain size is enlarged. As seen in Figure 7d, the resulting form factors due to varying the domain size in all directions are nearly the same with the domain size variation only in U/L_{PP} as seen in Figure 7a. As a result, the turbulence intensities are playing a more significant role in terms of modeling errors than the wake reaching the outlet plane and the blockage effect. The default domain size gives the smallest comparison error on average, and it is concluded that further enlarging the domain is not necessary.

5.1.4. Variation of the Model Scale Speed

The previous CFD studies presented by Raven et al. [42], Wang et al. [25], Dogrul et al. [26], Korkmaz et al. [27], Terziev et al. [24], Van et al. [43], and Korkmaz et al. [28] supported the existence of speed dependency for the form factors even though this should not be the case according to the hypothesis of Hughes [6]. Therefore, regardless of the choice of the CFD code, numerical methods, and settings, the choice of speed that the double body computations are performed for will have a significant impact on the CFD based form factors when the ITTC-57 model to ship correlation line is used. The towing tank tests are also not immune to the variation of form factors with changing the scale factor of the model as shown by García Gómez [21], Toki [22] and Van et al. [43].

The baseline grid, g_2, of each test case is simulated in three different speeds: the lowest speed tested in the towing tank, the design speed of the vessel, and an interim speed between the two speeds. The average non-dimensional first cell height, y^+, and other CFD settings are kept the same for all speeds. As can be seen in Figure 10a, all test cases indicate a definitive trend for the comparison error of factors which is based on the ITTC-57 line. As also explained in the earlier studies [22,28,42], the ITTC-57 line is the main reason for

form factors increasing with increasing Reynolds number due to its excessive steepness in model scale Reynolds numbers.

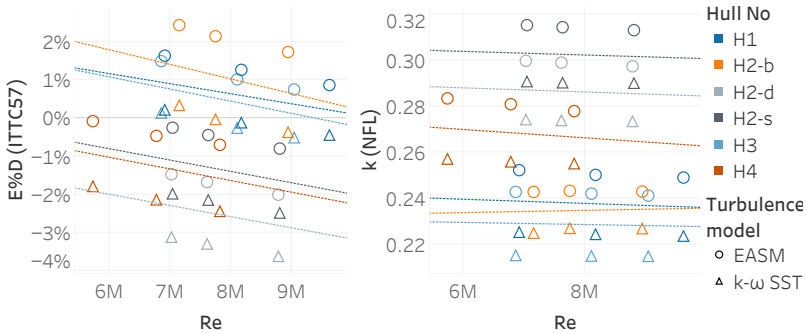

Figure 10. Comparison error of all test cases for the speed variations, (**a**) using the ITTC-57 line and (**b**) using the NFL.

Using the results of the same simulations but changing the friction line from the ITTC-57 line to a numerical friction line (NFL) [30] of the same CFD code and turbulence model reduced, and, in some cases nearly eliminated, the speed dependency of CFD based form factors, as can be seen in Figure 10b. As there is no experimental comparison point with the NFL, the form factors are directly plotted in Figure 10b. Contrary to other test cases, the H4 hull shows a decreasing trend with Reynolds number. The investigation in the local flow highlighted that the trend observed in H4 is due to the existence of mild flow separation at the stern. The separation is noticeably larger in the computations with the EASM than with the $k-\omega$ SST turbulence model. As Reynolds number is increased, the separation diminishes in intensity; therefore, the form factor is reduced as expected. Note that, according to the form factor hypothesis of Hughes [6], there should not be any flow separation in the model tests nor in the CFD. In such cases, the CFD simulations are recommended to be performed at higher Reynolds number until the separation is vanished. Except for the case with flow separation, the smallest average comparison error is observed at the slowest model tow speed. Therefore, it is recommended to perform the CFD simulations at the lower end of the model speed interval. However, such a conclusion may as well be different for other codes, numerical methods, or the size of the model used in towing tank tests.

5.1.5. Turbulence Model

The systematic variations applied to the CFD set-ups have been performed with the $k-\omega$ SST and EASM turbulence models. The conclusions regarding the other CFD settings: the non-dimensional cell height normal to the wall, additional grid refinement at the stern, domain size, and model scale speed, are valid for both turbulent models. The form factor predictions of all test cases using the $k-\omega$ SST model are approximately 10% higher than the computations with EASM using the same grid. As a result of this consistent difference between the form factors from different turbulence models, the full scale viscous resistance ($C_{VS} = (1+k)C_{FS}$) predictions using the $k-\omega$ SST model will be higher while the residual resistance (see Equation (2)) predictions will be lower than the predictions from EASM when the ITTC-57 line is used.

When the comparison error of the form factors is presented for each turbulence model with respect to the loading conditions, a certain prediction pattern is observed as presented in Figure 11. Computations at ballast, design, and scantling loading conditions are stacked in separate columns where box-and-whisker plots are placed with markers. The box plot can be identified with the gray color and sized with the lower and upper quartiles. Lines extending from the boxes (whiskers) extend to the data within 1.5 times the interquartile

range (IQR). The markers are colored with the test cases and sized according to the number of cells. The computational results from the finest two grids (original g_1 and g_2 from Section 5.1), from average $y^+ \leq 0.5$ presented in Section 5.1.1 and all grid refinements presented in Section 5.1.2 are presented in Figure 11. The form factor predictions from the $k-\omega$ SST model at ballast loading condition corresponds better to the experimentally determined form factors than the EASM turbulence model. However, the opposite trend is true for the design and scantling loading conditions. When the results are considered regardless of the loading condition, the average comparison error is 0.75% and −0.9% for the EASM and the $k-\omega$ SST turbulence models, respectively. Therefore, the absolute mean comparison error of the two turbulence models is similar.

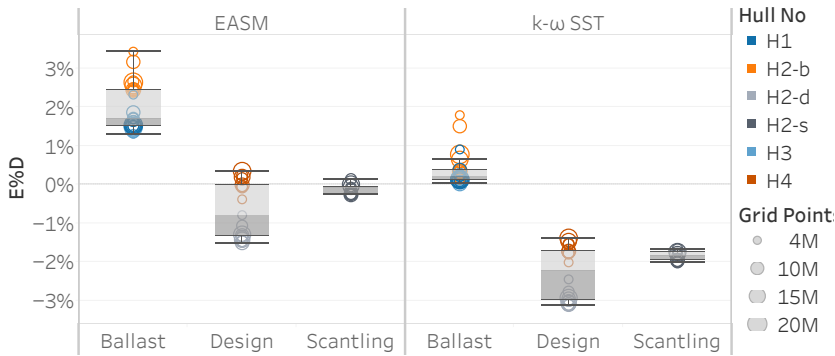

Figure 11. Comparison error of form factors for different loading conditions for the EASM and the $k-\omega$ SST turbulence models.

5.1.6. Validation in Model Scale

In order to complete the verification and validation study, experimental uncertainty needs to be determined [44]. As the experimental data used in this study were obtained through routine towing tank testing, thorough uncertainty analyses according to ITTC [45] could not be performed but instead the simplified implementation of this procedure as presented in ITTC [46] was used.

Using the standard uncertainty of calibration (SEE) for routine tests and the SSPA database of the repeatability of resistance tests, the uncertainties in resistance measurement [46] (without repeat tests) are calculated for each measurement point of each test case. However, the combined uncertainty of measured resistance, $u_c(R_T)$, cannot be used as direct indicatives of the uncertainties related to the form factors. Therefore, an additional step is required to consider the uncertainties due to the data reduction process of the form factor, i.e., the linear regression in the Prohaska method. The regression lines in Figures 12 and 13 are obtained by using the measurement uncertainties for the 95% confidence interval ($k_p = 2$) and applying the method explained in [47], which considers the experimental uncertainties in the regression progress and predicts the uncertainties in the form factor as well. The resulting regression line is indicated as York's method in Figures 12 and 13, where the uncertainty on the form factor is illustrated with magenta colored error bar at $Fn^4/C_F = 0$, and the measurement uncertainties are shown as the blue colored error bars. The uncertainty of the form factors, U_D, for the 95% confidence interval are varying between 0.015 and 0.023, which corresponds to 1.3% and 2.0% of the $(1 + k)$.

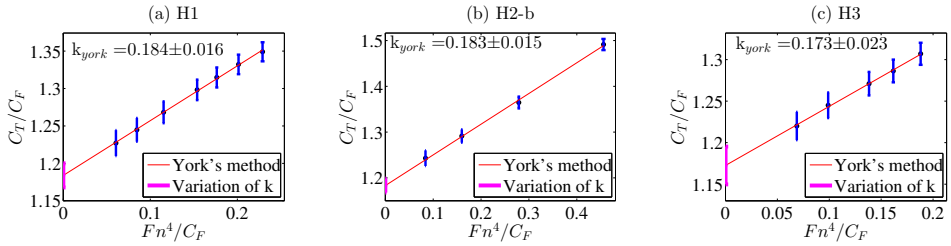

Figure 12. Prohaska plot of test cases in ballast loading condition: (**a**) H1, (**b**) H2-b, (**c**) H3.

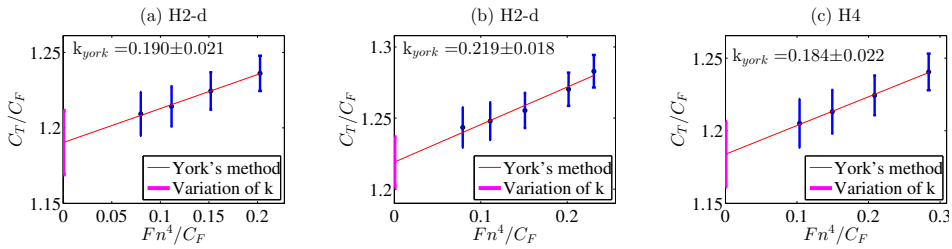

Figure 13. Prohaska plot of test cases in design and scantling loading conditions: (**a**) H2-d, (**b**) H2-d, (**c**) H4.

The numerical uncertainty, U_{SN}, of the CFD based form factors is calculated similar to form factor calculation in Equation (3),

$$U_{SN}(k) = \frac{U_{SN}(C_V)}{C_{FM}}, \tag{11}$$

where C_{FM} is the equivalent flat plate resistance in two-dimensional flow obtained from the same Reynolds number as the computations and obtained from the ITTC-57 line [4]. The validation uncertainty is calculated as $U_V = \sqrt{{U_{SN}}^2 + {U_D}^2}$.

The numerical and experimental uncertainties, absolute comparison error, and the validation uncertainties for the baseline grids (g_2) of all test cases are presented in Table 2 in percent of $(1 + k)$ where the form factor from the Prohaska method is used. The validation uncertainty, U_V, is bigger than the absolute comparison error for all test cases with the $k - \omega$ SST turbulence model. Except the H2-b test case with the EASM, all other test cases are also $|E| < U_V$; validation is achieved at U_V level, i.e., the comparison error is below the noise level. However, it should be noted that the U_V of H1 and H2-d test cases are exceptionally high due to very large numerical uncertainties as explained in Section 5.1. When only U_D and E are compared, the form factor predictions made with the $k - \omega$ SST are within the experimental uncertainty for the same number of test cases as the EASM turbulence model.

Table 2. Validation of the CFD based form factors.

Form Factor	Turb. Model	H1	H2-b	H2-d	H2-s	H3	H4
U_{SN}%D	EASM	7.6	2.0	11.7	5.4	2.9	7.0
	$k - \omega$ SST	11.2	2.5	10.7	5.6	3.2	3.2
U_D%D	-	1.3	1.3	1.8	1.5	2.0	1.8
|E|%D	EASM	1.6	2.4	1.1	0.3	1.5	0.1
	$k - \omega$ SST	0.2	0.3	2.8	2.0	0.1	1.8
U_V%D	EASM	7.7	2.4	11.9	5.7	3.5	7.2
	$k - \omega$ SST	11.2	2.8	10.8	5.8	3.8	3.7

The required uncertainty, U_{reqd}, is determined based on the typical $U_{SN}\%D$ and $U_D\%D$ values observed in Table 2. The numerical uncertainties of 2.5% to 3.5% and the experimental uncertainties of 1.3% to 1.8% were considered satisfactory levels in consideration of the U_{reqd}. The combination of $U_{SN}\%D$ and $U_D\%D$ indicates that $U_{reqd}\%D$ should be approximately 4%. This required uncertainty level results in approximately $\pm 4\%$ variation in the full scale power predictions. It can be seen in Table 2 that $U_{reqd}\%D = 4\%$ is larger than the comparison error of all test cases with a considerable margin. The comparison of $U_{reqd}\%D$ and $U_V\%D$ for H2-b, H3, and H4 (only with the $k-\omega$ SST) shows that required uncertainty is larger than the validation uncertainty, and, therefore, the validation of these cases is successful for a programmatic standpoint [44]. The rest of the test cases $U_{reqd}\%D$ is smaller than $U_V\%D$ due to substantial numerical uncertainties.

It should be noted that the experimental determination of the form factor, i.e., the Prohaska method [5], is not a direct measurement but obtained as a result of data reduction. The Prohaska method is solely an approximation to obtain the form factor described by Hughes [6]. Therefore, the comparison error of the form factor should be interpreted with care since the experimental form factors may not always represent the true value.

6. Demonstration of Quality by Comparison of Full Scale Predictions

In the final step of the proposed quality assurance procedure, full scale speed-power-rpm relations between speed trials and full scale predictions based on model tests carried out at SSPA are compared. In order for such comparisons to be meaningful, a large number of sea trials are required since the uncertainty of each trial is large. The combination of the precision and bias limits of single speed trial result in approximately 10% of total uncertainty as indicated by Werner and Gustafsson [48] and Insel [49].

Correlation of model test power predictions to the speed trials are quantified with the *correlation factors* which are also used as "correction for any systematic errors in model test and powering prediction procedure, including any facility bias" [50] in the 1978 Power Prediction method [20]. There are three different schemes of correlation factors that can be used: C_A, $C_P - C_N$ and $\Delta C_{FC} - \Delta w_C$. In this study, the correlation scheme of $C_P - C_N$ coefficients are applied. In order to obtain these coefficients, the correlation of each individual speed trial, $C_P^{'}$ and $C_N^{'}$, are calculated as

$$C_P^{'} = \frac{P_{D\ trial}}{P_{D\ tank}} \quad \text{and} \quad C_N^{'} = \frac{n_{trial}}{n_{tank}} \tag{12}$$

where the $P_{D\ trial}$ and n_{trial} are the power and propeller turning rate from a speed trial, while $P_{D\ tank}$ and n_{tank} represent the corresponding predictions based on the model test. The power, P_D, is derived from the faired speed-power curve at the design speed. After $C_P^{'}$ and $C_N^{'}$ are calculated for a large number of sea trials, an assembled correlation factor for C_P and C_N are determined by taking the median of $C_P^{'}$ and $C_N^{'}$ of all trials of sufficient quality [48]. In this study, assembled correlation factors are not disclosed, but the probability density functions (PDFs) of $C_P^{'}$ and $C_N^{'}$ are presented by shifting the median of PDFs to 1, i.e., normalizing the correlation factors.

In the determination of the ITTC 1978 Power Prediction Method, the standard deviation of normalized $C_P^{'}$ and $C_N^{'}$ were used as the main measure to rank different extrapolation methods. In this study, the same approach is adopted, and reduced scatter of the normalized $C_P^{'}$ and $C_N^{'}$ is interpreted as an improvement for the extrapolation methods explained in Sections 6.1 and 6.2.

6.1. Comparison of the Standard ITTC-78 Method and CFD Based Form Factors Using the ITTC-57 Line

Correlation of the speed trials to model test power predictions is quantified by using three different sources of form factors: the Prohaska method, CFD based form factors using EASM, and $k-\omega$ SST turbulence models. The ITTC-78 method [20] is used for all predictions with the ITTC-57 model to ship correlation line [4] and the correlation allowance

stated in Equation (4). A special wake scaling suggested in the ITTC 1999 method [51] is applied to the vessels with a pre-swirl stator type of device ahead of the propellers. All predictions used the same model test data, but only the source of the form factor is changed. The difference in the form factors among predictions leads to a change in the residual resistance as calculated in Equation (2) and the viscous resistance of the full scale ship ($(1+k) \times C_{FS}$) as calculated by using Equation (1). As a result of the change in C_{TS}, the predicted delivered power and propeller rate of revolution vary.

The probability density functions (PDFs) of the normalized correlation factors, $C_P^{'}$ and $C_N^{'}$, are calculated for the speed trials that have an uncertainty index less than eight using the different sources of the form factors. The uncertainty index, u, is an in-house developed index that quantifies the trustworthiness of each speed trial by summarizing the largest error sources and weighting them according to their impact on the results. In addition to the PDF curves, the standard deviations (σ) of $C_P^{'}$ and $C_N^{'}$ are also presented in Figure 14. The comparison of the standard deviations for the power predictions (C_P) indicates that the scatter is reduced considerably when the CFD based form factors from the EASM turbulence model are used compared to the Prohaska method. The PDF curve of CFD based form factors from EASM suggests that the frequency of predictions that are within $\pm 5\%$ of the sea trials is increased, while the predictions that are off more than 10% are slightly reduced. The PDF curve of CFD based form factors from $k-\omega$ SST for the power prediction remained nearly the same as the standard ITTC-78 method. The propeller rate of revolution predictions remained the same with EASM but slightly worsened by the predictions with CFD based form factors with $k-\omega$ SST model when the standard deviation is considered. It should be noted that the reduction of scatter in the power predictions is a more significant measure than the propeller turning rate since the scatter in power prediction is much larger than the prediction of rps. Hence, it can be concluded that the usage of CFD based form factors with ITTC-57 line improves the predictions in general or at least do not deteriorate them.

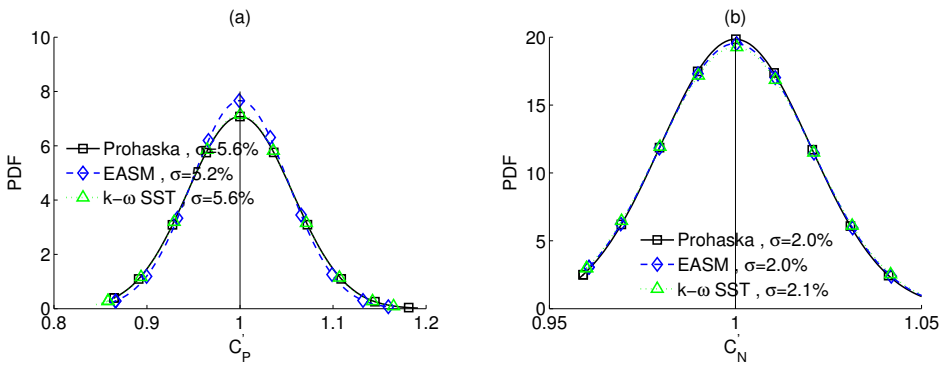

Figure 14. The probability density functions (PDFs) of the normalized correlation factors for the standard ITTC-78 method and using CFD-based form factors with two different turbulence models. (**a**) $C_P^{'}$ and (**b**) $C_N^{'}$.

6.2. Comparison of the CFD Based Form Factors Using the ITTC-57 Line and Numerical Friction Lines

To investigate if the predictions can be further improved by modifying the standard ITTC-78 method, the ITTC-57 model to ship correlation line is replaced by the numerical friction lines [30]. The CFD based form factor of each hull is recalculated using the same simulation results as in Section 6.1 for EASM and $k-\omega$ SST turbulence models using the corresponding numerical frictional line as explained in Section 2. Similar to the previous section (Section 6.1), the correlation of the speed trials to model test power predictions is

quantified using four different sources of form factors; CFD based form factors for EASM and $k-\omega$ SST using ITTC-57 line and NFLs.

The same population of the speed trials presented in the Section 6.1 are used for generating the PDFs of the normalized $C_P^{'}$ and $C_N^{'}$. As can be seen in Figure 15, the standard deviation of the predictions with the CFD based form factors is lower with the application of NFL compared to using the ITTC-57 line, while the scatter of $C_N^{'}$ increased slightly. Another distinctive result of using the NFLs is the reduced difference between the turbulence models. The previous studies [27,28] indicated that, when the numerical friction lines are used, the full scale viscous resistance ($C_{VS} = (1+k)C_{FS}$) is nearly the same regardless of using EASM and $k-\omega$ SST turbulence models for the derivation of the form factor. However, the residual resistance varies with regard to the turbulence model, and, therefore, leading to the different full scale total resistance (see Equation (1)). As observed in Figure 15, the form factors from using the EASM turbulence model and its numerical friction line correlates better than when using the $k-\omega$ SST model. In addition, the CFD based form factors using numerical friction lines considerably reduced the frequency of the predictions that differ from the speed trials more than 10%, which is the level of the total uncertainty of a speed trial [48,49].

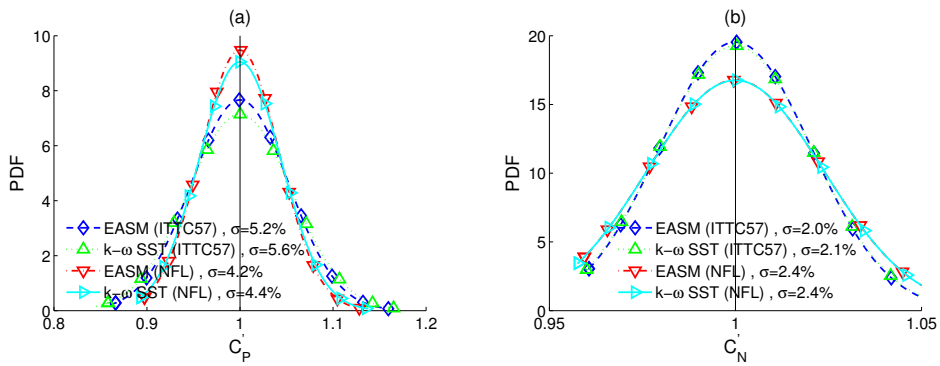

Figure 15. The probability density functions (PDFs) of the normalized correlation factors using the CFD based form factors with the ITTC-57 and the numerical friction lines. (**a**) $C_P^{'}$ and (**b**) $C_N^{'}$.

6.3. Analysis of the Extrapolation Methods and Speed Trials

The full scale speed-power-rpm relations between speed trials and full scale predictions using different extrapolation methods have been presented in Sections 6.1 and 6.2. It is important to make sure that the conclusions are not biased for a specific population of speed trials and also the speed trials with large error sources are excluded when general conclusions are made. Therefore, the statistical analysis on the $C_P^{'}$ is repeated for the speed trials with varying maximum uncertainty indexes. As presented in Table 3, three different levels of maximum uncertainty index, u, are used. In practice, the cut off uncertainty index should be as low as possible since the larger u index value of a speed trial indicates the existence of larger error or uncertainty sources such as large wave and wind corrections due to adverse weather conditions. However, the number of sea trials with very low uncertainty is limited and, as a result, the danger of drawing conclusions from small number of speed trials arise.

In Table 3, the statistics of different populations of speed trials with maximum cut off values of u varying between 4 and 8 are presented. The number of speed trials is 46 for the cut off value of $u = 4$. A lower u cut off value for the uncertainty index is not preferred since the size of the population decreases significantly. The comparison of the standard deviations between the corresponding u index shows that σ increases slightly with the increasing u index as there are more speed trials with lower quality in the larger

populations. However, the ranking of the magnitude of the standard deviations among each extrapolation method remains consistent. The scatter of the standard ITTC-78 method, where the form factors are obtained from the Prohaska method, is higher than all other extrapolation methods where the form factor is obtained from CFD except when $k-\omega$ SST is used with the ITTC-57 line. The standard deviations when using CFD based form factors with the ITTC-57 line are slightly in favor of the EASM turbulence model and also the percentage of the predictions with less than a 5% error are consistently higher when the EASM is used, while the predictions that differ from the speed trials more than 10% remained similar to the $k-\omega$ SST with the ITTC-57 line. The replacement of the ITTC-57 line with the numerical friction lines in combination with the CFD based form factors shows promising and consistent improvements towards not only reduction in the scatter but also decline in the number of speed trials where the prediction error is larger than 10% for both turbulence models. The correlation between the predictions and the speed trials is improved the most when the EASM turbulence model is used in combination with NFL.

Table 3. Statistics of the power predictions compared to speed trial.

u<	Number Speed Trials	Quantitiy	Standard ITTC-78	CFD Based k, ITTC-57 Line with EASM	CFD Based k, ITTC-57 Line with $k-\omega$ SST	CFD Based k, NFL with EASM	CFD Based k, NFL with $k-\omega$ SST
		σ	4.9%	4.7%	5.0%	4.3%	4.3%
4	46	5% < Error <10%	19%	15%	19%	13%	13%
		10% < Error	7%	9%	9%	4%	4%
		σ	5.8%	5.3%	5.7%	4.4%	4.6%
6	69	5% < Error <10%	21%	19%	24%	18%	19%
		10% < Error	9%	9%	9%	4%	4%
		σ	5.6%	5.2%	5.6%	4.2%	4.4%
8	78	5% < Error <10%	20%	20%	24%	11%	16%
		10% < Error	9%	8%	9%	4%	5%

The relatively large standard deviations observed in Table 3 are mainly due to the scatter in the speed trials of the sister ships. In order to illustrate this, an ideal prediction scenario has been prepared. Ideal case means if the model test prediction is fully correct compared to the speed trial. In theory, it would mean that the mean $C_P^{'}$ of a series of sisters would be 1. The resulting $C_P^{'}$ values are presented in Figure 16 together with the standard deviations of each ship series. As observed in Figure 16, the standard deviations among the sister ship series are varying between 2% to 6%. The standard deviation of all the $C_P^{'}$ values in the ideal prediction case is 3.6%, which is only marginally smaller than the predictions made with the CFD based form factor with the EASM turbulence model and NFL as shown in Table 3. Additionally, the percentage of predictions within 5% and the predictions that differ from the speed trials more than 10% are also nearly the same with the ideal prediction case and the predictions made with the CFD based form factors with the NFL. This indicates that it is hardly possible to achieve a better accuracy than this, unless the uncertainty of the speed trials become lower.

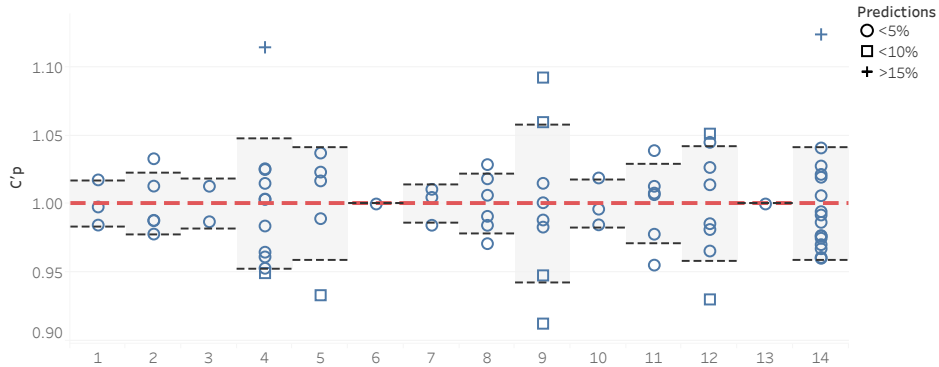

Figure 16. Illustration of the speed trial spread between sister ships for 14 ship series. $C_P^{'}$ values normalized to the mean of each series. Dashed black lines indicates the standard deviation.

6.4. Discussion

The analysis of the model test power predictions is further deepened by grouping the vessels based on their main dimensions, operational conditions, and general characters. Four main groups have been identified:

1. full block, large vessels ($L_{WL} > 320$ m) operating at $Fn < 0.16$;
2. full block, medium size vessels (220 m $< L_{WL} <$ 280 m) operating at $0.15 < Fn < 0.17$;
3. medium block, large vessels (280 m $< L_{WL} <$ 330 m) operating at $0.17 < Fn < 0.20$;
4. low block, medium size vessels (200 m $< L_{WL} <$ 240 m) operating at $0.22 < Fn < 0.23$.

The comparison error of the predictions to the speed trials on a group level is calculated as

$$P\%T = (\overline{C_P^{'}} - 1) \times 100 \quad (13)$$

where P represents predictions, T is the speed trials, and $\overline{C_P^{'}}$ is the average normalized $C_P^{'}$ of each group. $P\%T$ values are calculated for the five different extrapolation methods presented in Sections 6.1 and 6.2. The $P\%T$ values from CFD based form factor methods (Section 6.2) are compared to the $P\%T$ of the standard ITTC-78 method. This comparison, $\Delta P\%T$, is calculated by subtracting the absolute $P\%T$ values of the CFD based form factor methods from the absolute $P\%T$ values of the standard ITTC-78 method. As a result, the $\Delta P\%T = 0$ indicates that the prediction accuracy with the CFD based form factors remained the same as the standard ITTC-78 method, positive values $\Delta P\%T$ indicate improvement and negative values point out that the predictions are worsened for the corresponding prediction method relative to the predictions from the standard ITTC-78 method. $\Delta P\%T$ of CFD based form factor methods are presented in Figure 17 for the four groups. In order to give an indication of the uncertainty of the speed trials for each group, the standard deviation of the $C_P^{'}$ values from the standard ITTC-78 method is combined with the bias limit of 4% as estimated by Insel [49]. The resulting total uncertainties ($\sqrt{\sigma^2 + U_{bias}^2}$) are indicated in Figure 17 as error bars for each group. It should be noted that the total uncertainties of trials for the each group are larger than the corresponding comparison error from the standard ITTC-78 method, i.e., $P\%T$ is below the noise level. Therefore, the improvements (if any) as a result of using the CFD based form factors will be within the noise levels caused by the uncertainty of the trials. However, the changes in the accuracy of predictions, $\Delta P\%T$, are considered statistically valid as the number of speed trials are rather large.

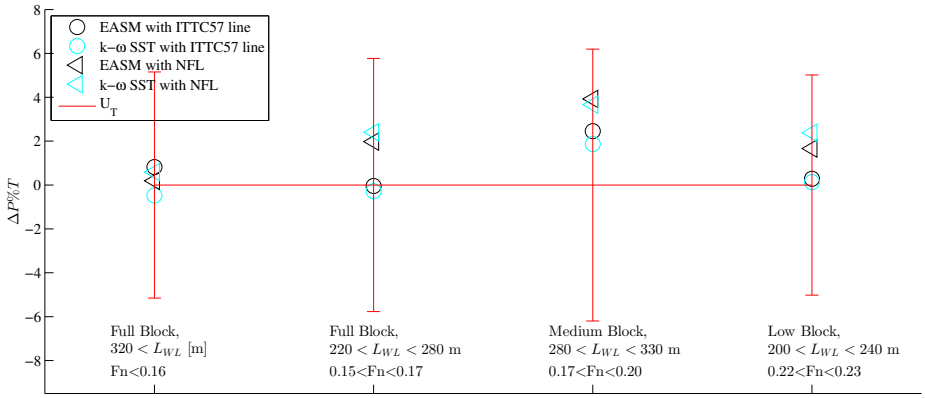

Figure 17. Relative change of the accuracy of the predictions, $\Delta P\%T = 0$, made with the CFD based form factors compared to the predictions with the standard ITTC-78 method, based on 18 test cases and 78 trials.

Starting with the extrapolations based on the CFD based form factors using the ITTC-57 line, there is no significant change in the accuracy of predictions for the full block and slow speed ($Fn < 0.17$) vessels. This outcome is expected since the form factor determination with the Prohaska method often functions well for such vessels and the CFD based form factors predict similar form factors to the Prohaska method as discussed in Section 5.1.6. As a result of obtaining nearly the same form factors from EFD and CFD while using the same friction line, the correlation between the predictions and speed trials remained nearly the same. However, it should be noted that the usage of $k-\omega$ SST turbulence model with the ITTC-57 line led to negative or too small C_R values in some test cases as a result of over-prediction of form factors which was also the observation in validation in the model scale (see Figure 11).

The accuracy of predictions for the low block vessels also remain nearly the same when the CFD based form factors are used in combination with the ITTC-57 line. This group of vessels are equipped with large protruding bulbous bows where the Prohaska method does not work in most cases. Therefore, the CFD based form factors are expected to introduce improvement to the predictions. The analysis performed on each vessel in this group showed that the CFD based form factors were up to 60% lower than the EFD based form factors. This caused the full resistance predictions to increase just enough to be predicted with similar accuracy but making it an over prediction on average instead of under prediction as it was the case for the standard ITTC-78 method.

The medium block and medium speed group are another group of vessels where a significant improvement is expected because the bulbous bow designs of these ships and typical loading condition for which the speed trials are performed for these vessels are not ideal for the Prohaska method. The CFD based form factors with the ITTC-57 line are predicted 25% to 50% lower than the form factors based on the Prohaska method. As can be seen in Figure 17, the predictions are in fact improved by implementation of the CFD based form factor for the both turbulence models.

The analysis is also performed for the CFD based form factors with the numerical friction lines. As can be seen in Figure 17, nearly all groups of vessels are predicted better than the standard ITTC-78 method and also the CFD form factors with the ITTC-57 line. The accuracy of the predictions for the full block vessels with LWL $>$ 320 m remained nearly the same as the predictions from the standard ITTC-78 method were already in good agreement with the speed trials. The improvement in the predictions for the medium block and medium speed vessels are doubled on average and the low block vessel indicates a gain in accuracy when the CFD based from factors with NFL are used compared to using the ITTC-57 line.

The full block vessels with 220 m < LWL < 280 m are also predicted better on average with the numerical friction line than other extrapolation methods. Considering that the form factors for the vessels in this group are nearly the same for EFD and CFD when the ITTC-57 line is used, it is significant to investigate why such an improvement is observed. When the CFD based form factors are obtained for the ITTC-57 line and the NFL, the same computation is used for a test case and turbulence model. This leads to variations in the full scale resistance predictions even when the same turbulence model is used. The origin of such variations is explained by the difference

1. between the form factor predictions as the C_{FM} values are significantly different in model scale between the friction lines [30].
2. in the model scale viscous resistance, C_{VM}, except at the Rn for which the simulation is performed and the form factors are obtained from. Note that C_{VM} at the model scale are calculated as $C_{VM} = (1 + k)C_{FM}$ and the slope of the ITTC-57 line and the numerical friction lines are different.
3. in the residual resistance (see Equation (2)) due to different C_{VM} values.
4. in the full scale viscous resistance of the smooth hull since it is calculated as $C_{VS} = (1 + k)C_{FS}$, where the form factors are substantially different for different friction lines, but the C_{FS} values are highly similar for the ITTC-57 line and the numerical friction lines in full scale as demonstrated in Korkmaz et al. [30].
5. in the correlation allowance (see Equation (4)) which is only included in the calculation of full scale resistance when ITTC-57 line as explained in Section 2.

The full scale resistance components explained above in the items 3 to 5 have varying effects on the final predictions as the main dimensions of each hull and its operational conditions such as Re and Fn are different. In Figure 18a, the difference between the full scale resistance predictions using the CFD based form factors with the EASM turbulence model but with different friction lines are presented. This difference is calculated as $((C_{TS}(NFL)/C_{TS}(ITTC57)-1)*100)$ where the friction line used for the prediction of C_{TS} is indicated in brackets. In order to simplify the visualization and evaluation, the speed C_{TS} curve of each test case is averaged. As seen in Figure 18a, the difference between the average total resistance of the predictions made with the NFL and the ITTC-57 shows a linear trend when plotted against L_{WL}. At around $L_{WL} = 240$ m, the total resistance predictions of both friction lines intersect, the vessels shorter than 240 m are under-predicted, and the ships longer than 240 m are over predicted up to 6% by the application of the numerical friction lines compared to using the ITTC-57 line.

Among the possible sources of the trend observed in the total resistance predictions, the full scale viscous resistance (the roughness and correlation allowances summed with $(1 + k)C_{FS}$) is identified as the main contributor. The comparison of C_{VS} for the rough hulls are calculated in a similar fashion to the C_{TS} comparison and presented in Figure 18b. It can be noticed that the trends for the difference between the predictions made with the NFL and the ITTC-57 line are highly similar for C_{TS} and C_{VS}, which is by far the biggest resistance component when combined with roughness and correlation allowances. The comparison between Figure 18b,c also suggests that the difference in the C_R when NFL and ITTC-57 line are used indeed has a noticeable effect on the total resistance, but it is limited when compared to the contribution of the viscous resistance.

The full scale viscous resistance for the smooth hull ($C_{VS} = (1 + k)C_{FS}$) could not have been the reason behind the trend observed in Figure 18b,c because the slope of C_{FS} curves for NFL and ITTC-57 line are highly similar at the Reynolds numbers that most of the conventional ships operate. Following this statement and the previous arguments, no other part of the extrapolation is left but the roughness allowance [10] and the correlation allowance as in Equation (4). In Figure 18c, the proportion of the $\Delta C_F + C_A$ and ΔC_F in the full scale total resistance of the each test case are presented for the predictions with the ITTC-57 line and the NFL, respectively. The contribution of the roughness allowance to the total resistance varies between 4% to 7% when NFL is used. However, the usage of the ITTC-57 line led 7% to 11.5% of the total resistance to be constituted by $C_F + C_A$.

The formulation of the C_A in Equation (4) is dependent on *Re* and clearly explains the trends observed in Figure 18c. The relationship observed in Figure 18b for the full scale viscous resistance including the roughness and correlation allowance is a direct result of the contribution of the C_A in Equation (4), which propagated into the full scale total resistance seen in Figure 18c.

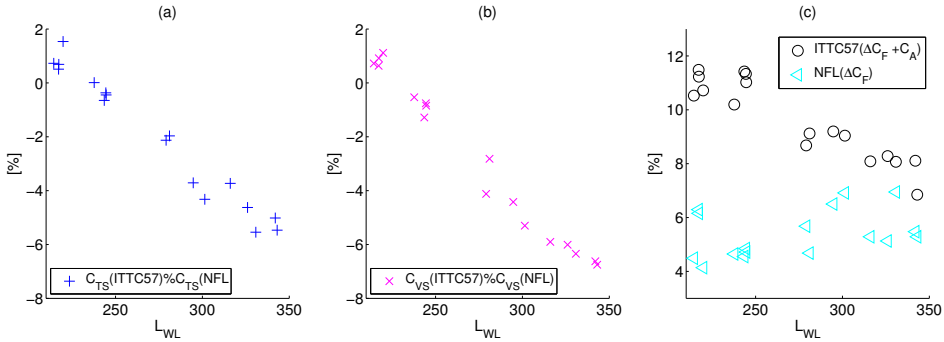

Figure 18. Difference between the (**a**) C_{TS}, (**b**) C_{VS} (including $\Delta C_F + C_A$), and (**c**) $\Delta C_F + C_A$ predictions using the CFD based form factors with the EASM turbulence model and different friction lines.

Going back to the discussion on correlation of the predictions and the speed trials for the full block vessels with 220 m < LWL < 280 m, it can be stated that the full scale resistance predictions vary 0 to 2% as a result of using different friction lines with CFD based form factors. Therefore, the improvement due to using NFL as presented in Figure 17 is arguably due to the combination of the changes in resistance predictions and also as a result of the overall changes in the whole population (shift in the median of the C_P' of all speed trials).

As explained in this section, the full scale speed-power-rpm relations between speed trials and full scale predictions using CFD based form factors can be improved compared to the standard ITTC-78 prediction method. This conclusion is confirmed for the different populations of speed trials where the trials were filtered through varying uncertainty indices as shown in Table 3. Using the numerical friction lines derived by Korkmaz et al. [30], correlation between the predictions and the speed trials are further improved in general. The difference in the predictions when the NFL and the ITTC-57 line is used with the CFD based form factors largely originates from the correlation allowance recommended by ITTC [20]. The correlation allowance was omitted when the numerical friction lines were used in the extrapolations since it is only fit to be used in combination with the ITTC-57 line. As a result of omitting the C_A term, the predictions are significantly improved for the 18 test cases. However, this may not be the case for the ships that are shorter than the test cases considered in this study because of the way the C_A term [20] is formulated. Since the C_A is a logarithmic function of the Reynolds number, the contribution of C_A increases rapidly with decreasing *Re*, i.e., the shorter vessels. At lower Reynolds numbers than the ones investigated in this study, it may be desirable to have new C_A in combination with the roughness allowance derived for the numerical friction lines to sustain the improvements. Therefore, the conclusions regarding the CFD based form factor method explained in this study is limited to the ships with $1.05 \times 10^9 < Re$ and 200 < L_{WL}.

7. Conclusions

In order to respond to the need for a practical procedure for the organizations that regularly perform CFD predictions on similar cases, a new procedure of quality assurance has been proposed by the ITTC Specialist Committee of Combined CFD and EFD Methods. This study serves as an example of how the procedure can be applied in practice to a problem: CFD based form factors. The quality assurance of this practical problem is

demonstrated in three parts: the content of the Best Practice guidelines of the specific CFD code used in this study as explained in Sections 3 and 5.1.1–5.1.5, the quality Assessment of the BPG methodology through verification and validation studies presented in Section 5.1.6, and finally the demonstration of quality by the comparisons of 78 speed trials to the predictions made by combined CFD/EFD methods explained in Section 6.

In order to investigate and derive a best practice guideline for CFD based form factors, systematic variations have been applied to the CFD set-ups. The non-dimensional cell height normal to the wall, additional grid refinement at the stern, domain size, and model scale speed were analyzed in Sections 5.1.1–5.1.4 and the following observations and recommendations were made:

- Mainly as a result of grid generation strategy of SHIPFLOW, monotonic convergence of the computed resistance coefficients may not always be possible, and, therefore, sometimes leading to excessive numerical uncertainties. However, the variation of C_V between all the grids is limited and less than 1% may be indicating that non-monotonic behavior is overly penalized by the numerical uncertainty determination method in this study.
- The differences between the two finest grids are less than 0.2% except one case where the viscous pressure resistance coefficient varies significantly more compared to other test cases due to an abrupt change of grid cell formation near the stagnation point at the bulb. This indicates that, even though the grid generator of the CFD code used in this study may occasionally introduce errors, the fine grids are of good quality for CFD based form factor determination.
- In order to make sure that nearly all no-slip cells are $y^+ < 1$, the target for the average y^+ should be maximum 0.5 for the SHIPFLOW code. Due to the curvature and the boundary layer growth of conventional hulls, y^+ is likely to vary significantly when fixed first cell height is applied for all CFD codes. Therefore, similar exercises are recommended for other codes when a wall resolved approach is used.
- Additional refinements added to the stern region of all the test cases had no significant impact on the predicted form factor. Therefore, additional refinements are redundant when the initial grid is fine enough.
- The variation of the domain size had extensive consequences on the computed resistance coefficients for SHIPFLOW. However, other CFD codes are expected to experience similar issues as the main reason was identified as the change in the turbulence quantities when the distance between the inlet boundary and the fore-perpendicular of the hull is increased.
- The investigations on the local skin friction coefficient, C_f, indicated that the flow is not all fully turbulent. The transition of flow in CFD occurred not later than the location where the turbulence stimulators are fitted in the model tests, making sure that the modeling errors due to different flow characteristics between CFD and EFD are negligible. Since the numerical methods, types of boundary conditions, and initial turbulence quantities (turbulent dissipation rate, turbulence kinetic energy) vary for each code, it is recommended that similar investigations should be performed for each code.
- The speed dependency of the form factors with the ITTC-57 line can be clearly observed for all test cases. Similar trends are expected by all CFD codes as the main reason for the dependency is the ITTC-57 line rather than the numerical methods. Considering that the experimental form factor determination is not immune to the scale effects (geosim models having different form factors with the ITTC-57 line), the model tow speed for CFD computations should be chosen with respect to the typical model sizes of the validation data.
- The application of numerical friction lines of the same code and turbulence model to the CFD based form factor determination, the speed dependency is nearly eliminated in all cases but one that is exhibiting mild flow separation. As the *Re* is increasing, the separation region is reduced; hence, the form factor changes as expected. According

to the form factor approach of Hughes [6], there shall be no flow separation to ensure its validity. Therefore, for the cases where flow separation is observed, higher *Re* numbers should be used for the simulations regardless of the friction line used.
- The turbulence modeling is the largest source of modeling error for the form factor determination. The form factor predictions of all test cases from the $k-\omega$ SST model are approximately 10% higher than the EASM with the same grid.
- All variations to the CFD setting were performed for both turbulence models ($k-\omega$ SST and EASM). The conclusions regarding to the other CFD settings are valid for both turbulent models.

In the second step of the proposed quality assurance procedure, verification and validation of the CFD based form factor method were performed. Experimental uncertainties of the six test cases were determined and the uncertainties on the form factors were derived. The following conclusions were made for the verification and validation studies:

- The validation in model scale indicated that the comparison error is below the noise level for all test cases with the $k-\omega$ SST turbulence model. Except for one test case with EASM, validation is achieved at the U_V level for simulations using the EASM turbulence model. However, these findings are rather inconclusive due to very large numerical uncertainties in two test cases.
- The comparison between experimental uncertainty and the comparison error of CFD based form factors showed that the form factor predictions made with the $k-\omega$ SST model are within the experimental uncertainty for the same number of test cases as with the EASM turbulence model, but the $k-\omega$ SST model is better at predicting the ballast loading condition while EASM is better for the design and scantling loading conditions.

The last step of the of the proposed quality assurance procedure, demonstration of quality, was performed by investigating the full scale speed-power-rpm relations between the speed trials and the full scale predictions based on different extrapolation methods but using the same model test data. In total, 18 test cases were simulated using the best practice guidelines presented in this study and CFD based form factors were determined. The conclusions regarding the comparison of the full scale predictions and speed trials are that:

- The sample size of the sea trials is large enough to rank the extrapolation methods as varying the population of speed trials led to the same conclusions.
- The scatter of the correlation factors for the power prediction, C_P', is higher with the standard ITTC-78 method, where the form factors are obtained from the Prohaska method, than the extrapolation methods where the form factor is obtained from CFD with the EASM turbulence model and with the $k-\omega$ SST in combination with the NFL. The opposite trend is observed for the shaft rate. However, the prediction accuracy of the correlation factors for the propeller turning rate is significantly higher than C_P' and the increase in the scatter of C_N' is smaller than the gains in power predictions when CFD based form factors are used.
- Compared to the standard ITTC-78 method, the standard deviation of the normalized C_P' is lower when the CFD based form factors are used with the EASM turbulence model.
- The CFD based form factors from the $k-\omega$ SST model led to negative or too small C_R values in some test cases as a result of the over-predicted form factors. Additionally, the scatter of C_P' are higher when the $k-\omega$ SST model is used in comparison with the EASM turbulence model.
- The usage of CFD based form factors with the EASM turbulence model in combination with the ITTC-57 line improves the predictions for the medium block, medium speed hulls noticeably, while the prediction accuracy remained the same for the other types of ships in comparison with the prediction from the standard ITTC-78 method.

- The most promising method out of the five investigated extrapolation methods is the CFD based form factors using the EASM turbulence model and the NFL. It reduces the standard deviation of $C_P^{'}$ and decreases the number of predictions with larger errors than 10%, while the number of predictions with errors less than 5% are increased significantly.
- The main contributor of the standard deviation of $C_P^{'}$ originates from the scatter of the speed trials among the sister ships. The standard deviation of $C_P^{'}$ is close to the minimum value that could be obtained from the speed trial data set when the CFD based form factors are used with the EASM turbulence model and the NFL.
- The group of vessels that improved most in prediction accuracy are the medium block and medium speed ($0.17 < Fn < 0.20$) ships which are typical difficult cases for the form factor determination using the Prohaska method.

Following the proposed quality assurance procedure, the CFD based form factor method has been investigated. As a result of the systematic variations applied to the CFD settings, a best practices guideline was derived for the CFD based form factor method. Using the BPG, form factor predictions have been made for a variety of ship types. The investigation on the correlations between the full scale power predictions and speed trials showed that the CFD based form factors can be considered as an alternative or supplementary method to the Prohaska method. As explained, the selection of friction lines in combination with CFD based form factors played a prominent role towards reducing the scatter between the predictions and trials. However, the change of the friction line would also require altering the well accustomed correlation factors.

It is worth remembering the statement of Gilbert Dyne who was the mastermind behind the ITTC 1978 Power Prediction Method: "It is ... relatively easy to criticise the different details of the...ITTC method. It is much more difficult to find an alternative which gives better power and RPM predictions" Lindgren and Dyne [52] (p. 14).

As stated by Dr. Dyne, there are still shortcomings with full scale resistance predictions. However, the combination of EFD and CFD is expected to provide immediate improvements to the 1978 ITTC Performance Prediction Method. Further studies should be performed with many more test cases to be used for the comparison of speed trials and power predictions with the CFD based form factors as the uncertainty of the speed trials are rather large.

Author Contributions: Conceptualization, K.B.K., S.W., and R.B.; methodology, K.B.K., S.W., and R.B.; validation, K.B.K.; formal analysis, K.B.K.; investigation, K.B.K., S.W., and R.B.; data curation, K.B.K.; writing—original draft preparation, K.B.K.; writing—review and editing, K.B.K., S.W., and R.B.; visualization, K.B.K.; supervision, S.W. and R.B.; project administration, S.W.; funding acquisition, S.W. All authors have read and agreed to the published version of the manuscript.

Funding: This research was funded by VINNOVA, the Swedish Governmental Agency for Innovation Systems, grant 2017-02953, and the computational resources provided by Chalmers Center for Computational Science and Engineering (C3SE).

Conflicts of Interest: The authors declare no conflict of interest. The funders had no role in the design of the study; in the collection, analyses, or interpretation of data; in the writing of the manuscript, or in the decision to publish the results.

References

1. Larsson, L.; Raven, H.C. *Ship Resistance and Flow*; The Society of Naval Architects and Marine Engineers: Jersey City, NJ, USA, 2010.
2. IMO. *Annex 19: Resolution MEPC.203(62)*; International Maritime Organization: London, UK, 2011.
3. ITTC. *D. Skin Friction*; International Conference of Ship Tank Superintendents: London, UK, 1948.
4. ITTC. *Subjects 2 and 4 Skin Friction and Turbulence Stimulation*; International Towing Tank Conference: Madrid, Spain, 1957.
5. Prohaska, C.W. A Simple Method for the Evaluation of the Form Factor and Low Speed Wave Resistance. In Proceeding of the 11th ITTC, Tokyo, Japan, 11–20 October 1966.

6. Hughes, G. *Friction and Form Resistance in Turbulent Flow, and a Proposed Formulation for Use in Model and Ship Correlation*; National Physical Laboratory: London, UK, 1954; Volume 96.
7. Bowden, B.S.; Davison, N.J. *Resistance Increments Due to Hull Roughness Associated with form Factor Extrapolation Methods*; National Physical Laboratory: London, UK, 1974.
8. ITTC. *Report of Performance Committee*; International Towing Tank Conference: Ottawa, ON, Canada, September 1975.
9. ITTC. *Report of Performance Committee*; International Towing Tank Conference: Hague, The Netherlands, 3–10 September 1978.
10. Townsin, R.L.; Dey, S.K. The Correction of Roughness Drag with Surface Characteristics. In Proceedings of the International Workshop on Marine Roughness and Drag, RINA, London, UK, 29 March 1990.
11. ITTC. Report of Power Performance Committee. In Proceedings of the International Towing Tank Conference, Madrid, Spain, 16–22 September 1990.
12. ITTC. *1978 ITTC Performance Prediction Method*; ITTC: Copenhagen, Denmark, 2014.
13. Michell, J. The wave resistance of a ship. *Philos. Mag.* **1898**, *45*, 106–123. [CrossRef]
14. Larsson, L. Will Computational Fluid Dynamics Completely Take the Role of Model Testing? In Proceedings of the 11th WEMT International Conference: The West European Maritime Industry in the Global Challenge of the Next, Century, Rotterdam, The Netherlands, 12–14 May 1998.
15. Larsson, L.; Stern, F.; Visonneau, M. *Numerical Ship Hydrodynamics: An Assessment of the Gothenburg 2010 Workshop*; Springer: Dordrecht, The Netherlands, 2014. [CrossRef]
16. Hino, T.; Stern, F.; Larsson, L.; Visonneau, M.; Hirata, N.; Kim, J. *Numerical Ship Hydrodynamics: An Assessment of the Tokyo 2015 Workshop*; Springer International Publishing: New York, NY, USA, 2020. [CrossRef]
17. Sun, W.; Qiong, H.; Jia, S.; Jie, X.; Jinfang, W.; Guofu, H. Numerical Analysis of Full-Scale Ship Self-Propulsion Performance with Direct Comparison to Statistical Sea Trail Results. *J. Mar. Sci. Eng.* **2020**, *8*, 24. [CrossRef]
18. Niklas, K.; Pruszko, H. Full-Scale CFD Simulations for the Determination of Ship Resistance as a Rational, Alternative Method to Towing Tank Experiments. *Ocean. Eng.* **2019**, *190*. [CrossRef]
19. Ponkratov, D. 2016 Workshop on Ship Scale Hydrodynamic Computer Simulation. In Proceedings of the Loyd's Register Workshop on Ship Scale Hydrodynamics, Southampton , UK, 25 October 2016.
20. ITTC. *1978 ITTC Performance Prediction Method*; ITTC: Wuxi, China, 17–22 September 2017.
21. García Gómez, A. On the Form Factor Scale Effect. *Ocean. Eng.* **2000**, *26*, 97–109. [CrossRef]
22. Toki, N. Investigation on Correlation Lines through the Analyses of Geosim Model Test Results. *J. Jpn. Soc. Nav. Archit. Ocean. Eng.* **2008**, *8*, 71–79. [CrossRef]
23. Pereira, F.S.; Eça, L.; Vaz, G. Verification and Validation Exercises for the Flow around the KVLCC2 Tanker at Model and Full-Scale Reynolds Numbers. *Ocean. Eng.* **2017**, *129*, 133–148. [CrossRef]
24. Terziev, M.; Tezdogan, T.; Incecik, A. A Geosim Analysis of Ship Resistance Decomposition and Scale Effects with the Aid of CFD. *Appl. Ocean. Res.* **2019**, *92*. [CrossRef]
25. Wang, Z.Z.; Xiong, Y.; Shi, L.P.; Liu, Z, H. A Numerical Flat Plate Friction Line and Its Application. *J. Hydrodyn.* **2015**, *23*, 383–393. [CrossRef]
26. Dogrul, A.; Song, S.; Demirel, Y.K. Scale effect on ship resistance components and form factor. *Ocean. Eng.* **2020**, *209*, 107428. [CrossRef]
27. Korkmaz, K.B.; Werner, S.; Bensow, R. Investigations for CFD Based Form Factor Methods. In Proceedings of the Numerical Towing Tank Symposium (NuTTS 2019), Tomar, Portugal, 29 September–1 October 2019.
28. Korkmaz, K.B.; Werner, S.; Sakamoto, N.; Queutey, P.; Deng, G.; Yuling, G.; Guoxiang, D.; Maki, K.; Ye, H.; Akinturk, A.; et al. CFD Based Form Factor Determination Method. *Ocean. Eng.* **2021**, *220*, 108451. [CrossRef]
29. Wang, J.B.; Yu, H.; Feng, Y. Feasible Study on Full-Scale Delivered Power Prediction Using CFD/EFD Combination Method. *J. Hydrodyn.* **2019**, *31*. [CrossRef]
30. Korkmaz, K.B.; Werner, S.; Bensow, R. Numerical Friction Lines for CFD Based Form Factor Determination Method. In Proceedings of the VIII International Conference on Computational Methods in Marine Engineering MARINE 2019, Göteborg, Sweden, 13–15 May 2019.
31. Broberg, L.; Regnström, B.; Östberg, M. *SHIPFLOW Users Manual*; FLOWTECH International AB: Gothenburg, Sweden, 2014.
32. Deng, G.; Visonneau, M. Evaluation of eddy-viscosity and second-moment turbulence closures for steady flows around ships. In Proceedings of the 21st ONR Symposium on Naval Hydrodynamics,Trondheim, Norway, 24–28 June 1996; pp. 453–469.
33. Menter, F.R. Two-equation eddy-viscosity turbulence models for engineering applications. *AIAA J* **1994**, *32*, 1598–1605. [CrossRef]
34. Regnström, B. *Introduction to Overlapping Grids in SHIPFLOW*; FLOWTECH International AB: Gothenburg, Sweden, 2008.
35. Hellsten, A. Some improvements in Menter's k-omega SST turbulence model. In Proceedings of the 29th AIAA, Fluid Dynamics Conference, Albuquerque, NM, USA, 15–18 June 1998. [CrossRef]
36. ITTC. *Preparation, Conduct and Analysis of Speed/Power Trials*; ITTC: Wuxi, China, 17–22 September 2017.
37. ISO. *Ships and Marine Technology—Guidelines for the Assessment of Speed and Power Performance by Analysis of Speed Trial Data*; ISO: Geneva, Switzerland, 2015.
38. Eça, L.; Hoekstra, M. A procedure for the estimation of the numerical uncertainty of CFD calculations based on grid refinement studies. *J. Comput. Phys.* **2014**, *262*, 104–130. [CrossRef]
39. Eça, L.; Hoekstra, M. The Numerical Friction Line. *J. Mar. Sci. Technol. Mar. Sci. Technol.* **2008**, *13*, 328–345. [CrossRef]

40. Eça, L.; Pereira, F.S.; Vaz, G. Viscous flow simulations at high Reynolds numbers without wall functions: Is $y^+ \simeq 1$ enough for the near-wall cells? *Comput. Fluids* **2018**, *170*, 157–175. [CrossRef]
41. Schlichting, H.; Gersten, K. *Boundary-Layer Theory*; Springer: Berlin/Heidelberg, Germany, 2000.
42. Raven, H.C.; van der Ploeg, A.; Starke, A.R.; Eça, L. Towards a CFD-based prediction of ship performance—Progress in predicting full-scale resistance and scale effects. *Int. J. Marit. Eng.* **2008**, *150*, 31–42.
43. Van, S.H.; Ahn, H.; Lee, Y.Y.; Kim, C.; Hwang, S.; Kim, J.; Kim, K.S.; Park, I.R. Resistance Characteristics and Form Factor Evaluation for Geosim Models of KVLCC2 and KCS. In Proceeding of 2nd International Conference on Advanced Model Measurement Technology for EU, Newcastle upon Tyne, UK, 4–5 April 2011, pp. 282–293.
44. ITTC. *Uncertainty Analysis in CFD Verification and Validation Methodology and Procedures*; ITTC: Wuxi, China, 17–22 September 2017.
45. ITTC. General Guideline for Uncertainty Analysis in Resistance Tests. In Proceedings of the ITTC—Recommended Procedures and Guidelines, 7.5–02.02–02, Revision 02, Copenhagen, Denmark, 31 August–5 September 2014.
46. ITTC. Practical Guide for Uncertainty Analysis of Resistance Measurement in Routine Tests. In Proceedings of the ITTC—Recommended Procedures and Guidelines, 7.5–02.02–02.2, Revision 00, Copenhagen, Denmark, 31 August–5 September 2014.
47. York, D.; Evensen, N.; Ló, M.; Nez, M.; De, J.; Delgado, B. Unified equations for the slope, intercept, and standard errors of the best straight line. *Am. J. Phys.—Am. Phys.* **2004**, *72*. [CrossRef]
48. Werner, S.; Gustafsson, L. Uncertainty of Speed Trials. In Proceedings of the HullPIC 2020, Hamburg, Germany, 26–28 October 2020.
49. Insel, M. Uncertainty in the analysis of speed and powering trials. *Ocean. Eng.* **2008**, *35*, 1183–1193. [CrossRef]
50. ITTC. Guidelines on the determination of model-ship correlation factors. In Proceedings of the ITTC—Recommended Procedures and Guidelines, 7.5-04-05-01, Revision 0, Wuxi, China, 17–22 September 2017.
51. ITTC. *Report of Propulsion Committee*; ITTC: Seul, Korea; Shanghai, China, 5–11 September 1999.
52. Lindgren, H.; Dyne, G. Ship Performance Prediction. In Proceedings of the International Symposium on Advances in Marine Technology, Trondheim, Norway, June 1979.

Paper V

Scaling of wetted-transom resistance for improved full-scale ship performance predictions

Ocean Engineering 266 (2022) 112590

Contents lists available at ScienceDirect

Ocean Engineering

journal homepage: www.elsevier.com/locate/oceaneng

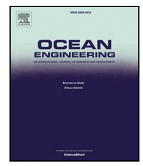

Scaling of wetted-transom resistance for improved full-scale ship performance predictions

Kadir Burak Korkmaz [a,b,*], Sofia Werner [a], Rickard Bensow [b]

[a] SSPA SWEDEN AB, Chalmers Tvärgata 10, Box 24001 Se-400 22, Göteborg, Sweden
[b] Chalmers University of Technology, Sweden

ARTICLE INFO

Keywords:
Ship resistance
Form factor
CFD
Combined CFD/EFD methods
Transom flow
Wetted-transom

ABSTRACT

Determining a ship's propulsive power is a critical stage in the design phase in which the evaluation of the stern plays a crucial role. Different flow regimes can be observed depending on the position and shape of the transom. This paper investigates the wetted-transom flow characteristics and their implications on the 1978 ITTC Performance Prediction Method. In the case of flow separation, such as the wetted-transom flow, the current ITTC-78 procedure does not provide an alternative method. Therefore, two alternative methods were proposed based on the investigations of CFD computations on seven hull forms. The firstly proposed method is a combined EFD&CFD method called the two form factor method. It requires CFD computations in model and full-scale, and it can handle any case of flow separation, including the wetted-transom flow. The second proposed method is an empirical correction formula for the hulls with a wetted-transom flow. Finally, the full-scale speed-power relations between the speed trials and the full-scale predictions from the two alternative methods and the standard ITTC-78 method were presented. It is observed that the two suggested methods considerably improve the correlation between the predictions and the speed trials.

1. Introduction

Predicting a ship's power requirement at the design stage is critical for a successful design. Meanwhile, as the ship design progresses from the initial phases to the end, the required confidence level for the speed-power prediction increases. Therefore, the speed attained at a specific power consumption needs to be verified by the most accurate prediction method for the final design. This need arises not only because of the contractual agreement on the speed-power performance of a new ship between the yard and the ship owner but also due to the legal requirements posed by the International Maritime Organisation (IMO). To reduce greenhouse gas emissions from shipping, the IMO (2011) introduced the Energy Efficiency Design Index (EEDI). The regulations require the speed-power relation of a ship to be determined through model tests. However, the model testing and the extrapolation methods used for predicting the speed-power relations face challenges for ships with substantially submerged transoms. Considering that the EEDI calculations are performed at the scantling draught, where the transoms of many vessels are submerged, it is significant to improve the accuracy and reliability of the EEDI values further.

Nearly all modern cargo vessels have a transom stern. The flow regime behind the transom can be characterised under three main categories as suggested by Larsson and Raven (2010): regular, dry-transom, and wetted-transom flow. In the case of a regular transom flow, the lower edge of the transom is above the still water level, and the waves leave the hull smoothly, similar to a cruiser stern design. The dry-transom flow indicates the free-surface, and the flow smoothly leaves the transom edge tangential to the buttocks. The criterion for dry-transom flow occurrence is that the pressure at the edge of the transom must be equal to the atmospheric pressure (Larsson and Raven, 2010). Increasing the transom submergence of a vessel or decreasing the speed will increase the required hydrodynamic pressure to sustain the dry-transom flow. As a result, the upward curvature of the streamlines of the flow behind the transom will increase. The increased steepness of the streamlines and the momentum deficit of the flow leaving the hull due to the boundary layer will cause the longitudinal velocity to disappear at a certain point and leads to the emergence of a spilling wave breakers between the transom and the first wave crest (Starke et al., 2007). Increasing the transom submergence or decreasing the speed further will lead the spilling breaker to reach the transom. As a result, a recirculation region emerges and gives rise to the wetted-transom flow, which is the main subject of this paper.

The transom stern submergence can vary significantly depending on the ship type and operational profile. Some full block vessels, such as

* Corresponding author at: Chalmers University of Technology, Sweden.
E-mail addresses: burak.korkmaz@sspa.se, korkmaz@chalmers.se (K.B. Korkmaz).

https://doi.org/10.1016/j.oceaneng.2022.112590
Received 22 June 2022; Received in revised form 7 September 2022; Accepted 13 September 2022
Available online 30 September 2022

tankers and bulk carriers, and some low block fast vessels, often feature submerged transoms at rest for design and scantling draughts. The full block vessels operate at low Froude numbers; hence, obtaining a dry-transom flow is difficult due to the thick boundary layer, substantial transom submergence, and low speeds. The wetted-transom flow can be observed for some ships even though the low block vessels such as Ro-Ro, Ro-Pax, and PCTCs are designed to operate with a dry-transom. These vessels may have substantially large submerged transoms due to the loading condition of the ship (a significant aft trim) combined with speeds lower than the design speed that may result in wetted-transom flow.

The towing tank testing and extrapolation procedures have been used since the 19th century to predict the performance of a ship in deep and calm water. The International Towing Tank Committee (ITTC) put forward a towing tank testing and extrapolation procedure denoted as 1978 ITTC Performance Prediction Method (ITTC, 2021a) as a result of decades-long developments and discussions. One of the main pillars of this procedure is the form factor concept (Hughes, 1954) used for scaling the viscous resistance from model to full-scale. As explained in Section 2, the form factor approach is invalid when there is a flow separation in the boundary layer surrounding the hull. However, flow separation can occur in different ways for a vessel. Hence, it is essential to differentiate the mechanisms and causes of flow separations observed at flows around ships.

The first common type of flow separation is the bubble type (Larsson and Raven, 2010) which may be present at the stern of full block vessels. The bubble type separation is often a result of a sudden increase of pressure after passing a low-pressure region such as the bilge region. The distinct feature of this type of separation is that it results from an interaction between the boundary layer and the pressure distribution. The pressure distribution around the hull is the main driver of the boundary layer development. However, the pressure also is influenced by the boundary layer due to the displacement effect. Due to this relation, the bubble type separation often disappears with the increasing Reynolds number (Re) as presented in Korkmaz et al. (2021). Increasing Re reduces the viscosity effects and eases the adverse pressure. As a result, the flow separation dissipates, reducing the form factor.

The second type of flow separation is the recirculation flow region behind a substantially submerged transom, similar to a flow through a backward-facing step. The mean velocities around the stern overhang of a vessel are subjected to the sudden increase of cross-sectional area, causing the flow separation, as the mean velocities cannot follow the sharp turn. As a result, a low-pressure region is formed behind the transom, and the water surface is lower than the surrounding water levels. If the vessel speed increases or the transom submergence decreases, the water surface reaches the transom edge, and eventually, the transom becomes dry again, and the flow separation disappears. It is noteworthy to emphasise that flow separation behind the transom differs from the bubble type separation since the boundary layer effects and the pressure gradient are not the root causes of a largely submerged transom. Therefore, the full-block vessels with substantial transom submergence are most likely to experience wetted-transom (separated flow) both in model and full-scale. However, extra caution is needed for the vessels with a partially wetted-transom (coexisting smooth free-surface and significant spill breakers) as scale effects may result in different flow regimes in model and full-scale (Starke et al., 2007).

The wetted transom flows do pose issues with the 1978 ITTC Performance Prediction Method due to the separated and turbulent flow behind the transom, where a substantial amount of water is trailing the hull rather than the surrounding flow. This issue is reported by the ITTC (2021e) for the form factor derivation method as "it should be noted that Prohaska's method should not be used for any vessel with substantial transom sterns for which the transom runs wet at the speed range for the Prohaska test". However, no alternative method is suggested by the ITTC. One towing tank institution is known to employ an empirical correction for the transom submergence in their extrapolation procedure; however, neither the derivation nor the demonstration of this correction is open in the literature. Several studies (Farkas et al., 2018; Islam and Guedes Soares, 2019) investigated the hydrodynamic characteristics of full-scale ships at different draughts and trim conditions; however, no recommendations were provided for the issues caused by the wetted-transom flow. Given the importance of accurate methods for speed power predictions for EEDI and contracts, an alternative method or a correction procedure is needed for the vessels with substantial transom submergence. Due to the extreme scarcity of sea trial data carried out at scantling draught, it is difficult for towing tanks to derive correlation factors that account for these effects. Therefore, this paper aims to

- explain the wetted-transom flow characteristics in model and full-scale,
- highlight the issues with the 1978 ITTC Performance Prediction Method when flow separation exists
- quantify the resistance caused by the wetted-transom
- propose an alternative combined EFD/CFD method which can handle flow separations in the extrapolation process
- propose an empirical correction formula that can be integrated into the existing ITTC-78 method without the need for CFD computations.

This paper is structured as follows: Section 2 briefly describes the standard extrapolation of the towing tank resistance measurements from model to full-scale. The resistance extrapolations with and without a flow separation caused by a wetted-transom flow are illustrated. Additionally, an alternative method denoted as two form factor is suggested in Section 2. The geometrical features and parameters for a submerged transom are defined in Section 3. The numerical set-up used for the investigation of the transom flow is described in Section 4. The computational conditions and the test cases used in this study are presented in Section 5. In Section 6, a grid dependency study (Section 6.1), a qualitative (Section 6.2) and quantitative analysis (Section 6.3) of the flow behind the transom in model and full-scale are presented. Section 7 introduces an alternative empirical method for extrapolation of a towing tank test to full-scale resistance. The comparison of speed trials to the different prediction methods is presented in Section 7.1. Finally, the conclusions are summarised in Section 8.

2. Extrapolation of resistance from model tests to full scale, and the two form factor method ($2-k$ method)

2.1. Standard ITTC-78 method

In this study, the procedure recommended by ITTC (2021a) is used to extrapolate the towing tank test results to full scale. According to the 1978 ITTC Performance Prediction Method, the total resistance coefficient of the full-scale ship is calculated as

$$C_{TS} = (1+k)C_{FS} + \Delta C_F + C_A + C_R + C_{AAS}, \quad (1)$$

where k is the form factor, C_{FS} is the frictional resistance coefficient in full scale (the subscript 'S' signifies the full-scale ship), C_R is the residual resistance coefficient, ΔC_F represents the roughness allowance, C_A is the correlation allowance, and C_{AAS} is the air resistance coefficient.

According to the recommended procedure of ITTC (2021e), the form factor is obtained by the Prohaska method (Prohaska, 1966) in the model scale. Additionally, the determination can be supported by CFD calculations according to ITTC (2021b) following the procedures described in ITTC (2021c). The residual resistance, which is assumed to be the same in model and full-scale, is then obtained as

$$C_R = C_{TM} - (1+k)C_{FM}, \quad (2)$$

where C_{TM} is the total resistance coefficient (the subscript 'M' signifies the model scale). C_{TM} is measured at each speed in the towing tank,

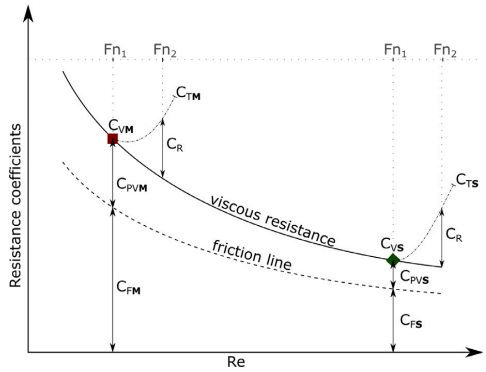

Fig. 1. The form factor hypothesis.

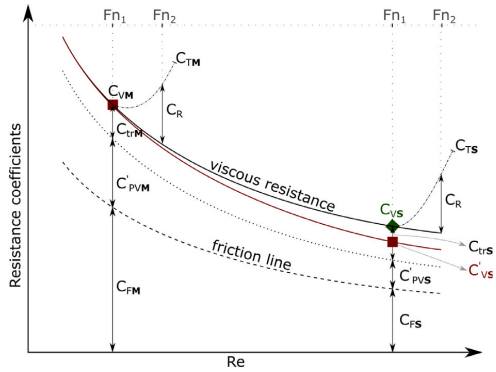

Fig. 2. Extrapolation method with a deeply submerged transom. (For interpretation of the references to colour in this figure legend, the reader is referred to the web version of this article.)

and C_{FM} is obtained from the friction lines. In this study, the Prohaska and CFD based form factor determination methods were used for the form factor derivations as described in ITTC (2021e). The latter method follows the assumptions of Hughes (1954) and is derived using the relation:

$$(1+k) = \frac{C_F + C_{PV}}{C_{FM}} = \frac{C_V}{C_{FM}}, \tag{3}$$

where the frictional resistance coefficient (C_F) and viscous pressure coefficient (C_{PV}) are obtained by the double-body CFD simulation. C_{FM} in the denominator of Eq. (3) is the equivalent flat plate resistance in two-dimensional flow obtained from the same Reynolds number as the computations. When the CFD based form factor determination is used, C_{FM} in Eq. (3), C_{FM} in Eq. (2) and C_{FS} in Eq. (1) are derived from the same friction line.

In this study, the frictional resistance coefficients, C_{FM} and C_{FS}, are obtained by using three different friction lines: the ITTC-57 model-ship correlation line (ITTC, 1957), and two numerical friction lines for EASM and k–ω SST turbulence models, respectively, proposed by Korkmaz et al. (2019b).

The validity of the form factor approach and the ITTC-78 extrapolation method shown in Eq. (1) is based on several criteria stated in Hughes (1954),

- the C_{PV} is proportional to the C_F when the flow is turbulent and free from separation
- the given hull is smooth and has a symmetrical form when towed at zero incidence angle.

Assuming this preconditions are fulfilled, the Eq. (1) can be visualised as in Fig. 1 excluding the roughness (ΔC_F), correlation allowance (C_A) and air resistance (C_{AAS}) terms for simplicity. To obtain the C_{TS}, model tests should be performed following the Fr similarity. Once the C_{TM} is measured and the form factor is determined, the C_R is obtained as shown in Eq. (2). As the form factor is the same at the model and full-scale, the full-scale viscous resistance is calculated as $C_{VS} = (1+k)C_{FS}$. The summation of the residual and viscous resistance for a given Fr will result in full-scale total resistance coefficient.

2.2. The two form factor method

In the case of a vessel with a deeply submerged transom for which the transom runs wet, the form factor approach as described in ITTC (2021e) is destined to fail as the wake of the transom constitutes separated flow which violates the preconditions of the form factor approach (Hughes, 1954). The recirculating flow behind the wake of the transom differs from the bubble type separation often observed around the stern bulbs of full block vessels in model scale but not in full scale. As discussed in Section 6, the recirculating flow behind the transom is persistent through the model scale to the full-scale Reynolds numbers. As a result of this persistent recirculating flow, using the same form factor in model and full-scale will result in an under-prediction of the full-scale viscous resistance. In Fig. 2, this is illustrated by decomposing the viscous resistance coefficient, C_{PVM}, which is the form resistance as described in Hughes (1954),

$$C_{PVM} = C'_{PVM} + C_{trM}, \tag{4}$$

where C'_{PVM} is the part that is proportional to the frictional resistance coefficient of a friction line, and the flow behind the wet transom is the cause of C_{trM}. Note that C_{trM} is the part that is *not* proportional to the C_F. As argued later in Section 6, the size of the C_{trM} remains approximately the same in model and full-scale Reynolds numbers. Hence, using the same form factor in model and full-scale implies that both C'_{PVM} and C_{trM} scales down proportional to the C_F as visualised as the continuous red line in Fig. 2. Therefore, the viscous resistance scaling as Eq. (1) has to be either corrected or predicted directly by CFD for the vessels with a wetted transom flow. The latter method is referred to as the two form factor method or $2-k$ *method* throughout the paper. The authors demonstrated earlier in Korkmaz et al. (2021) that the two form factor method is helpful for hulls with mild flow separation at the stern (bubble type). This paper employs the same technique on the substantially submerged transoms. The $2-k$ *method* is applied by the following steps:

1. C_{TM} is obtained from the towing tank tests.
2. The model-scale form factor, k_M is determined either by the Prohaska method (Prohaska, 1966) or by CFD (Korkmaz et al., 2021).
3. The residual resistance is calculated as $C_R = C_{TM} - (1+k_M)C_{FM}$
4. The full-scale form factor, k_S, is calculated using CFD based form factor method
5. The full-scale total resistance coefficient is calculated as

$$C_{TS} = (1+k_S)C_{FS} + \Delta C_F + C_A + C_R + C_{AAS}\ , \tag{5}$$

where,

- Residual resistance is obtained by using the model-scale form factor
- Viscous resistance is obtained by using the full-scale form factor.

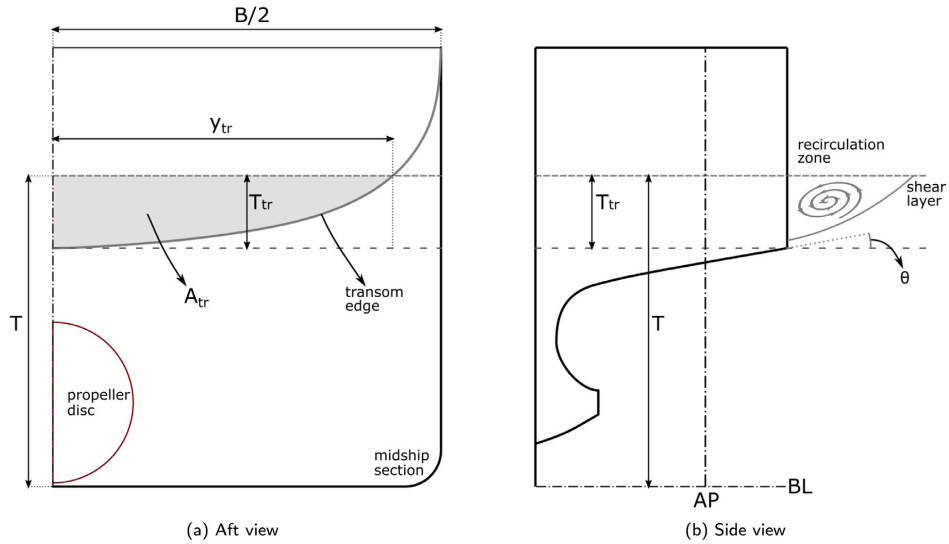

Fig. 3. Geometrical descriptions of a submerged transom.

As an alternative to the $2-k$ method, a correction method is suggested in Section 7. This correction aims to counterpoise the viscous resistance deficit in the case of a wetted-transom when the standard ITTC-78 method (ITTC, 2021a) is used, as illustrated in Fig. 2.

3. Terms and definitions for a submerged transom

Several parameters are defined to describe the transom flow, and a submerged transom is illustrated in Fig. 3. The draught and beam of the vessel are signified as T and B, respectively. The submerged part of the transom is indicated with light grey shading in Fig. 3(a), and the area of the submerged transom is presented as A_{tr}. Between the undisturbed water surface to the bottom-most part of the transom is indicated as the transom submergence, T_{tr}. The intersection point between the transom edge (light grey solid line) and the water surface is horizontally measured by the maximum width of the transom, y_{tr}. The last geometrical feature is the slope of the stem profile near the transom, θ, as shown in Fig. 3(b). The parameters related to waterline shapes or angles are disregarded as the flow around the stern rarely follows the waterlines; instead, the buttocks (or diagonals) represent the flow better.

For the submerged transom cases, the transom Froude number (Saunders, 1957),

$$Fr_{tr} = \frac{V}{\sqrt{gT_{tr}}}, \tag{6}$$

is a significant parameter that may indicate (even though with little validity) what flow type occurs behind the transom as indicated by Larsson and Raven (2010).

Two parameters are derived from the submerged transom area. The first parameter is the ratio between the A_{tr} and the maximum cross-section area, A_{max}. This area ratio is defined as:

$$tr_{ratio} = A_{tr}/A_{max} \ . \tag{7}$$

The other parameter indicates how full is the transom edge section. Observing this parameter may help to distinguish the effects caused by V-shaped or U-shaped shaped sections. The fullness of the transom is measured as:

$$tr_{fullness} = A_{tr}/(2y_{tr}T_{tr}) \ . \tag{8}$$

4. Flow solver, grid generation, computational domain, and boundary conditions

The XCHAP module of SHIPFLOW version 6.6 is used for solving the steady-state viscous flow (Broberg et al., 2014). The finite volume method is utilised to solve Reynolds Averaged Navier–Stokes (RANS) equations. The discretisation of the convective terms is achieved by the first order accurate Roe scheme, and an explicit flux correction is applied to increase the order of accuracy. Two turbulence models are available in the XCHAP solver: explicit algebraic stress model (EASM) as described by Deng and Visonneau (1996) and $k-\omega$ SST as described by Menter (1994). In this study, both turbulence models are used.

The viscous flow solver XCHAP accepts only structured grids, which can be in H-H, H-O, or O-O topologies. The grid generator of SHIPFLOW, XGRID, is used for the study to generate all the grids. The parametrised nature of grid generation with XGRID makes it possible to generate almost identical grid distribution in the longitudinal and circumferential directions for most of the conventional hulls simulated. However, the grid distribution in the normal to the hull surface can vary for each hull since the Reynolds number differs. As a result, different first cell sizes in the normal direction to the wall and cell growth ratios are obtained to achieve (approximately) the same y^+ values.

The CFD computations for the form factor calculations in this study were performed as double-body (DB) RANS computations with rudders integrated into the flow domain with an overlapping grid technique (Regnström, 2008). In addition, for a limited number of cases, free-surface (FS) RANS computations were also performed using the XCHAP solver to investigate the flow around the transom region. Detailed information about the free-surface treatment and the solver for the FS RANS method is explained by Orych and Larsson (2015).

The computational domain is shaped as a quarter of a cylinder. The distance between inlet and fore-perpendicular (FP) is $2.0L_{PP}$, outlet plane is located at $1.0L_{PP}$ behind the aft-perpendicular, and the radius of the cylindrical outer boundary is $3L_{PP}$.

Boundary types employed in XCHAP are no-slip, slip, inflow, outflow, and interior. The Inlet boundary condition sets a fixed uniform velocity (U_∞), a zero pressure gradient normal to the inlet boundary,

and the estimated turbulent quantities. The turbulence quantities, specific turbulence dissipation rate, and turbulent kinetic energy at the inlet are estimated as explained in Korkmaz et al. (2021). Outflow condition only consists of a Neumann boundary condition for velocity, turbulent kinetic energy, and pressure. As all computations were performed with half the body, the symmetry condition is used at the centre plane. The symmetry condition is similar to the slip condition where the normal velocity and normal gradient of other variables are set to zero. The no-slip condition specifies the velocity components, turbulent kinetic energy, and normal pressure component as zero at the wall, such as the hull and the rudder surfaces. The turbulence closure modelling is valid up until the no-slip wall. Therefore, computations were performed with the wall resolved approach, i.e. no wall functions.

5. Test cases and computational conditions

Seven different vessels have been investigated. Five of the test cases (referred to as H1, H2, H3, H4, and H5) are common cargo vessels which have been model tested, and four of the hulls have corresponding full-scale speed trials performed either at design or scantling loading conditions where the transoms were submerged at rest. Even though no full-scale measurement exists, the KVLCC2 and KCS hull forms are included in this study to diversify the ship types. The hull and rudder geometries were obtained from Tokyo (2015) and SIMMAN (2008) workshops for KCS and KVLCC2, respectively. The L_{PP} of the vessels are ranging from 170 m (denoted as m) to 320 m, and block coefficients (C_B) vary between 0.6 and 0.85. The Froude numbers (the achieved speed at 75% MCR except for KVLCC2 and KCS) cover the range of 0.14 to 0.2.

Two of the hull forms had one sea trial performed per vessel. The other vessels were built in series, and speed trials were performed for each sister ship. The data set consists of 10 sea trials in total. The trial measurements were conducted by the yards and analysed by SSPA with an in-house software according to ITTC Recommended Procedures and Guidelines for Preparation, Conduct and Analysis of Speed/Power Trials (ITTC, 2017b) and ISO Ships and marine technology—Guidelines for the assessment of speed and power performance by analysis of speed trial data (ISO, 2015). The sea trials conform to the ISO 15016/ITTC limits on weather conditions.

The computational conditions for each test case replicate the same conditions in the corresponding towing tank tests, such as the non-dimensional quantities, Re and Fr, loading condition, and geometrical features.

6. Results

The analysis of approximately 500 double-body and 40 free-surface RANS computations of the seven hulls under the conditions stated in Section 5 is discussed in this section.

6.1. Grid dependence study

Grid dependence studies were performed only for the H1 test case in model and full-scale to quantify the numerical uncertainties (U_{SN}). Following the best practice guidelines for the double-body computations (Korkmaz et al., 2021), geometrically similar six grids were generated. As the H1 test case is computed at the scantling draught, where the transom is deeply submerged, the flow behind the transom is likely to include a separated flow. Therefore, before the grid dependence study, the grid resolution behind the transom was investigated with the help of a grid refinement zone (Broberg et al., 2014). Unfortunately, the H1 hull form cannot be presented due to confidentiality. Instead, the KCS hull was used to visualise the generated grids as they are similar to the H1 grids. The grid density of the second-finest grid (denoted as g_2) without refinement is presented in Figs. 4 and 5 for the KCS hull at 12.85 m draught. As seen in Fig. 4, the longitudinal and circumferential grid distribution on the hull, the rudder, and the grid resolution behind the transom are shown. The grid resolutions of the hull and the rudder in the normal direction are presented in Fig. 5. The grid behind the transom is stretched towards the transom edge as the pressure and velocity gradients are expected to be high where the separation initialises. As an alternative to no refinement, a grid refinement was added to the region marked with the solid red lines in Figs. 4 and 5. After the refinement, each grid cell within the solid red lines was divided into 64 pieces, hence, heavily refining the grid behind the transom. Between the refined and non-refined grids, the computed viscous resistance differed 0.7% and 1.3% with the EASM turbulence model for the model and full-scale, respectively. Considering the additional resources spent on the added 3.3 million cells behind the transom and the small differences in the integrated forces between the two grids, the non-refined grids, shown in Figs. 4 and 5, were selected for the grid dependence study. The total number of grids and the grid refinement ratios ($h_1/h_i = \sqrt[3]{N_{grid_1}/N_{grid_i}}$) are presented in Table 1 for the six grids for model (MS) and full-scale (FS) computations.

All computations were performed in double precision to eliminate the round-off errors. The iterative uncertainties were quantified by the standard deviation of the force in percent of the average force over the last 10% of the iterations. Iterative uncertainty (U_I) for C_F, C_{PV} and C_V are presented in Table 2 for the six grids for model and full-scale computations. The maximum standard deviations for C_F, C_{PV} and C_V were kept below 0.02%, 0.51% and 0.1%, respectively. Even though a large recirculating flow follows the wake of the transom, the average U_I of geometrically similar six grids are reasonably small, and they are largely similar between the model and full-scale computations as seen in Table 2. In the light of these observations, it was assumed that the numerical errors are dominated by the discretisation errors and both iterative errors and round-off errors are neglected.

Table 1
Total number of cells, and the grid refinement ratios for the grid dependence study.

Grid	MS		FS	
	Cell count [M]	h_1/h_i	Cell count [M]	h_1/h_i
g_1	12.6	1.00	18.14	1.00
g_2	7.7	1.18	10.99	1.18
g_3	4.7	1.39	6.69	1.39
g_4	2.8	1.65	3.97	1.66
g_5	1.7	1.94	2.47	1.94
g_6	1.1	2.28	1.50	2.30

Table 2
Standard deviation of C_F, C_{PV} and C_V over the last 10% of the iterations.

U_i	Turb. model	MS		FS	
		max	mean	max	mean
C_F	EASM	0.01	0.00	0.00	0.00
	$k-\omega$ SST	0.02	0.00	0.01	0.00
C_{PV}	EASM	0.45	0.21	0.08	0.06
	$k-\omega$ SST	0.51	0.20	0.35	0.25
C_V	EASM	0.09	0.04	0.02	0.01
	$k-\omega$ SST	0.10	0.04	0.10	0.07

Table 3
Numerical uncertainty of the finest grid, g_1.

$U_G\%S_1$	Turb. model	MS	FS
C_F	EASM	1.3	1.6
	$k-\omega$ SST	0.7	1.5
C_{PV}	EASM	11.7	30.2
	$k-\omega$ SST	55.2	14.0
C_V	EASM	0.68	5.09
	$k-\omega$ SST	2.9	1.7

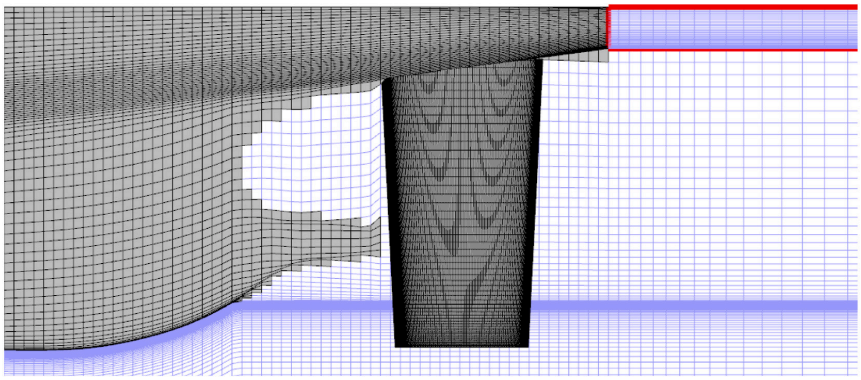

Fig. 4. Second finest grid, g_2, of KCS from side view. (For interpretation of the references to colour in this figure legend, the reader is referred to the web version of this article.)

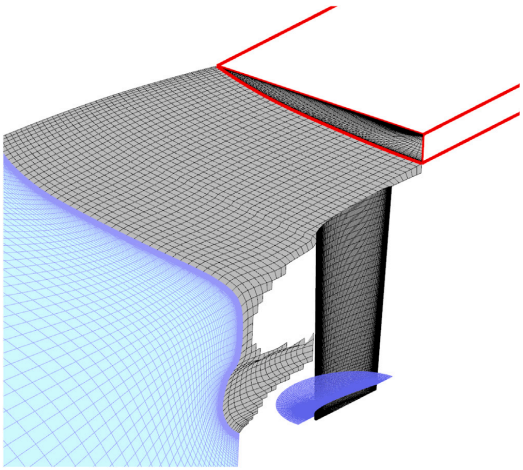

Fig. 5. Second finest grid, g_2, of KCS from aft perspective view. (For interpretation of the references to colour in this figure legend, the reader is referred to the web version of this article.)

Table 4
Numerical uncertainty of the second finest grid, g_2.

$U_G\%S_2$	Turb. model	MS	FS
C_F	EASM	2.0	2.4
	$k-\omega$ SST	1.0	2.2
C_{PV}	EASM	16.5	39.5
	$k-\omega$ SST	57.6	18.4
C_V	EASM	0.9	6.9
	$k-\omega$ SST	2.9	2.2

The procedure proposed by Eça and Hoekstra (2014) was used to predict the grid uncertainties (U_{SN}) which are presented for the finest (g_1) and the second finest (g_2) grids as a ratio of the computed value ($U_{SN}\%S_1$ and $U_{SN}\%S_2$ where S_i represents the computed value) in Tables 3 and 4, respectively. The grid uncertainties on C_F vary between 0.7 to 1.6 per cent of the computed result of S_1, while the grid uncertainty on C_{PV} varies greatly between model and full-scale and also the different turbulence models. The variation of U_G on C_V is somewhat less compared to the viscous pressure resistance. The large fluctuation in the grid uncertainties is explained by the scatter in the computed values, which strongly penalises the estimated uncertainties (Eça and Hoekstra, 2014). Computed values for C_F, C_{PV} and C_V are presented in Fig. 6 in a percentage of the result of the finest grid. The C_F and C_{PV} values in Fig. 6 shows oscillatory behaviour, which is observed significantly more for the latter. The main cause of these fluctuations can be traced back to the grid generation technique, a structured grid with a stair-step profile in the stern and stem profiles. Due to rapid curvature changes around the bulbous bow and aperture between the stern bulb and stern overhang, the structured grid captures the stern and stem profiles differently. This abrupt grid change near the sensitive regions, such as the stagnation pressure point, can lead to noticeable fluctuations, especially in the pressure resistance coefficient, as observed in Fig. 6. Another significant observation is that the grid dependency is significantly larger in full-scale computations than in the model scale. The C_V varies less than 0.5% for the four finest grids (g_1 to g_4) in model scale, while the variation of C_V in full scale is up to 2%.

The estimated numerical uncertainties are shown in Tables 3 and 4, and the fluctuations of the computed resistance coefficients are largely similar to the earlier study (Korkmaz et al., 2021) where the same code and grid generation technique was applied to different hulls and loading conditions. However, due to the drawbacks of the grid generation, the numerical uncertainties on C_{PV} are rather significant. However, its reflection on C_V is limited, and the variation on the predicted form factors is relatively small. Therefore, the grid setup of the second finest grid, g_2, has been chosen for the rest of the investigations for the other hulls. As a result, the grid cell count was reduced to approximately 7.7 and 11.0 million in model and full-scale, respectively, and computational time was shortened compared to the finest grid. Considering that over 500 computations were performed for this study, a significant computational effort was saved without sacrificing numerical uncertainty on C_V too much.

6.2. Transom stern flow

This section will investigate the transom stern flow of the test case H1 in detail. The draught of the vessel was varied in three steps. As a result, different transom submergence levels were computed in model and full-scale for EASM and k-ω SST turbulence models.

6.2.1. The effect of free-surface modelling

In order to calculate the CFD based form factors, double-body (DB) RANS computations are needed since the Eq. (3) requires the viscous resistance as the input instead of the total resistance, which can be obtained from a free-surface (FS) RANS computation. As mentioned earlier, the transom flow regime depends on not only the hull shape and

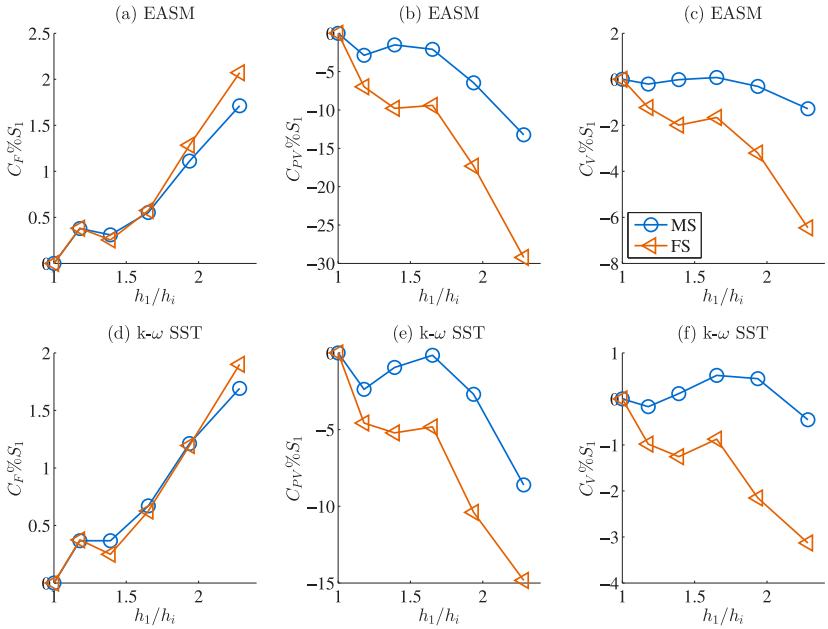

Fig. 6. Computed values for H1 test case: (a) C_F, (b) C_{PV} and (c) C_V with the EASM model and (d) C_F, (e) C_{PV} and (f) C_V with the $k-\omega$ SST model vs. grid refinement ratio, h_1/h_i.

the viscous flow around the stern but also the wave pattern upstream and the relation between the hydrodynamic and the hydrostatic pressure at the transom edge (Larsson and Raven, 2010; Starke et al., 2007). Therefore, investigation of the flow behind the transom only with a double-body RANS approach can be misleading unless the transom flow is reasonably similar with and without a free-surface. Therefore, DB and FS RANS computations were performed to investigate the flow behind the transom with and without a free-surface, in model and full-scale.

The scale effects on the stern wave system and the wetted-transom flow between the model and full-scale require further consideration for the full-scale FS RANS computations. The primary source of this scale effect is the different boundary layers around the stern between the model and full-scale, as suggested by Raven et al. (2008) and Farkas et al. (2017, 2018). As a newly built ship at the sea trial cannot be hydrodynamically smooth but with a certain hull roughness, its effect on the boundary layer should also be assessed. Otherwise, an FS RANS computation with hydrodynamically smooth surfaces will predict a thinner boundary layer in full scale than the actual ship. As a result, the pressure distribution around the stern and the wave pattern aft of the transom will differ. The hull roughness can especially be critical when the wetted-transom flow is in a transitionary phase. Therefore, the full-scale FS RANS computations included the hull roughness effect, which affects the boundary layer, the pressure distribution, and the wave pattern around the stern. The roughness is implemented by a modification of the boundary conditions for the specific dissipation rate (ω) and the turbulent kinetic energy (k) as explained by Orych et al. (2021). The roughness value used for the computations is quantified by the sand grain roughness equivalent to the standard hull roughness value recommended by ITTC (2021a). Since the main goal is to use the full-scale form factors in the extrapolation process, double-body computations were performed with no roughness effects as required by the form factor hypothesis (Hughes, 1954). Both DB and FS computations were performed at fixed even keel conditions, i.e. dynamic sinkage and trim were omitted to compare the same transom submergence levels for each loading condition.

In Fig. 7, the flow behind the transom in full scale is presented for the FS (Figs. 7(a), 7(c), and 7(e)) and DB (Figs. 7(b), 7(d), and 7(f)) RANS computations. All computations were post-processed at the same camera angle, and hulls are situated at the same location in the figures. The streamlines were generated from seeding 20 equidistant points behind the transom for both computation types. The colour of the streamlines was determined by the non-dimensionalised speed, u/U, where u is the local velocity, and U is the free stream velocity. The light blue isosurface in Fig. 7, represents $u/U = 0$ condition, hence, signifying the separated flow. Additionally, the free-surface is visualised by a transparent light purple isosurface for the FS RANS computations.

In order to be able to use double-body computations for the form factor calculations, it should be ensured that the flow behind the transom is reasonably similar for both FS and DB approaches when the transom is substantially submerged. Starting from the original scantling draught in full scale (Figs. 7(e) and 7(f)), it can be observed that the recirculating flow region (light blue surface) extends approximately to the same longitudinal position. A large dead-water region does not trail the side of the transom in both FS and DB approaches. The flow pattern is also notably similar, as indicated by the streamlines and the grey-coloured arrows visualising the flow directions. The slightly larger size of the recirculation region in free-surface computation is caused mainly by the interference of the large bow wave crest and the stern waves.

The next loading condition is $T=T_{scantling} - 1m$ which has the submerged transom area equals to 10% of the maximum cross-section area ($tr_{ratio} = 0.10$). The observations on the flow features seen in Figs. 7(c) and 7(d) is similar to the original $T_{scantling}$ draught. The free-surface does not seem to play a major role, and the double-body assumption seems to capture the major flow characteristics behind the transoms of the two deepest draughts. When the transom submergence is reduced one step further ($T = T_{scantling} - 2m$), some differences appear in the shape of the recirculation zone, namely the side of the transom. In double-body computations, the dead-water zone abruptly vanishes, moving from the centre line to the side of the transom. However, FS

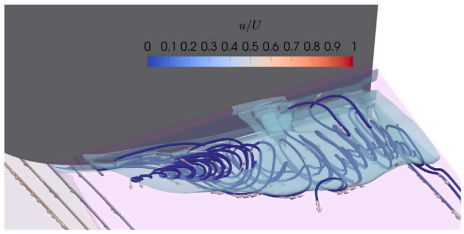

(a) FS RANS at $T=T_{scantling} - 2m$, $Fr_t = 2.29$, $tr_{ratio} = 0.043$

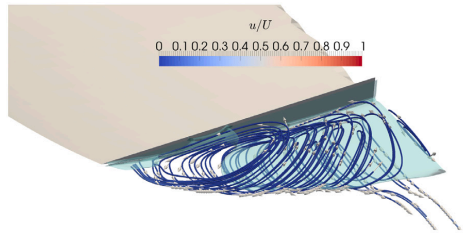

(b) DB RANS at $T=T_{scantling} - 2m$, $Fr_t = 2.29$, $tr_{ratio} = 0.043$

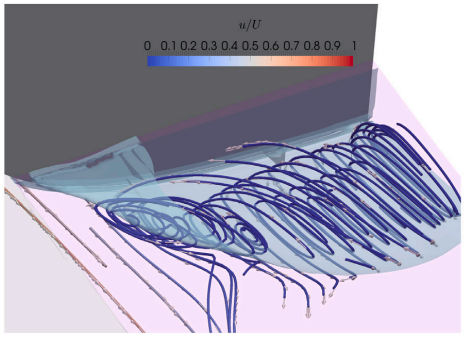

(c) FS RANS at $T=T_{scantling} - 1m$, $Fr_t = 1.62$, $tr_{ratio} = 0.10$

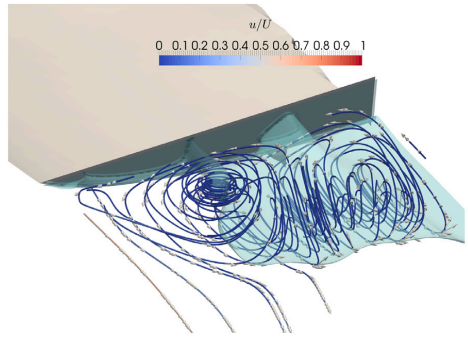

(d) DB RANS at $T=T_{scantling} - 1m$, $Fr_t = 1.62$, $tr_{ratio} = 0.10$

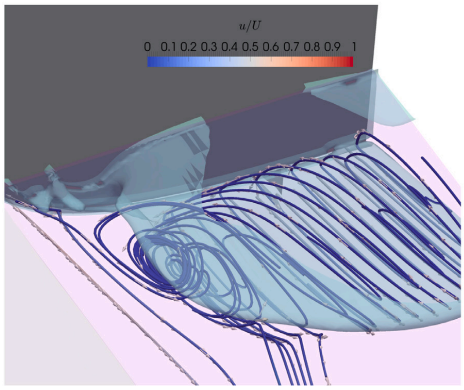

(e) FS RANS at $T=T_{scantling}$, $Fr_t = 1.37$, $tr_{ratio} = 0.16$

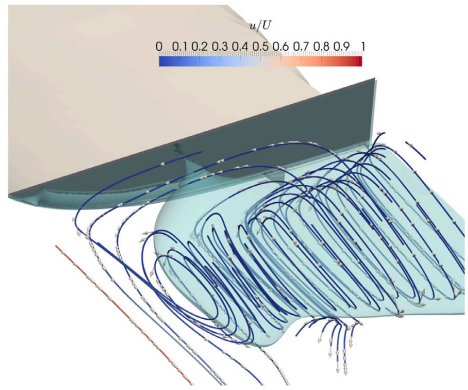

(f) DB RANS at $T=T_{scantling}$, $Fr_t = 1.37$, $tr_{ratio} = 0.16$

Fig. 7. Local flow behind the transom of the H1 test case (port side only) at various draughts at *full scale* at $Fr = 0.172$ using EASM turbulence model. (For interpretation of the references to colour in this figure legend, the reader is referred to the web version of this article.)

RANS results indicate a more gradual shrinkage of recirculating flow region, as observed in Fig. 7(a). This difference between DB and FS computations may lead to slightly under-predicted form factors for the cases where the transom submergence is rather small as the momentum loss can be slightly more in DB than the FS computation.

The comparison of DB and FS RANS computations in model scale are presented in Fig. 8. The conclusions from the comparison of full-scale results are also mostly valid in model scale. The flow characteristics from DB and FS are mainly similar at the original scantling draught and $T_{scantling} - 1m$. However, the light loading condition, $T_{scantling} - 2m$, shows a more significant difference in model scale than the full-scale when DB and FS results are compared. The recirculation region is notably smaller in double-body compared to free-surface, extending to the transom's side. This observation is somewhat expected since the role of the boundary layer, and the hydrodynamic pressure distribution at the transom becomes ever more critical when the submergence is decreased. Further decrease of transom submergence will lead the turbulent shear layer to create free-surface fluctuations, then give way to spill breakers, and eventually ventilation of the transom. As indicated by Maki (1997), the transition from wetted-transom to dry-transom flow regime (and vice versa) is strongly unsteady. Moreover, partially wetted-transoms are subjected to significant scale effects (Starke et al.,

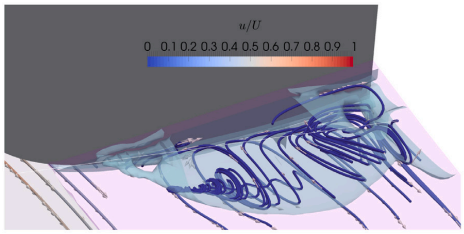

(a) FS RANS at T=$T_{scantling} - 2m$, $Fr_t = 2.29$, $tr_{ratio} = 0.043$

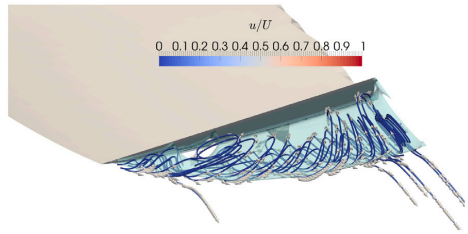

(b) DB RANS at T=$T_{scantling} - 2m$, $Fr_t = 2.29$, $tr_{ratio} = 0.043$

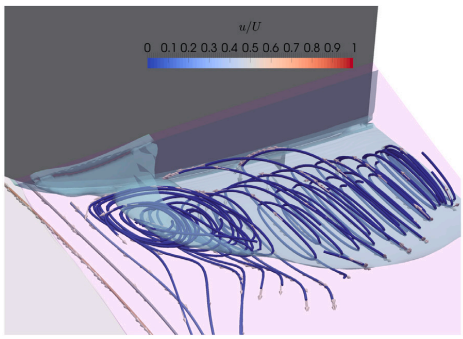

(c) FS RANS at T=$T_{scantling} - 1m$, $Fr_t = 1.62$, $tr_{ratio} = 0.10$

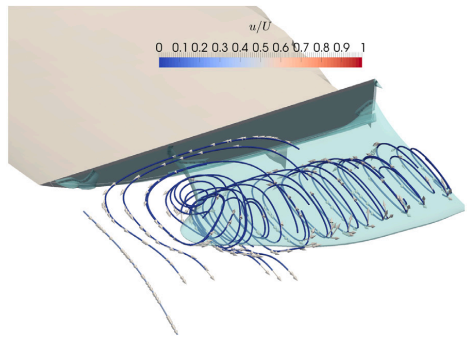

(d) DB RANS at T=$T_{scantling} - 1m$, $Fr_t = 1.62$, $tr_{ratio} = 0.10$

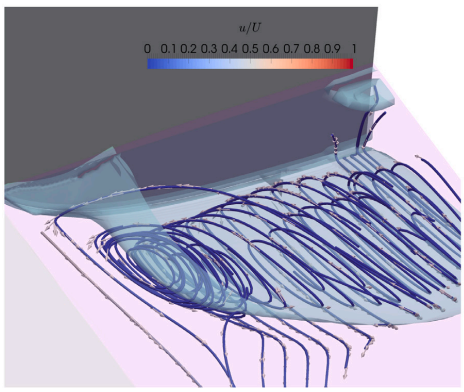

(e) FS RANS at T=$T_{scantling}$, $Fr_t = 1.37$, $tr_{ratio} = 0.16$

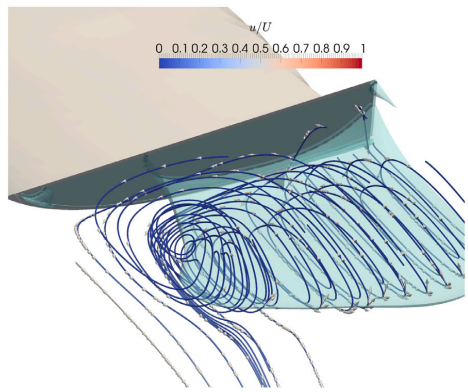

(f) DB RANS at T=$T_{scantling}$, $Fr_t = 1.37$, $tr_{ratio} = 0.16$

Fig. 8. Local flow behind the transom of the H1 test case at various draughts at *model scale* at $Fr = 0.172$ using EASM turbulence model.

2007). Therefore, the partially wetted transoms are outside this study's scope as the double-body computations cannot simultaneously capture the correct flow physics in model and full-scale.

6.2.2. Characterisation of the flow and the scale effects

As shown earlier, the flow behind the transom is largely similar for double-body and free-surface computations when the transom is substantially submerged. Therefore, the local flow of H1 is suitable for further investigation using the DB computations. In Fig. 9, the u/U contours have been presented for model and full-scale at a position that is slightly behind the transom ($x/L_{PP} = -0.03$ where $x/L_{PP} = 0$ is the aft perpendicular). As expected, velocity contours indicate that u/U is shrinking in the region outside the wake of the transom from model to full-scale. However, the flow behind the transom shows little to no change even though the Reynolds number is greatly increased from model to full-scale. The limiting streamlines are generated at the $x/L_{PP} = -0.03$ and $x/L_{PP} = -0.13$ slices together with the u/U contours as presented in Fig. 10. The limiting streamlines just behind the transom indicate only marginal difference between model and full-scale as can be seen from the Figs. 10(a) and 10(c). Except at both ends of the transom edge (bold black line), the limiting streamlines converge behind the transom (similar to a vortex sheet separation). They follow nearly identical paths in model and full-scale. When the flow downstream is investigated as shown in Figs. 10(c) and 10(d), a large vortex is observed near the side of the transom for both model and full-scale. In addition, the bilge vortex can also be seen at approximately $z/l_{PP} = 0.04$ near the centre plane. When model and full-scale computations are compared, the wake behind the hull, including the bilge vortex size, shrinks with the increasing Re. However, the same cannot be stated for the large vortex generated behind the transom. These observations are

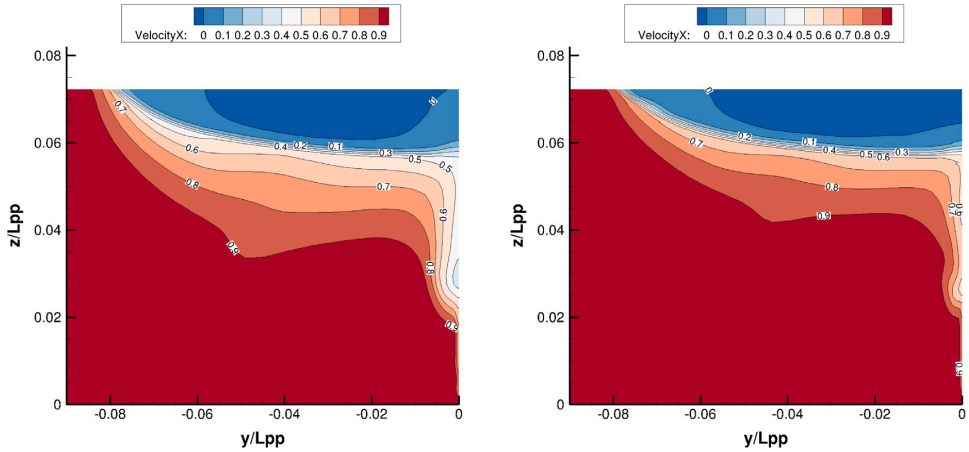

Fig. 9. Local flow behind the transom of the H1 test case at scantling draught at model (left) and full (right) scale using EASM turbulence model.

the foundation reasons for the authors to propose dividing the C_{PVM} term, i.e. form resistance (Hughes, 1954), into two parts (Eq. (4)): C'_{PVM} and $C_{tr\mathbf{M}}$. The former term aims to capture the change of C_{PVM} proportional to the frictional resistance coefficient, while the latter term represents the part of the form resistance that is not proportional to C_F.

The u/U contours with limiting streamlines are presented in Fig. 11 for the other two draughts, $T_{scantling} - 2m$ and $T_{scantling} - 1m$. The local flow for the latter loading condition shows the same tendencies as the deepest draught. However, the lightest draught indicates a somewhat different local flow between model and full-scale. The clearly defined converged limiting streamlines disappeared as opposed to the other conditions. Instead the limiting streamlines are converged to approximately $y/l_{PP} = 0.03$ at model scale and $y/l_{PP} = 0.02$ in full scale.

6.2.3. The effect of turbulence modelling

The prediction of the local flow quantities in the stern region is highly dependent on the choice of the turbulence model, as concluded at the 2015 Tokyo CFD Workshop (NMRI, 2015). The comparison of the extensive local flow measurements and the CFD results with varying turbulence models indicated that two-equation models underpredict the longitudinal vorticity significantly compared to the anisotropic models (Hino et al., 2020). On the other hand, the mean absolute error of resistance predictions in the Tokyo 2015 Workshop (as well as in the 2010 Gothenburg Workshop Larsson et al., 2014) was smaller for the two-equation models than for the anisotropic models. Therefore, it is relevant to investigate further the local flow obtained from k-ω SST and EASM turbulence models. In Fig. 12, the iso contours of the second invariant of the velocity gradient tensor $Q = 10$ (coloured by vorticity) are presented together with the streamlines around the transom using the same grid (double-body assumption) with k-ω SST and EASM turbulence models in model scale. It can be observed in Fig. 12(a) that even with definitive V-type stern sections, a bilge vortex is generated, and its extension is marked by the Q iso surface from the results from EASM. However, k-ω SST indicates a relatively weak longitudinal vorticity as the Q iso-surface following the stern bulb dies out quickly. Similar observations were also concluded by Hino et al. (2020) since more longitudinal vorticity with the EASM turbulence model was associated with increased vorticity production thanks to turbulence anisotropy.

The large vortex initiated from the side of the transom, which was also highlighted in Fig. 10(c), are clearly depicted by the iso contours of the second invariant of the velocity gradient tensor for both turbulence models as seen in Fig. 12. It is worth mentioning that the difference between the turbulence closures is significantly less for the vortex trailing the side of the transom compared to the vortex trailing the stern bulb. This observation can be explained by the role of the boundary layer in making the vortices. As argued earlier, the flow behind the substantially submerged transoms is not too dependent on the boundary layer generated along the hull. The recirculating flow region, however, shows modest differences between the two turbulence models. The iso wake contours (u/U) from the k-ω SST and the EASM turbulence models are presented in Fig. 13 which shows that the flow reattachment point is further downstream for the EASM compared to the k-ω SST both in model and full-scale. In other terms, the recirculation region is slightly larger for the EASM turbulence model as it is commonly observed for the non-linear anisotropic turbulence closures (Hino et al., 2020). It is concluded that there are indeed minor differences in resistance and the local flow predictions between the two turbulence models. However, the main conclusions about the flow characteristics and scale effects are valid for both turbulence closures.

6.3. Quantitative analysis of results

In this section, the results of approximately 450 double-body computations will be investigated quantitatively. This analysis is initially aimed to check if there are relationships between the relative change of form factors from model to full-scale and the geometrical transom parameters (see Section 3), ship hydrostatics, and the Reynolds number. In case definitive relations are discovered, the next goal of the quantitative analysis is to describe these relations with an equation, as explained in the next section, so the corrections for the transom submergence can be applied even without using CFD.

All seven hull forms were computed at their respective design or scantling draughts and additional draughts with even keel conditions in model and full-scale. Except for the KCS hull form, the other hulls already featured submerged transom at their respective design or scantling draughts. Therefore, the selection of additional draughts other than the original loading conditions was made to cover lighter and heavier loading conditions. However, the KCS hull form was only submerged more than the original design draught in successive steps. Additionally, the effect of trim was investigated on two hull forms by trimming the vessels by the bow and stern. The pivot point for applying the trim was the midship of the vessels, and summation of the change in forward

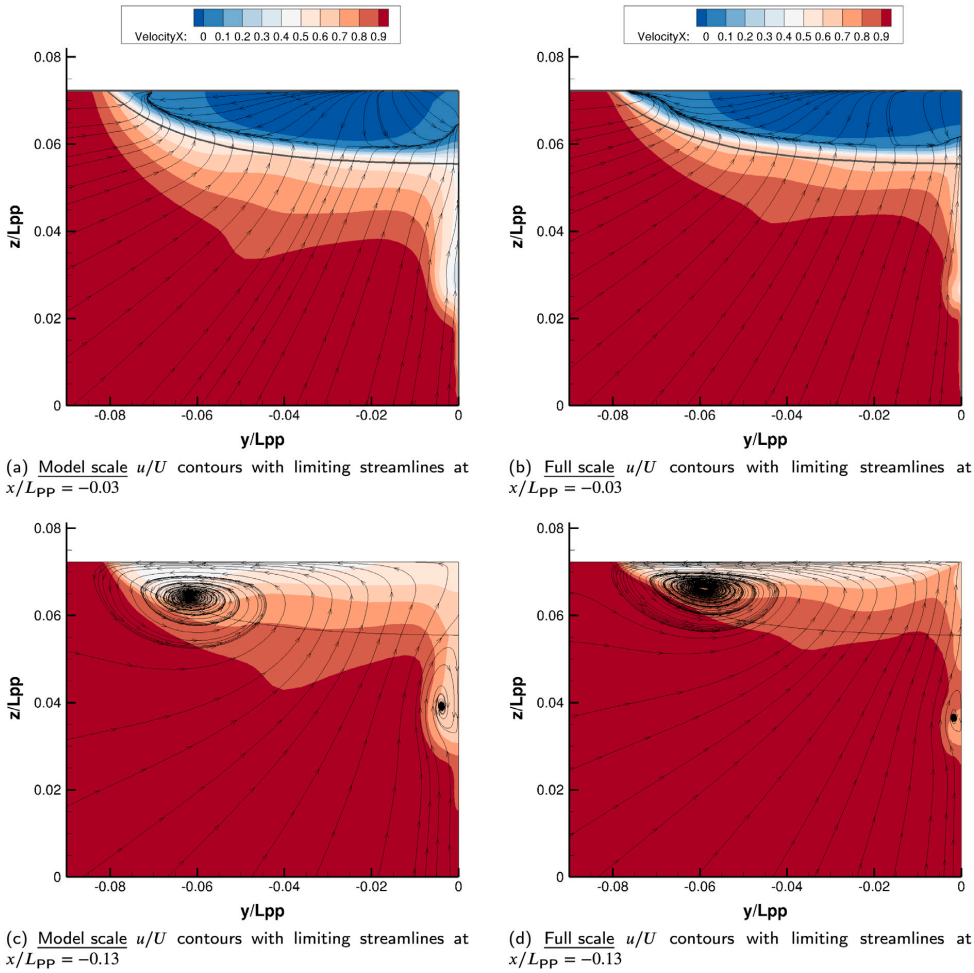

(a) Model scale u/U contours with limiting streamlines at $x/L_{PP} = -0.03$

(b) Full scale u/U contours with limiting streamlines at $x/L_{PP} = -0.03$

(c) Model scale u/U contours with limiting streamlines at $x/L_{PP} = -0.13$

(d) Full scale u/U contours with limiting streamlines at $x/L_{PP} = -0.13$

Fig. 10. Local flow behind the transom of the H1 test case at scantling draught ($T_{scantling}$) at model (left column) and full (right column) scale using EASM turbulence model.

and aft draughts equated to the trim. Finally, the same two hulls were also used for investigating the Reynolds Number effects by varying the "scale factor" of the model.

The qualitative analysis of the flow behind the substantially submerged transom revealed that the flow separation is neither disappearing nor shrinking proportionally to the frictional resistance coefficient. Therefore, using the standard ITTC-78 method for the resistance extrapolation (i.e. the Hughes (1954) form factor assumption) will result in under-prediction of the viscous resistance, as illustrated in Fig. 2. On the other hand, in the case of a hull with a bubble type separation in model scale and without a transom stern submergence, the effect is the opposite since this flow separation is likely to diminish in full scale; hence, the viscous resistance will be over-predicted. In order to quantify the deficiency (transom submergence) or the surplus (bubble type separation) of the extrapolated full-scale viscous resistance, the "error" caused by the Hughes hypothesis when there is flow separation can be expressed as

$$E = C_{VS} - C'_{VS} \,, \tag{9}$$

where C_{VS} is the true full-scale viscous resistance, and C'_{VS} is the extrapolated full-scale viscous resistance based on the standard ITTC-78 method (see Fig. 2). In this study, C_{VS} is directly obtained from the full-scale double-body RANS computations, while C'_{VS} is calculated as

$$C'_{VS} = C_{FS}(1 + k_M) \,, \tag{10}$$

where C_{FS} is the full-scale frictional resistance coefficient obtained from a friction line, and k_M is the CFD based form factor obtained from model-scale DB RANS computations.

The error defined in Eq. (9) can represent the two different separation types;

- persistent separation, which occurs in both model and full-scale (e.g. large transom submergence),

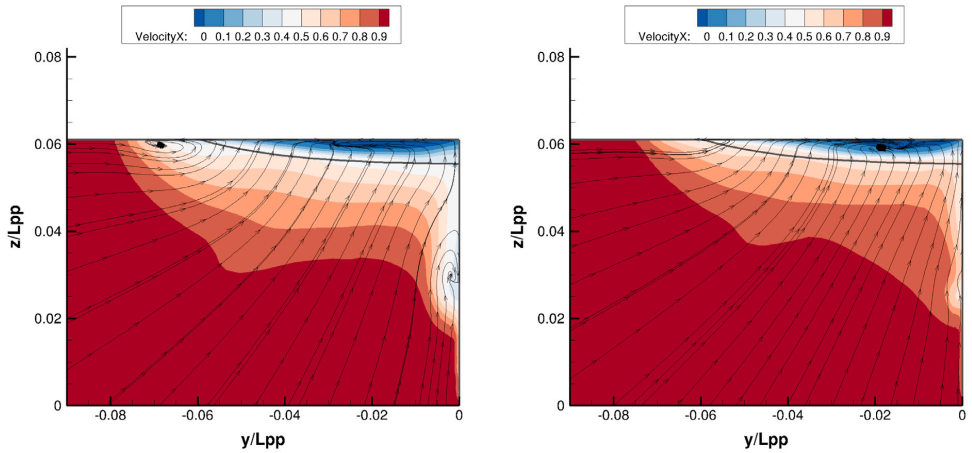

(a) Model scale at $T=T_{scantling} - 2m$, u/U contours with limiting streamlines at $x/L_{PP} = -0.03$

(b) Full scale at $T=T_{scantling} - 2m$, u/U contours with limiting streamlines at $x/L_{PP} = -0.03$

(c) Model scale at $T=T_{scantling} - 1m$, u/U contours with limiting streamlines at $x/L_{PP} = -0.03$

(d) Full scale at $T=T_{scantling} - 1m$, u/U contours with limiting streamlines at $x/L_{PP} = -0.03$

Fig. 11. Local flow behind the transom of the H1 test case at various draughts at model (left column) and full (right column) scale using EASM turbulence model.

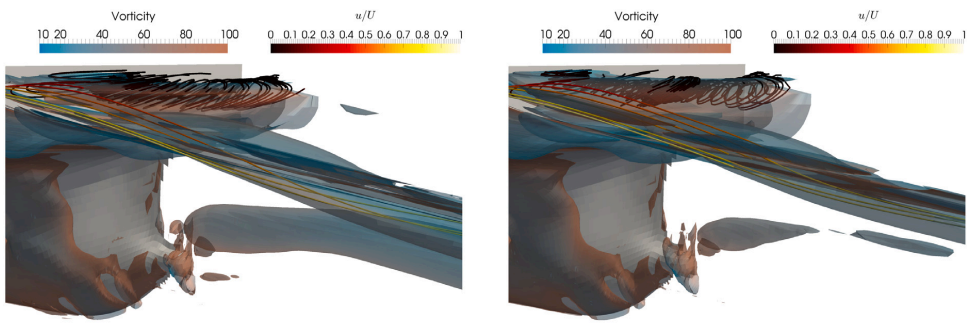

(a) EASM

(b) k-ω SST

Fig. 12. The iso contours of the second invariant of the velocity gradient tensor, $Q = 10$, at the stern of H1 at scantling draught and model scale. (For interpretation of the references to colour in this figure legend, the reader is referred to the web version of this article.)

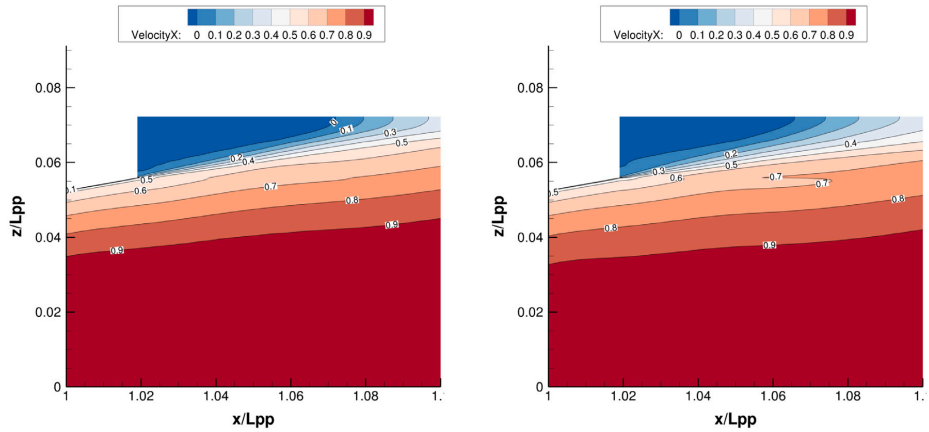

(a) Model-scale V_x contours at $y/L_{PP} = -0.02$ with EASM

(b) Model-scale V_x contours at $y/L_{PP} = -0.02$ with k-ω SST

(c) Full-scale V_x contours at $y/L_{PP} = -0.02$ with EASM

(d) Full-scale V_x contours at $y/L_{PP} = -0.02$ with k-ω SST

Fig. 13. Local flow behind the transom of the H1 test case at scantling draught at model (left column) and full (right column) scale.

- and separation occurs in model scale but not in full scale (e.g. bubble type separation around the stern bulb).

The error term in Eq. (9) can also be expressed similar to a form factor,

$$k_{error} = \frac{C_{VS} - C'_{VS}}{C_{FS}} = \frac{C_{FS}(1+k_S) - C_{FS}(1+k_M)}{C_{FS}} \tag{11}$$

where $C_{FS}(1+k_S)$ is the viscous resistance obtained from the full-scale CFD computation, $C_{FS}(1+k_M)$ is the extrapolated full-scale viscous resistance using the model-scale form factor, and C_{FS} is the full-scale frictional resistance coefficient obtained from a friction line. Formulation of the error similar to a form factor makes the quantification of the error possible to perform one computation at each scale instead of computations carried out at each speed. The Eq. (11) will not be valid; however, if the flow separation size and character vary significantly within the model-scale Reynolds numbers. For example, a vessel with a substantially submerged transom for which the transom does **not** run wet throughout the speed range is not too suitable for the form factor representation of the error as in Eq. (11).

As discussed in Section 2, the viscous pressure resistance was decomposed into C'_{PVM} and C_{trM} where the latter indicated the form resistance that is not proportional to the friction line. Keeping Fig. 2 in mind and assuming that there is no bubble-type flow separation at the stern (which is true for all test cases used in this study), the formulation of k_{error} can also be written as

$$k_{error} \simeq k_{tr} = \frac{C_{trS}}{C_{FS}} \,. \tag{12}$$

where k_{tr} is called as the *transom form factor*. Hence, the deficit of the viscous resistance when the model-scale form factor, k_m, was used for the extrapolation from model to full-scale is quantified as k_{tr} shown in Eq. (12). As discussed in Section 6.2, the flow separation is persistent for the case of a substantial transom in both model and full-scale hence C_{trS} must exist. However, when there is no submerged transom and no flow separation in the flow, C_{trM} and C_{trS} terms disappear (as in Fig. 1) and the form factor in model and full-scale becomes equal. This hypothesis (Hughes, 1954) was thoroughly tested by Korkmaz et al. (2020, 2021, 2019a), and confirmed that the form factors in model and full-scale are nearly the same when there is no flow separation in the flow, and an appropriate friction line is used. In order to disregard the

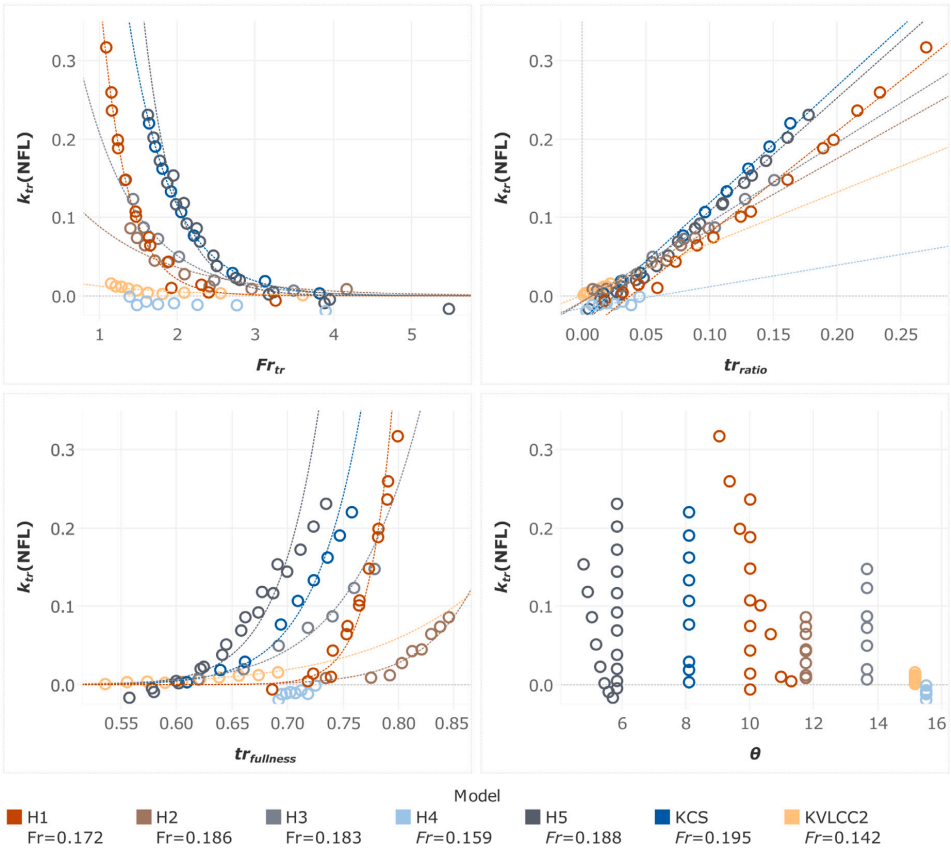

Fig. 14. Transom form factors with k-ω SST model vs. transom parameters; transom Froude number (top left), tr_{ratio} (top right), $tr_{fullness}$ (bottom left), and θ (bottom right). (For interpretation of the references to colour in this figure legend, the reader is referred to the web version of this article.)

scale effects on form factor caused by the usage of the ITTC-57 model to ship correlation line, the two numerical friction lines (NFL) (Korkmaz et al., 2019b) of the same CFD code and turbulence model were used. It was shown in Korkmaz et al. (2021) that usage of NFLs nearly eliminated the speed dependency of CFD based form factors. Therefore, quantification of C_{trS} term will be more accurate when the NFLs are used rather than the ITTC-57 line.

The transom form factor values have been calculated using the numerical friction line (Korkmaz et al., 2019b) and plotted in Fig. 14 against the transom parameters explained in Section 3. The Froude number of each test case is constant and noted in the legend of Fig. 14. The first parameter to investigate is Fr_{tr}, which is often used as an indicator (even with limited validity) of the flow regime behind the transom. As observed in the top-left Fig. 14, the k_{tr} values of all hulls (except H4) reasonably follows the exponential curves fitted for each hull. An exponential curve cannot be fitted to the k_{tr} values of H4 since they are slightly below zero, which indicates that flow separation behind the transom disappeared or decreased its size when the Re is increased from model to full-scale. The second observation is that there are three distinct clusters of points as the Fr_{tr} decreases, which is equivalent to increased transom submergence as the speed was kept the same. The three different clusters are in line with the type of vessels; the flattest curve is followed by the very large, high block, slow steaming vessels (H4 and KVLCC2); the cluster in the middle is medium to small sized high block vessels (H1, H2 and H3); the cluster of the point that follows the steepest curve are the slender and fast going vessels (H5 and KCS). As it is for determining the flow regime behind the transom, the Fr_{tr} values alone cannot indicate which k_{tr} values should be expected. However, all k_{tr} values tend to converge towards zero after $3.5 < Fr_{tr}$ where the flow regime is likely to be partially wetted or fully dry and not suitable for double-body computations.

The second transom parameter to investigate in Fig. 14 is tr_{ratio} (see Section 3). The ratio between the submerged area of the transom and the maximum cross-section area at rest indicates a highly linear correlation with the k_{tr} values. The linear lines fitted to the k_{tr} values of each hull indicate similar slopes for most hulls except the H4 and KVLCC2. It should also be noted that as the tr_{ratio} values decreases, k_{tr} values converge towards zero ($k_M \approx k_S$) as expected.

The third parameter, $tr_{fullness}$, indicates how full the transom edge section is, and it is presented in the bottom right scatter plot in Fig. 14. It can be observed that no specific trend exists neither among the hulls nor similar ship types. Hence, the V-shaped or U-shaped transom seems to play little to no role in the quantity of the transom form factor.

The last parameter plotted in Fig. 14 against the k_{tr} is the slope of the stem profile near the transom, θ (see Fig. 3(b)). Similar to $tr_{fullness}$, the θ angle does not appear to have a significant effect on k_{tr}. Instead, the submerged transom area can be regarded as the most influential parameter for the transom form factor. In other terms, the size of the

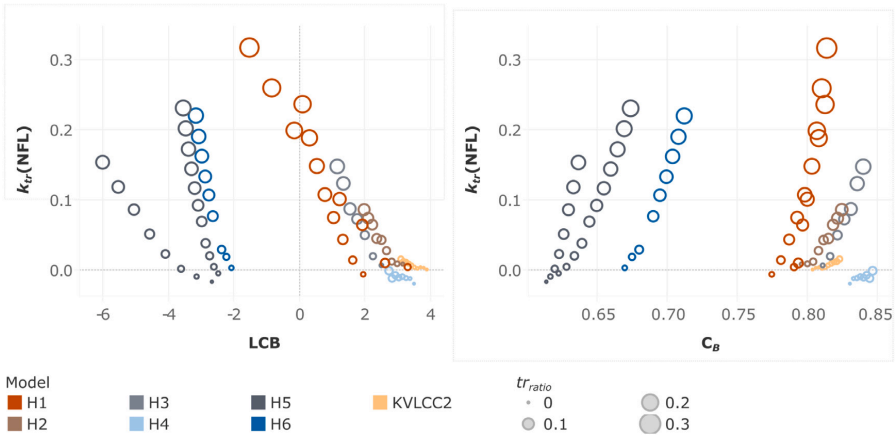

Fig. 15. Transom form factors with k-ω SST model versus hydrostatics; centre of buoyancy, rel. to $L_{pp}/2$ (left), block coefficient (right).

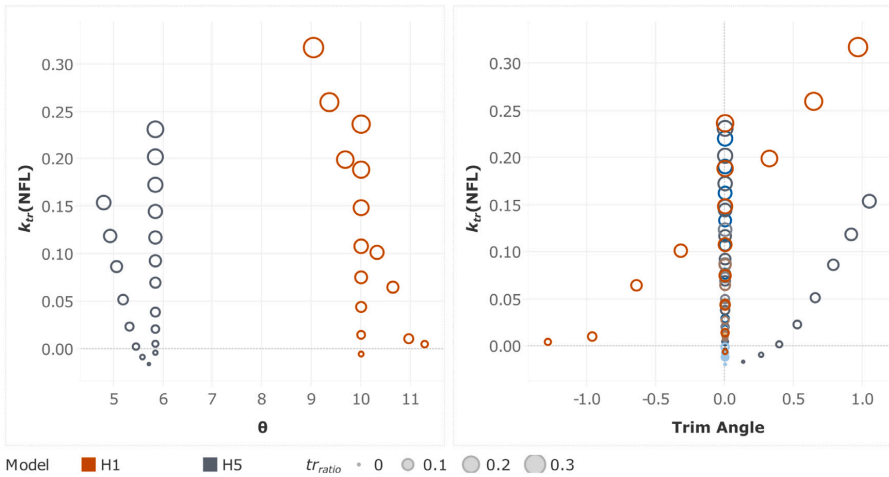

Fig. 16. Transom form factors with k-ω SST model versus trim angle (right) and stem profile angle near transom (left).

viscous resistance deficiency, C_{trS}, is mainly dependent on the area of the submerged transom.

In addition to the transom parameters, hydrostatics are compared against k_{tr} values. As presented in Fig. 15; LCB, and C_B are plotted against the transom form factor. The same colour scheme is kept for distinguishing different hull forms, but the markers are sized with respect to tr_{ratio} values of the corresponding computation. It can be observed in Fig. 15 that changing the draught or trimming the vessel has a large effect on the hydrostatics. At first, increasing the block coefficient or shifting the LCB to stern may seem to increase k_{tr}. However, when the marker sizes (tr_{ratio}) are also taken into account, it can be argued that the effect of hydrostatics on k_{tr} values is rather limited. As discussed earlier in Section 6.2, the recirculating flow did not largely dependent on the boundary layer generated along the hull, which will certainly be affected by the significant changes in the hydrostatics. Later investigations on LCB showed that the longitudinal centre of buoyancy is indeed instrumental in the determination of the slope of the linear tr_{ratio} vs k_{tr} relations between the high and low block vessels as explained in Section 7.

The two vessels trimmed around the midship, H1 and H5, are plotted against k_{tr} and presented in Fig. 16. The slender H5 vessel was only trimmed by the stern as the transom will rise out of the still water level if trimmed by the bow. As can be seen in Fig. 16, trimming the vessel by the stern has a substantial effect on the tr_{ratio}, and as a result, increases the k_{tr} values sharply. However, when the trim angle is considered together with the θ angle, it can be argued that trimming the vessel has no substantial effect on its own as quite different trim angles (or θ) with similar tr_{ratio} values result in similar k_{tr} values.

After the submerged transom area, the second most important factor is the Reynolds number at the model and full-scale for the size of the transom form factor. As argued earlier, the form factor is not independent of the Reynolds number in the case of a wetted-transom; hence, the difference between the model and full-scale form factors will increase or decrease when the model-scale or full-scale Re substantially changes. The model-scale Re of H1 and H5 were changed successively while the full-scale Re and loading condition kept the same, and the k_{tr} values were plotted against the Reynolds number and C_F in Fig. 17. As expected, the gap between the model and full-scale form factors, k_{tr}, decreases as the Re in the model scale increases.

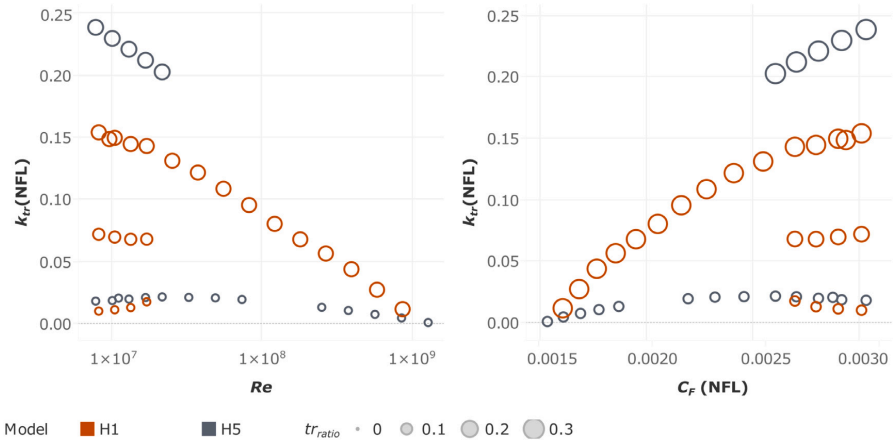

Fig. 17. Transom form factor with k-ω SST model against Reynolds number and frictional resistance coefficient derived from ITTC-57 line.

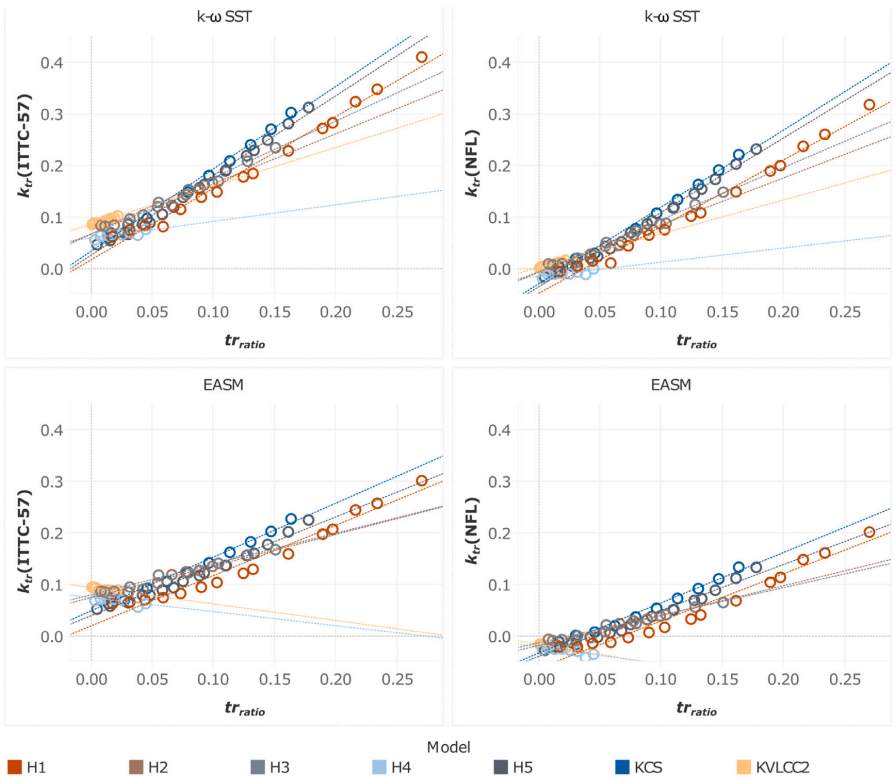

Fig. 18. Transom form factors based on ITTC-57 line (left column) and NFL (right column) for k-ω SST (top row) and EASM (bottom row) turbulence models.

The importance of the friction line for the CFD based form factors cannot be overstated since the validity of the form factor hypothesis (Hughes, 1954) entirely depend on it. Earlier studies (García Gómez, 2000; Toki, 2008; Pereira et al., 2017; Terziev et al., 2019; Wang et al., 2015; Korkmaz et al., 2020, 2021; Raven et al., 2008; Wang et al., 2015; Dogrul et al., 2020) indicated that there are scale effects on form factors when the ITTC-57 model to ship correlation line is used. However, scale effects on form factors were reduced with the usage of Katsui line (Katsui et al., 2005), and it nearly disappeared when numerical friction lines of the same code and turbulence model were used as the

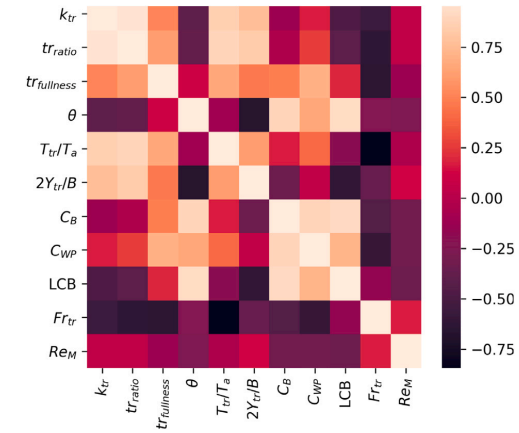

Fig. 19. Correlation matrix for the possible regression variables, colours represent the correlation values.

double-body RANS computation (Korkmaz et al., 2020). As can be seen in Fig. 18, the k_{tr} values when ITTC-57 line was used (indicated as k_{tr}(ITTC-57) in y-axis) approaches towards approximately 0.05 for both turbulence models when the tr_{ratio} is near zero, i.e. close to no transom submergence and no flow separation. Instead, the model and full-scale form factors should have been equal ($k_{tr} = 0$) as is observed when the numerical friction lines (indicated as k_{tr}(NFL) in the y-axis) were used, as shown in Fig. 18.

The other critical subject is the choice of turbulence closure which becomes more important when there is a flow separation. As can be seen in Fig. 18, the EASM model not only predicted lower k_{tr} values than the k-ω SST model in general but also presents a significantly lower slope of k_{tr} with regards to the tr_{ratio}.

7. An empirical correction for transom submergence

The existence of flow separation in model or full-scale makes the form factor approach of current recommended procedures for scaling of the towing tank tests (ITTC, 2021a) invalid, as noted by the ITTC (2021e, p. 11). As explained in Section 2, the $2-k$ method was proposed to take into account all kinds of flow separation, including the recirculating flow behind the transom. However, the $2-k$ *method* requires capabilities of double-body RANS computations in model and full-scale where an organisation is required to demonstrate (ITTC, 2021d): a Best Practice Guideline (BPG), quality assessment of the BPG, and demonstration of quality. An alternative empirical correction method is developed for

- a quick and approximate quantification of the transom form factor where many different loading conditions were model tested, such as trim optimisation tests,
- organisations that do not have the CFD capabilities.

The resistance caused by a wetted-transom can be explained in an analogy with airfoil shapes with truncated trailing ends. As explained in Starke et al. (2007), it can be considered that "the transom stern resistance as a 'base drag' as occurs on aerodynamic shapes with cutoff trailing ends. This base drag is caused by a reduction of the hydrodynamic pressure on the base, caused by the 'jet-pump' effect of the surrounding flow that exerts an entraining force on the recirculation region aft of the base". The investigations of Hoerner (1965) on projectiles and foil shapes with truncated trailing edges concluded that relatively simple equations could largely model the base drag. Therefore, an attempt has been made to obtain an empirical correction formula through a regression analysis of the results presented in Section 6.3.

The regression analysis is based on predicting the k_{tr} values from the k-ω SST model and the numerical friction line. As argued earlier and presented in Fig. 18, the k_{tr} values from the ITTC-57 line include the scale effects introduced by the friction line itself; hence, they cannot be used for quantification of viscous resistance deficit in full scale. Additionally, the form factor predictions from EFD and CFD in the model scale compared significantly better with the k-ω SST model.

The independent variables for the regression model are determined through an initial check on the correlation between the dependent variable, k_{tr}, and the correlation between the independent variables to sustain non-collinearity. The correlation matrix is presented in Fig. 19 for the dependent and all independent variables considered. It can be seen that the correlation between k_{tr} and tr_{ratio} is highest (0.98), while the correlation between k_{tr}, T_{tr}/T_a (where T_a represents draught at the aft perpendicular), and $2Y_{tr}/B$ variables are followed with 0.85 and 0.79. Keeping in mind Fig. 3, tr_{ratio} parameter can be considered as the combination of the T_{tr}/T_a, and $2Y_{tr}/B$ parameters, and also there is high collinearity among them. Therefore, the T_{tr}/T_a, and $2Y_{tr}/B$ parameters are disregarded and instead the tr_{ratio} values are used as the first independent variable.

As can be seen in Fig. 19, there are no other independent variable that is highly correlated with k_{tr}. However, the effect of the Reynolds number on the k_{tr} was significant, as shown in Fig. 17 and must be considered. Therefore, the Reynolds number in the model scale, Re_M, was chosen as the second independent variable.

After initial attempts of regression analysis with k_{tr} and Re_M, an additional independent variable was added to capture the slight difference between low block and high block vessels, which can be seen in Fig. 14. Therefore, the longitudinal centre of buoyancy (relative to $L_{pp}/2$) was added to the regression model. The scatter plots for all independent and dependent variables are presented in Fig. 20 together with the histograms. It can be argued that a large spectrum of all three variables is covered by results from the seven hull forms in various loading conditions and Reynolds numbers.

As a result of the regression analysis, the equation below is suggested, (see Box I) where $\overline{Re_M}$ is the average of Reynolds numbers in the model scale, and the LCB is relative to $L_{pp}/2$ (in per cent of L_{pp}).

The comparison between the k_{tr} values from CFD and the empirical correction formula (Eq. (13)) is presented in Fig. 21(a). The agreement between the two prediction methods is deemed satisfactory, and the standard deviation of the residuals (subtraction of k_{tr} values from CFD and the empirical) is approximately $\sigma = 0.010$. Considering that the numerical uncertainties are 2%–3% in model and full-scale double-body RANS computations, the residuals are small enough. They somewhat resemble a normal distribution as shown in Fig. 21(b) to conclude the empirical correction formula.

The extrapolation procedure with the suggested empirical method is as follows

1. C_{TM} is obtained from the towing tank tests.
2. The model-scale form factor, k_M is determined either by the Prohaska method (Prohaska, 1966) or by model-scale CFD as described in the ITTC (2021b).
3. The residual resistance is calculated as $C_R = C_{TM} - (1 + k_M)C_{FM}$
4. The full-scale form factor, k_S, as $k_S = k_M + k_{tr}$ where
   - if $tr_{ratio} \leq 0.025$, $k_{tr} = 0$
   - if $tr_{ratio} > 0.025$, k_{tr} is calculated from the Eq. (13)
     - if the calculated $k_{tr} \leq 0$ then $k_{tr} = 0$
     - if the calculated $k_{tr} > 0$ then k_{tr} value can be used.
5. The full-scale total resistance coefficient is calculated as

$$C_{TS} = (1 + k_S)C_{FS} + \Delta C_F + C_A + C_R + C_{AAS}\ , \tag{14}$$

where,

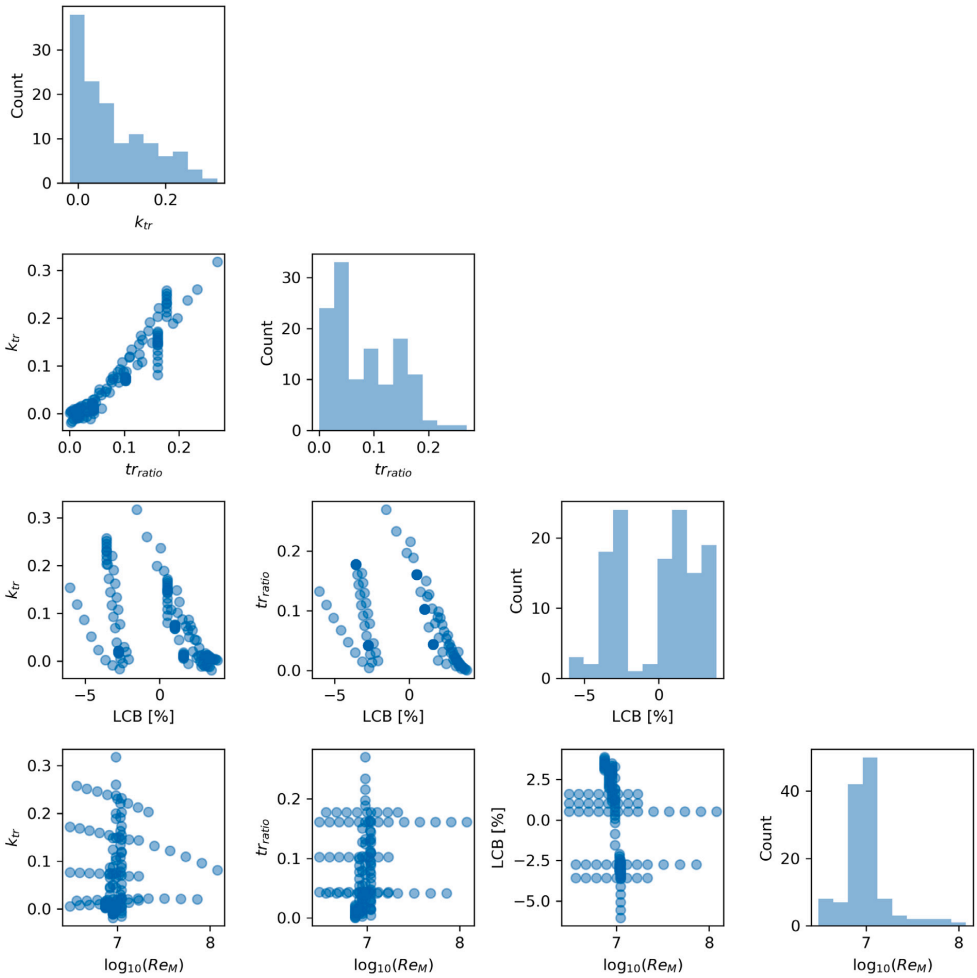

Fig. 20. Dependent and independent variables used for the regression analysis.

$$k_{tr} = \left[-0.025 + tr_{ratio}\left(1.5 - 2.3tr_{ratio} - 0.07\mathrm{LCB}\right)\right] \times \left[-5.45 + \log_{10}(\overline{Re_M})\left(1.415 + 4.32tr_{ratio}\right) - \left(\log_{10}(\overline{Re_M})\right)^2\left(0.081 + 0.55tr_{ratio}\right)\right] \quad (13)$$

Box I.

- Residual resistance is obtained by using the model-scale form factor
- Viscous resistance is obtained by using the full-scale form factor.

Note that the correction is proposed with a minimum transom area threshold since small tr_{ratio} values may result in partially wetted-transom or dry-transom flow. The limitation of $tr_{ratio} \leq 0.025$ approximately corresponds to $Fr_{tr} < 3.2$ for the test cases used in this study. According to Saunders (1957), the critical transom Froude number, after which the transom runs fully dry, is between 4 and 5. However, more recent studies on a 2D transom stern by Maki (1997) and Starke et al. (2007) indicated that approximately 2.5 is the critical Fr_{tr}. Thorough investigations by Doctors (2003) on the partly wetted-transom and dry transom flows resulted in a regression model which predicts the water surface drop with respect to the calm water level. Further extensive experiments by Robards and Doctors (2003) on flat-bottomed and rectangular-shaped transoms confirmed the critical Fr_{tr}

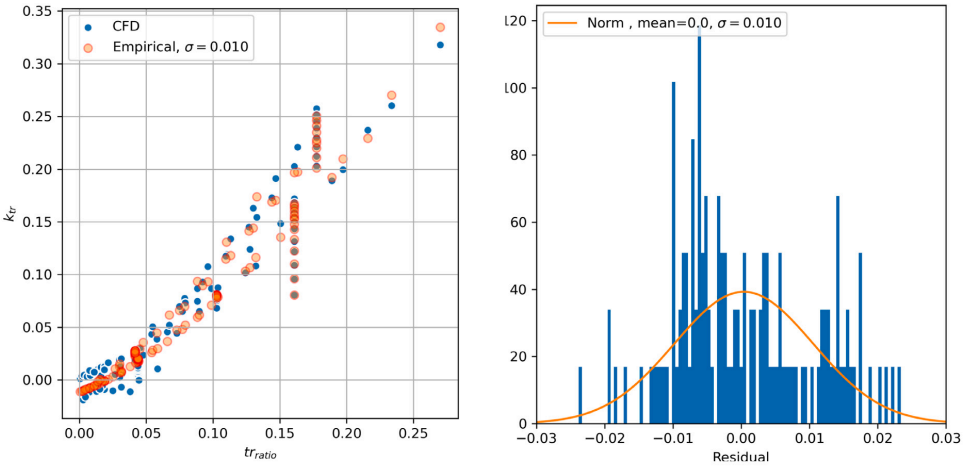

(a) k_{tr} predictions from the CFD and the empirical correction Eq 13

(b) Residuals of the regression model

Fig. 21. Local flow behind the transom of the H1 test case at scantling draught at model (left column) and full (right column) scale.

as approximately 2.5. A re-analysis of this study (Doctors, 2006) proposed an improved regression model to predict the water depreciation level behind the transom. The regression model of Robards and Doctors (2003) and Doctors (2006) were tested against the FS RANS computations presented in Section 6.2.1 to check if they could provide an accurate threshold for the empirical correction proposed in this study. The comparison of the water level predicted by the FS RANS and the regression models of Robards and Doctors (2003) and Doctors (2006) indicated opposite trends. The regression models predict that the H1 test case at the lowest draught should be almost completely in the dry-transom flow regime; however, the FS RANS computations indicate a wetted-transom (see Figs. 7 and 8). A similar observation was noted by Maki et al. (2006) where the transition of the transom flow from wet to dry for a realistic ship model was predicted prematurely by a nearly identical regression model by Doctors (2006). Based on the earlier studies, it is concluded that the prediction of the flow regime behind the transom by simple regression models is not reliable enough. The flow behind the transom depends on the overall geometry of the vessel and the wave pattern generated by the hull (Maki et al., 2006); therefore, it is recommended that the flow regime should be confirmed for small transom submergence with the help of FS RANS computations or model tests. In the case of a dry-transom or partially wetted-transom, the double-body assumptions are violated (in model or full-scale), which is a case that Eq. (13) is no longer valid regardless of the tr_{ratio} value.

7.1. Demonstration of the 2 − k method and the empirical correction procedure against the sea trials

In this study, two methods are proposed for taking into account the effects of substantial transom submergence, which is lacking in the literature and the current 1978 ITTC Performance Prediction Method (ITTC, 2021a). This section compares full-scale speed-power relations between the speed trials and full-scale predictions based on model tests. Unfortunately, due to the extreme scarcity of speed trials performed at design or scantling draughts where the transom is submerged at rest, only ten trials of sufficient quality (Werner and Gustafsson, 2020) belonging to the four hulls (H1, H2, H3, H4) could be used for the comparison.

The comparison between the speed trial measurements and the model test power predictions was performed through the correlation factors (ITTC, 2017a) used in the 1978 Performance Prediction method (ITTC, 2021a). Among three different schemes of correlation factors, C_P–C_N method was used. In this study, the correlation factor, C'_P, is calculated as

$$C'_P = \frac{P_{D\ trial}}{P_{D\ tank}} \tag{15}$$

where the $P_{D\ trial}$ is the power from a speed trial, while $P_{D\ tank}$ represents the corresponding prediction based on the model test. After individual C'_P values for each speed trial are calculated, an assembled correlation factor, C_P, is obtained by taking the median of C'_P of all trials. Due to confidentiality, the assembled correlation factors are not disclosed, but the normalised C'_P values of each prediction method are presented by shifting the median of each prediction method to 1.

The standard deviation of the normalised C'_P is considered the measure of success for different prediction methods as it was the main criterion for the determination of the original ITTC 1978 Performance Prediction Method. Considering that the precision and bias limits of a single-speed trial result amounts to nearly 10% total uncertainty as indicated by Werner and Gustafsson (2020) and Insel (2008), a meaningful reduction in scatter (standard deviation) is expected to claim an improvement confidently.

Normalised correlation factors of each hull are calculated using the same model tests results, which were extrapolated with different prediction methods,

- the standard ITTC-78 method (ITTC, 2021a) using the Prohaska method where the model and full-scale form factors are equal,
- $2 - k$ form factor method using separate CFD based form factors in model and full-scale (see Section 2),
- and the empirical correction method using Prohaska method for form factor in model scale and the corrected form factor in full scale (see Section 7).

The power predictions were made with the ITTC-57 model to ship correlation line (ITTC, 1957). In addition, the vessels with an energy-saving device ahead of the propellers were treated with a special wake scaling suggested in the ITTC 1999 method (ITTC, 1999). As explained earlier, only the calculation method of form factors in the model and full-scale differs among the three methods.

The normalised correlation factors, C'_P, are calculated for the speed trials with low to acceptable uncertainty levels, which indicates the

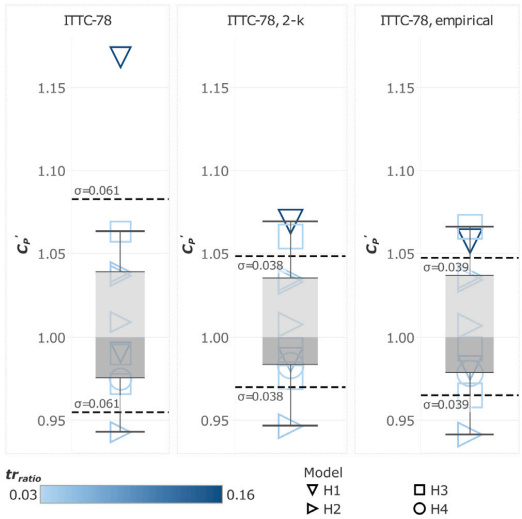

Fig. 22. Normalised correlation factors from the standard ITTC-78 method (left), CFD based $2-k$ form factor method (middle), and the empirical correction procedure (right).

trustworthiness of each speed trial by summarising the most significant error sources and weighting them according to their impact on the results. C'_P values of each prediction method are presented in Fig. 22 where the tr_{ratio} of each hull is distinguished with colour, and the different hulls are represented with different markers, the standard deviations (σ) of C'_P is presented with horizontal dashed lines, and the box plots can be identified with the grey colour, and sized with the lower and upper quartiles with the whiskers extending to the data within 1.5 times the interquartile range (IQR).

The normalised correlation factors for the standard ITTC-78 method are presented in Fig. 22 (left). It can be observed that all but the H1 hull at the scantling draught were predicted within approximately $\pm 5\%$. However, the H1, which has the largest transom submergence, is greatly under-predicted by nearly 16% which is far greater than the uncertainty of a single-speed trial. According to the findings of this study, this result is expected. All hulls except the H1 at the scantling draught have relatively small transom submergence ($tr_{ratio} < 0.049$), which requires marginal corrections, i.e. the standard ITTC-78 method should mostly work well.

C'_P values from the CFD based $2-k$ form factor method is shown in Fig. 22 (middle). Compared to the predictions from the standard ITTC-78 method, the scatter (σ) was reduced from 0.061 to 0.038 when the $2-k$ form factor method was used. This reduction was largely possible thanks to the improvement in the prediction of the H1 possessing large transom submergence but also the minor improvements in all other hull forms. In order to judge the success of the $2-k$ form factor method, further analysis was performed on the size of the standard deviation. As seen in Fig. 22, two of the hulls have sister ships (different speed trials) which indicate up to 9% difference in measured power from speed trials. As discussed thoroughly in Korkmaz et al. (2021), relatively large standard deviations of C'_P are mainly due to the scatter in the speed trials of the sister ships. To demonstrate this claim, an ideal prediction condition was prepared. The ideal condition is that the mean of C'_P of a series of sisters (H2 and H3) and single trials (H1 and H4) would be 1. The standard deviation in the ideal prediction scenario yields $\sigma = 0.035$, which is very close to the scatter observed from the $2-k$ form factor method predictions.

Moving to the empirical correction procedure presented in Fig. 22 (right), the similarity of the predictions between this method and the $2-k$ method is remarkable. The scatter was effectively reduced compared to the standard ITTC-78 method; however, slightly higher than the $2-k$ form factor method. This result is somewhat expected since the form factor correction, k_{tr}, was derived from a relatively simple equation (Eq. (13)) instead of a full-scale double-body RANS computation, as is the case for the $2-k$ form factor method.

8. Conclusions

This paper investigates the wetted-transom flows often observed for the vessels with substantially submerged transoms. First, the assumptions underlying the form factor approach were discussed. Then, the shortcomings of the current 1978 ITTC Performance Prediction Method have been explained when there is a flow separation in the boundary layer surrounding the vessel. Finally, after a detailed qualitative and quantitative analysis of the wetted-transom flow, two alternative procedures were proposed to take into account the effects of the recirculating water behind the transom.

As recognised by the ITTC, the current recommended procedures of the form factor approach for any vessel with a substantial transom stern for which the transom runs wet is not valid. It is demonstrated that the form factor is not independent of the Reynolds number when there is flow separation in the boundary layer. When the same model and full-scale form factors are used to extrapolate the resistance, the full-scale viscous resistance is under-predicted in the case of a wetted-transom flow.

The two form factor method, a combined EFD/CFD method, is proposed as an alternative to the current ITTC-78 extrapolation procedure. The $2-k$ method replaces the extrapolated full-scale viscous resistance with the CFD based viscous resistance, which includes

- the form resistance that is proportional to the frictional resistance coefficient, such as the additional skin friction caused by curvature effects, flow in transverse directions, and eddy-making (typical form resistance),
- the contribution of the flow separation behind the transom that is not proportional to the frictional resistance coefficient.

Dividing the model-scale viscous pressure coefficient into two parts, $C_{PVM} = C'_{PVM} + C_{trM}$, is based on the observations on the flow features

- the shrinking of the axial velocity component, u/U, in the region outside of the wake of the transom, which indicates little to no change as the Reynolds number is increased from model to full-scale,
- the large vortex near the side of the transom close to the water surface remaining nearly the same in both scales.

This division of the form resistance is instrumental in quantifying the viscous resistance deficit emerging when the standard ITTC-78 method is used for the vessels with wetted-transom. The deficit of C_{VS} is formulated as a fraction of the frictional resistance coefficient, i.e. the transom form factor k_{tr}. It is observed that k_{tr}

- is almost exclusively correlated with the submerged area of the transom
- showed no tangible trends for the section shape of the transom ($tr_{fullness}$) or the slope of the buttocks of the stern overhang (θ)
- is highly Reynolds number dependent; hence, different model sizes may result in significantly different k_{tr} values.

The regression analysis on the transom form factor indicated that the deficit of C_{VS} can be modelled with a relatively simple equation. Therefore, an empirical correction procedure is also suggested in addition to the $2-k$ method. The empirical equation (Eq. (13)) is derived so that it can be integrated into the current 1978 ITTC Performance

Prediction Method with a simple modification of the full-scale form factor. Furthermore, the suggested empirical correction is compatible with the Prohaska method of determining the model-scale form factor and the ITTC-57 model to ship correlation line.

The power predictions from the two proposed procedures were compared to the predictions from the standard ITTC-78 method and the speed trials. The conclusions regarding the comparison of the full-scale predictions and speed trials are that:

- The precision is improved compared to the standard ITTC-78 method.
- The sample size of the validation cases is somewhat limited, but the improvement achieved by both suggested procedures is significant and in line with the theory.
- The main contributor of the standard deviation of the normalised correlation factors originates from the scatter of the speed trials among the sister ships. The standard deviation of C'_p is noticeably close to the minimum value that could be obtained (the ideal condition) from the speed trials when the $2-k$ method is used with the $k-\omega$ SST turbulence model.

In this paper, the wetted-transom flow characteristics were explained together with the shortcomings of the current ITTC Performance Prediction method, and two alternative methods were presented. The two form factor method, which combines EFD and CFD, is expected to provide immediate improvements to the power predictions of the vessels with any type of flow separation, including the wetted-transom flow due to substantial transom submergence. The empirical correction method, which requires no CFD, can be incorporated into the current ITTC-78 method as a second alternative. It can accurately restore the deficit of the extrapolated full-scale viscous resistance in the event of a wetted-transom flow. The two suggested alternative methods are expected to be instrumental in improving the accuracy and reliability of the EEDI predictions performed at the scantling draught, where the transoms of many vessels are submerged.

Further studies should be performed with more test cases, especially hulls with large transom submergence, where the speed trials are available. However, considering the extreme scarcity of sea trial data carried out at design or scantling draught where the transom is submerged at rest, free-surface RANS computations can be considered to predict full-scale conditions. As the correction required for a deeply submerged transom can be significantly large, the accuracy of state-of-the-art full-scale CFD computations may suffice to test the proposed alternative methods.

CRediT authorship contribution statement

Kadir Burak Korkmaz: Conceptualization, Methodology, Validation, Formal analysis, Investigation, Data curation, Writing – original draft preparation, Writing – review & editing, Visualization. **Sofia Werner:** Conceptualization, Methodology, Investigation, Writing - review & editing, Supervision, Project administration, Funding acquisition. **Rickard Bensow:** Conceptualization, Methodology, Investigation, Writing – review & editing, Supervision.

Declaration of competing interest

The authors declare that they have no known competing financial interests or personal relationships that could have appeared to influence the work reported in this paper.

Data availability

The data that has been used is confidential.

Acknowledgements

This research was funded by Energimyndigheten, the Swedish Energy Agency, grant 2020-018759, and the computational resources provided by SSPA Sweden AB. The authors declare no conflict of interest. The funders had no role in the design of the study; in the collection, analyses, or interpretation of data; in the writing of the manuscript, or in the decision to publish the results.

References

Broberg, L., Regnström, B., Östberg, M., 2014. SHIPFLOW Users Manual. FLOWTECH International AB, Gothenburg, Sweden.

Deng, G., Visonneau, M., 1996. Evaluation of eddy-viscosity and second-moment turbulence closures for steady flows around ships. In: 21st ONR Symposium on Naval Hydrodynamics, Trondheim, Norway. pp. 453–469.

Doctors, L.J., 2003. Hydrodynamics of the flow behind a transom stern. In: Twenty-Ninth Israel Conference on Mechanical Engineering, Technion, Haifa, Israel. p. 11.

Doctors, L.J., 2006. A numerical study of the resistance of transom-stern monohulls. In: 5th International Conference on High Performance Marine Vehicles, Sydney, Australia.

Dogrul, A., Song, S., Demirel, Y.K., 2020. Scale effect on ship resistance components and form factor. Ocean Eng. 209, 107428. http://dx.doi.org/10.1016/j.oceaneng.2020.107428, URL: http://www.sciencedirect.com/science/article/pii/S0029801820304534.

Eça, L., Hoekstra, M., 2014. A procedure for the estimation of the numerical uncertainty of CFD calculations based on grid refinement studies. J. Comput. Phys. 262, 104–130. http://dx.doi.org/10.1016/j.jcp.2014.01.006.

Farkas, A., Degiuli, N., Martic, I., 2017. Numerical simulation of the viscous flow around a tanker model. Brodogradnja 68 (2), 109–125. http://dx.doi.org/10.21278/brod68208, URL: http://hrcak.srce.hr/index.php?show=clanak&id_clanak_jezik=263572&lang=en.

Farkas, A., Degiuli, N., Martić, I., 2018. Assessment of hydrodynamic characteristics of a full-scale ship at different draughts. Ocean Eng. 156, 135–152. http://dx.doi.org/10.1016/j.oceaneng.2018.03.002, URL: https://linkinghub.elsevier.com/retrieve/pii/S0029801818302336.

García Gómez, A., 2000. On the form factor scale effect. Ocean Eng. 26, 97–109.

Hino, T., Stern, F., Larsson, L., Visonneau, M., Hirata, N., Kim, J., 2020. Numerical Ship Hydrodynamics: An Assessment of the Tokyo 2015 Workshop. Springer International Publishing, URL: https://doi.org/10.1007/978-3-030-47572-7.

Hoerner, S., 1965. Fluid-Dynamic Drag. Hoerner Fluid Dynamics, Bakersfield, California.

Hughes, G., 1954. Friction and form resistance in turbulent flow, and a proposed formulation for use in model and ship correlation. R. I. N. A. 96.

IMO, 2011. Annex 19: resolution MEPC.203(62).

Insel, M., 2008. Uncertainty in the analysis of speed and powering trials. Ocean Eng. 35 (11), 1183–1193. http://dx.doi.org/10.1016/j.oceaneng.2008.04.009, URL: http://www.sciencedirect.com/science/article/pii/S0029801808000929.

Islam, H., Guedes Soares, C., 2019. Effect of trim on container ship resistance at different ship speeds and drafts. Ocean Eng. 183, 106–115. http://dx.doi.org/10.1016/j.oceaneng.2019.03.058, URL: https://www.sciencedirect.com/science/article/pii/S0029801819301477.

ISO, 2015. Ships and marine technology – guidelines for the assessment of speed and power performance by analysis of speed trial data. 15016:2015.

ITTC, 1957. Subjects 2 and 4 skin friction and turbulence stimulation.

ITTC, 1999. Report of propulsion committee.

ITTC, 2017a. Guidelines on the determination of model-ship correlation factors. ITTC – Recommended Procedures and Guidelines 7.5-04-05-01.

ITTC, 2017b. Preparation, conduct and analysis of speed/power trials. ITTC – Recommended Procedures and Guidelines 7.5-04-01-01.

ITTC, 2021a. 1978 ITTC performance prediction method. ITTC – Recommended Procedures and Guidelines 7.5-02-03-01.4.

ITTC, 2021b. Practical guidelines for ship resistance CFD. ITTC – Recommended Procedures and Guidelines 7.5–03–02–04.

ITTC, 2021c. Quality assurance in ship CFD application. ITTC – Recommended Procedures and Guidelines 7.5–03-01–02.

ITTC, 2021d. Quality assurance in ship CFD application. ITTC – Recommended Procedures and Guidelines 7.5-03-01-02.

ITTC, 2021e. Resistance test. ITTC – Recommended Procedures and Guidelines 7.5-02-02-01.

Katsui, T., Asai, H., Himeno, Y., Tahara, Y., 2005. The proposal of a new friction line. In: Fifth Osaka Colloquium on Advanced CFD Applications to Ship Flow and Hull Form Design, Osaka, Japan.

Korkmaz, K.B., Werner, S., Bensow, R., 2019a. Investigations for CFD based form factor methods. In: Numerical Towing Tank Symposium (NuTTS 2019).

Korkmaz, K.B., Werner, S., Bensow, R., 2019b. Numerical friction lines for CFD based form factor determination method. In: VIII International Conference on Computational Methods in Marine Engineering MARINE 2019.

Korkmaz, K.B., Werner, S., Bensow, R., 2021. Verification and validation of CFD based form factors as a combined CFD/EFD method. J. Mar. Sci. Eng. 9 (1), http://dx.doi.org/10.3390/jmse9010075, URL: https://www.mdpi.com/2077-1312/9/1/75.

Korkmaz, K.B., Werner, S., Sakamoto, N., Queutey, P., Deng, G., Yuling, G., Guoxiang, D., Maki, K., Ye, H., Akinturk, A., Sayeed, T., Hino, T., Zhao, F., Tezdogan, T., Demirel, Y.K., Bensow, R., 2020. CFD based form factor determination method. Ocean Eng..

Larsson, L., Raven, H.C., 2010. Ship Resistance and Flow. The Society of Naval Architects and Marine Engineers, Jersey City, New Jersey.

Larsson, L., Stern, F., Visonneau, M., 2014. Numerical Ship Hydrodynamics: An Assessment of the Gothenburg 2010 Workshop. Springer, URL: https://doi.org/10.1007/978-94-007-7189-5.

Maki, K.J., 1997. Transom Stern Hydrodynamics (Doctoral dissertation). Naval Architecture and Marine Engineering, University of Michigan, Michigan.

Maki, K., Doctors, L., Beck, R., Troesch, A., 2006. Transom-stern flow for high-speed craft. Aust. J. Mech. Eng. 3, 191–199. http://dx.doi.org/10.1080/14484846.2006.11464508.

Menter, F.R., 1994. Two-equation eddy-viscosity turbulence models for engineering applications. AIAA J. 32 (8), 1598–1605. http://dx.doi.org/10.2514/3.12149, arXiv:https://doi.org/10.2514/3.12149.

NMRI, 2015. Tokyo 2015 a workshop on CFD in ship hydrodynamics. URL: http://www.t2015.nmri.go.jp/.

Orych, M., Larsson, L., 2015. Hydrodynamic aspects of transom optimization. In: 5th High Performance Yacht Design Conference, Auckland, New Zealand. pp. 247–256.

Orych, M., Werner, S., Larsson, L., 2021. Validation of full-scale delivered power CFD simulations. Ocean Eng. 238, 109654. http://dx.doi.org/10.1016/j.oceaneng.2021.109654, URL: https://linkinghub.elsevier.com/retrieve/pii/S0029801821010301.

Pereira, F.S., Eça, L., Vaz, G., 2017. Verification and validation exercises for the flow around the KVLCC2 tanker at model and full-scale Reynolds numbers. Ocean Eng. 129, 133–148, URL: https://doi.org/10.1016/j.oceaneng.2016.11.005.

Prohaska, C.W., 1966. A simple method for the evaluation of the form factor and low speed wave resistance. In: Proceeding of 11th ITTC.

Raven, H.C., van der Ploeg, A., Starke, A.R., Eça, L., 2008. Towards a CFD-based prediction of ship performance - progress in predicting full-scale resistance and scale effects. Int. J. Marit. Eng. Trans. R. Inst. Naval Archit. A.

Regnström, B., 2008. Introduction to Overlapping Grids in SHIPFLOW. FLOWTECH International AB, Gothenburg, Sweden.

Robards, S.W., Doctors, L.J., 2003. Transom hollow prediction for high-speed displacement vessels. In: International Conference on Fast Sea Transportation, Ischia, Italy. pp. A1.19–A1.26.

Saunders, H. (Ed.), 1957. Hydrodynamics in Ship Design, Vol. 2. Society of Naval Architects and Marine Engineers, pp. 529–531.

SIMMAN, 2008. SIMMAN 2008 workshop verification and validation of ship manoeuvring simulation methods. http://www.simman2008.dk/KVLCC/KVLCC2/kvlcc2_geometry.html.

Starke, B., Raven, H., van der Ploeg, A., 2007. Computation of transom-stern flows using a steady free-surface fitting RANS method. In: 9th International Conference on Numerical Ship Hydrodynamics. p. 18.

Terziev, M., Tezdogan, T., Incecik, A., 2019. A geosim analysis of ship resistance decomposition and scale effects with the aid of CFD. Appl. Ocean Res. 92, URL: https://doi.org/10.1016/j.apor.2019.101930.

Toki, N., 2008. Investigation on correlation lines through the analyses of geosim model test results. J. Japan Soc. Naval Archit. Ocean Eng. 8, 71–79.

Tokyo, 2015. Tokyo 2015 a workshop on CFD in ship hydrodynamics. https://t2015.nmri.go.jp/kcs.html.

Wang, Z.Z., Xiong, Y., Shi, L.P., Liu, H., 2015. A numerical flat plate friction line and its application. J. Hydrodyn. 23, 383–393.

Werner, S., Gustafsson, L., 2020. Uncertainty of speed trials. In: HullPIC 2020, Rotterdam, Holland.

Paper VI

Investigations on experimental and computational trim optimisation methods

Investigations on experimental and computational trim optimisation methods

Kadir Burak Korkmaz[a,b,*], Sofia Werner[a] and Rickard Bensow[b]

[a]RISE-SSPA SWEDEN AB, Chalmers Tvärgata 10, Box 24001 Se-400 22, Göteborg, Sweden
[b]Chalmers University of Technology Sweden

ARTICLE INFO

Keywords:
trim optimisation
CFD
combined EFD/CFD methods
transom flow
ship monitoring
verification and validation

ABSTRACT

Shipping is vital for global trade but also emits significant greenhouse gases. To address this issue, various measures have been proposed, including improved ship design, alternative fuels, and improved operational practices. One such cost-effective operational measure is trim optimisation, which involves operating the ship at the hydrodynamically optimal forward and aft draughts.

This study focuses on investigating the trim trends of a RoPax vessel using experimental fluid dynamics (EFD) and computational fluid dynamics (CFD) methods. The trim trends are derived in resistance and self-propelled modes. Multiple CFD methods are examined, along with different extrapolation techniques for experimental results. Uncertainty assessment is conducted for the experimental data, and a verification and validation study is performed. Furthermore, the predictions are compared with real operational data. The findings reveal that determining trim trends solely in towed mode is inadequate due to the profound influence of the operating propeller. Some of the investigated CFD methods demonstrate good agreement with the model test results in self-propelled mode, while others exhibit limitations. By selecting appropriate models and configurations, the study demonstrates that trim trends can be determined with sufficient precision, as evidenced by the comparison between ship operational data and predictions from EFD and CFD methods.

1. Introduction

Seaborne transportation plays a crucial role in global trade by mobilising more than 80% of the cargo carried worldwide but emitting almost 3% of global greenhouse gas (GHG) emissions (IMO, 2021). According to the long-term economic and energy scenarios, IMO (2021) projects that the shipping emissions will increase by 90-130% compared to the levels of 2008 by 2050. Considering the steady growth in seaborne trade over decades and the goals set by IMO to reduce GHG emissions from shipping, one of the most feasible paths is to increase the energy efficiency of ships. In line with the vision, IMO has introduced regulations to mitigate the harmful emissions from shipping, such as the Energy Efficiency Design Index (EEDI) (IMO, 2011). The EEDI regulations aim to promote high energy efficiency designs and eliminate inefficient ships from joining the market. As calculating the EEDI index is now a mandatory step, the applicable ships must undergo pre-verification during the design phase of a new ship. Therefore, solutions towards higher efficiency that can be implemented during the design phase, such as hull form optimisation and utilising energy saving devices, gained attention.

The two new regulations introduced by IMO taking effect from the beginning of 2023, Energy Efficiency Existing Ship Index (EEXI) (IMO, 2022b) and Carbon Intensity Indicator (CII) (IMO, 2022a), are aiming to measure existing ships' energy efficiency and to monitor a ship's operational carbon intensity, respectively. IMO defines carbon intensity as a measure of GHG emissions per the amount of cargo carried over the distance travelled and sets goals to gradually reduce the carbon intensity levels (40% by 2030). Unlike the EEDI and EEXI, the CII value can also be improved by better operation of the vessel, such as speed and route optimisation, hull and propeller cleaning, lowering the power consumption of the auxiliary systems, and trim optimisation (IMO, 2023).

As noted by Bertram (2020), possible energy savings for each alternative depend on many factors, such as the ship type, hull design, interaction with other energy saving devices or techniques, ship size, and sea state. The main topic of this study, trim optimisation, is applicable to almost all vessel types and typically results in a reduction of fuel consumption ranging from 0.5% to 5%, without requiring any modifications to the vessel's design or structure (IMO, 2023). The trim of the vessel can be adjusted by loading the vessel accordingly, ballasting the vessel, or shifting ballast water between the tanks. Trim optimisation has larger energy saving potential for medium and slender vessels often trading in partial load conditions (Sames and Köpke, 2012) than the full block vessels with limited flexibility on trim variations (IMO, 2023). Moreover, each vessel's hull design and propulsion arrangement will result in different energy-saving potentials since the flow phenomena observed in combinations of different draught, trim, and speed are unique for each design.

The concept of trim optimisation originates from the fact that ship resistance and propulsive efficiency vary with different trim angles at a given displacement and ship speed. During the design phase, the hydrodynamic performance of vessels is often optimised for several loading conditions (e.g. design and ballast loading conditions) and speeds. However,

[*] Investigations on experimental and computational trim optimisation methods

[*]Corresponding author
burak.korkmaz@ri.se , korkmaz@chalmers.se (K.B. Korkmaz)
ORCID(s): 0000-0001-7136-7932 (K.B. Korkmaz)

real-life ship operations will occur not only in the 'optimised conditions' but also in partial loading conditions and speeds. The lowest propulsive power does not always occur at the even keel condition or some other fixed trim value for all combinations of different displacements and speeds. Instead, the minimum power can often be obtained at different trim angles at for various conditions and speeds. Therefore, the final design needs to be further evaluated at the design and off-design conditions by obtaining the delivered power at various displacements, trims, and speeds. This information can be used as a decision support tool by the crew. As a result, the optimum trim can be selected to achieve the minimum delivered power at a given displacement and speed during operation.

The decision support for trim optimisation can be generated in three ways: experimental methods (experimental fluid dynamics, EFD), computational methods (computational fluid dynamics, CFD), and through the analysis of real operations based on data measured by the onboard systems. The experimental method involves model testing in a towing tank, and then the model test results are extrapolated to full scale. Both steps, testing and scaling, introduce different uncertainty sources to the final predictions for the trim optimisation trends of the full-scale vessel. The measurement uncertainties related to the towing tank tests are incredibly scarce in the literature. Quantification of the measurement uncertainty is not only a valuable input to determine the confidence in the test results but a mandatory input for the validation of computational methods at model scale (Korkmaz, Werner, Sakamoto, Queutey, Deng, Yuling, Guoxiang, Maki, Ye, Akinturk, Sayeed, Hino, Zhao, Tezdogan, Demirel and Bensow, 2021b; Korkmaz, Werner and Bensow, 2021a).

The uncertainties related to the extrapolation methods are caused by the assumptions involved in scaling from the model to full-scale. As discussed in Section 2.1 and Section 2.2, the 1957 ITTC Performance Prediction Method and the 1978 ITTC Performance Prediction Method almost entirely differ in the scaling of the resistance and self-propulsion results. Moreover, the model test scope required for each extrapolation method differs; for example, the ITTC-57 method requires only self-propulsion tests, while the ITTC-78 method requires resistance, self-propulsion, and propeller open water tests. Reichel, Minchev and Larsen (2014) investigated extrapolation methods with several different assumptions, such as individual form factors or thrust deduction for each loading condition versus fixed form factor and thrust deduction obtained from the even keel loading. It was observed that the optimum trim predictions from different scaling procedures differ by varying degrees at slow, medium and high speeds. Considering that the simplified method could have decreased the towing tank scope significantly while producing somewhat comparable results to the more extensive testing and detailed extrapolation procedure, Reichel et al. (2014) concludes that the choice of the scaling procedure is a compromise between the required level of accuracy and the resources dedicated to towing tank testing.

A challenge for the extrapolation methods that may occur frequently in trim optimisation investigations is the flow recirculation behind the transom. As the trim optimisation tests are performed at trim by bow and stern, the transom submergence will likely be substantial in some stern trim conditions. If the transom is followed by a flow recirculation (i.e. wetted transom or partially dry transom), Korkmaz, Werner and Bensow (2022) showed that the recommended procedure of the International Towing Tank Committee (ITTC), ITTC-78 method, is not suitable for extrapolation because the form factor assumption (Hughes, 1954) is violated and viscous resistance is underpredicted in full scale. In such cases where the transom submergence is significant, and flow separation is observed behind the transom, a correction method was proposed in Korkmaz et al. (2022) for correcting the full-scale viscous resistance.

The second approach to determine trim optimisation trends is the computational methods. The most popular contemporary computational technique used in the literature is the free-surface (FS) Reynolds-averaged Navier-Stokes (RANS) approach (Chen, Yu and Shen, 2019; Islam and Guedes Soares, 2019; Mahmoodi, Ghamari, Hajivand and Mansoori, 2023; Mahmoodi and Hajivand, 2022; Sun, Tu, Chen, Xie and Zhou, 2016; Shivachev, Khorasanchi and Day, 2017). According to the literature mentioned, the computations are most commonly performed in model scale, and the resistance simulations are overwhelmingly more common than the self-propulsion computations. The validation of free-surface RANS computations with the experimental results indicates that the numerical methods are mature enough to reasonably provide the trim trends in model scale (Sun et al., 2016; Shivachev et al., 2017; Lemb Larsen, Simonsen, Nielsen and Holm, 2012). Recent publications presented (Mahmoodi et al., 2023; Mahmoodi and Hajivand, 2022) simulated the trim optimisation tests not only for resistance but also for self-propulsion. They concluded that the trim considerably affects the propulsive factors, and their effects are not negligible. The importance of performing self-propulsion tests was also emphasised through towing tank tests by Lemb Larsen et al. (2012) as approximately 20% of the total gain in energy efficiency originates from the increased propulsive efficiency at the optimum trim condition.

Another computational method for obtaining the trim trends is the potential flow approach. As explained in (Hansen and Freund, 2010), the potential flow code is used to obtain the wave resistance (or residual resistance), and the viscous resistance is approximated through a friction line and a form factor; hence, the total resistance is obtained for each loading condition, and trim trends are obtained. However, the potential flow fails to model highly viscous effects, such as the recirculation zone at the stern. In such cases, the trim matrix can be adjusted or calibrated with full-scale RANS computations as noted in (Hansen and Freund, 2010). The comprehensive investigations performed by Lemb Larsen et al. (2012) show that the potential flow provides similar trim guidance as the EFD and RANS approach,

but it largely underpredicts the trim trends. Additionally, the potential flow codes can experience convergence problems when the wave deformation is sharp, such as for breaking waves (Lemb Larsen et al., 2012); therefore, computing the whole trim, draught, and speed combinations poses a challenge for some ships.

According to the literature, more advanced numerical approaches such as detached eddy simulation (DES) or large eddy simulation (LES) are not commonly used for trim optimisation determination, probably due to overwhelmingly higher computational demand for DES and LES than RANS (Kanninen, Peltonen and Vuorinen, 2022).

The last approach to determine trim optimisation trends is through the analysis of real operations-based data, referred to as *ship monitoring data* in this study. Depending on the analysis type (white box numerical models, black box models, and grey box models), the ship monitoring data is used to construct a model to predict the ship's behaviour in terms of resistance or self-propulsion with a set of variables, such as ship speed, draught, trim, and environmental conditions (Coraddu, Oneto, Baldi and Anguita, 2017). As the trim is one of the independent variables (also referred to as a feature in machine learning) for the model, the trim trends can be effectively extracted, or the optimum trim can be calculated for an arbitrary loading condition and ship speed (Hüffmeier, Lundman and von Elern, 2020).

This study aims to address the knowledge gap in comparing different methods for extracting trim trends, which are crucial for decision support onboard. Previous literature lacks a comprehensive comparison of the various methods in terms of cost and accuracy. Therefore, it is important to conduct a direct comparison of these methods to determine their suitability and provide valuable guidance for selecting the most appropriate method. This study fills this gap in the literature and offers insights that can enhance decision-making processes onboard, considering both the cost and accuracy of the methods used for trim trend extraction. The scope of this study includes investigations on the trim optimisation trends of a RoPax vessel using both experimental and computational methods. Resistance and self-propulsion model tests have been performed together with an estimation of the measurement uncertainty. The model scale trim trends from the resistance and self-propulsion tests have been compared to the predictions from different CFD methods together with a thorough verification and validation exercise. Full-scale power predictions from different extrapolation methods have been calculated for each displacement, trim, and speed. The extrapolated predictions are compared to full-scale CFD predictions from two different methods. The trim trends obtained in model and full scale are discussed, and the differences are explained through flow visualisations. The final step compares the full-scale predictions to the ship monitoring data. Through the analysis of the trim trends, this paper aims to

- explain the physics behind the trim optimisation trends
- quantify the differences between the trim trends obtained at model and full scale
- assess the accuracy of different CFD methods and suggest a recommended CFD approach through verification and validation
- highlight issues with model test extrapolation methods regarding the trim optimisation tests and discuss the implications
- compare the ship monitoring data with the predictions from EFD and CFD.

Overall, this study aims to provide valuable insights into trim trend extraction methods, guiding ship owners and operators in selecting the most appropriate method.

This paper is structured as follows: Section 2 describes the experiment based model to full-scale extrapolation methods. The two flow solvers used in this study, SHIPFLOW and FINE^{TM}/Marine codes, are introduced together with the numerical methods, computational domain and boundary conditions in Section 3. In addition, a coupled CFD-empirical method is presented in Section 3 as an alternative to the full scale self-propulsion CFD computations. In Section 4, the test case used in this study is presented together with the full-scale ship monitoring data collection process, and the conditions for the experiments and computations. The details for the resistance and self-propulsion tests, the testing facility, measurement equipment and the results of the measurement uncertainty analysis are presented in Section 5. The verification and validation (V&V) results in model scale, and the verification results in full scale for resistance and self-propulsion are presented including the modified V&V procedure, and details for the grid generation in Section 6. The model scale trim trends obtained from the towing tank tests and multiple CFD methods are compared together with a discussion of the flow physics behind the trim trends, the change of the resistance components with regards to trim and the effect of a working propeller in Section 7. Section 8 presents the full-scale trim optimisation trends from different extrapolation methods, CFD computations and ship monitoring data. In addition, the implications and the shortcoming of using different model to full scale extrapolation techniques are discussed together with the scale effects observed between the model and full scale CFD computations in Section 8. Moreover, the data analysis process of full-scale ship monitoring data is explained in Section 8.4. Finally, the conclusions are summarised in Section 9.

2. EFD Based Model for Full-Scale Extrapolation Methods

In this study, three model to full scale extrapolation methods are utilised: 1957 ITTC Performance Prediction Method, the standard 1978 ITTC Performance Prediction Method (ITTC, 2021a), and the 1978 ITTC Performance Prediction Method with the empirical transom correction (Korkmaz et al., 2022). The same towing tank test results

are employed for different extrapolation methods to predict full scale speed-power relations.

2.1. 1957 ITTC Performance Prediction Method

The ITTC-57 method significantly differs from the contemporary extrapolation methods, as it does not require resistance and propeller open water tests to predict the delivered power (P_{DS}) and propeller rotation rate (n_S). To predict the power and the rate of revolutions, a self-propulsion test is required, where the model is towed at speeds that yield the same Froude numbers (Fr) as those for the full-scale ship. The propeller rate of revolutions is adjusted during each run so that the towing force (R_a) is attained. The simple extrapolation from the model (denoted with M in the subscript) to full scale (denoted with S in the subscript) is performed using with Froude's law of similarity. For each Froude number, n_S and Q_S are obtained as follows:

$$n_S = n_M/\sqrt{\lambda}, \tag{1}$$

where λ is the scale factor (ship dimension/model dimension), and,

$$Q_S = Q_M \frac{\rho_S}{\rho_M} \lambda^4, \tag{2}$$

where ρ_S is the mass density of seawater and ρ_M is the mass density of the towing tank water.

The laws of similarity in Eq. 1 and Eq. 1 are applicable when the model propeller is unloaded with the towing force, which accounts for the difference between the frictional resistance of the model and the frictional resistance of the ship converted into the model scale with a friction correction. The delivered power is calculated as

$$P_{DS} = n_S Q_S 2\pi \, . \tag{3}$$

2.2. The Standard 1978 ITTC Performance Prediction Method

The ITTC-78 method, as recommended by ITTC (2021a), is employed without any modification to extrapolate the towing tank test results to full scale. To predict the power and the propeller turning rate, tests for resistance, self-propulsion and, propeller open water are required, as the scaling procedure is more detailed than the ITTC-57 method.

As recommended in (ITTC, 2021a), the ITTC-57 model-ship correlation line (ITTC, 1957) is used in the extrapolation of the resistance. In accordance with the recommended procedure of ITTC (2021g), the form factors of each loading condition were determined by the Prohaska method (Prohaska, 1966), supplemented by the CFD based form factor method (Korkmaz et al., 2021b,a; ITTC, 2021d,e). The scaling of the resistance is performed with the assumption that the form factor is the same in the model and full scale, even though the form factor prerequisite of not having separated flow (Hughes, 1954) , violated in some loading conditions due to a partially wet transom.

The scaling of the resistance, propeller open water, and self-propulsion tests are explained in detail in the procedures (ITTC, 2021g), (ITTC, 2021c), and (ITTC, 2021a), respectively.

2.3. ITTC-78 Method with Empirical Transom Correction

This method is identical to the standard 1978 ITTC Performance Prediction Method for extrapolating propeller open water and self-propulsion tests, but it differs in the scaling of the resistance from model to full scale.

As mentioned in Section 2.2, some loading conditions involve substantial transom submergence, causing transom flow to be wetted or partially wetted. As explained by Korkmaz et al. (2022), wetted transom flow results in flow separation behind the transom, rendering the form factor approach recommended in current procedures for scaling of the resistance invalid (ITTC, 2021g, p. 11). Therefore, the model and full-scale form factors are distinguished. The model scale form factor (k_M) remains the same as the standard ITTC-78 method (Section 2.2) and is obtained from the Prohaska and CFD-based form factor methods. The full-scale form factor (k_S) is calculated

$$k_S = k_M + k_{tr} \, , \tag{4}$$

where the k_{tr} is obtained from the empirical formula described in Korkmaz et al. (2022). The total resistance coefficient in full scale

$$\mathrm{C_{TS}} = (1 + k_S)\mathrm{C_{FS}} + \Delta\mathrm{C_F} + \mathrm{C_A} + \mathrm{C_R} + \mathrm{C_{AAS}}, \tag{5}$$

where k_S is the full scale form factor, $\mathrm{C_{FS}}$ is the frictional resistance coefficient, $\mathrm{C_R}$ is the residual resistance coefficient, $\Delta\mathrm{C_F}$ represents the roughness allowance, $\mathrm{C_A}$ is the correlation allowance, and $\mathrm{C_{AAS}}$ is the air resistance coefficient. Similarly to the ITTC-78 method, the residual resistance in Eq. 5 is assumed to be the same in model and full-scale and it is obtained as

$$\mathrm{C_R} = \mathrm{C_{TM}} - (1 + k_M)\mathrm{C_{FM}}, \tag{6}$$

where $\mathrm{C_{TM}}$ is the total resistance coefficient (the subscript 'M' signifies the model scale).

3. Computational Methods

The SHIPFLOW and FINE$^{\mathrm{TM}}$/Marine codes were employed for the computations. The former was utilised for the double-body RANS and the potential flow computations, while the latter was employed for the free-surface RANS simulations related to resistance and self-propulsion.

3.1. Double-Body RANS – SHIPFLOW

SHIPFLOW version 6.5 was used to solve the steady state viscous flow. The solver, XCHAP, is based on the finite volume method (Broberg, Regnström and Östberg, 2014), and it can handle only structured grids. The grids for each loading condition were generated with SHIPFLOW's grid generator, XGRID. The hull was generated as a single block of structured grid and, the rudder, which is included in the form factor determination, was modelled in the computations using the overlapping grid technique Regnström (2008). The no-slip boundary condition was implemented

using the wall resolved approach. Therefore, the first cell size in the normal direction to the hull was selected to ensure that the non-dimensional cell size y^+ value would be lower than 0.25 on average. The double-body computations were computed using the $k-\omega$ SST (Menter, 1994) turbulence model. Further details regarding to the flow solver, grid generation, computational domain, and boundary conditions can be found in Korkmaz et al. (2021a), where the quality assurance, as described in ITTC (2021f), was demonstrated for the CFD based form factor calculation method. This study followed the best practice guidelines outlined in Korkmaz et al. (2021a), with the exception of the domain size, which was increased longitudinally by a factor of 2 in the present study.

3.2. Fully Nonlinear Potential Flow

The fully nonlinear potential flow solver of SHIPFLOW Motions version 7.0 was employed to obtain the wave resistance for each loading condition. The solver includes an unstructured automatic free surface mesh generator with adaptive grid refinement capability. However, in this project, the discretization of the hull and the rudder (the other appendages were too far from the free surface and thus ignored) was performed manually. The grid density at the aftbody was generated especially fine because the solver keeps track of which grid panels are wet and thereby includes them in the boundary value problem. This precaution was taken since some loading conditions resulted in the stern waves just skimming the stern overhang; hence, the finer stern grid would provide more accuracy in determining the wetness. For more details about the SHIPFLOW Motions solver, see Kjellberg, Gerhardt and Werner (2022).

3.3. RANS-VOF

FINE$^{\text{TM}}$/Marine computing suite version 10.2 is used for the free-surface RANS computations. The incompressible RANS equations were solved with the ISIS-CFD flow solver based on the finite volume method. The face-based method is generalised for a multitude of grid types, including the three-dimensional unstructured grids. The velocity field is obtained from the momentum conservation equations, and the pressure is extracted from the continuity equation. In the same way as the momentum equations, the transport equations for turbulence modelling is discretized and solved. The AVLSMART discretisation scheme is used for both momentum and turbulence transport equations. All free-surface RANS computations were performed in steady state with $k-\omega$ SST (Menter, 1994) turbulence model (Menter, 1993). The detailed description of the solver is presented in Queutey and Visonneau (2007).

The free surface is modelled with a multi-phase flow approach (i.e. Volume of Fluid, VOF). In ISIS-CFD, the Blended Reconstructed Interface Capturing Scheme (BRICS) scheme is used for the multi-fluid discretization scheme. Further details regarding the surface capturing method used in ISIS-CFD are given in Wackers, Koren, Raven, van der Ploeg, Starke, Deng, Queutey, Visonneau, Hino and Ohashi (2011).

The unstructured hexahedral grids were generated with the HEXPRESS$^{\text{TM}}$ module of the FINE$^{\text{TM}}$/Marine suite. The volume-to-surface approach is utilised for generating the non-conformal body-fitted full hexahedral unstructured grids around the hull and the appendages. Boundary layers were inserted between the no-slip wall and the surrounding hexahedral grids, as seen in Figure 1a. The grids were further refined with a local zone of refinement near the free surface in the entire domain to eliminate large grid spacing in the z-direction. The free surface refinement covers approximately all the draughts, while its extension in longitudinal and lateral directions was not restricted. In the case of self-propulsion, an additional cylindrical local refinement region is added just around the actuator disc to eliminate interpolation errors between the background grid and actuator disc. Further grid refinements were performed with the help of the Adaptive Grid Refinement (AGR) technique (Wackers, Deng, Guilmineau, Leroyer, Queutey and Visonneau, 2014) while the computation is running. The usage of AGR in the context of this study is thoroughly explained in Section 6.1.

Instead of generating separate grids for each loading condition and speed, one grid is generated per speed. For example, the model scale resistance computations for three speeds, three trims, and two displacements (six loading conditions, eighteen computations) were performed with three sets of grids. For each grid corresponding to a certain speed, only the first cell size normal to the no-slip wall is varied to aim for the same y^+ value. Hence, three grids only vary marginally in the boundary layer cells but are identical elsewhere. For a given speed, the base grid is generated for the static even keel (zero trim) heavy displacement condition. The grids for the other five loading conditions (aft and fore trims at heavy and light displacement) for each speed are obtained by an analytically weighted mesh deformation technique for body motion. In all computations, the body is fixed in surge motion but free to sink and heel. Therefore, the mesh is effectively deformed to follow the body motion.

The computational domains for all computations are shaped as a rectangular prism. The distances between the inlet to the fore perpendicular and the outlet to the aft perpendicular are 1.5 L_{PP} and 3 L_{PP}, respectively. The side of the domain is 2 L_{PP} from the centre-plane. The top and bottom boundaries of the domain are 1 L_{PP} and 1.5 L_{PP} from the baseline, respectively.

The solid wall boundaries (hull and the appendages) are modelled with a wall-law boundary condition in model and full-scale computations. The full-scale self-propulsion computations were performed with roughness, which is also modelled through a wall function approach. The sand-grain roughness height of 30 μm is chosen to represent the typical anti-fouling coating as recommended by Schultz (2007). Thanks to the twin-screw propulsion arrangement, both resistance and self-propulsion computations were computed with the symmetry condition at the centre-plane. The inlet, outlet, and the side boundaries are classified as far-field condition, which can be Dirichlet or a Neumann condition depending on the local entering or leaving the domain. The

top and bottom boundaries are set as Dirichlet condition that is based on the prescribed pressure, which is updated based on the hydrostatic pressure to account for the mesh moving vertically or the free surface position. The fluid is free to enter or exit from the top and bottom boundaries, simulating the unconstrained water depth and air.

The effect of the propellers was simulated with the actuator disc model of the ISIS-CFD solver. The body force terms from the actuator disc are included in the momentum equations of the cells where the centre of a control volume is located inside the actuator disc. The force distribution around the actuator disc can be default, uniform, user-defined or can be calculated with a propeller code. In this study, the default distribution (with normal and tangential forces) is used for self-propulsion computations. The torque and propeller rotation rate are predicted with the help of the propeller open water curve (POW). The POW values of K_T and K_Q against J were not computed with CFD but adopted from the model tests. The full-scale computations were performed with the extrapolated POW curves according to ITTC (2021c). The thrust of the actuator disc equals the drag in absolute value. However, external forces were applied to the hull in the model (the towing force R_a) and full scale (air resistance). Therefore, the thrust equals the summation of the drag and external force vectors but with a negative sign. The thrust, torque, and propeller turning rate are updated at every time step.

3.4. Combined RANS-VOF Resistance and Empirical Propulsion Model

This method is considered as an alternative to the full-scale propulsion CFD computations, which are considerably more resource-demanding compared to the resistance computations. Therefore, the alternative method uses the full-scale resistance values from the CFD computations and predicts the propulsive performance with an empirical method.

The empirical method is based on statistical analysis and the propeller open-water curves of the standard propeller series of SSPA. The thrust deduction, full-scale wake fraction, and relative rotative efficiency are obtained from a statistical analysis of SSPA's database, which has more than 8000 model test results. Through filtering of the relevant ship types, main dimensions, non-dimensional coefficients (i.e. block coefficient, LCB position, etc.), and propulsive arrangement, the propulsive factors were obtained. The changes in thrust deduction, full-scale wake fraction, and relative rotative efficiency with respect to the trim are also gathered from earlier trim optimisation tests.

In the empirical prediction program, the propeller diameter, pitch of the propeller at 70% radii, propeller type (fixed and controllable pitch), number of blades, and blade area ratio are entered as input. From the standard propeller series of SSPA, the relevant open-water curves are obtained. Using the full-scale resistance computations with FINE$^{\text{TM}}$/Marine (see Section 3.3), propulsive factors, and propeller characteristics, the delivered power and propeller rotation rate for the full-scale ship are predicted.

In this study, the test case is a twin-screw vessel; hence, the burden on the computational resources is not extremely different between full-scale resistance and self-propulsion computations. However, for a single skeg vessel, both sides of the hull have to be discretized for the self-propulsion computations. In addition, instead of an actuator disk, the propeller geometry can also be discretized (sliding mesh). In such cases, the required computational resources for a complete trim optimisation test scope will greatly differ between the resistance and self-propulsion computations. Therefore, the combined CFD and empirical method can be a cost-efficient alternative.

4. Test Case, Full-Scale Data Collection, Experimental and Computational Conditions

The test case used in this study is a RoPax vessel that was built more than a decade ago and is still in operation. The vessel operates only between two harbours; hence, the route remains the same. The vessel has a twin-screw propulsive arrangement. Each shaft line is tilted and supported by shaft bossings, an I-bracket, and a V-bracket. The transversal positions of the rudders are positioned nearly at the same y-position as the shaft line. In terms of hull lines, shaft arrangement, propulsion setup, and the propeller design, the test case can be considered as an ordinary RoPax vessel; however, due to the confidentiality of the hull lines and the propulsive arrangement, the images or drawings cannot be shared in this paper.

The trim optimisation scope is determined by a statistical analysis of the ship monitoring data. As a result, three speeds and two displacements were selected. The two displacements are named as light (denoted L) and heavy (called H) throughout the paper. Three trim conditions, 1.5 m trim by the bow, even keel, and 1.5 m trim by stern, were model tested. The trim is calculated as

$$trim = T_f - T_a \tag{7}$$

where T_f is the draught at the fore perpendicular, and T_a represents the draught at the aft perpendicular. As a result of the Eq. 7 convention, the trim by the bow is represented with a positive sign (trim>0), while the trim by the aft is shown with a negative sign (trim<0) in the paper.

The experimental conditions are thoroughly explained in Section 5.1. The model scale computations replicated the same conditions (speed, temperature, salinity, the model geometry as built, towing force in the self-propulsion computations, etc.).

The full-scale computations were performed for seawater at 15°C. The superstructure of the vessel was not included in the computations. Instead, the same geometry as the model scale was used in full-scale computations, and the resistance due to air resistance is added as an external force in the computations. The air resistance was calculated as in ITTC (2021g) for each loading condition (two displacements

Table 1
The components and the combined expanded uncertainties in percentage of the average forces for all loading conditions and the speed corresponding to 15 kn

	L+1.5m n =2, t_{95}=12.71	L n =2, t_{95}=12.71	L-1.5m n =2, t_{95}=12.71	H+1.5m n =2, t_{95}=12.71	H n =4, t_{95}=3.18	H-1.5m n =4, t_{95}=3.18
Wetted area	0.180	0.180	0.180	0.179	0.179	0.179
Speed	0.128	0.128	0.128	0.128	0.128	0.128
Water temp.	0.021	0.021	0.019	0.021	0.021	0.018
Water Density	0.003	0.003	0.003	0.003	0.003	0.003
Dynamometer	0.298	0.295	0.261	0.292	0.281	0.245
Repeat test, Deviation	3.058	3.479	5.650	1.674	1.539	0.785
Combined for single test (prediction limit)	3.080	3.499	5.660	1.714	1.580	0.852
Repeat test, Deviation of mean	1.765	2.009	3.262	0.967	0.688	0.351
Combined for test avg (confidence limit)	**1.804**	**2.042**	**3.280**	**1.034**	**0.775**	**0.482**

and three trims). All computations were calculated for deep and unconstrained waters.

4.1. Ship Monitoring Data

The ship is equipped with a multitude of sensors that monitor and record the condition of the ship (draught at fore and aft perpendiculars, heel angle, speed over ground, speed through water), environment (current, depth below keel, water temperature, apparent and true wind speed and direction, now-casting based swell and wave height and period), and the performance of the vessel (propeller turning rate and shaft torque per propeller, fuel consumption). The data received from the ship owners start from 2015 to 2022, with a time interval of 10 minutes between each measurement. Installation of the sensors and collection of the ship monitoring data are performed by the ship owners; hence, the scope of this study is limited to the analysis of the collected data.

5. Model Tests

Based on the drawings from the ship owner, a model made of plastic foam material called Divinycell was manufactured at SSPA with a 5-axis CNC milling machine. The appendages (shaft bossings, I-bracket, and V-bracket) were produced with high-precision 3-D printing, and the rudder was milled out of wood. After the surface finishing and painting, a 1mm thick trip wire was mounted at 5% of L_{PP} aft from the fore perpendicular for the turbulence stimulation. The model is equipped with all the appendages, rudders, and dummy propeller hubs for the resistance tests.

The model tests were performed at SSPA's 260m long, 10m wide, and 5 meters deep towing tank. The complete scope of the test matrix, covering two displacements and three trim angles, was completed by the tests carried out in February and October of 2022. Two of the six loading conditions were repeated in both testing sessions, while the other four were tested only in October. Total resistance, sinkage, and trim were measured at each loading condition for three speeds. No blockage correction was applied to the measurements, as the area of the maximum transverse section of the model among all loading conditions is 0.64% of the sectional area of the tank, and the depth Froude number is low.

5.1. Measurement Uncertainty Analysis of the Resistance Tests

The uncertainty analyses of measurements of the total resistance in the resistance tests were performed according to ITTC (2021b). In an earlier study, the measurement uncertainty of KVLCC2 in ballast loading condition was presented in Korkmaz et al. (2021b) where ITTC (2014) was used. It should be noted that the procedures outlined in ITTC (2014) and ITTC (2021b) are broadly similar procedures. One of the main differences is the presentation of the uncertainties, which are reported as expanded uncertainty (95% confidence interval) in ITTC (2021b). The individual uncertainty components, wetted area, speed, water temperature, water density (absent in ITTC (2014)), dynamometer, repeat test deviation, and the combined uncertainties for the test average will be explained and presented in this section.

The uncertainties regarding the wetted surface area are quantified by measuring the model ballasting, i.e. the model and calibrated weights. Each calibrated weight (typically around 25 pieces) could not be measured for all six loading conditions due to the time limit. However, the statistics from the earlier study (Korkmaz et al., 2021b) were used together with the bias limits of two scales. As a result, the discrepancy between the actual displacement of the model and the nominal displacement obtained from hydrostatics was assumed to be similar to the earlier test with the KVLCC2 model (0.0375%).

The water temperature variation during the tests is also adopted from the earlier tests as the temperature variation

Table 2
The components and the combined expanded uncertainties in percentage of the average forces for all loading conditions and the speed corresponding to 17 kn

	L+1.5m n =3, t_{95}=4.30	L n =3, t_{95}=4.30	L-1.5m n =3, t_{95}=4.30	H+1.5m n =3, t_{95}=4.30	H n =5, t_{95}=2.78	H-1.5m n =4, t_{95}=3.18
Wetted area	0.180	0.180	0.180	0.179	0.179	0.179
Speed	0.113	0.113	0.113	0.113	0.113	0.113
Water temp.	0.021	0.021	0.019	0.020	0.021	0.018
Water Density	0.003	0.003	0.003	0.003	0.003	0.003
Dynamometer	0.236	0.237	0.212	0.225	0.222	0.197
Repeat test, Deviation	0.785	0.126	1.355	0.585	1.994	1.155
Combined for single test (prediction limit)	0.848	0.343	1.388	0.662	2.017	1.190
Repeat test, Deviation of mean	0.393	0.063	0.678	0.293	0.814	0.516
Combined for test avg (confidence limit)	**0.506**	**0.325**	**0.741**	**0.426**	**0.870**	**0.592**

Table 3
The components and the combined expanded uncertainties in percentage of the average forces for all loading conditions and the speed corresponding to 19 kn

	L+1.5m n =2, t_{95}=12.71	L n =2, t_{95}=12.71	L-1.5m n =2, t_{95}=12.71	H+1.5m n =2, t_{95}=12.71	H n =4, t_{95}=3.18	H-1.5m n =3, t_{95}=4.30
Wetted area	0.180	0.180	0.180	0.179	0.179	0.179
Speed	0.101	0.101	0.101	0.101	0.101	0.101
Water temp.	0.019	0.021	0.019	0.019	0.020	0.018
Water Density	0.003	0.003	0.003	0.003	0.003	0.003
Dynamometer	0.184	0.189	0.173	0.173	0.174	0.159
Repeat test, Deviation	1.467	2.298	3.615	1.768	3.413	1.849
Combined for single test (prediction limit)	1.493	2.315	3.625	1.789	3.424	1.868
Repeat test, Deviation of mean	0.847	1.327	2.087	1.021	1.526	0.925
Combined for test avg (confidence limit)	**0.891**	**1.356**	**2.104**	**1.056**	**1.550**	**0.961**

was less than 0.1°C (Korkmaz et al., 2021b). The water temperature difference between the two testing sessions in February and September was less than 2°C as SSPA's towing tank is heated in cold temperatures and sheltered from direct sunlight. In addition, the temperature difference between the model workshop and the towing tank was approximately 5°C. Therefore, the thermal deformation of the model is expected to be limited. As described in ITTC (2021b), the measured resistance is converted to 15.0°C, and the resulting expanded uncertainties on the water temperature and water density variation were calculated for the water temperature variation of 0.1°C.

The expanded uncertainties of the towing speed are assessed by the bias limit of the towing carriage speed. As the towing speed for each run slightly deviates from the nominal value, the measured resistance is corrected for the nominal speed as described in ITTC (2021b).

The calibration uncertainty for the dynamometer originates from the uncertainty in the applied force during the calibration, the standard deviation of the time series from the Data Acquisition System (DAS), and the uncertainty of the linear curve fit. As indicated by ITTC (2021b), the first two terms are negligible for the calibration; therefore, the uncertainty of the dynamometer calibration was quantified by the standard error of estimate (SEE) from linear regression analysis. The dynamometer calibration range is approximately ten times larger than the maximum measured force. The dynamometer should also be considered when coupled with the DAS, where the data sampling rate, sampling period, and filtering are applied to obtain a single reading. During the tests, a sampling rate of 100 Hz was used. The time series

were filtered with a 4^{th} order low pass Butterworth filter with a cutoff frequency of 0.5 Hz. The standard uncertainties of the average of the sampling history of all runs are, on average, approximately 0.038%. Therefore, the uncertainty of a single "reading" (i.e., the average of a time history) from the DAS is considered negligible.

Based on the analysis described in ITTC (2021b), all components of uncertainties are summarised and combined through RSS (Root-Sum-Square) as listed in Tables 1 to 3. The vertical columns in the tables represent results for different loading conditions, which include a letter (L for light loading and H for heavy loading) and the following numbers indicating the amount of trim (+1.5m indicates trim by the bow and -1.5m indicates trim by the stern). If a number does not follow the letter L or H, the trim is zero (i.e. even keel condition). The n and t_{95} values under the loading conditions represent the number of repetitions and the T critical value from the Student's t distribution, respectively. As suggested in ITTC (2021b), the Student-t value, t_{95}, is adopted as the coverage factor since the number of repeats is small for many of the loading conditions due to the time limitations in the towing tank.

As seen in Tables 1 to 3, the contribution of the expanded uncertainties for the wetted surface, speed, water temperature and water density to the combined uncertainties is mostly insignificant. On the other hand, the major sources of the uncertainties originate from the dynamometer and the deviation of the repeat tests. The dynamometer uncertainty can be considered a secondary source of the combined uncertainty for 15 kn and 17 kn as seen in Table 1 and Table 2. However, at the fastest speed as presented in Table 3, 19 kn, the dynamometer's uncertainty drops as the calibration's SEE becomes too small relative to the measured forces, which are much larger at this speed. The biggest contributor to the combined uncertainties is the deviation of the repeat tests for all loading conditions and speeds. The "Repeat test, Deviation" term in Tables 1 to 3 is calculated by

$$U = t_{95}\sigma\sqrt{1+1/n}\,, \tag{8}$$

where σ is the standard deviation of the force measured in the repeat tests. The "Repeat test, Deviation of mean" term is obtained by

$$U_{\overline{R}_T} = t_{95}s/\sqrt{n}\,. \tag{9}$$

The standard deviation, σ, of the repeat tests, on average, is 0.28%. However, the repeat test deviation terms, U and $U_{\overline{R}_T}$, are much larger because of the large coverage factors (t_{95}) used for calculating the uncertainties within the 95% confidence interval. As can be observed in the Tables 1 to 3, the t_{95} values used for the Eq. 8 and Eq. 9 can be very high due to the limited number of repetitions. As an example, the "L+1.5m" loading condition in Table 1 indicates the standard uncertainty for the repeat test deviations U and $U_{\overline{R}_T}$ are multiplied by 15.56 and 12.71, respectively, to cover 95% confidence interval.

The combined uncertainties in measurement for resistance are presented in two different forms, prediction limit and confidence limit. The former is calculated using the U term in Eq. 8 and ITTC (2021b) recommends using the prediction limit if the results are applied to the model to full-scale extrapolation. In the context of the present study, the uncertainty analysis is used for the validation of the CFD computations; hence, the combined for test average (confidence limit) will be used. As seen in Tables 1 to 3, the combined uncertainties are varying between 0.325% and 3.28%. This large variation can be mainly attributed to the number of repeat tests. However, the repeat test deviations can be relatively larger when flow around the hull features largely unstable flow phenomena: separation, breaking wave, and spill breakers, as observed in some loading conditions but not in others.

6. Verification and Validation

This section discusses the verification and validation of the computation results from the RANS-VOF method (see Section 3.3). Grid refinement studies were performed for resistance and self-propulsion in both model and full scale. Therefore, four verification exercises are presented in Section 6.3 and Section 6.4. The validation results are only available in model scale as full-scale measurements with uncertainty estimations are not available.

6.1. Grid Generation

The grid refinement study did pose challenges because unstructured grids were used with the RANS-VOF method, while one of the main requirements for verification is using geometrically similar grids (ITTC, 2021h). Using regular unstructured grid generators to obtain a constant ratio of cell sizes between two meshes, which should have cells of similar shape and orientation in any given position, is challenging, if not impossible. Therefore, the adaptive grid refinement technique is employed to generate a series of anisotropically refined meshes as recommended by ITTC (2021h).

The adaptive grid refinement (AGR) technique is implemented in FINEMARINE's ISIS-CFD solver. The original hexahedral grids generated by the grid generator can be further refined with AGR during the computation. Depending on the criterion selected, original cells can be divided into finer cells in either an isotropic or anisotropic way. The refinement of the same cell can be repeated several times, or earlier refinements can be undone until the AGR criterion is fulfilled with the desired cell sizes. As thoroughly explained in Wackers, Deng, Guilmineau, Leroyer, Queutey, Visonneau, Palmieri and Liverani (2017), anisotropic grid refinement is achieved by utilising metric tensors as refinement criteria, making it possible to determine cell sizes to be inversely proportional to the magnitude of the refinement criteria.

The refinement criterion used in this study is based on the combination of the Hessian matrix of second spatial derivatives and free surface refinement. The Hessian matrix of second spatial derivatives is interpreted as a measure

of the truncation error for a second-order finite-volume discretisation (Wackers et al., 2017). The AGR criterion used throughout the RANS-VOF computations is based on Hessians of both the pressure and the velocity, which are weighted as they appear in the flux. The main advantage of the flux-component Hessian (FCH) criterion is that both pressure-based flows (waves, vortices) and boundary layers, shear layers and wakes can be tracked, and grids are refined precisely where needed.

Two protective measures have been implemented to keep the number of cell sizes at a certain level and improve the refined grids' regularity. The first measure is imposing a minimum cell size, which prevents infinite refinement around flow singularities and spurious refinement where large errors can be observed, such as the high aspect-ratio cells of the near-wall boundary layer grid. The minimum cell size was set to $1 \times 10^{-4} \times L_{ref}$, where the L_{ref} is the length between perpendiculars in model or full scale for the corresponding computations.. The second measure is to protect the boundary layer grids where the original grid has layers of wall-aligned cells. To keep the number of wall-aligned layers the same, refinement is constrained to add cells parallel to the wall within the boundary layer grids. However, if a cell within the boundary layer grid needs refinement in the normal direction, all cells are refined from the wall to the outer layer; hence, the column/layer structure is preserved (Wackers et al., 2017). The first cell size normal to the wall is selected to obtain $y^+ \approx 30$ and $y^+ \approx 300$ for model and full-scale computations.

As mentioned, the AGR procedure divides the cells to refine the original grid. However, for geometrical similarity, the cells need to be divided in the middle, which can only be achieved by reducing the refinement criterion, T_r, by a power of two. If T_r is reduced in any other factor than a power of two, the cell sizes are divided by the nearest power of two. In this case, the grids are not formally geometrically similar but closely resemble each other. In addition, the grid size is not inversely proportional to the refinement criterion in the regions where the criterion is already satisfied, and the original grid is not refined.

An example from the grids generated for the grid refinement study is presented in Figure 1. The grid cuts are in the y-z plane, cutting the shaft partially (the quarter circle in the bottom right corner) and longitudinally positioned just downstream of the V-brackets. As seen in Figure 1, the grid is gradually refined with decreasing AGR criterion, T_r. It is easier to spot where the geometric similarity is not achieved than the other way around. Starting with the boundary layer grids around the no-slip wall of the shaft, no additional wall-aligned layers were added to the four layers from the original grid, as is the desired behaviour for grids with law-of-the-wall boundary conditions. Secondly, the cells at the bottom left corner of Figures 1a to 1c indicate no change as the original grid already satisfies the AGR criterion. As explained in Wackers et al. (2017), improving geometrical similarity in the unrefined region is far less critical in reducing the numerical errors, and it does not hinder the verification study as this method is recommended by ITTC (2021b).

6.2. Verification Procedure

ITTC (2021h) recommends that Richardson extrapolation and Least Squares Regression methods should be used for estimating the numerical uncertainties for unstructured grids. Therefore, the verification procedure is based on the method explained by Eça and Hoekstra (2014), wherein the numerical error is estimated as a function of the typical cell size. As discussed in Section 6.1, the systematically refined grids with AGR should, in principle, have typical cell size inversely proportional to the AGR criterion (T_r). Thus, the basic equation to estimate the discretisation error ϵ_S is:

$$\epsilon_S \simeq S_i - S_0 = \alpha(T_r)_i^p \,, \tag{10}$$

where S_i is the non-dimensionalised force coefficient, S_0 represents the estimate of the exact solution, p is the observed order of grid convergence, α is a constant for the power series expansion fit, and T_r is the AGR criterion which indicates the typical cell size. Note that only the refinement criterion of the flux-component Hessian criterion, T_r, will be mentioned in the verification study as the free surface refinement criterion is always changed with the same ratio as T_r for each grid.

The error estimation is performed in the least squares sense by minimising a set of functions (regular and weighted approaches), as explained in Eça and Hoekstra (2014), to determine S_0, p, and α. In addition, the standard deviation of the fits, denoted as σ, serves as a measure of the quality of the fits. Finally, depending on the observed order of convergence and the standard deviations obtained from regular and weighted approaches, the error is estimated, and the safety factor, as recommended by Roache (2009) is applied to ensure that the uncertainty estimation falls within the 95% confidence interval.

6.3. V&V Results in Model Scale

6.3.1. Resistance Computations

A grid refinement study for the resistance computations was performed with seven different AGR thresholds (i.e., seven systematically refined grids) as explained in Section 6.1. As shown in Table 4, the difference in T_r between the finest and coarsest grids is eight, and each successive grid is not increased by a factor of two. Although, for strict geometrical similarity, the threshold value increase should be by a factor of 2 between the successive grids, selecting such a factor for would have been excessively resource-intensive especially for the finest grids. In the case of seven grids, the difference between the cell sizes would have been 64 times if a factor of two was chosen between the grids. Instead, two pairs of geometrically similar grid families were created: g1, g3, g5, g7 and g2, g4, g6. The adaptive grid refinement criterion of the flux-component Hessian criterion, T_r, and the free surface refinement criterion for the coarsest grid were determined by trial and error. The AGR criteria that increased in the total number of cells approximately 10%

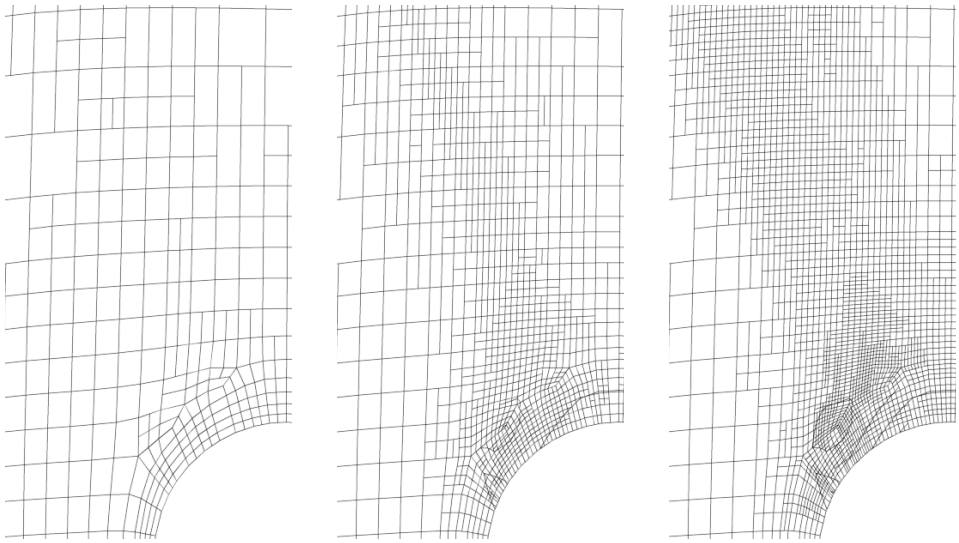

(a) $T_r = 4.0$ (b) $T_r = 2.0$ (c) $T_r = 1.00$

Figure 1: Grid cells for different AGR criteria

compared to the original grid was selected as the coarsest grid, g7. The flux-component Hessian criterion for the g7 approximately corresponds to $T_r = 4 \times 10^{-7} Re$, where Re is the Reynolds number. The free surface refinement criterion for the coarsest grid corresponds to $L_{W0} \times 0.025$ where L_{W0} is the fundamental wave length (Larsson and Raven, 2010, p.25),

$$L_{W0} = 2\pi Fr^2 L_{ref} \,, \tag{11}$$

where L_{ref} is the model scale waterline length. The g7 belongs to the first geometrically similar grid family, while g6 is the coarsest grid for the second geometrically similar grid family. The AGR criterion difference between g6 and g7 is adopted from Wackers et al. (2017). Within each grid families (g1, g3, g5, g7 and g2, g4, g6), the adaptive grid refinement criterion of the flux-component Hessian criterion, T_r, for each successive grid changes by a factor of two as presented in Table 4. As shown in Wackers et al. (2017), the two grid families are globally similar to each other and can be used for uncertainty estimation by the least squares approach. Therefore, estimation of the numerical errors were performed on the whole range of grids (g1, g2, g3, g4, g5, g6 and g7).

The computations were performed in double precision to discard the round-off errors. To eliminate the iterative convergence errors, the computations were performed with strict convergence tolerances, an exhaustively large number of time steps (approximately 7500) with ten non-linear iterations between each time step, and a relatively conservative time step of 0.01 seconds, which is approximately half of the recommended time step of $t = 0.0035 L_{ref}/V_M$ by Tezdogan, Incecik and Turan (2016). Therefore, it was assumed that discretisation errors dominate the numerical errors.

The numerical errors, U_{SN}, were estimated by the procedure proposed by Eça and Hoekstra (2014) as explained in Section 6.2. The numerical errors for viscous and pressure resistance coefficients are presented as error bars in Figure 2. The numerical uncertainties and the computed values are plotted as a ratio of the finest grid solution $\mathrm{U_{SN}}\%S_1$ and $S_i\%S_1$, respectively. In addition, the power expansion curves based on regular and weighted observed order of accuracy, p and p_w, are presented in Figure 2. It is observed that both C_V and C_P exhibit monotonic convergence. The finest grid's numerical uncertainty for C_V and C_P is 0.31% and 8.70%, respectively. Some fluctuations can be observed between the computed values from successive grids, which can be attributed to the fact that the successive grids are not strictly similar, as mentioned earlier. Possibly, a higher-order error is present, considering the complexity of the flow. However, the standard deviation of the difference between the computed values on all grids and the power-law values are 0.17% and 1.9% of S_0 for C_V and C_P, respectively, indicating that the series of meshes produce asymptotic convergence reasonably well.

Verification and validation (V&V) analysis can be performed for the total resistance coefficient as the measurement uncertainties were determined in Section 5.1. The results of the V&V study are presented in Table 4. The comparison error E, numerical uncertainty U_{SN} and validation uncertainty U_V are presented as a ratio of the measured force

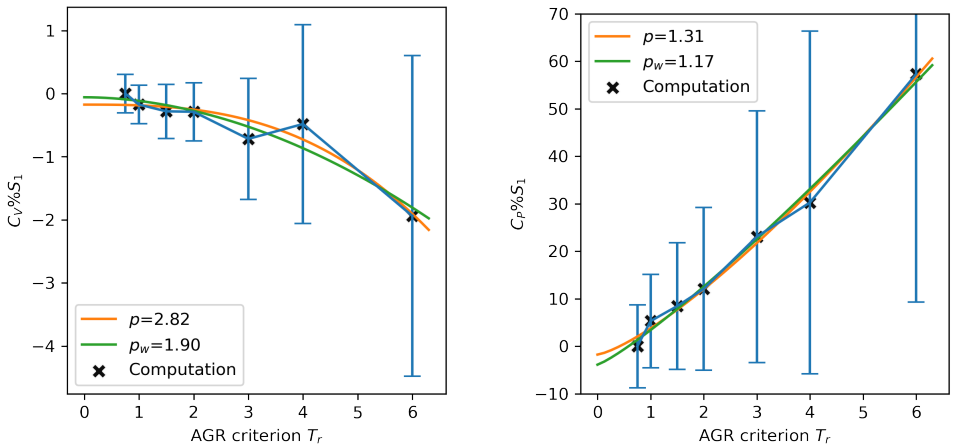

(a) Viscous Resistance Coefficient

(b) Pressure Resistance Coefficient

Figure 2: Computed resistance coefficients relative to the finest grid solution (S_1) with numerical uncertainties as error bars, and observed order of convergences against the AGR criteria

Table 4
Verification and validation for total resistance coefficient C_T, $\sigma = 0.15\%$ of the exact solution and $U_D\%D = 0.87\%$

Grid	Cells [M]	T_r	$E\%D$	$U_{SN}\%D$	$U_V\%D$
g1	11.55	0.75	0.64	1.24	1.51
g2	6.81	1	-0.06	1.61	1.83
g3	3.36	1.5	-0.46	2.17	2.34
g4	2.68	2	-1.03	2.96	3.09
g5	1.50	3	-2.41	4.60	4.68
g6	1.28	4	-3.73	6.40	6.46
g7	1.12	6	-6.78	10.07	10.11

D. The non-dimensional comparison error is

$$E\%D = (D - S_i)/D \times 100\,. \tag{12}$$

Table 4 shows that the comparison errors are approximately within $\pm 1\%$ for the four finest grids. Remarkably, g4, with only 2.68M cells, is able to predict the resistance with such accuracy, considering that the test case is an open shaft vessel with a considerable number of appendages and rather challenging wave-making characteristics that will be discussed in the later sections.

The non-dimensional numerical uncertainty is calculated as

$$U_{SN}\%D = U_{SN}/D \times 100\,. \tag{13}$$

Similar to the C_V and C_P, the total resistance coefficient also converges monotonically. The numerical uncertainty $U_{SN}\%D$ for C_T is 1.24% for the finest grid. As shown in Figure 3, the fluctuations of the computed values between

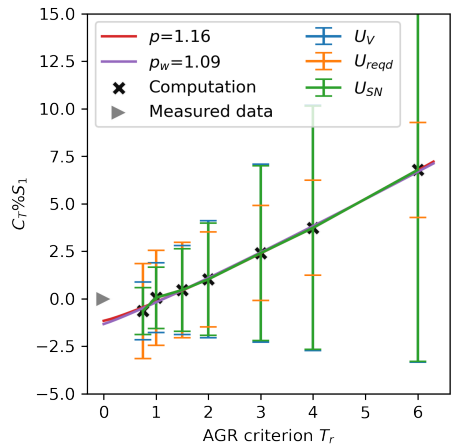

Figure 3: Total Resistance Coefficient

the successive grids are significantly reduced. The standard deviation of the difference between the computed values on all grids and the power-law values, σ, is 0.015% indicating that the grid series generated with the AGR refinement converge mostly asymptotically.

Assuming that input parameter uncertainty, U_{input}, is negligible, the validation uncertainty is calculated as

$$U_V^2 = U_{SN}^2 + U_D^2\,, \tag{14}$$

Table 5
Comparison error and numerical uncertainty $E\%D$, $U_{SN}\%D$ of thrust, torque, propeller rotation rate and delivered power in model scale

			T_M		Q_M		n_M		P_{DM}	
Grid	Cells [M]	T_r	$E\%D$	$U_{SN}\%D$	$E\%D$	$U_{SN}\%D$	$E\%D$	$U_{SN}\%D$	$E\%D$	$U_{SN}\%D$
g1	16.22	0.75	4.03	0.77	0.57	0.68	0.89	0.29	1.45	0.95
g2	10.40	1	3.62	0.99	0.21	0.89	0.75	0.39	0.95	1.26
g3	6.82	1.5	3.16	1.57	-0.17	1.38	0.64	0.60	0.47	1.93
g4	5.57	2	2.18	2.72	-1.04	2.41	0.30	0.94	-0.74	3.31
g5	4.79	3	1.14	5.45	-1.90	4.66	0.05	1.64	-1.85	6.28
g6	4.53	4	-2.39	8.46	-4.77	7.07	-0.80	2.32	-5.61	9.41

where the measurement uncertainty is the combined for test average value ($U_D\%D$) from Table 2 for the heavy loading even keel condition (denoted as H). As shown in Table 4, the validation uncertainty is less than 2% for the two finest grids, thanks to low measurement and numerical uncertainties.

In order to exercise the validation procedure of ITTC (2021h), the three variables U_V, $|E|$, and U_{reqd} should be compared with each other. The required uncertainty, U_{reqd}, is determined as 2.5%, which should be the combination of typical values on U_{SN} (2%) and U_D (1%). According to the six combinations of the comparison of U_V, $|E|$, and U_{reqd} values in ITTC (2021h), all grids indicate that validation is achieved ($|E| < U_V$), and the comparison error is below the noise level. In addition, the finest three grids show the condition $|E| < U_V < U_{reqd}$, which means the validation is successful from a programmatic standpoint. For the finest three grids, attempting to estimate modelling errors is not feasible because the numerical and modelling errors are well within the reasonably small levels.

6.3.2. Self-Propulsion Computations

A grid dependence study was performed for self-propulsion at the model scale. The original grid generation for the self-propulsion computations is the same as the the resistance simulations, except an additional cylindrical local refinement region is added around the actuator disc for the propulsion computations. The adaptive grid refinement criteria, the number of non-linear iterations, and the time step were identical to the resistance computations. To maintain the same standard of selecting the coarsest grid for the resistance and self-propulsion computations the same, the coarsest grid in the resistance computations, g7, is skipped for the self-propulsion computations as the number of cells added by the AGR was less than 10% of the cell count of the original grid. However, as seen in Table 5, the total number of cells in the self-propulsion computations is 40% to 250% larger with the same AGR criteria in self-propulsion computations compared to the resistance simulations. A large number of additional cells indicates that even with a simplistic propeller model (actuator disc), resolving the relatively simple propeller jet adds considerable cost in terms of computational resources.

The comparison errors are calculated, and the numerical uncertainties are estimated for thrust (T_M), torque (Q_M), propeller rotation rate (n_M), and delivered power (P_{DM}). The self-propulsion results are presented in Table 5. Starting with the finest grid (g1), the comparison errors are less than 1.5% for Q_M, n_M, and P_{DM}, while the T_M is 4% under-predicted. These results require further attention as the thrust is the only value obtained directly, i.e. the pressure jump created by the propeller model. The torque and propeller rotation rate are obtained from the actuator disc program where the K_{TM} and K_{QM} from the POW curves are used as inputs. The resulting propeller turning rate and the advance ratio (J_{TM}) are used to calculate the predicted wake fraction

$$w_{TM} = 1 - \frac{J_{TM} D_M n_M}{V}, \tag{15}$$

where D_M is the model scale propeller diameter, and V is the free stream velocity. It is observed that the w_{TM} resulted in over-prediction, which partially counterbalanced the effect of a 4% under-prediction of thrust by shifting the advance ratio towards the model test value. As a result, the CFD predictions for the torque and rps read from the corresponding J_{TM} value in POW curves are significantly closer to the model test results compared to the thrust.

The estimated numerical uncertainties for T_M, Q_M, n_M, and P_{DM} are presented in Table 5 and visualised in Figure 4. The order of accuracy for all self-propulsion characteristics and the fluctuations between the successive grids are similar. This similarity is expected as the self-propulsion computation is mainly based on the thrust value, which balances the resistance minus the towing force.

Even though the measurement uncertainties for the self-propulsion tests were not determined for thrust, torque, and the propeller turning rate, an attempt was made for a validation study. It is assumed that the measurement uncertainties will be similar in resistance and self-propulsion measurements; however, the $U_D\%D$ value from the resistance test (see Section 5.1) is multiplied by two as a safety factor for the self-propulsion. U_{reqd} is determined by assuming $U_D\%D \approx 1.75\%$ and $U_{SN}\%D \approx 2.5\%$ as typical values. Based on these assumptions, the validation study indicates that the comparison error is below the noise level for the fine grids' torque, propeller turning rate, and delivered power. However, the comparison error for the thrust is above the noise level,

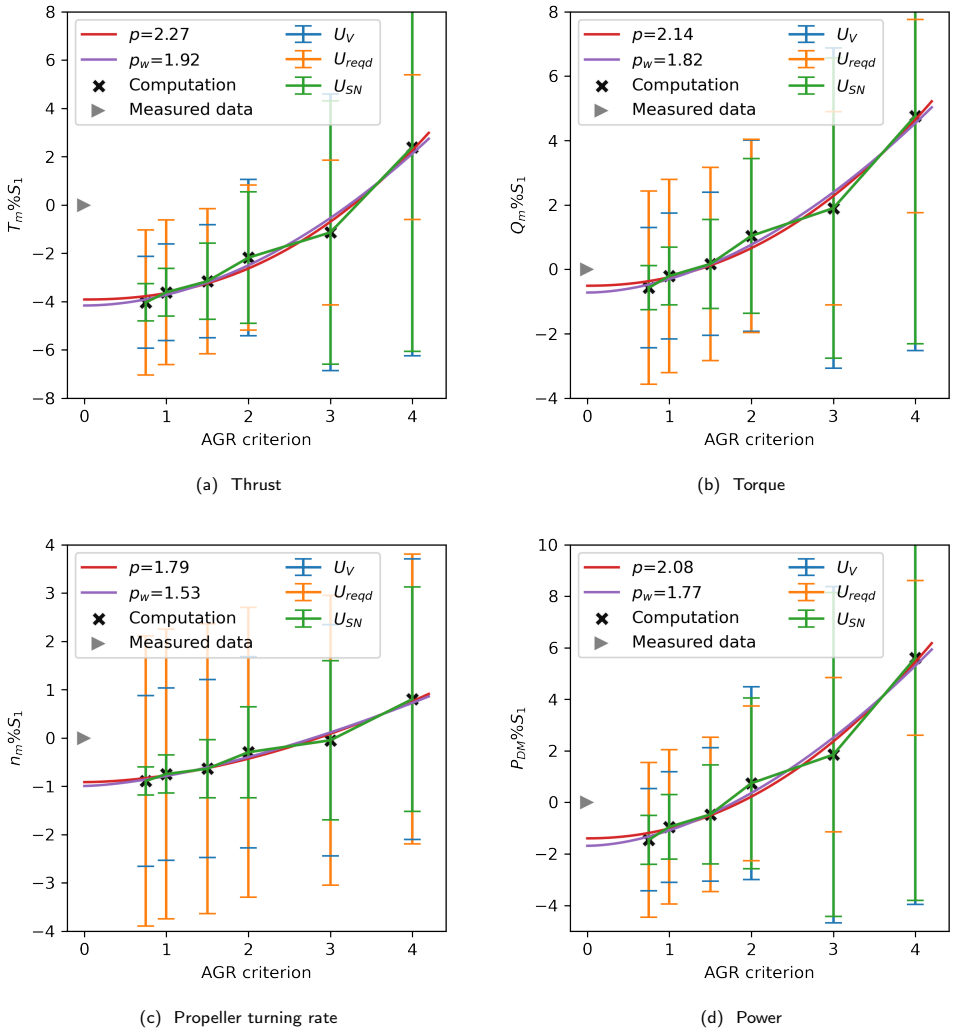

Figure 4: Computed model scale self-propulsion results relative to the finest grid solution (S_1) with numerical uncertainties as error bars and observed order of convergences against the AGR criteria

indicating that the modelling errors are significant. Considering the relative simplicity of the effective wake generated by the actuator disk model, this conclusion is expected.

6.4. V&V Results in Full Scale

6.4.1. Resistance Computations

A grid refinement study for the full-scale resistance computations was performed with seven different AGR thresholds similar to the model scale. From model to full scale, T_r values have been increased by a factor of 64 to keep the number of cells at reasonable levels. The original grid in full scale is nearly geometrically similar to the model scale original grid, except for the boundary layer grids where more layers were inserted parallel to the wall to capture the higher velocity gradients in full scale. Similar to model scale computations, a large number of time steps were computed with ten non-linear iterations between each time step. The time step is determined by $t = 0.0035 L_{ref}/V_S$ as proposed by Tezdogan et al. (2016) where V_S represents the full-scale ship speed.

The numerical uncertainties are estimated as explained in Section 6.2 and are presented in Table 6 for the viscous, pressure, and total resistance coefficients. The regular

Table 6
Numerical uncertainty $U_{SN}\%S_1$ of viscous, pressure and total resistance coefficient in full scale

Grid	Cells [M]	T_r	$U_{SN}\%S_1$		
			C_V	C_P	C_T
g1	13.81	48	1.34	4.42	0.79
g2	9.67	64	1.67	6.50	1.14
g3	5.99	96	2.11	10.37	1.85
g4	4.91	128	2.48	14.38	2.74
g5	3.68	192	3.28	28.56	5.95
g6	3.22	256	3.87	43.93	9.57
g7	2.70	384	4.76	76.52	18.00

observed order of accuracy (p) for C_V, C_P, and C_T are 0.69, 1.74 and 1.93, respectively. Even though all coefficients indicate monotonic convergence, the p value for C_V indicates a considerable difference between the model and the full scale. In addition, the numerical uncertainties are significantly larger for C_V in full scale than in the model scale. At the same time, the $U_{SN}\%S_1$ for the total resistance coefficients decreased from model to full scale.

The numerical uncertainties, power-of-law curve fits and computed values for C_T are presented in Figure 5. Similar to the model scale, g5 and g6 show some considerable fluctuations, which could be caused by the imperfect geometrical similarity between them but also the presence of higher-order errors. However, the standard deviation of the difference between the computed values on all grids and the power-law values is only 0.39% of the exact solution. Therefore, it can be argued that the series of meshes produce asymptotic convergence reasonably well.

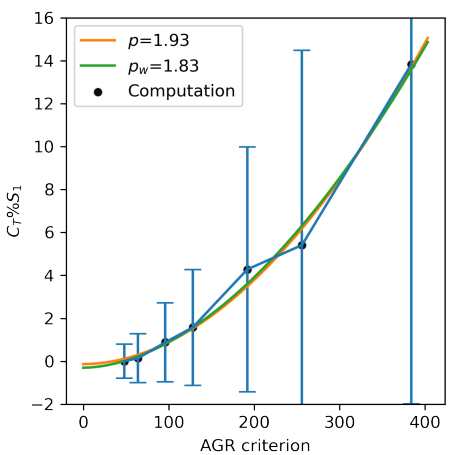

Figure 5: Numerical uncertainties for the total Resistance Coefficient

Table 7
Numerical uncertainty $U_{SN}\%S_1$ of thrust, torque, propeller rotation rate and delivered power in full scale

Grid	Cells [M]	T_r	$U_{SN}\%S_1$			
			T_S	Q_S	n_S	P_{DS}
g1	17.57	48	1.35	1.24	0.37	1.60
g2	13.26	64	1.39	1.30	0.42	1.69
g3	10.01	96	2.63	2.42	0.69	3.09
g4	8.49	128	3.45	3.21	1.00	4.20
g5	7.53	192	7.13	6.53	1.89	8.46
g6	7.32	256	10.08	9.13	2.55	11.81

6.4.2. Self-Propulsion Computations

A grid dependence study was performed for self-propulsion at full scale. The original grid generation for the full-scale self-propulsion computations is the same as the full-scale resistance simulations, except for an additional cylindrical local refinement region is added just around the actuator disc for the propulsion computations. The adaptive grid refinement criteria, the number of non-linear iterations, and the time step were identical to the full-scale resistance computations. However, as presented in Table 7, the total cell count in self-propulsion computations is considerably higher than in the resistance computations since the propeller jet needs to be resolved by the added cells from AGR. In addition, the law-of-the-wall boundary condition is modified in self-propulsion computations to simulate the standard hull roughness recommended by ITTC (2021g).

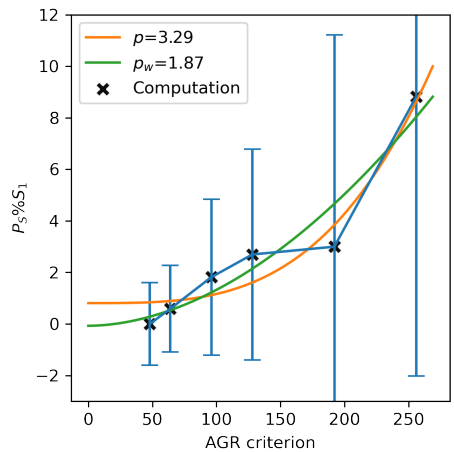

Figure 6: Numerical uncertainties for the delivered power in full scale

The estimated numerical uncertainties are presented in Table 7. Compared to the model scale, $U_{SN}\%S_1$ is larger in full-scale self-propulsion computations. However, the resemblance of the observed order of accuracy of the thrust

and the other torque and propeller rotation rate is similar in model and full scale as a consequence of using the actuator disc model. As seen in Figure 6, the computed values fluctuate around the power-law curve fits the most in full-scale self-propulsion computations compared to the full-scale resistance and model-scale computations. In addition, the standard deviation of the difference between the computed values on all grids and the power-law values from the weighted fit is 0.88%, significantly higher than in the earlier conditions. Considering the observed order of accuracy of 1.87 for the weighted fit, the series of six grids indicate asymptotic convergence at an acceptable level.

6.5. Selection of the Grid for Further Computations

Based on the verification of a series of grids in the model and full-scale for resistance and self-propulsion computations, an AGR threshold can be determined for further computations. The AGR threshold should be sufficiently low to ensure reasonable numerical accuracy while maintaining manageable computational costs. However, the grid refinement study was limited to only one loading condition (H) out of six (see Section 4). In addition, the trimmed conditions from the towing tank experiments exhibited challenging flow phenomena such as breaking waves, separated flow and spill breakers. Therefore, it is anticipated that trimming by the bow and by the stern pose greater numerical challenges as either the transom stern significantly submerges and the bulbous bow pierces the still water surface or the transom stern lifts up, and the bow with a large flare submerges.

The heavy loading condition at even keel (zero trim) condition was verified and validated for model-scale resistance computations as explained in Section 6.3. Using the same original grid as the $V\&V$ study, the trim by the bow (H+1.5m) and the trim by the stern (H-1.5m) conditions were simulated with the AGR thresholds corresponding to g1, g2, and g6 (see Table 4). The final grid for each loading condition should be globally similar, as the same AGR thresholds are used, and the mesh deformation technique is employed to solve the heave and trim motions of the vessel. In other words, the grids for the trimmed conditions originate from the same original grid as the even keel condition, and the mesh deformation technique achieves the final dynamic sinkage and trim condition for each loading condition while keeping the AGR threshold the same. Therefore, it is reasonable to assume that numerical uncertainties for the trimmed conditions are similar to those of the even keel condition.

The comparison errors for different loading conditions and grid fineness (AGR threshold) are presented in Table 8. Firstly, it should be noted that $E\%D$ values for the even keel condition (H) in Table 8 are not precisely the same as those reported in $V\&V$ (see Table 4), because the results in Table 8 were simulated again with less strict convergence tolerances, such as a smaller number of time steps and non-linear iterations between each time step. Performing the computations with fewer time steps and non-linear iterations is expected to introduce iterative errors. As a consequence, the numerical errors for the computations with less stringent convergence tolerances will be higher than the values obtained in the V&V study where the iterative errors were kept minimal. The comparison error for the g1, g2 and g6 at the even keel condition in Table 8 varies 0.27%, 0.33%, and 0.33% from the comparison errors obtained from the verification study, respectively. Considering that these differences in the comparison errors are 5, 5, and 20 times smaller than the discretization errors of the corresponding grids estimated in the verification study (see Section 6.3), performing the computations with fewer time steps and non-linear iterations are considered reasonable. Since the calculation of the relative change in resistance or propulsion characteristics between trimmed conditions and the even keel (e.k.) loading is sufficient for trim optimisation study, the calculation of the absolute values is not as critical. As a result of less stringent convergence, the computational time is reduced by 3 to 4 times compared to the computations for the verification study, while the comparison error remains reasonably similar. Therefore, the computations for the rest of the study are performed with the less stringent convergence tolerances.

The trim by the bow loading condition (H+1.5m) exhibits similar $E\%D$ values to the even keel condition. On the other hand, the trim by the bow indicates about three per cent larger comparison error, which suggests the presence of modelling errors, more than the even keel condition for the two finest grids. The comparison error seems to decrease from even keel to trimming by the stern for the g6 grid. Considering the increased complexity of the flow, this reduction in $E\%D$ for g6 is likely due to numerical and modelling errors cancelling each other. Therefore, g6 is deemed to be too coarse to continue with the rest of the simulations. The g1 and g2 show similar comparison errors for the three loading conditions. The mean absolute value of the comparison errors for the three loading conditions for g1, g2, and g6 are 4.01%, 4.16%, and 9.55%, respectively. Therefore, the second finest grid, g2, provides nearly the same accuracy while reducing the computational effort by more than half compared to g1. Besides capturing the absolute values of the resistance force, the relative change in the resistance between trimmed conditions and even keel (e.k.) loading is even more relevant for the trim optimisation study. All three grids showed similar trends between the trimmed and zero trim conditions. Considering the numerical errors and complexity of the flow, the second finest grid is the right compromise between the computational cost and accuracy. Therefore, further computations are computed with the corresponding AGR threshold of g2 in the model and the full scale.

7. Comparison between the towing tank tests and different CFD methods

7.1. Resistance

The trim optimisation test scope of two displacements, three trims, and three speeds is discussed in this section.

Table 8
Comparison errors for different AGR thresholds corresponding to the g1, g2 and g6

Loading	$E(g1)\%D$	$E(g2)\%D$	$E(g6)\%D$
H-1.5m	2.99	3.43	-1.20
H	0.37	0.27	-4.06
H+1.5m	-0.38	-0.67	-4.61

The towing tank test results with the measurement uncertainties (Section 5.1), free-surface RANS computations (Section 3.3), and the combination of double-body RANS (Section 3.1) and potential flow (Section 3.2) computation results were used for the comparison. The change in the quantity of interest between the trimmed and the even keel conditions for each displacement and speed is calculated; for example, for the resistance force,

$$\Delta R_{TM} = \frac{R_{TM}(trim) - R_{TM}(trim = 0)}{R_{TM}(trim = 0)} \times 100\,, \quad (16)$$

where ΔR_{TM} is the relative change in resistance force in a given trim condition ($R_{TM}(trim)$) in per cent of the resistance of the zero trim condition ($R_{TM}(trim = 0)$).

Note that even though this section only presents model tests and computations performed at the model scale, the vessel's speed is always indicated with the corresponding full-scale speed in knots. This decision is based on the fact that the same full-scale speed at different loading conditions cannot be addressed with a single Froude number because the waterline lengths vary significantly between the loading conditions.

7.1.1. Towing Tank Tests

The results of the trim optimisation towing tank tests are presented in Figure 7. The measured data from the tests are represented by black markers, with measurement uncertainties indicated by the accompanying error bars. Each subfigure in Figure 7 illustrates the relative change in resistance under trimmed conditions compared to the even keel condition for a specific displacement and speed, as noted in the captions. An overall analysis of the ΔR_{TM} trends in Figure 7 suggests that the potential for reducing resistance by trimming at the bow is negligible in 19 kn, modest at in 17 kn and somewhat limited at 15 kn. Conversely, trimming the vessel by stern results in increased resistance across all displacements and all speeds. The potential gains are overshadowed by the possible resistance penalties incurred when operating the vessel under non-optimal conditions, amounting to as much as 15%.

A comparison between the light (top row) and the heavy displacements (bottom row) at their respective speeds reveals little difference, despite the disparity in displacement volumes of approximately 10%. This similarity can be attributed, in part, to the forebody design. The bulbous bow was optimised for narrow operational conditions due to its length and the positioning of the bulb's volume centre relatively close to the water surface and the forward end of the bulb close to the tip. Consequently, the loading conditions where the bulb is too close to the water surface (trim $<$ 0) and low Froude numbers (Fr) result in unfavourable wave patterns, occasionally leading to breaking waves, as observed in Figure 8d. Other characteristics of the forebody design, such as significant flare and a relatively blunt waterline entrance angle above the design waterline, cause the water surface to rise along hull as a thin sheet (heights up to 30% of the draught from the water surface) before rolling on the sides when trimmed by the bow (trim $>$ 0) at higher speeds, as depicted in Figure 9d. The similarity in ΔR_{TM} trends for each speed in different displacements can largely be explained by the fact that similar flow phenomena, albeit with varying intensities, are observed in both displacements, rather than entirely distinct wave patterns.

The flow regime behind the transom exhibits significant variation depending on trim and speed conditions, including the dry-transom, wetted-transom and partially dry-transom flows observed in the towing tank tests. However, the case of regular transom flow (Larsson and Raven, 2010), where the lower edge of the transom is above the still water level and waves smoothly leave the hull, was not observed, as the wave crest at the stern consistently exceeded the transom edge at all conditions. Conversely, the dry-transom flow, where the flow smoothly leaves the transom edge tangential to the buttocks, was only observed at the highest speed (19 kn or $Fr = 0.21$) in the light displacement even keel condition, as depicted in Figure 9a, as well as in and both displacements with trim by the bow conditions. The majority of the other trim conditions and speeds resulted in partially dry-transom flows.

To sustain the dry-transom flow, the pressure at the transom edge must be equal to the atmospheric pressure (Larsson and Raven, 2010). Consequently, decreasing the speed or increasing the transom submergence through trimming increases the required hydrodynamic pressure for achieving dry-transom flow. This leads to an increase of the upward curvature of the streamlines behind the transom. Eventually, the steepening streamlines, coupled with momentum deficit in the boundary layer, results in the longitudinal velocity to disappear (Starke, Raven and van der Ploeg, 2007). As a consequence, spilling wave breakers emerge between the transom and the first wave crest, as seen in Figure 9b. Further increases in transom submergence or speed reduction will cause the spill breakers to reach the transom, leading to the formation of a recirculation region behind the transom, categorised as wetted-transom flow, as observed in Figure 8b. The wetted transom flow regime only occurred with the high displacement trim by the stern and the slowest speed ($Fr = 0.166$ and $Fr_{tr} = 2.75$).

7.1.2. Double-Body RANS and Potential Flow Combined (DB-XPTD)

This trim optimisation method combines RANS-DB and potential flow computations (XPTD). The computations were limited to only 17 kn, as the success of this method in replicating the towing tank test results was limited.

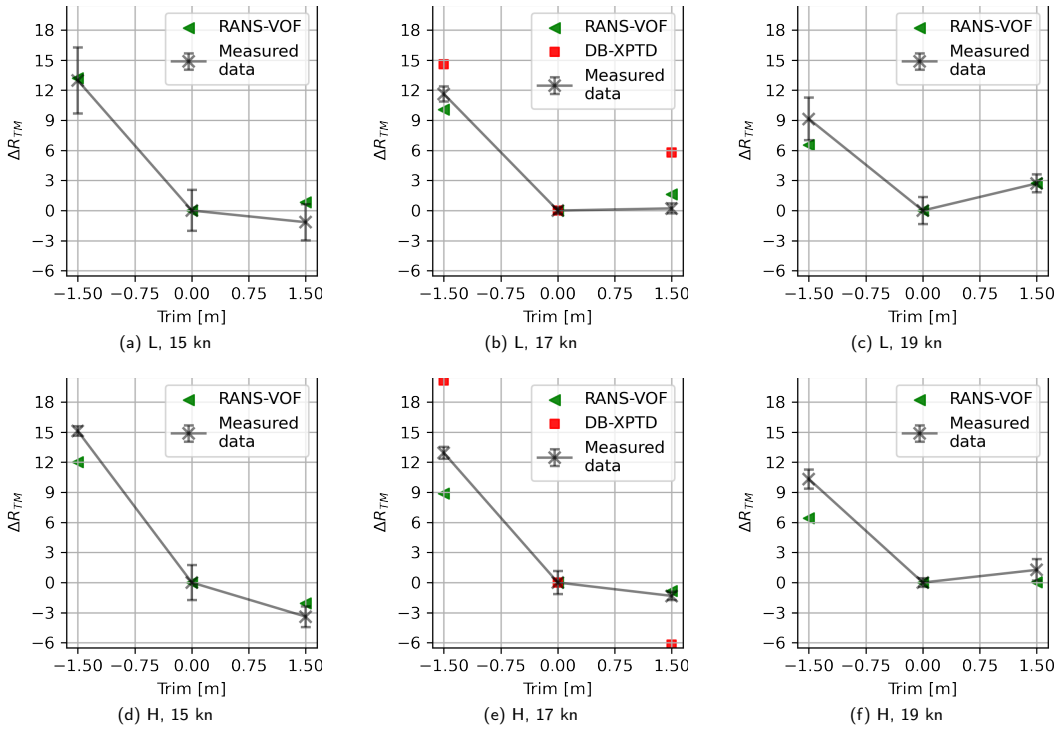

(a) L, 15 kn (b) L, 17 kn (c) L, 19 kn

(d) H, 15 kn (e) H, 17 kn (f) H, 19 kn

Figure 7: Trim optimisation results of resistance from the towing tank measurements, RANS-VOF computations and the combined DB-XPTD simulations.

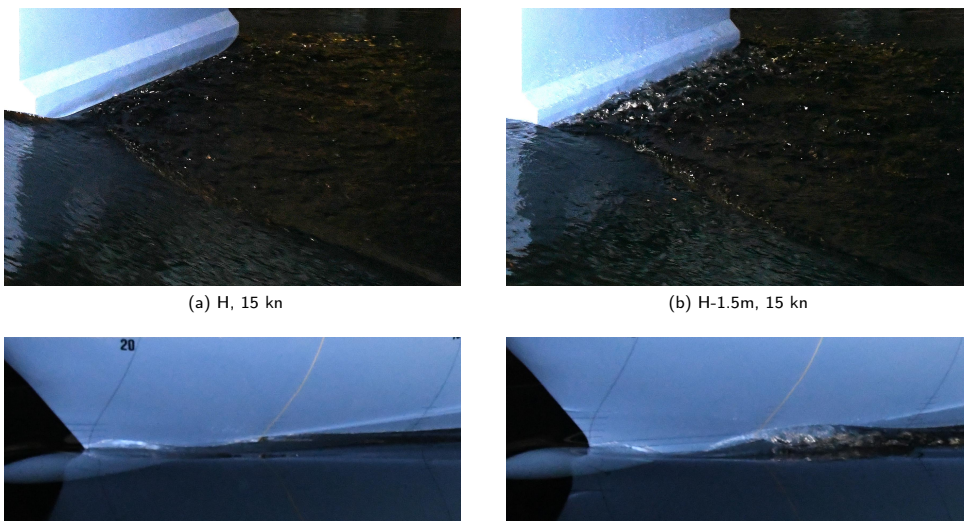

(a) H, 15 kn (b) H-1.5m, 15 kn

(c) H, 15 kn (d) H-1.5m, 15 kn

Figure 8: Towing tank resistance tests from the bow and stern views

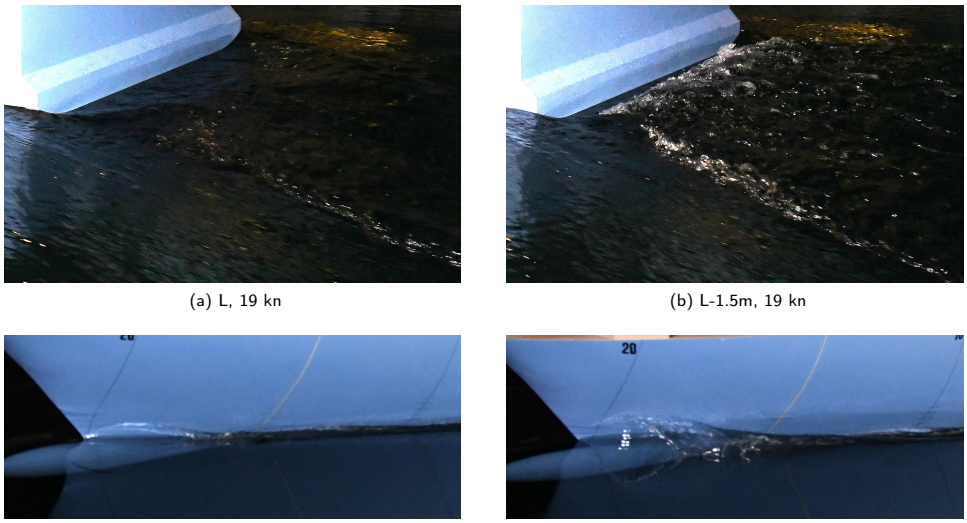

(a) L, 19 kn (b) L-1.5m, 19 kn

(c) L, 19 kn (d) L+1.5m, 19 kn

Figure 9: Towing tank resistance tests from the bow view

RANS-DB and potential flow computations were performed as explained in Section 3.1 and Section 3.2, respectively. As previously mentioned, not all loading conditions at 17 kn result in wetted-transom flow, which is required for the double-body assumption (Korkmaz et al., 2022). One way to address this issue is to replace the transom with a pseudo extension of the stern overhang that connects the flat free surface and the hull. In cases where pseudo-extension wall cells are classified as the slip boundary condition and excluded in the integration of the viscous pressure force, double-body computations can be used for a dry-transom condition. However, at 17kn, the flow regime behind the transom is partially dry-transom, which is not significantly different from the wetted-transom flow condition. Therefore, the double-body assumption is considered valid.

The potential flow computations (XPTD) for the trim by the bow conditions presented some challenges as the free surface "just skimmed" the stern overhang, leading to numerical difficulties. However, the even keel and the trim by the stern conditions were computed using the XPTD method without any issues. The total resistance coefficient is approximated by summing the viscous resistance from the DB RANS computations and the wave resistance from the potential flow computations. This total resistance coefficient is denoted as "DB-XPDT" and is shown with red square markers in Figure 7b and Figure 7e. It is important to note that the total resistance from the "DB-XPTD" is an approximation, as the viscous resistance from the double-body computations neglects the viscous effects due to the free-surface deformation, and the wave resistance is obtained without accounting for the viscous effects and breaking waves.

The resistance trends from the DB-XPDT method are correct in a general sense for the trim by the stern. However, ΔR_{TM} predictions are 3% and 7% higher than the measurements for the light and heavy displacements, respectively. ΔR_{TM} predictions for the trim by the bow are inconsistent, with a considerably high deviation from the towing tank measurements. To understand the source of this deviation, the total resistance from the DB-XPTD method is decomposed into frictional (R_{FM}), viscous pressure (R_{PVM}), and wave-making resistance (R_{WM}). The first two resistance components are obtained from the DB RANS computations, and their summation yields the viscous resistance R_{VM}. As shown in Table 9, the relative change in resistance components and the total resistance between the trimmed and even keel conditions are calculated in a similar manner to Eq. 16. The double-body computations reveal a sharp increase in viscous pressure resistance with trim by the stern, which is attributed to increased transom submergence in both displacements. Conversely, the L+1.5m condition shows a marginal change in R_{PVM} as the transom remains outside of the water in both L and L+1.5m conditions. Finally, the significant drop in viscous resistance from H to H+1.5m is primarily due to a decrease in the frictional resistance component, as most of the stern overhang lifts out of the still water surface in the double-body computations. As observed in the model tests, the wave crest at the stern was large enough to submerge the entire stern overhang, so the substantial reduction in ΔR_{FM} and consequently in ΔR_{TM} for the H+1.5m loading condition is not realistic but rather a consequence of the double-body assumption.

The change in wave resistance, ΔR_{WM}, in trimmed conditions is much more significant than the other resistance

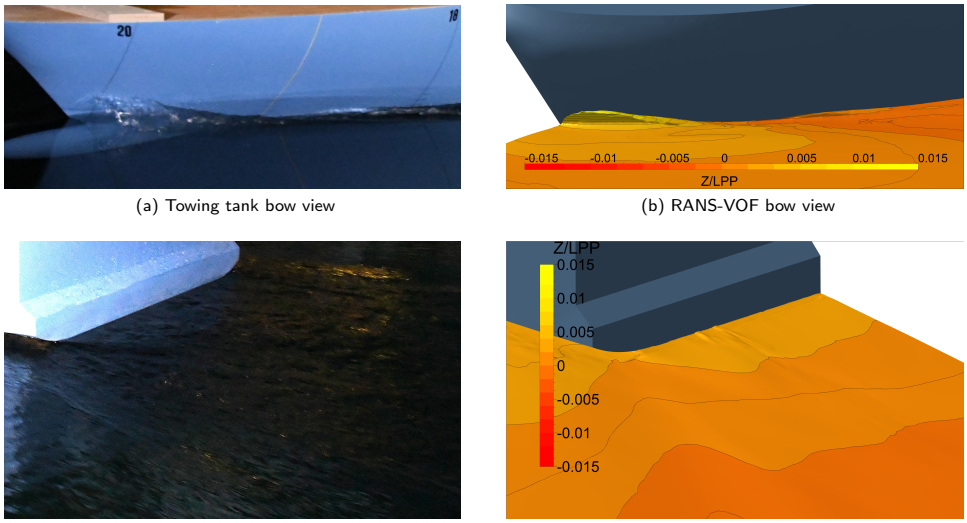

(a) Towing tank bow view

(b) RANS-VOF bow view

(c) Towing tank stern view

(d) RANS-VOF stern view

Figure 10: Wave pattern from the towing tank resistance tests and RANS-VOF computations in model scale, trim by the bow condition (H+1.5m) at 17 kn

Table 9
The relative change of resistance components and the total resistance between the trimmed and even keel conditions from DB-XPDT computations

Loading Condition	ΔR_{FM}	ΔR_{PVM}	ΔR_{VM}	ΔR_{WM}	ΔR_{TM}
L-1.5m	1.1	47.4	4.3	447.8	14.6
L+1.5m	-0.9	-0.2	-0.8	282.7	5.8
H-1.5m	-0.5	87.6	6.7	333.3	20.1
H+1.5m	-6.2	-20.9	-7.4	21.1	-6.2

components and varies between 21% to 448%. Given the complexity of the breaking waves, the thin sheet wave observed at the forebody, and the spilling wave breakers seen at the aft body, it is challenging, if not impossible, for potential flow to accurately model the flow phenomena in the trimmed conditions for this hull. The resulting ΔR_{WM} values are too large and cause an overshoot in ΔR_{TM} in L-1.5m, L+1.5m, and H-1.5m loading conditions.

7.1.3. RANS-VOF – Resistance

The final method for trim optimisation is the RANS-VOF method. ΔR_{TM} values are presented in Figure 7 as green triangle markers. It can be argued that ΔR_{TM} predictions accurately replicated the towing tank measurements, as the mean of the absolute values of the differences between ΔR_{TM} predictions from the RANS-VOF and model tests is only 1.82% (excluding zero trim conditions).

As seen in Figure 7, the RANS-VOF predictions are particularly successful in predicting the trim by the bow, where the transom submergence is decreased compared to the even keel condition. The wave pattern of the H+1.5m condition is visualised from the images of the towing tank experiments and the RANS-VOF in Figure 10. The flow behind the transom is far less complicated than in the even keel and the trim by the stern conditions, as the wake behind the transom is smooth, free from recirculating flow and spill breakers as seen in Figure 10c. The computed wave pattern from the RANS-VOF method closely resembles the towing tank tests, as seen in Figure 10d. This result is expected since modelling assumptions such as time averaging and turbulence modelling should not prevent capturing the flow characteristics behind the transom.

On the other hand, the flow phenomenon at the bow differs from the stern in the H+1.5m condition due to its unsteady nature. As seen in Figure 10a, a thin sheet of water climbs up the hull rapidly and reaches approximately $Z/L_{PP}= 0.015$ (Z denotes water surface elevation with respect to the still water level) in the towing tank test. Then, the quasi-stable thin sheet of water rolls sideways to meet with the water surface again. The thin sheet of water is, in general, captured by the RANS-VOF method, as seen in Figure 10b; however, the wave height is slightly smaller ($Z/L_{PP}= 0.012$), and the rolling of the water sheet sideways is missing in the CFD. The following diverging wave initiated between stations 19 (95% of L_{PP} from the AP) and 18 is also steep and breaking in the towing tank tests. However, the RANS-VOF method predicts the diverging waves with significantly less steepness and breaking.

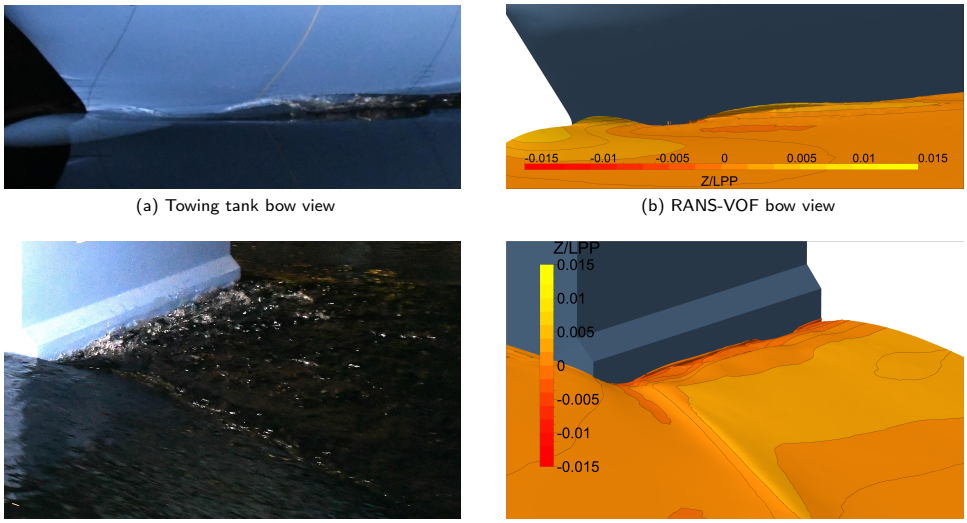

(a) Towing tank bow view

(b) RANS-VOF bow view

(c) Towing tank stern view

(d) RANS-VOF stern view

Figure 11: Wave pattern from the towing tank resistance tests and RANS-VOF computations in model scale, trim by the stern condition (H-1.5m) at 17 kn

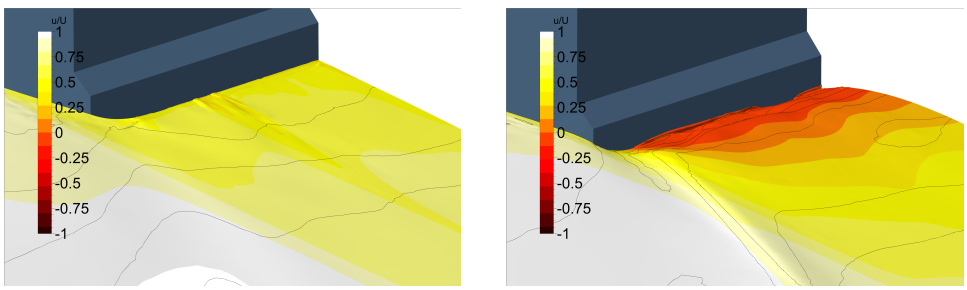

(a) H+1.5m

(b) H-1.5m

Figure 12: Non-dimensional longitudinal velocity on the free surface from RANS-VOF computations in model scale at 17 kn

The difference of ΔR_{TM} between the towing tank measurements and RANS-VOF predictions varies from 0.2% to 4% in the trim by the stern conditions. As seen in Figure 7, the light displacement was predicted more accurately than the heavy displacement in aft trim conditions. As the transom and the bow are submerged more in the light displacement than in the heavy displacement, it is expected that the severity of breaking waves in the forebody, and spill breakers and eddies in the aft body will increase. Therefore, numerical and modelling errors (time averaging, turbulence modelling) significantly affect prediction accuracy. The numerical errors were investigated in Section 6.5, and it was concluded that increasing the number of cells (i.e., decreasing the AGR threshold) helps only marginally; therefore, modelling errors should be the main reason for the prediction accuracy. The wave pattern of the H-1.5m condition is presented in Figure 11 with the photographs from the towing tank experiments and the post-processed images from the RANS-VOF computations.

The wave pattern at the forebody in Figure 11a shows the effect of the bulbous bow being too close to the water surface in aft trim conditions. As it is easier to understand the surface elevation in the post-processed image from RANS-VOF in Figure 11a, the large wave crest precisely on top of the bulb can be identified. The interpolation of the bulb and the bow stem wave systems results in a sharp wave trough between Station 19 (where the white trip wire is mounted) and 20 (the vertical line at the fore perpendicular). The wave crest, followed by the sharp and deep wave trough, then breaks at Station 19 (95% of L_{PP} from the AP), initiating diverging

waves. As seen in Figure 11a, RANS-VOF can capture the forebody waves, except the breaking waves were not fully resolved.

The free surface and flow structures at the stern are presented in Figure 11c for the trim by the stern condition. Contrary to the trim by the bow at the same displacement and speed (Figure 10c), the flow behind the transom is complicated with unsteady flow features such as recirculation, spilling wave breakers, and eddies in the aft trim conditions. In addition, a steep diverging wave system is radiated from the corner of the transom. The transom wake is followed by significantly large transverse waves, which RANS-VOF predicts well. As seen in Figure 11d, the free surface predicted by RANS-VOF is smooth and missing the spilling wave breakers and eddies visible on the surface from the towing tank image (Figure 11c). Not being able to replicate such complex flow structures is a direct consequence of the cost-effective grid resolution and modelling methods (time averaging, RANS method coupled with k$-\omega$ SST turbulence model). However, ΔR_{TM} between the towing tank measurements and RANS-VOF predictions shows that the integrated forces in aft trim conditions are predicted with acceptable accuracy, as seen in Figure 7.

As seen in Figure 12, the wake behind the transom is visualised by plotting the non-dimensional longitudinal velocity contours (u/V where u is longitudinal velocity and V is the free stream velocity) at the free surface. The negative u/U values indicate that water on the free surface is moving in the same direction as the model, trailing the hull. The contour lines in Figure 12 mark the $Z/\mathrm{L_{PP}}$ levels with the an interval of 0.001, and they are inherited from the earlier surface elevation plots (e.g., Figure 11d) to maintain the sense of wave formation on the free surface. As mentioned earlier, the H+1.5m condition at 17 kn had a definitive dry-transom. As seen in Figure 12a, the wake behind the transom leaves the hull smoothly with some momentum loss due to the boundary layer formed along the hull and the appendages. However, the H-1.5m condition at 17 kn with the partially dry-transom shows flow trailing the hull ($u/V < 0$) immediately behind the transom, as seen in Figure 12b. In fact, the spill breakers (white and irregular protruding patches on the free surface) observed in the towing tank tests (Figure 11a) mostly emerge in the recirculation region, which is marked with negative u/U values in the CFD computations. Therefore, it can be argued that even though CFD could not model some of the flow details observed in the towing tank tests, the main flow features, such as the transom dryness, recirculation zone, and wave pattern, are captured by the RANS-VOF model accurately.

7.1.4. Decomposing the Total Resistance Coefficient to Understand the Gains and Losses in Trimmed Conditions

The trim optimisation results for the total resistance and the flow features observed at different trim conditions were discussed in Section 7.1.1 and Section 7.1.3. This section divides the total resistance coefficient into its constituent parts to identify the sources of gains or losses in each loading condition and speed. From a free-surface RANS computation, the total resistance coefficient is obtained

$$C_{TM} = C_{FVM} + C_{PM} \,, \tag{17}$$

where C_{FVM} is the viscous frictional resistance coefficient and C_{PM} represents the pressure coefficient. C_{FVM} includes flat plate friction (C_{F0}) and form effect friction components, while C_{PM} term constitutes viscous pressure (form effect pressure C_{PVM}) and wave making (wave pattern and wave breaking, C_{WM}) terms (Larsson and Raven, 2010). Even though obtaining C_{PVM} and C_{WM} components separately is not possible through free-surface RANS computations, the form factor approach (Hughes, 1954) can be adopted from ITTC extrapolation procedures to approximately separate C_{PM} from the RANS-VOF computations. The viscous pressure resistance

$$C_{PVM} = C_{F0} \times k \,, \tag{18}$$

where k is the form factor. According to ITTC (2021g) and Hughes (1954), the frictional resistance coefficient should be derived from a flat plate but using C_{FVM} from RANS-VOF computation is considered as a reasonable approximation since the form effect friction component in C_{FVM} will be of a similar size (approximately 3-4% of C_{FVM}) in all loading conditions. The form factors for each loading condition are adopted from the Prohaska method (Prohaska, 1966), supported by the double-body computations (ITTC, 2021g; Korkmaz et al., 2021a). Consequently, the wave resistance is

$$C_{WM} = C_{PM} - C_{PVM} \,. \tag{19}$$

The total resistance coefficients, C_{FVM}, C_{PVM}, and C_{WM} in the trimmed conditions are converted back to forces and are presented in Figure 13. Similar to previous plots (e.g. Figure 7), the total resistance and its components ($R_{TM} = R_{FVM} + R_{PVM} + R_{WM}$) in the trimmed conditions are presented relative to the even keel condition for each speed and the displacement. In addition, R_{FVM}, R_{PVM}, and R_{WM} are represented as percentages of R_{TM} for each condition. The y-axis of the stacked bar plots in Figure 13 starts from 60% and to enhance the visualisation of the minor differences between the loading conditions. For instance, in Figure 13a, viscous friction resistance accounts for 85% of the R_{TM} in the L condition. Moreover, the total resistance coefficient in the L-1.5m condition is 13% higher than in the L condition, and R_{WM} in the L-1.5m condition is nearly three times the size of the wave resistance in the L condition at 15kn.

As depicted in Figure 13, the proportion of R_{VM} in the total resistance decreases with the increasing speed, as the viscous effects are inversely proportional to the Reynolds number, and wave resistance increases its relative size with an increasing Froude number. Furthermore, the change in R_{VM} between the different conditions at the same speed and displacement is limited. Consequently, the frictional

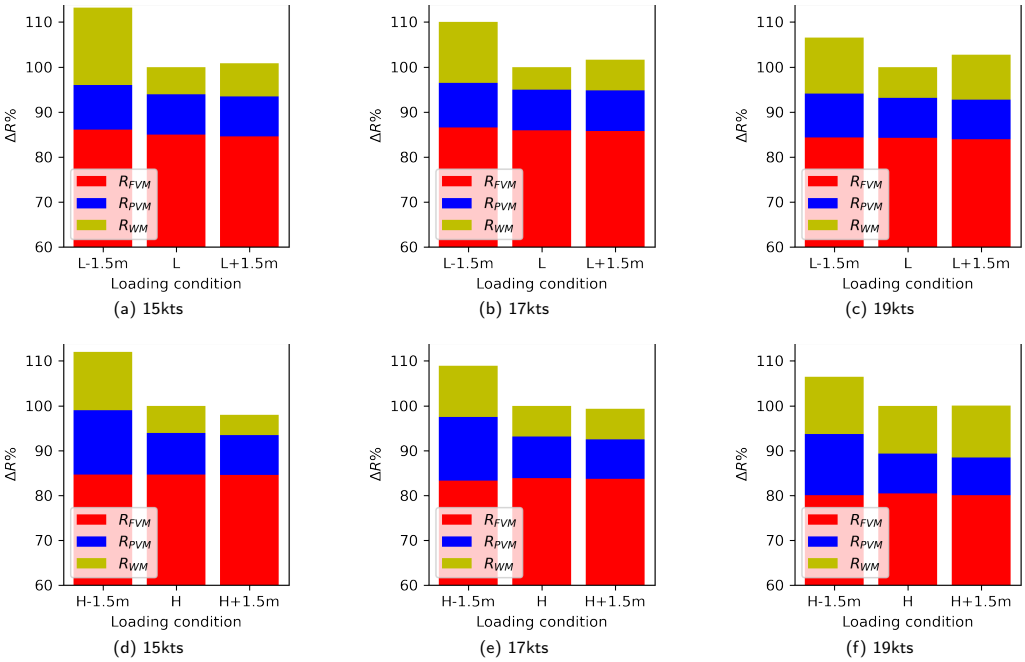

Figure 13: The change of resistance components R_{FVM}, R_{PVM}, R_{WM} with respect to speed and loading condition

resistance component can be considered predominantly a neutral term in this trim optimisation.

The viscous pressure resistance R_{PVM} remains relatively consistent in the light displacement for all speeds and trim conditions. However, R_{PVM} undergoes significant changes in the heavy displacement. As observed in Figure 13d, the increase in R_{PVM} from the even keel to the H-1.5m condition (trim by stern) is the most substantial. This is attributed to the H-1.5m loading condition having the greatest transom submergence and the smallest Froude number.Consequently, the transom remains mostly submerged (see Figure 8b), leading to a resistance increase due to the pressure drop at the transom caused by the recirculating flow, which is reflected in R_{PVM} component (Korkmaz et al., 2022). As demonstrated in Korkmaz, Werner and Bensow (2019), R_{PVM} is relatively insensitive to the mild trim changes when the main flow characteristics, such as flow separation, wake behind the transom, and eddy making, remain similar. This can be observed between the even keel and L+1.5m conditions, as the R_{PVM} term remains similar with respect to the frictional resistance term for each speed and displacement, as shown in Figure 13.

The wave resistance R_{WM} comprises wave pattern and wave-breaking resistance components. As illustrated in Figure 13, R_{WM} is the resistance component that exhibits the most significant variation with respect to the trim conditions, as also concluded by Lemb Larsen et al. (2012). The wave patterns at 17 kn are presented in Figure 14 for all loading conditions. Beginning with the even keel conditions (Figure 14b and Figure 14e), it is evident that neither condition radiates significant diverging wave systems from the forebody. Mild breaking waves are observed in the light displacement with zero trim due to the bulb being too close to the water surface. Conversely, the bow wave height is higher than in the heavy displacement and even keel condition compared to the light loading, but no significant breaking waves are observed in the forebody. Trimming by the bow eliminates the breaking waves altogether in both displacements but triggers diverging waves, as seen in Figure 14c and Figure 14f. Trimming by the stern brings the bulb closer to the free surface, increasing the breaking wave height. In conclusion, the wave patterns at the forebody do not differ significantly between the two displacements with trimming by the bow or the stern.

On the other hand, the wave patterns for the even keel conditions at the aft body differ significantly between the light and heavy displacement, as the H condition has a substantial transom submergence. Due to the transom submergence, the transverse waves are more prominent in the H condition than in the L loading, and the diverging waves break in the heavy displacement, unlike the light loading condition. Further increasing the transom submergence by aft trim triggers breaking diverging waves in the light displacement, but the wave heights behind the transom are slightly reduced

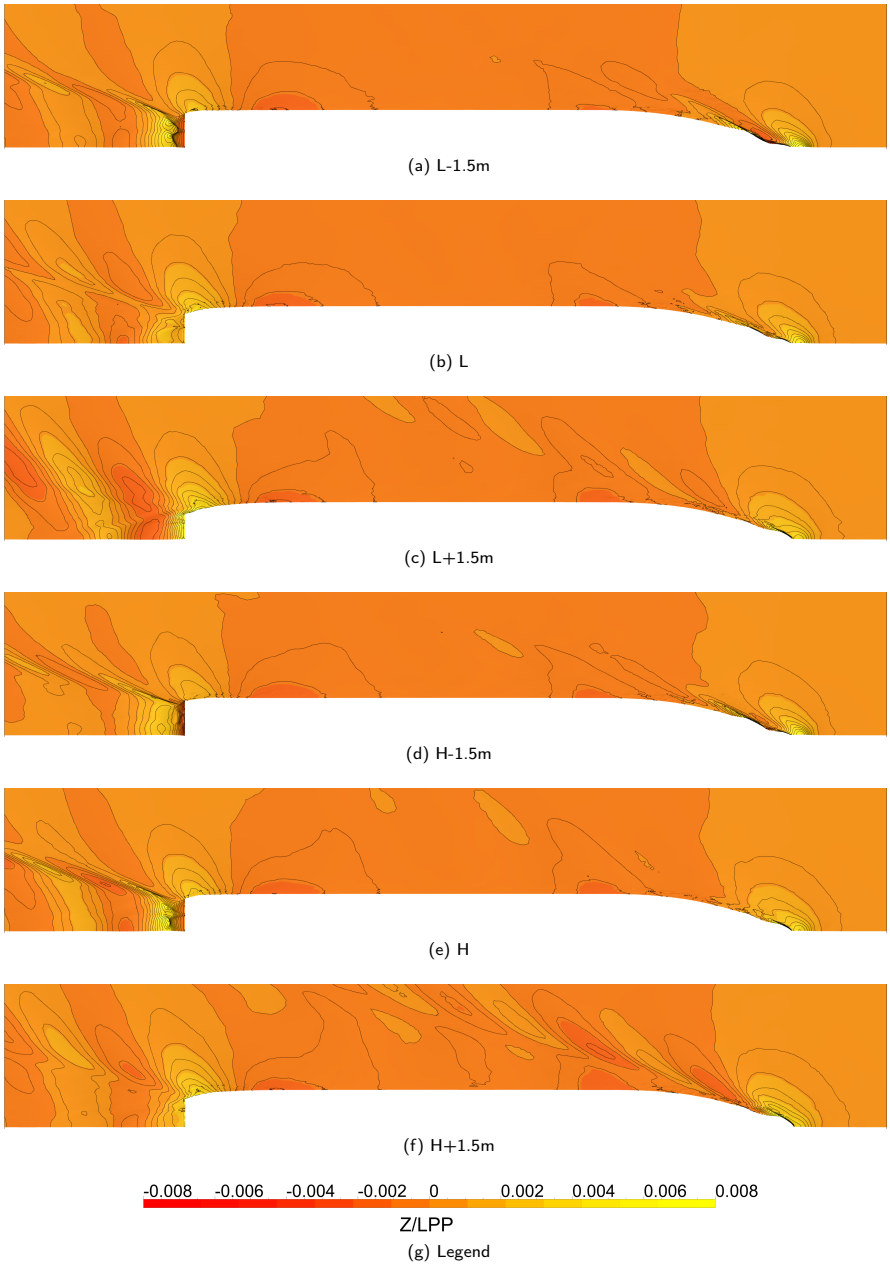

Figure 14: Wave pattern contours for different loading conditions at 17kn

in the heavy displacement. Trim by the bow improves the wave resistance in the aft for heavy displacement, as the transom becomes mostly dry, but increases the wave heights in the light loading.

In conclusion, trimming by the stern worsens the overall wave pattern as the bulb gets too close to the water surface and transom submergence increases. However, gains and losses due to the changes in wave patterns from the forebody and the aft body are not always in the same direction.

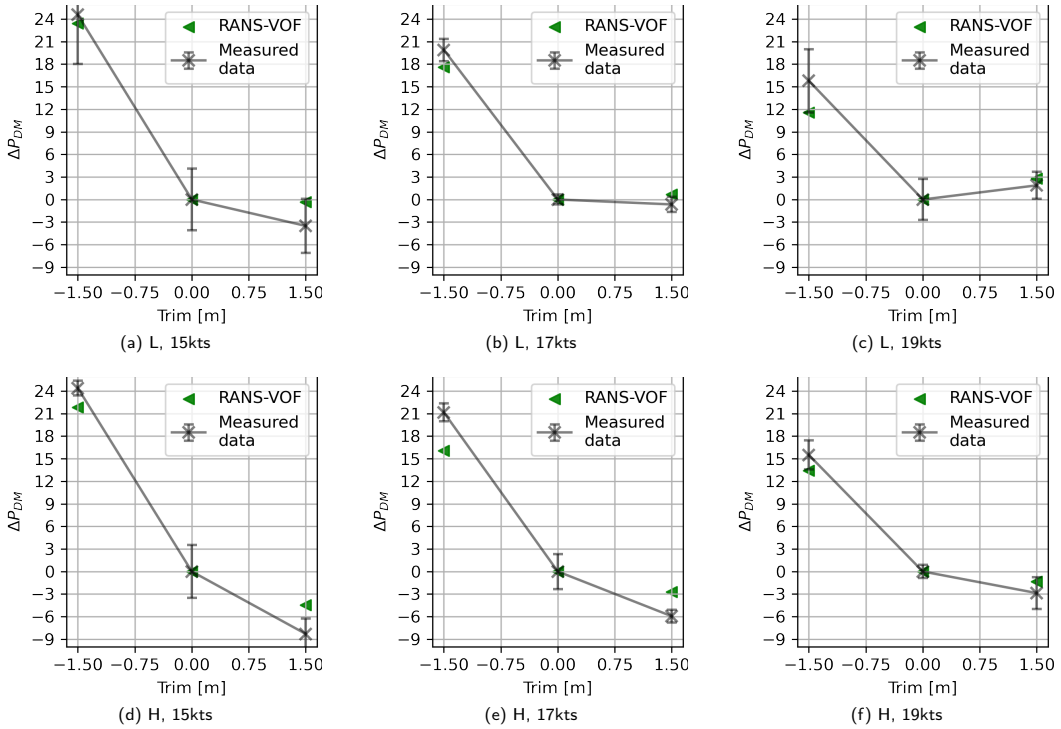

Figure 15: Trim optimisation results of delivered power from self-propulsion from the towing tank measurements and RANS-VOF computations

Therefore, the change in R_{WM} is significantly less for the bow trim compared to the aft trim, as seen in Figure 13.

7.2. Self-Propulsion

This section presents the results of the self-propulsion towing tank tests and computations. The same trim optimisation test conditions as those in the resistance tests (see Section 7.1) were employed; two displacements, three trims, and three speeds. The delivered power in the model scale was calculated from the measured torque and propeller rotation rate, with their measurement uncertainties were predicted as explained in Section 5.1. Compared to the measurements, only the RANS-VOF method (Section 3.3) method was used, as the combination of double-body RANS and potential flow computation results could not accurately predict the resistance trends. The change in delivered power between the trimmed and the even keel conditions for each displacement and speed is calculated

$$\Delta P_{DM} = \frac{P_{DM}(trim) - P_{DM}(trim = 0)}{P_{DM}(trim = 0)} \times 100\,, \quad (20)$$

where $P_{DM}(trim)$ is the delivered power at a given trim condition and $P_{DM}(trim = 0)$ represents the power at the zero trim condition.

7.2.1. Towing Tank Tests – Self-Propulsion

The self-propulsion results from the trim optimisation towing tank tests are presented in Figure 15. The measured data from the tests are denoted by black markers, with the approximated measurement uncertainties indicated by the error bars. Each sub-figure in Figure 15 represents the relative change in delivered power (ΔP_{DM}) under the trimmed conditions with respect to the even keel condition for a specific displacement and speed. A comparison between the total resistance obtained from resistance tests (Figure 7) and the delivered power from self-propulsion tests (Figure 15) shows that trim trends are consistent across most of the loading conditions and speeds. In both sets of tests, trimming by the stern leads to high penalties, while trimming by the bow can result in gains or losses depending on the displacement and speed compared to the even keel condition.

The most notable distinction between the resistance and self-propulsion tests is that the amount of possible gains or losses by trimming the hull seems to be much larger in self-propulsion. For instance, at the H-1.5m condition and 15 kn, ΔR_{TM} is 15% and ΔP_{DM} is 24%. This disparity is not solely attributable to propulsive efficiency but is largely influenced by the differences in the test setups. As required by the ITTC-78 method, the self-propulsion tests were carried out with a

Table 10
Trim trends at 17kts for adjusted total resistance from the resistance tests ($\Delta(R_{TM} - R_a)$), and thrust (ΔT_M), torque (ΔQ_M), propeller turning rate (Δn_M) and delivered power (ΔP_{DM}) from the self-propulsion tests

	Resistance test	Self-propulsion test			
Loading	$\Delta(R_{TM} - R_a)$	ΔT_M	ΔQ_M	Δn_M	ΔP_{DM}
L-1.5m	16.7	15.0	14.0	5.2	19.9
L+1.5m	0.5	0.1	0.3	-1.0	-0.7
H-1.5m	17.6	16.5	15.3	5.1	21.2
H+1.5m	-2.4	-3.5	-4.0	-2.1	-5.9

towing force (R_a), which is unloading the propeller in the tests to account for the difference between frictional resistance coefficients in the model and full scale, and the roughness allowance. In other words, in self-propulsion tests, the propeller thrust does not entirely counteract the resistance observed in the resistance test; instead it is supplemented by a towing force. Consequently, the effective power, as seen in Figure 7 ($P_{EM} = V_M \times R_{TM}$, where V_M represents the model scale velocity and R_{TM} is the resistance from the resistance test), and the power in self-propulsion test, as shown in Figure 15 ($P_{DM} = 2\pi n_M \times Q_M$), cannot be directly compared.

For a fairer comparison, the towing force applied during the self-propulsion test needs to be subtracted from the total resistance obtained in the resistance test. Table 10 displays the trim trends at 17 kn for the adjusted total resistance from the resistance tests ($\Delta(R_{TM} - R_a)$), and thrust (ΔT_M), torque (ΔQ_M), propeller turning rate (Δn_M) and delivered power (ΔP_{DM}) from the self-propulsion tests. The change in thrust from the even keel to the aft trim conditions (L-1.5m and H-1.5m) is lower than the adjusted total resistance ($\Delta(R_{TM} - R_a)$), indicating a lower thrust deduction in the aft trim condition compared to the even keel. However, the sharp increase in the propeller turning rate (approximately 5%) in the aft trim condition compared to the even keel indicates that the wake fraction is also decreased. The hull efficiency

$$\eta_H = \frac{1-t}{1-w_{TM}}\,, \tag{21}$$

where t represents the thrust deduction and w_{TM} is the wake fraction at the model scale. The hull efficiency is reduced from even keel condition to aft trimming. In addition, trimming the vessel by the stern causes a shift in the propeller loading condition (K_{TM}/J_{TM}^2, where K_{TM} is the non-dimensional thrust coefficient, and J_{TM} is the advance ratio) due to the sharp increase in resistance, resulting in a drop in the propeller efficiency. The relative rotative efficiency shows limited change when the vessel is trimmed by the stern; however, the torque increase closely follows the thrust trends. As the delivered power is proportional to the product of torque and propeller turning rate, ΔP_{DM} ends up being larger than the change in adjusted resistance. In other words, the adverse effects of trimming by the stern are exacerbated by reduced propulsive efficiency.

As shown in Table 10, the trim by the bow leads to lower increase in thrust in the L+1.5m condition and a greater decrease in the H+1.5m condition due to reduced thrust deduction in both cases. In contrast to trim by aft, the wake fraction increases during bow trimming, resulting in higher hull efficiency compared to the even keel condition. The propeller and relative rotative efficiencies exhibit relatively minor sensitivity to bow trimming. Consequently, total efficiency increases with trimming by the bow, particularly in heavy displacement, increasing the potential for gains in self-propulsion compared to the resistance.

The findings at other speeds further underscore the differences between self-propulsion and resistance tests. While resistance tests provide a general indication of trim trends, an accurate quantification of optimal trim and potential gains or losses requires self-propulsion tests, which offer a more precise reflection of actual ship operation.

7.2.2. RANS-VOF – Self-Propulsion

The towing tank test conditions for self-propulsion, including the towing force, were computed using the RANS-VOF method, and the ΔP_{DM} values are presented in Figure 15. In the plots, these computation results are denoted as "RANS-VOF" and represented with green triangle markers. Similar to the total resistance predictions in the resistance tests (Figure 7), the RANS-VOF method accurately replicated the trim trends for delivered power from the towing tank. The mean of the absolute values of the differences between ΔP_{DM} predictions from the RANS-VOF method and model tests is 2.62% (excluding zero trim conditions). Considering the simple propeller model employed in the self-propulsion computations, the overall prediction accuracy of the trim trends is remarkably similar to the resistance computations. Therefore, it can be suggested that the actuator disc model adequately captured thrust deduction, wake fraction and propeller loading changes between the trim conditions with reasonable precision.

As observed in Figure 15, ΔP_{DM} is under-predicted 1% to 5% for the trim by the stern. Similar observations were made when predicting resistance in Section 7.1.3, leading to the conclusion that the lack of accuracy in aft trim conditions arises from modelling errors attributed to the presence of severe breaking waves and highly unsteady spill breakers and eddies. Therefore, the under-prediction of ΔP_{DM} is more likely due to the under-prediction of the resistance (or thrust) in the self-propulsion computations rather than the propeller modelling. The RANS-VOF predictions are more successful in predicting the change of power at the trim by the bow than in the aft trim, as the flow is significantly less complex for the trim by the bow compared to the aft trim.

7.3. Comparison of Resistance and Self-Propulsion

The trends in trim optimisation for resistance, obtained from resistance tests, and delivered power, determined through

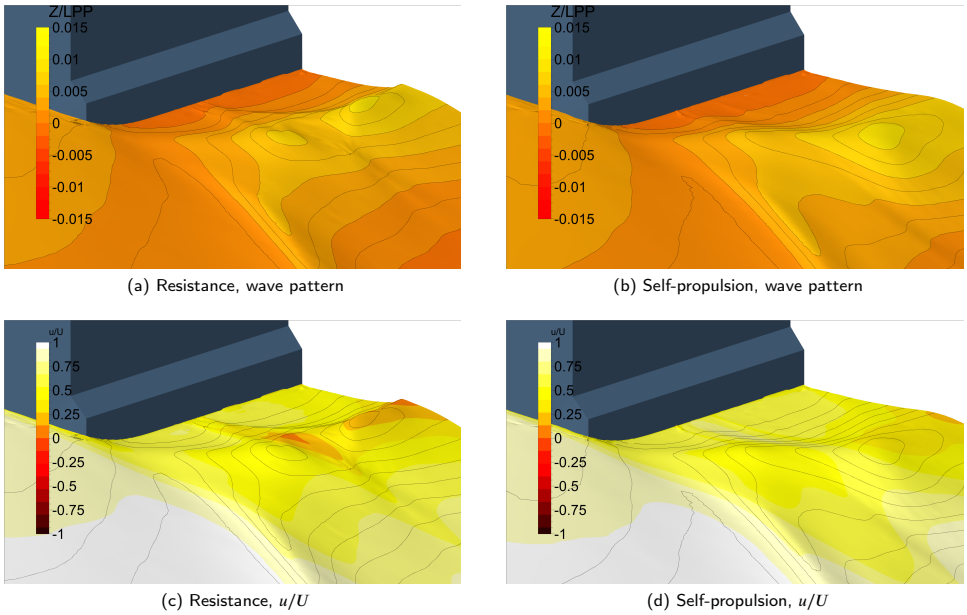

(a) Resistance, wave pattern

(b) Self-propulsion, wave pattern

(c) Resistance, u/U

(d) Self-propulsion, u/U

Figure 16: Wake behind the transom from the RANS-VOF computations in model scale, heavy displacement even keel condition, 19 kn

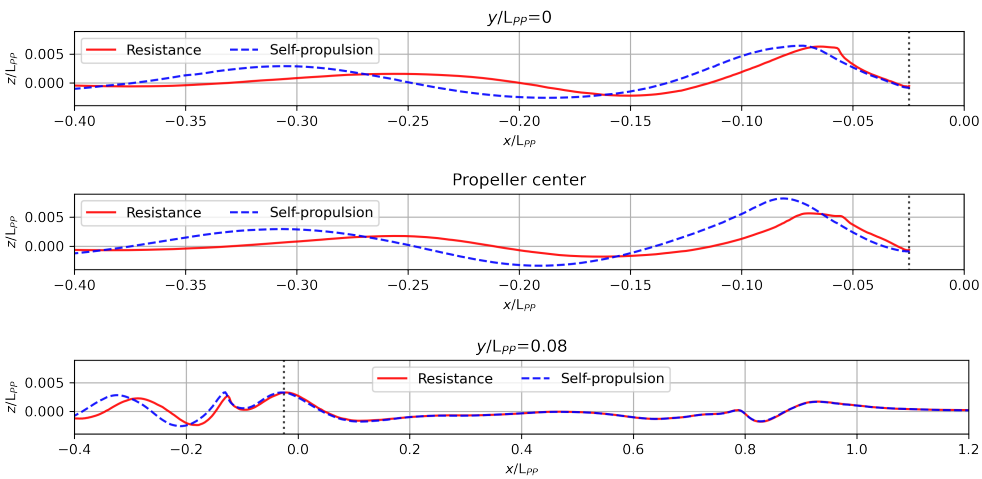

Figure 17: The longitudinal wave cuts from RANS-VOF computations in model scale, heavy displacement even keel condition, 19 kn

self-propulsion tests, are discussed in Sections 7.1.1 and 7.2.1, respectively. It is evident that propulsive efficiency significantly influences the trim trends. This section explores the distinctions in the flow fields between the resistance and the self-propulsion tests and computations. The latter more closely resembles the full-scale ship operating at sea, as it also models the propeller and its effects. The operational propeller introduces significant variations in the pressure distribution at the aft body, and the local flow upstream, and particularly downstream of the propeller location. The pressure drop induced by the propeller at the hull and the appendages, such as the rudder, causes an increase in the dynamic sinkage at the aft body and alters the wave pattern in the hull's wake compared to the resistance mode. Moreover,

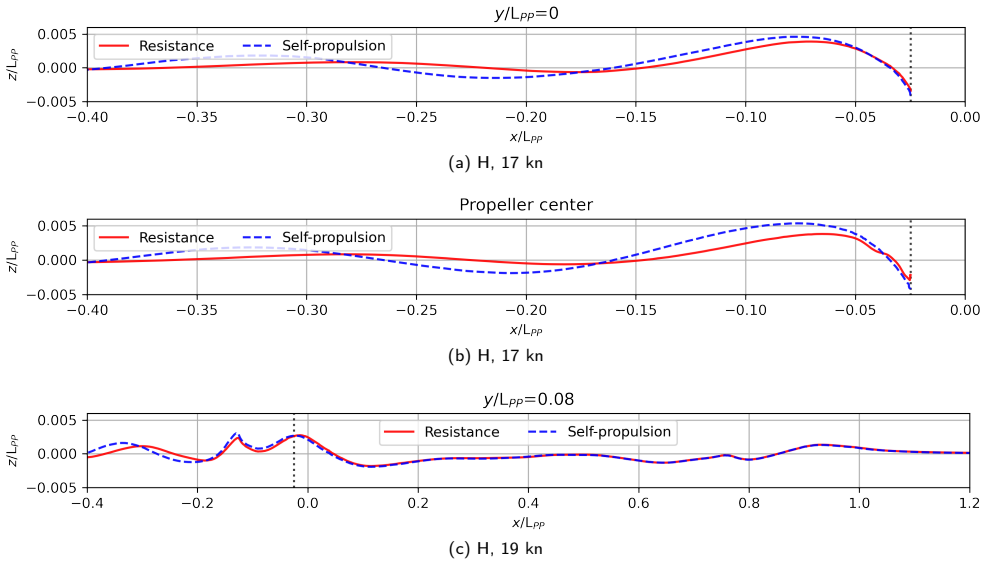

Figure 18: The longitudinal wave cuts from RANS-VOF computations in model scale, heavy displacement trim by the stern, 19 kn

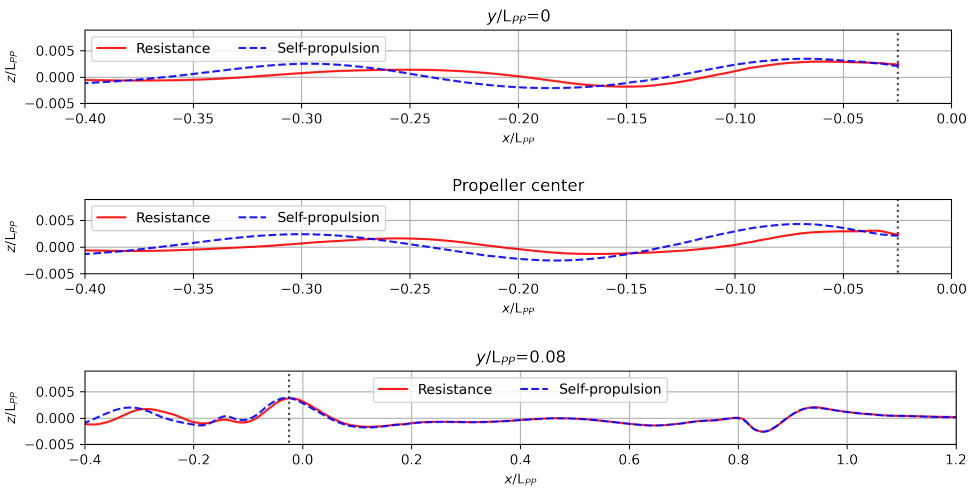

Figure 19: The longitudinal wave cuts from RANS-VOF computations in model scale, heavy displacement trim by the bow, 19 kn

the propeller's jet effect extends not only downstream of the propeller but also reaches up to the free surface, potentially modifying the flow behind the transom.

Due to confidentiality constraints, the pressure distribution on the hull and the appendages cannot be presented. Instead, the wave pattern and the non-dimensional longitudinal velocity (u/V) from the resistance and self-propulsion computations at the heavy displacement even keel condition (H) at 19 kn are presented in Figure 16. As argued earlier, the altered pressure distribution, sinkage at the aft body and the propeller jet cause a profound change in the wave pattern behind the transom as seen in Figure 16a and Figure 16b. In the resistance computation, the trace left by the rudder (originating from approximately the middle of the centre line and side of the transom) can be observed longitudinally from the transom through the first transverse wave crest after the transom. The transverse wave is divided into two, forming a valley where the longitudinal velocity (u/V) drops below

zero, indicating the flow recirculation. In self-propulsion, Figure 16b, the wave trace from the rudder vanishes, and the recirculating flow is eliminated not only just behind the propeller but also at the wave crest along the centre line as seen in Figure 16d.

To comprehend the differences in the wave pattern between resistance and self-propulsion, three longitudinal wave cuts were generated. These wave cuts are positioned transversely at $y/L_{PP} = 0$ (at the centerline), at the transverse location of the propeller centre, and at $y/L_{PP} = 0.08$ from the centerline. In Figure 17, the wave cuts from the resistance and self-propulsion computations are represented by a solid red line, and blue dashed line, respectively. The vertical black dotted line indicates the longitudinal position of the transom. The wave cuts at the centre line and the propeller centre reveal a significant decrease in the steepness of the first wave crest in self-propulsion compared to the resistance. As mentioned earlier in Section 7.1.3, negative u/V values indicated the existence of the flow recirculation where intense spill breakers are observed (see Figure 12b and Figure 11c). From the CFD predictions, it can be argued that the smooth wave profiles as in Figure 17 and non-negative u/V contours on the free surface in the self-propulsion reduced or eliminated the flow recirculation and decreased the intensity of the severe spilling wave breakers compared to the resistance. In fact, the observations from the towing tank tests align with the CFD predictions regarding the flow behind the transom.

Another distinction between the resistance and self-propulsion simulations is that the wave heights downstream of the transom are considerably increased in self-propulsion as seen Figure 16 and Figure 17. The longitudinal wave cuts at the centre-line and the transverse position of the propeller centre shows that the wave heights after the first wave crest behind the transom are increased in self-propulsion by approximately 39% and 76% compared to the resistance, respectively. The wave cuts from $y/L_{PP} = 0.08$ at the downstream of the stern also shows differences between the two simulations but the change is around 14%; hence not as significant as the downstream of the propeller jet and transom. On the other hand, the wave pattern upstream of the aft body shows little to no change as the wave cuts at $y/L_{PP} = 0.08$ from both computations overlap perfectly.

The longitudinal wave cuts from the same transversal position for the H-1.5m and the H+1.5m conditions at 19 kn are presented in Figure 18 and Figure 19, respectively. It is evident that both trim conditions exhibit fewer differences between resistance and self-propulsion computations compared to the even keel condition. The primary reason for this observation is the flow regimes behind the transom for each loading condition. The H+1.5m at 19 kn shows a definitive dry transom flow that is less affected by the altered pressure distribution at the aft body and the propeller jet. Similarly, the H-1.5m condition exhibits nearly wetted transom flow, where extensive recirculation and spilling wave breakers occur immediately after the transom; thus, the difference in pressure and local flow between resistance and self-propulsion has a minor effect. In contrast, the even keel condition features a partially dry transom that is highly unsteady and sensitive to the more minor changes in pressure differences. Therefore, the significance of conducting self-propulsion simulations is greater for the cases where partially dry transom flow is observed.

8. Comparison of Full-Scale Delivered Power Predictions

The trim optimisation towing tank tests have been extrapolated to full scale using the methods described in Section 2. In addition, the predictions from full-scale resistance simulations combined with empirical method (see Section 3.4) and self-propulsion computations (see Section 3.3) are presented. Unlike the model scale, where towing tank tests were conducted with uncertainty estimations, there is no experimental data (i.e. speed trials at the exact loading conditions) with uncertainty estimations in full scale. However, the ship monitoring data, though less accurate than speed trials, can be used to check the trends predicted by different methods.

8.1. Trim Trends from Extrapolation Methods and CFD

The comparison of full-scale predictions is inherently more ambiguous than at the model scale because there is no *true* reference to compare predictions from different methods. Figure 20 presents the trim optimisation results of the delivered power. In a manner similar to the earlier plots (Figure 15 and 7), the non-dimensional delivered power predictions at trimmed conditions are presented with respect to the even keel loading at each speed and displacement (see Eq. 20). 1957 ITTC Performance Prediction Method is denoted as 'ITTC-57', the Standard 1978 ITTC Performance Prediction Method is represented as 'ITTC-78', the ITTC-78 method with the empirical transom correction is denoted as 'ITTC-78tr', and the combined RANS-VOF and empirical self-propulsion method is denoted as 'RANS-VOF-emp' in Figure 20.

8.2. Extrapolation Methods

The towing tank tests were extrapolated using three different methods. As depicted in Figure 20, there is noticeable agreement in the ΔP_{DS} predictions for the trim by the bow (trim>0) among the various scaling procedures. For light displacement with bow trim (left column of plots in Figure 20), the predictions from all three methods are within 0.2%, whereas the heavy displacement shows discrepancies among different methods of up to 1.2%. It's worth noting that the results from ITTC-78 and ITTC-78tr are identical, as there is no transom submergencein the case of bow trim for both displacements.

However, in the case of aft trim (trim<0), as observed in Figure 20, the agreement in ΔP_{DS} predictions among the three scaling procedures is less compared to the trim by the bow. The ΔP_{DS} predictions differ by up to 2.2% for

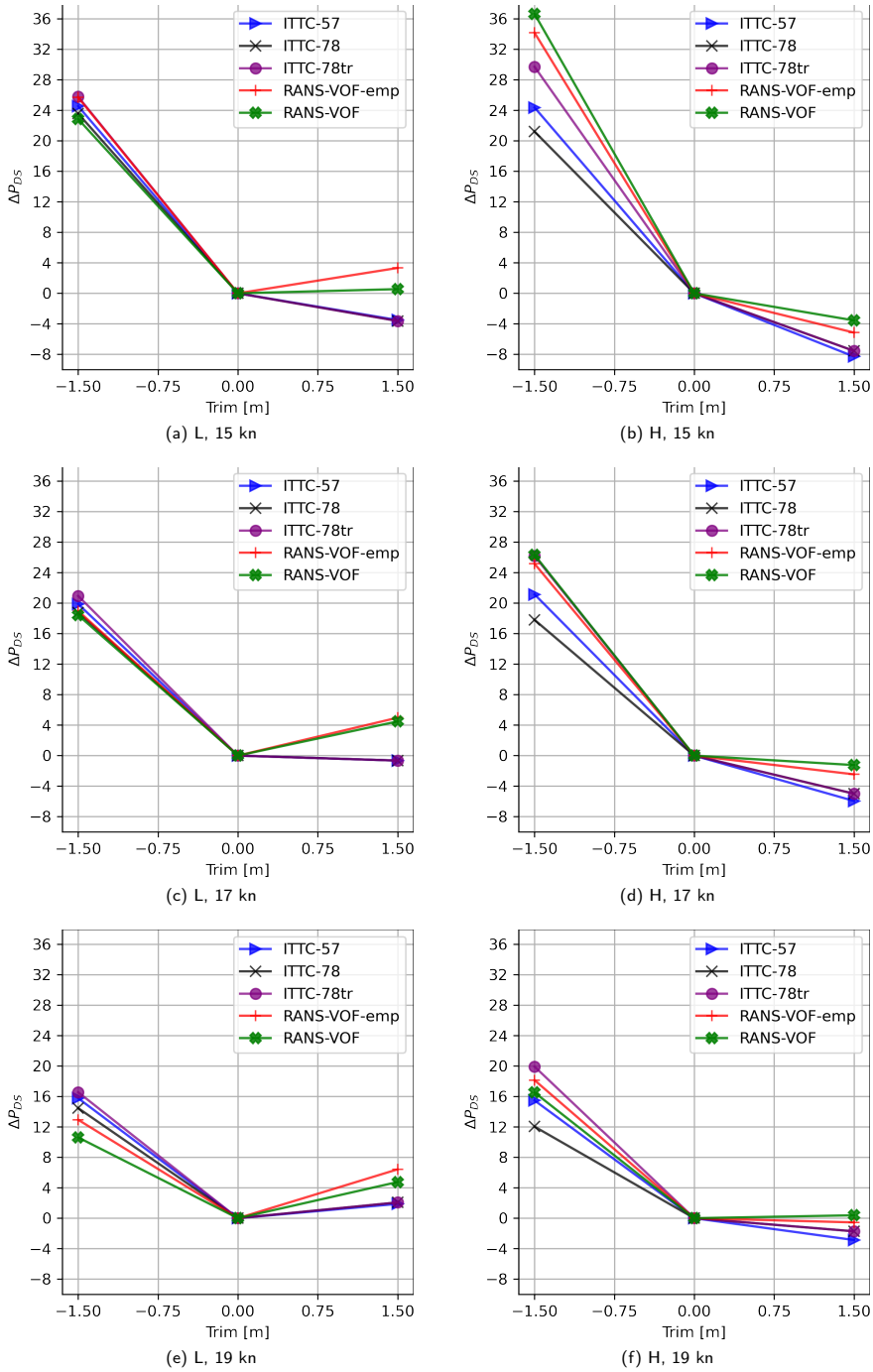

Figure 20: Trim optimisation results of delivered power from the extrapolation methods, RANS-VOF computations and the combined RANS-VOF-empirical method

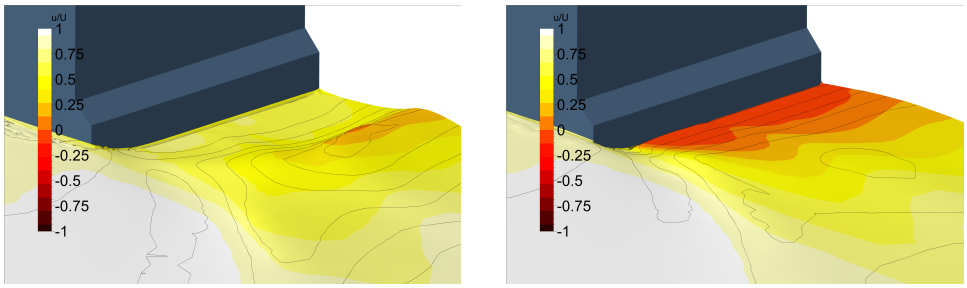

(a) L-1.5m (b) H-1.5m

Figure 21: Non-dimensional longitudinal velocity on the free surface from RANS-VOF computations in full scale at 15 kn

light displacement aft trim conditions. The most significant difference is between the ITTC-78 and ITTC-78tr, as the transom is submerged at rest for the aft trim loading condition, and the transom correction is applied in the ITTC-78tr method. As previously discussed, the transom correction is valid when wetted transom flow is present (Korkmaz et al., 2022). Even though the flow behind the transom at aft trim at 15 kn indicates partially wetted transom flow, the higher speeds of 17 kn and 19 kn lean more towards a dry transom. Consequently, the transom corrections at 17 kn and 19 kn result in an artificially increased delivered power, as observed in Figure 20c and Figure 20e.

The discrepancy in ΔP_{DS} predictions is most significant in the case of heavy displacement with aft trim at 15 kn, as shown in Figure 20b. In this condition, nearly wetted transom flow was observed in the towing tank tests as shown in Figure 8b. If the flow pattern behind the transom is similar in the model and full scale, the ITTC-78 method is unsuitable since the scaling of the viscous pressure resistance leads to under-prediction of the total resistance and delivered power as discussed by Korkmaz et al. (2022). The under-prediction stems from the flow recirculation (i.e. separated flow) behind the transom, which violates the form factor assumptions (Hughes, 1954) used in scaling the resistance. The ITTC-78tr method introduces a correction assuming that flow separation occurs in both the model and full scale, leading to differences in ΔP_{DS} predictions of up to 8.5% between ITTC-78 and ITTC-78tr methods. At other speeds (17 kn and 19 kn) with heavy displacement and aft trim, partially dry transom flow was also observed in model scale, as shown in Figure 11c. Therefore, the ITTC-78tr method includes a correction for submerged transom, assuming a wetted transom in both the model and full scale. This assumption likely does not hold in model scale and probably not in full scale either, causing the ITTC-78tr method to potentially over-predict delivered power in aft trim for heavy displacement, especially at higher speeds.

8.3. CFD Computations

The relative changes in delivered power, ΔP_{DM}, predicted by the two CFD based methods are presented in Figure 20. It is observed that predictions of ΔP_{DS} from both the RANS-VOF and RANS-VOF-emp methods exhibit substantial similarity, despite the latter method being computationally less intensive. In the case of a single screw vessel, the disparity in required computational resources would be even more pronounced, given that the symmetry condition at the centre-plane cannot be applied to self-propulsion computations. Thus, combining full-scale resistance computations with empirical self-propulsion predictions could be considered as an alternative approach to the free-surface RANS self-propulsion computations.

There is no *true reference* in full scale to compare the ΔP_{DS} predictions from the RANS-VOF method. However, the prediction accuracy of the RANS-VOF method in model scale self-propulsion can offer valuable insights when comparing full-scale predictions obtained through extrapolation methods and CFD. The prediction pattern of RANS-VOF exhibit similarities between model and full scale under the loading conditions where transom submergence is either absent or negligible. For instance, the model scale ΔP_{DM} predictions from the RANS-VOF method consistently under-predict the trim by the bow condition when compared to model tests. Similarly, in Figure 20, the full-scale RANS-VOF predictions are 3-4% higher than those obtained from extrapolation methods in the trim by the bow condition.

Conversely, at heavy displacement and aft trim conditions, where the transom is substantially submerged (with the submerged transom area comprising approximately 10% of the maximum cross-section area at rest), predictions from all methods diverge significantly, especially at the lowest speed of 15 kn. The contrast between the agreement of the predictions from different methods for the light and heavy displacements with aft trim at 15 kn is significant, as seen in Figure 20a and Figure 20b. Therefore, the wave pattern and non-dimensional longitudinal velocities on the free surface from RANS-VOF computations under these loading conditions are visualised in Figure 21. The RANS-VOF predicts that the flow behind the transom is dry for the light displacement case. However, for heavy displacement, a partially dry transom is followed by a substantial flow recirculation zone. As previously argued, the flow separation complicates the

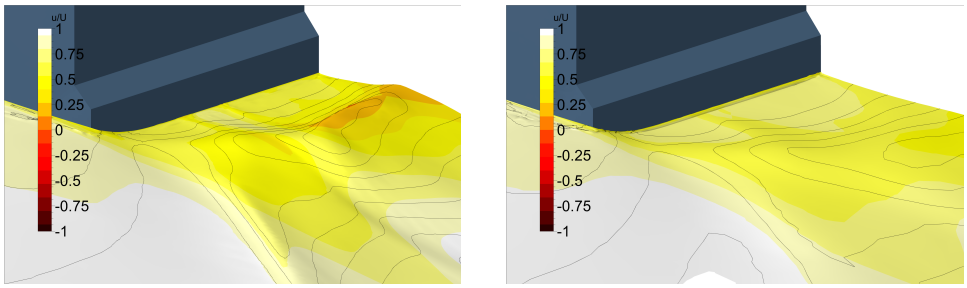

(a) Model scale (b) Full scale

Figure 22: Non-dimensional longitudinal velocity contours on the free surface from RANS-VOF computations in model and full scale at even keel heavy displacement loading and 17 kn

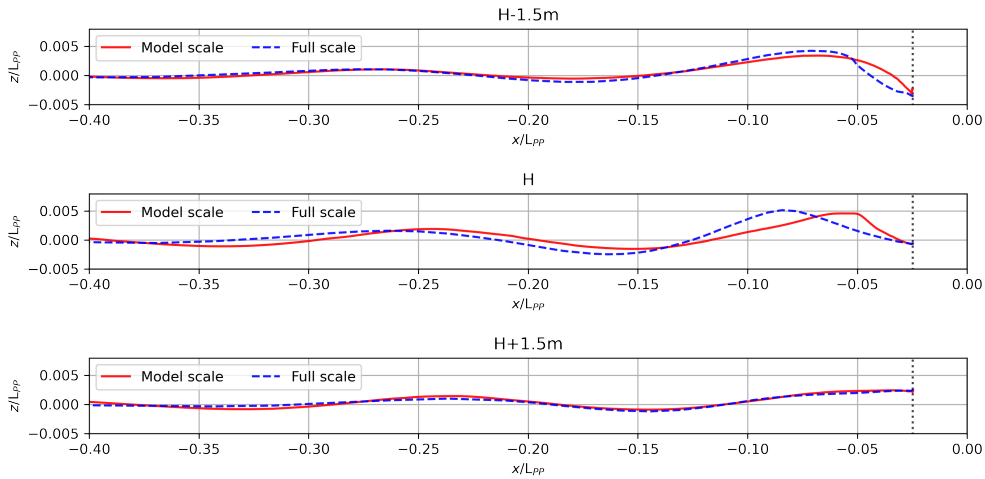

Figure 23: The longitudinal wave cuts at $y/L_{PP} = 0$ (at the centre-line) from model and full-scale RANS-VOF computations at H-1.5m, H and H+1.5m loading conditions at 17 kn

scaling procedure for the extrapolation methods. As a result, different extrapolation methods yield vastly different ΔP_{DS} values at the aft trim condition. As depicted in Figure 20b, the predictions from the RANS-VOF method are closest to the ITTC-78tr method, which incorporates a correction for the wetted-transom flow. With increasing speed, the transom flow regime transitions from partially dry to completely dry transom, and the discrepancies among the different prediction methods reduces in the H-1.5m condition, as shown in Figure 20b, Figure 20d, and Figure 20f.

8.3.1. Model and Full-Scale Comparison

Free-surface RANS self-propulsion computations were employed to compare the flow characteristics between the model and full scale. This comparison holds significance due to a substantial variation in loading conditions and speeds, resulting in partially dry transoms, a few instances of dry transoms, and even conditions with wetted-transom flow. As highlighted by Starke et al. (2007), partially-dry transoms are subjected to large scale effects, potentially leading to distinct flow regimes in model-scale and full-scale scenarios. An illustration of this can be observed in Figure 22, where the model-scale RANS-VOF computations predict a dry transom, but the subsequent wave crest is steep, indicating spill breakers due to low or negative u/V values on the free surface. On the other hand, the full-scale prediction indicates a fully dry transom without a flow recirculation. The primary reason for this scale effect lies in the disparities in the boundary layer and the pressure distribution around the stern between the model and the full scale. With the boundary layer in the full scale being thinner, even when accounting for roughness effects in full-scale computations, the momentum deficit around the wave crest is mitigated, resulting in fully dry transom flow. This change in the boundary layer from model to full scale, in turn, influences the pressure distribution at the stern, which manifests itself

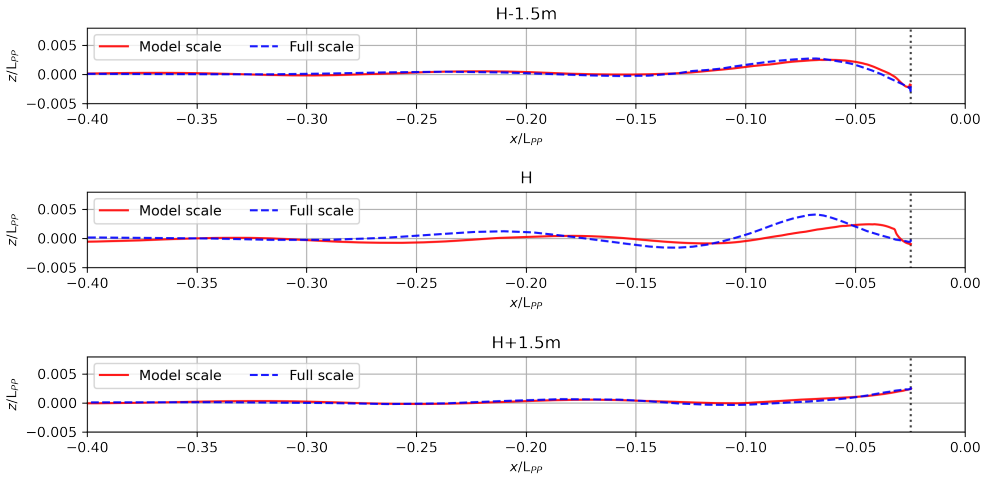

Figure 24: The longitudinal wave cuts at $y/L_{PP} = 0$ (at the centre-line) from model and full-scale RANS-VOF computations at H-1.5m, H and H+1.5m loading conditions at 15 kn

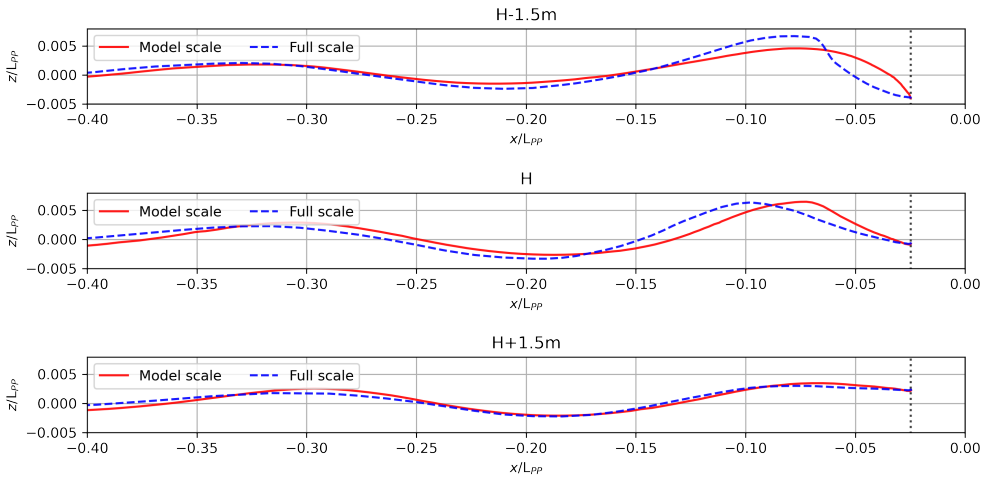

Figure 25: The longitudinal wave cuts at $y/L_{PP} = 0$ (at the centre-line) from model and full-scale RANS-VOF computations at H-1.5m, H and H+1.5m loading conditions at 19 kn

in the wave pattern, as seen in Figure 22. At even keel, heavy displacement, and the speed of 17 kn, the steepness of the first transverse wave crest after the transom, as well as the diverging waves radiating from the transom's side, is significantly reduced. The alteration of the transverse wave profile under these conditions can be observed more clearly in the longitudinal wave cuts in Figure 23 (middle plot), where the model and full-scale computations are compared.

The longitudinal wave cuts at the centre-line for H+1.5m condition, where the transom outside of the water at rest, exhibit only marginal differences between the model and full scale at speeds of 15 knots, 17 knots, and 19 knots, as seen in Figure 24, Figure 23 and Figure 25, respectively. The trim by the bow condition (H+1.5m) consistently results in dry transom flow at all speeds, signifying that the pressure at the transom's edge must be equal to atmospheric pressure, and the variation in the boundary layer between the model and full scale does not significantly affect the wave pattern behind the transom.

On the other hand, the trim by the stern (H-1.5m) condition results in a substantially submerged transom followed by a partially dry transom and is influenced by large scale effects. H-1.5m condition at 15 kn showed a considerable variation in ΔP_{DS} predictions among different methods as

shown in Figure 20. An examination of the wave cuts shown in Figure 24 reveals that the transition from model to full scale does not alter the wave pattern behind the transom for the H-1.5m condition, with the recirculating flow region persisting in full scale, as shown in Figure 21. On the other hand, the even keel condition, H, shifts the flow regime from the partially dry transom to a dry transom. Since ΔP_{DS} represents the relative change in delivered power between the trimmed and even keel conditions, the significant variation in ΔP_{DS} under the H-1.5m condition can be attributed to the persistent flow separation in H-1.5m condition and the changing transom flow regime in the H condition.

The wave pattern behind the transom at 19 kn is also influenced by scale effects in both H and H-1.5m conditions as shown in Figure 25. Similar to 17 kn at these loading conditions, the H-1.5m condition at 19 kn indicates that the flow leaves the transom clearly, but the momentum deficit and steep upward curvature of the wave crest lead to spill breakers; hence, partially dry transom flow is observed in full-scale.

8.4. Ship Monitoring Data

This section compares the full-scale predictions obtained through extrapolation methods and CFD to the ship monitoring data. The full-scale predictions are compared between the delivered power predictions and the power obtained through the propeller turning rate and the shaft torque measurements.

The analysis process is visualised in Figure 26. Firstly, regression analyses (model **A**) were performed on the full-scale predictions, which are denoted as CFD & EFD predictions, at the two displacements (light and heavy), three trims (-1.5m, even keel and 1.5m) and three speeds. Through the regression model for each method, the full-scale delivered power can be predicted not only under the six loading conditions and three speeds but also under the other conditions that were outside of the towing tank test and CFD scope.

Secondly, the ship monitoring data is filtered (designated as filter **I**) to eliminate data points with significant environmental effects such as current, wind, wave and water depth, since the predictions were made for the calm and deep water. The filtered data is then sliced into six subsets based on the draught and speed criteria. Each data slice approximately corresponds to the conditions tested in the towing tank. The filtered ship monitoring data points within each slice were utilised to construct a regression model (model **B**).

Finally, the power predictions from the model **A** (predictions) and model **B** (measurements) are compared for the trim trends at the three speeds and two displacements.

8.4.1. CFD & EFD Predictions

Full-scale predictions were made for two displacements, three trims and three speeds as described earlier in Section 8. Nevertheless, it is crucial to acknowledge that the actual operating conditions of the ship extends well beyond the 18 conditions derived from the CFD and EFD predictions.

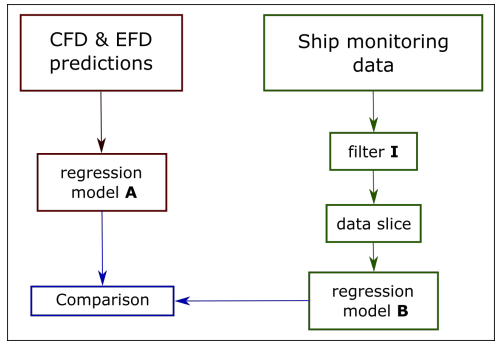

Figure 26: Full-scale analysis process

Consequently, the development of a surrogate model becomes necessary to approximate the conditions between the predicted conditions.

The polynomial response surface approach has been selected for constructing a surrogate model for each prediction method. The three independent variables– draught at midship (T_M), trim and ship speed– are utilised in the regression analysis to predict the dependent variable, namely, delivered power. Given the limited data points available for each independent variable, determining the polynomial degree presents a challenge. Since only two draughts are available, the polynomial's degree cannot exceed one, resulting in a linear regression. However, initial attempts with linear regression attempts yielded unsatisfactory results. The quality of the fit was assessed using the standard deviation of the errors (the difference between the dependent variable and regression predictions) in per cent of the mean delivered power, resulting in a standard deviation of the errors of 5.8% for the linear regression. Therefore, it was decided to artificially increase the number of data points through linear interpolation for the independent variables of draught and trim. Figure 27 illustrates the eighteen original predictions (red markers) and the interpolated additional points (black markers) in three-dimensional scatter plots for each speed.

Following linear interpolation, quadratic and cubic polynomials were fitted to the data points, resulting in standard deviations of errors of 1.0% and 0.7%, respectively. The polynomial response surfaces of both fits were checked since the cubic regression might encounter issues due to incorporating three speeds in the regression. Although the quadratic and cubic response surfaces exhibited similarities, the cubic regression, with its lower standard deviation of errors, was selected for further analysis.

The cubic response surface is visualised for the ITTC-78 method predictions in Figure 27 together with the independent variables (both original and interpolated). To maintain confidentiality, the power is presented in non-dimensional form, and the midship draught is represented by 'Heavy' and 'Light' labels approximately corresponding to the heavy and light displacements, respectively. For each plot (representing

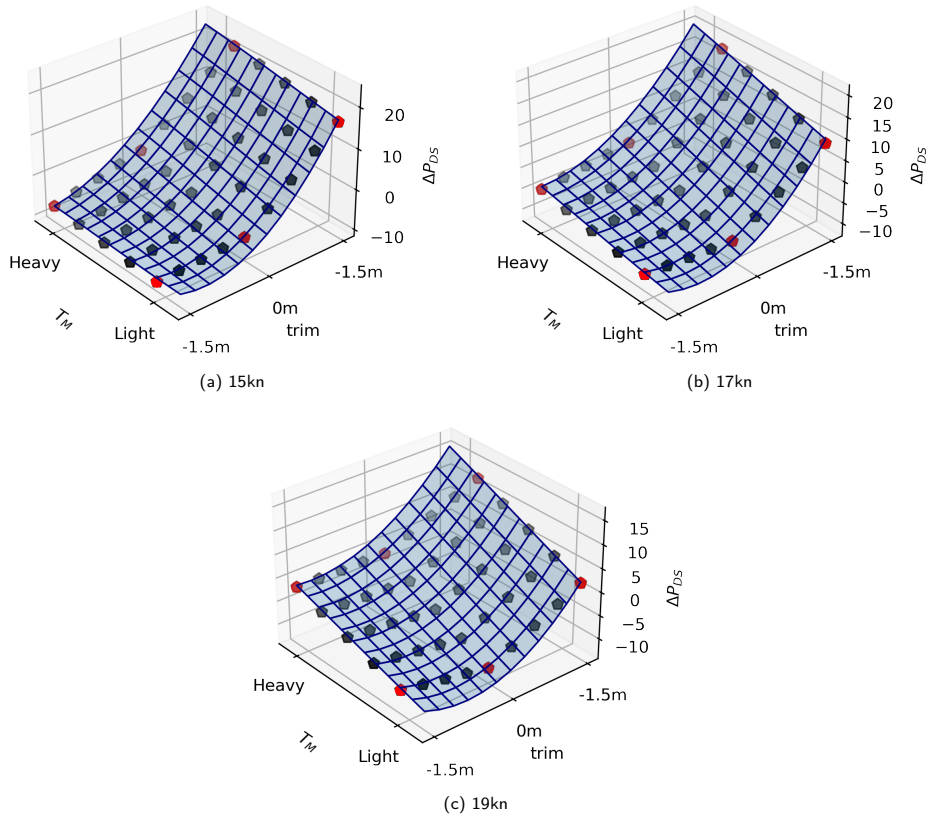

Figure 27: Data points and the response surface for the ITTC-78 method predictions

each speed) in Figure 27, the power is non-dimensionalised by dividing the delivered power at each draught and trim condition by the power at the heavy displacement even keel condition. Qualitatively assessing the similarity between the trim trends from the data points and the resulting response surfaces at each speed reveals satisfactory agreement, as depicted in Figure 27.

8.4.2. Ship Monitoring Data Processing

In the initial stage, a selection of relevant variables is made from the extensive sensor data available. These selected variables characterise the ship's loading conditions, including draught at fore and aft perpendiculars, environmental factors such as current, depth below keel, apparent and true wind speed and direction, and now-casting-based swell and wave height and period. Additionally, variables describing the speed-power performance of the vessel, such as propeller turning rate, shaft torque per propeller, speed over ground, and speed through water, are included in the selection. Subsequently, a thorough examination of the data set is conducted for each recording to ensure the presence and integrity of all selected variables. Regrettably, the now-casting-based data for wave height and period were found to be absent for the first few years of the recording. Therefore, these variables have been removed from the selection of the variables as it would have caused the loss of a significant part of the data. The exclusion of wave height and wave period variables is justifiable, given that the vessel primarily operates in waters sheltered from the open ocean swells. In such conditions, the true wind speed and direction can serve as suitable indicators of wave conditions.

After the data set was cleaned, a set of filters were applied to obtain conditions that closely resemble the calm and deep waters. This step is marked as filter **I** in the visualisation of the full-scale analysis process depicted in Figure 26. The objective of the filter **I** is to render the delivered power describable through a regression model with only draught, trim, and the ship speed as independent variables, mirroring the approach employed in the CFD and EFD prediction methods.

The filtering process begins by selecting between speed over ground (SOG) and speed through water (STW) to

Table 11
Data slices

Slice No	V_S [kn]	T_M	Target
1	15.0 to 16.5	L-0.1m to L+0.2m	light, 15 kn
2	16.5 to 17.5	L-0.1m to L+0.2m	light, 17 kn
3	17.5 to 19.0	L-0.1m to L+0.2m	light, 19 kn
4	15.0 to 16.5	H-0.2m to H+0.1m	heavy, 15 kn
5	16.5 to 17.5	H-0.2m to H+0.1m	heavy, 17 kn
6	17.5 to 19.0	H-0.2m to H+0.1m	heavy, 19 kn

represent the ship's speed. A comparison between SOG and STW reveals that the discrepancy between the two is mostly less than 2 knots. The information received from the ship operators indicated that STW were accurately obtained by the current predictions. Therefore, speed through water is chosen as the representation of ship speed. STW values less than 14.5 kn and greater than 19.5 kn were excluded from the data set, as the CFD and EFD predictions cover speeds between 15 kn and 19 kn.

The vessel continually operates between two specific harbours, with a substantial portion of the waterway between them being relatively shallow. Consequently, data from the shallow segments of the voyage must be excluded to facilitate a meaningful comparison between ship monitoring data, and CFD and EFD predictions. To achieve this, the depth Froude number (Fr_H), the h/Tm ratio (where h refers to the water depth), and the shallow water correction on the viscous resistance component suggested by Raven (2019) are calculated. Data points where $Fr_H > 0.6$ are removed to ensure that the vessel's operation remains within the subcritical range, and shallow water effects do not significantly affect wave patterns. Additionally, data points with $h/T_m < 5$ are filtered out to minimise the shallow water effects on the viscous flow. Finally, the data points where Raven's shallow water correction (Raven, 2019) would exceed 3% of the viscous resistance are also removed. The resulting data is assumed closely resemble conditions in the deep and unconstrained waters.

The vessel's twin-screw propulsive arrangement and engine-gearbox-propeller setup provide the ship master with a wide range of operational flexibility. Depending on the environmental conditions and speed requirements, the vessel does not always operate with equal loads on each shaft line. However, the predictions from EFD and CFD were made for equal propeller loading. Consequently, the data points where either one of the shaft lines bears less than 30% or more than 70% of the total power are removed from the selection.

As previously mentioned, sea wave conditions are was considered highly correlated with wind, given that the vessel operates in somewhat sheltered waters characterised by a median true wind speed of approximately 6.5 m/s, with predominant wind direction being consistent throughout the year. Consequently, the apparent wind direction indicates that the vessel usually experiences the wind from the bow. Accordingly, the maximum limit is set slightly less than twice the ship speed, and the apparent wind speeds exceeding 18 m/s are filtered out.

In addition to speed, data points with draught at midship and trim values falling outside the scope of towing tank tests are excluded. The resulting number of data points is 9.5% of the original recordings in the data set. In other words, filter **I** excludes approximately 90% of the data to align conditions similar to the full-scale CFD and EFD predictions. Histograms of ship speed (denoted as V_S), draught at midship, and trim are presented in Figure 28a, Figure 28b, and Figure 28c, respectively. The histograms reveal that the speed (15, 17 and 19 knots) and draught conditions (L and H) used for the predictions are not evenly distributed. Moreover, the range of trim values in the filtered data is significantly narrower than the towing tank test range (-1.5m to 1.5m), with a pronounced bias towards bow trim.

In addition to classical histograms, two-dimensional histograms are presented to visualise the distribution of points for each combination of trim and speed values in Figure 28d, and for draught and trim values in Figure 28e. The two-dimensional histograms also confirm uneven distribution of data in terms ship speed, draught, and trim conditions. Therefore, a regression analysis on the whole filtered data set is not considered appropriate as the data is highly skewed. Instead, the filtered data is divided into slices presented in Table 11. Each subset is aimed to represent the loading condition and the speeds tested in the towing tank earlier indicated as 'Target' in Table 11. Like the regression model A explained in Section 8.4.1, each data subset is processed with a regression analysis where the independent variables are ship speed, draught at midship and trim and the dependent variable is the total power. As evident in Figure 28d and Figure 28e, there is a shortage of trim values at the extremities. To mitigate potential bias stemming from limited trim values, each regression model corresponding to a data subset is constructed where a sufficient number of trim values is available, as presented in Section 8.4.3.

As illustrated in Figure 26, regression model **B** is employed to predict the precise conditions under which full-scale predictions were conducted. To assess the performance of each data subset's regression model, residuals are calculated. These residuals represent the difference between the measured and predicted power within each data subset using model **B**. The residuals are normalised based on the power prediction at even keel conditions at the 'Target' displacement and speed specified in Table 11. The residuals and an approximation of the probability density function are presented in Figure 29. The residuals are distributed close to a normal distribution, and the standard deviation of the normalised residuals ranges between 8% to 11%. Considering that the combined bias and precision limit of a single speed trial is approximately 8% (Insel, 2008), and that ship monitoring data collection generally exhibits less precision than speed trials conducted under relatively controlled environmental conditions, the prediction accuracy of regression model **B** step for each data subset is deemed satisfactory.

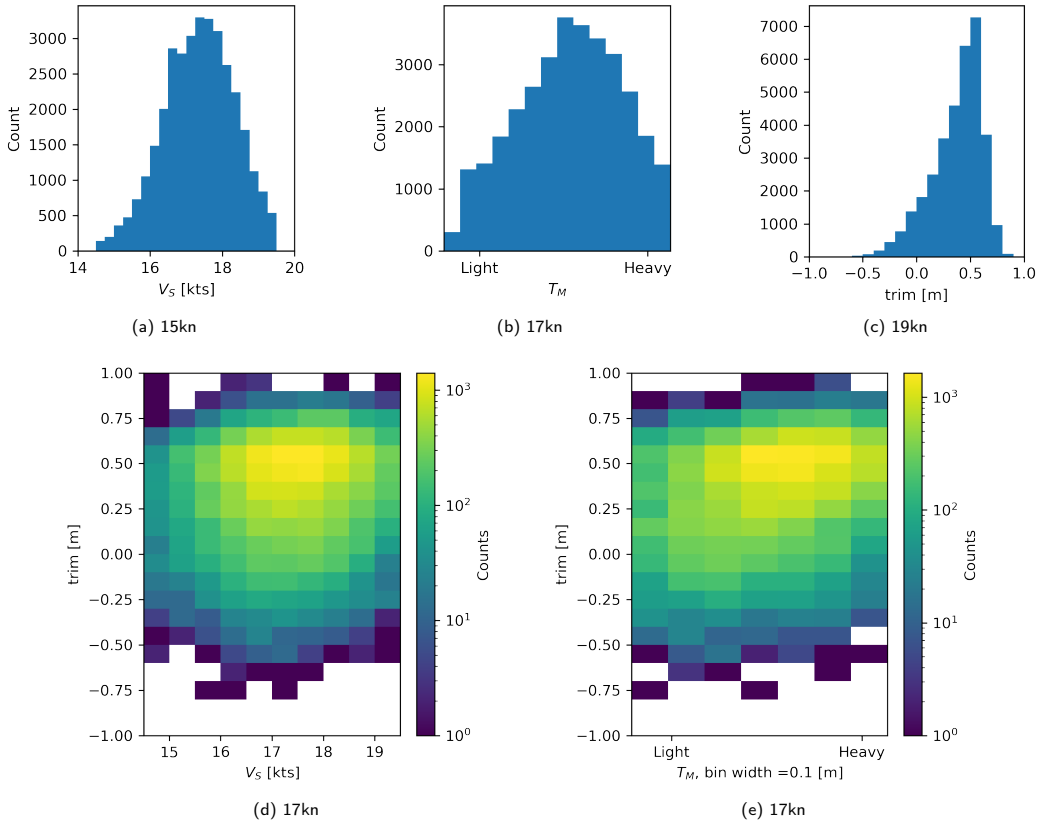

(a) 15kn (b) 17kn (c) 19kn

(d) 17kn (e) 17kn

Figure 28: Histograms of V_S, T_M and trim from the ship monitoring data

8.4.3. Comparison of Predictions and Ship Monitoring Data

The final step in the full-scale analysis process involves comparing the measured and predicted power. As shown in Figure 26, the two regression models (**A** and **B**) can be used to estimate the trends in trim optimisation conditions explored in the preceding sections: light and heavy displacement, three speeds and the appropriate range of trim values within each data subset. In Figure 30, predictions derived from extrapolation methods and CFD are presented alongside the trim trends derived from the ship monitoring data, denoted as data fit. Notably, the combined RANS-VOF and empirical self-propulsion (RANS-VOF-emp) method is omitted from the plot, as its full-scale predictions largely overlap with those of RANS-VOF. A reference band (the light blue shaded region) of $\pm 5\%$ is placed around the data fit curve, and histograms of the trim values are displayed above each plot. The x-axis of these histograms and the plots below them are aligned to indicate the frequency and skewness of the trim values in each data slice. The comparison of each prediction method and data fit is confined to the range where a sufficient number of trim values are available. The extent of the curves in each plot corresponds to the trim values used to generate the regression model **B** for the respective data slices. The y-axis, denoted as ΔP_{DS}, represents the change in power with varying trim values in per cent of the power prediction of each method at zero trim, for each displacement and the speed indicated in the caption. Lastly, the number of points in each data slice is indicated with N in the histogram plots.

Figure 30 is organised and presented similarly to the earlier full-scale predictions shown in Figure 20. The foremost and most significant observation is that all predictions from the extrapolation and CFD methods fall within the 5% reference band. Given the uncertainties associated with ship monitoring data collection and curve fitting, this strong agreement between the predictions and measurements across the entire range of loading conditions and ship speeds is noteworthy. In addition, all prediction methods and the data fit concur that trimming by the stern increases the delivered power demand at all loading conditions and speeds. While the measurements and the predictions for the trim by the

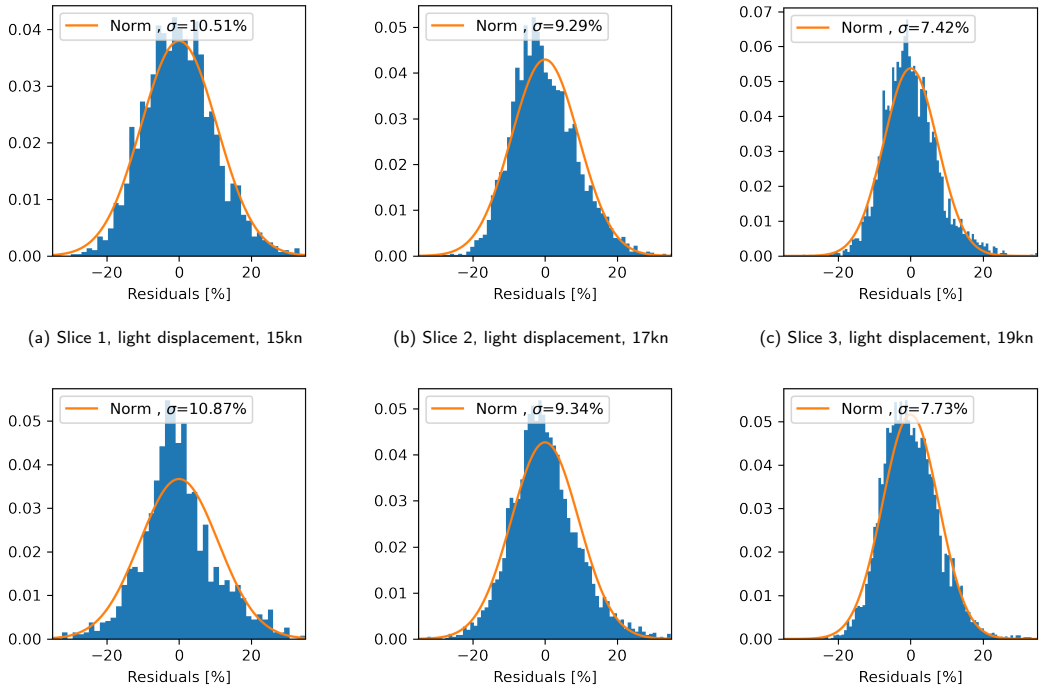

(a) Slice 1, light displacement, 15kn (b) Slice 2, light displacement, 17kn (c) Slice 3, light displacement, 19kn

(d) Slice 4, heavy displacement, 15kn (e) Slice 5, heavy displacement, 17kn (f) Slice 6, heavy displacement, 19kn

Figure 29: The normalised distribution of errors for the regression model **B** for each data slice

bow largely align, the data fit suggests that the optimum trim occurs at smaller trim values compared to the prediction methods.

It is worth noting that the trim trends derived from the ship monitoring data fit exhibit some inconsistencies. For instance, the data fit indicates changes in delivered power of approximately -6%, -1% and -4% for the heavy displacement, 0.75m trim at the speeds 15 kn (Figure 30b), 17 kn (Figure 30d), and 19 kn (Figure 30f), respectively. However, this trend cannot be justified, as flow phenomena observed in the towing tank tests and the CFD computations suggest a monotonic change. Therefore, the trim trends derived from the ship monitoring data should only be used as an indication with a considerable reference band that can account for some of the fluctuations observed in the data curve fits.

9. Conclusions

In this study, the trim optimisation trends of a RoPax vessel were investigated using experimental and computational methods. The accuracy of various CFD methods in the model scale was assessed through comparisons made with towing tank tests. Subsequently, full-scale predictions obtained from both experimental and computational methods were compared with the ship monitoring data.

Four grid dependence studies were conducted using adaptive grid refinement technique. The resistance and self-propulsion computations, covering both model and the full scales, exhibited a pattern of monotonic and asymptotic convergence for the series of meshes. It is noteworthy that imperfect geometrical similarity , coupled with the potential existence of higher-order errors, may have contributed to modest fluctuations observed between the power-of-law curve fits and computed values. Nevertheless, the utilisation of grid adaptation predicated on metric tensors (i.e. the adaptive grid refinement) proved effective in generating series of meshes suitable for grid convergence studies, both at the model and the full-scale Reynolds numbers.

The model scale computations were validated against the model test results with measurement uncertainty estimations at the even keel heavy displacement loading condition. The validation was achieved from a programmatic standpoint for the total resistance from the resistance computations with the finest three grids. However, the comparison error for the thrust from the self-propulsion computation exceeded the validation uncertainty, pointing towards nonnegligible

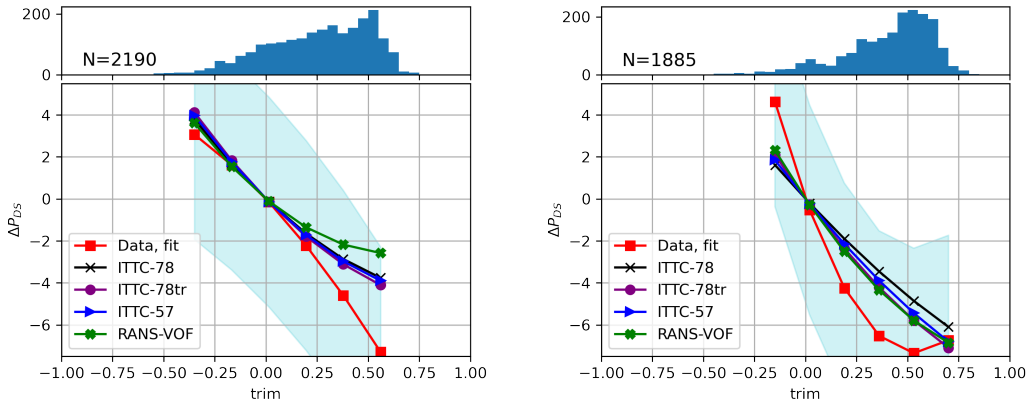

(a) Slice 1, light displacement, 15kn

(b) Slice 4, heavy displacement, 15kn

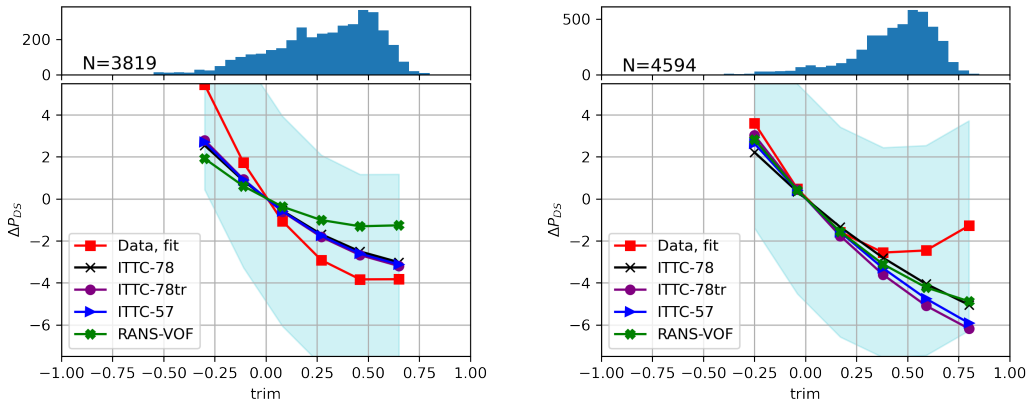

(c) Slice 2, light displacement, 17kn

(d) Slice 5, heavy displacement, 17kn

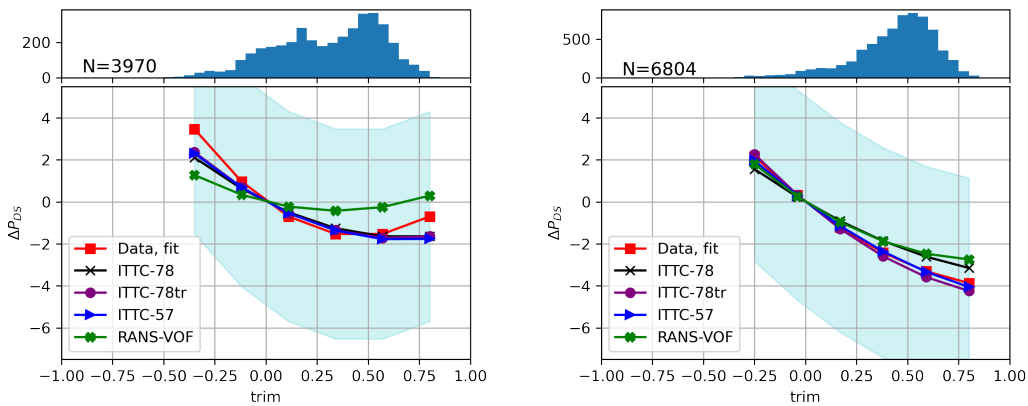

(e) Slice 3, light displacement, 19kn

(f) Slice 6, heavy displacement, 19kn

Figure 30: The comparison between the trim trends from the ship monitoring data, the extrapolations methods and RANS-VOF

modelling errors. Considering the simplistic approach of the actuator disc model used in this study, some modelling errors are expected. However, the off-prediction of the absolute values can be tolerated concerning the trim optimisation studies as the relative change between the loading conditions is more important to capture than the absolute value.

Towing tank resistance tests revealed limited potential for resistance reduction through trimming by the bow, while trimming by the stern resulted in significant resistance penalties across all loading conditions and speeds. Comparison between different CFD methods and the towing tank resistance tests yielded the following insights:

- the combined double-body RANS and potential flow method proved inadequate in accurately predicting resistance trim trends for the test case. The double-body approach struggled to model loading conditions with substantial changes in submerged geometry due to wave patterns or dry transoms. In addition, the potential flow method were challenged by loading conditions involving significant breaking waves and the transom flow regimes characterised by high viscous effects, such as wetted and partially dry transom flows. While this method may yield more reliable results for full block and slow-steaming vessels, it is not recommended for slender vessels operating at medium to high Froude numbers.

- The RANS-VOF method provided generally accurate replication of towing tank resistance tests. Notably, its prediction accuracy was significantly higher for the trim by the bow conditions compared to the trim by the stern. This observation is attributed to the modelling errors caused by highly unsteady and complicated flow phenomena observed when the transom is substantially submerged. Nonetheless, the primary flow features such as transom dryness, recirculation zones, and wave patterns were predicted accurately by the RANS-VOF method.

- Examination of resistance components in various loading conditions and speeds showed that changes in frictional resistance component with respect to trim was insignificant. The viscous pressure resistance also shows a limited variation with respect to trim, unless the flow regime behind the transom changes. In contrast, wave resistance (or residual resistance) exhibited significant variations with different trims, making it the primary contributor to potential gains or losses resulting from trimming.

- The trim trends of a vessel are primarily influenced by transom submergence and the consequent flow regimes behind the transom. However, the design of the forebody, including the bulbous bow, also played a significant role in determining optimal trim. It is essential to note that bulbous bows optimised for specific narrow operational conditions could lead to undesirable wave patterns and increased resistance when the vessel is in a trimmed state.

In addition to resistance tests, self-propulsion tests were conducted in the towing tank. The trim trends observed for resistance and self-propulsion tests were generally in agreement. However, significant variations in propulsive efficiency variation with trim were noted. Consequently, accurately quantifying the optimum trim and potential gains or losses necessitates self-propulsion tests. The effect of the propeller jet was also found to have a substantial impact on dynamic sinkage and trim, and local flow.

Self-propulsion towing tank tests were replicated using the RANS-VOF method with a relatively simple actuator disc model. While prediction accuracy in power was slightly lower for self-propulsion simulations compared to predicting resistance from the resistance tests, the actuator disc model effectively captured variations in propulsive efficiency. Furthermore, the propeller jet generated by the actuator disc reproduced the local flow differences, particularly in conditions involving partially dry transoms, as observed in resistance and self-propulsion tests.

Full-scale predictions for delivered power were made using three different extrapolation methods: one computational method and one combined CFD & empirical method. Comparison of these prediction methods revealed that

- transom submergence is the most decisive factor for the agreement between prediction methods. The trim trends for power predictions from the extrapolation methods closely aligned when transom submergence was minimal (i.e., light displacement at even keel and bow trim, and heavy displacement in trim by the bow). Conversely, power predictions for the trim by the stern (involving large transom submergence) exhibited substantial variation.

- predictions from the direct full-scale CFD (RANS-VOF) and the combined CFD & empirical method were largely similar. Given the significantly lower computational resources required for the latter, it presents a viable alternative to full-scale self-propulsion computations. However, the combined CFD & empirical method necessitates estimations for the propulsive factors, which may pose challenges for users lacking a robust reference or database.

- among the three EFD based extrapolation methods, the ITTC-78 method with transom correction exhibited the closest agreement with full-scale CFD predictions.

In addition to comparing flow fields between the resistance and self-propulsion at the model scale, free surface RANS self-propulsion computations were employed to compare local flow between the model and full scale. Conditions involving partially-dry transom flow exhibited significant scale effects. In some cases, the flow regime behind the transom was fully dry at full scale but partially dry at

the model scale. In other instances, both scales exhibited partially dry transom, but wake and wave pattern behind the transom varied considerably between the model and full scale. Scale effects were less pronounced when the transom was fully wetted or dry.

Comparison between ship monitoring data and predictions from extrapolation methods and full-scale CFD revealed similar trim trends across various loading conditions and ship speeds. While optimum trim angle indications from ship monitoring data were slightly smaller than those suggested by EFD and CFD based predictions, all prediction methods' trim trends were are within 5% of the measurements. It is advisable to use ship monitoring data as an indication with a reference band of 5% or more, which can account for the artificial fluctuations observed in the data curve fits.

In summary, the full-scale self-propulsion CFD method (denoted as RANS-VOF) emerges as a reasonably accurate and cost-effective approach for determining trim trends. However, it is crucial to acknowledge the potential presence of modelling errors in specific loading conditions, underscoring the importance of thorough verification and validation studies are advised. In case of towing tank testing, results should be extrapolated using a method that incorporates corrections for the substantially submerged transom.

The conclusions and recommendations derived from this study are applicable primarily to deep and calm sea conditions, which may not always reflect real ship operation scenarios. Consequently, further research is needed to investigate the impact of shallow waters and waves on trim trends.

CRediT authorship contribution statement

Kadir Burak Korkmaz: Conceptualization, Methodology, Validation, Formal analysis, Investigation, Data curation, Writing - Original draft preparation, Writing - Review & Editing, Visualization. **Sofia Werner:** Conceptualization, Methodology, Investigation, Writing - Review & Editing, Supervision, Project administration, Funding acquisition. **Rickard Bensow:** Conceptualization, Methodology, Investigation, Writing - Review & Editing, Supervision.

Acknowledgements

This research was funded by Energimyndigheten, the Swedish Energy Agency, grant 2020-018759, and the computational resources provided by RISE-SSPA Sweden AB.

The authors declare no conflict of interest. The funders had no role in the design of the study; in the collection, analyses, or interpretation of data; in the writing of the manuscript, or in the decision to publish the results.

References

Bertram, V., 2020. Fairy Tales Revisited – Energy Efficiency Options, in: 5th Hull Performance & Insight Conference, Hamburg, Germany.

Broberg, L., Regnström, B., Östberg, M., 2014. SHIPFLOW Users Manual. FLOWTECH International AB, Gothenburg, Sweden.

Chen, J., Yu, C., Shen, L., 2019. Study of Trim Optimization Based on Design of Experiments and RANS Simulation, in: 11th International Workshop on Ship and Marine Hydrodynamics, Hamburg, Germany.

Coraddu, A., Oneto, L., Baldi, F., Anguita, D., 2017. Vessels fuel consumption forecast and trim optimisation: A data analytics perspective. Ocean Engineering 130, 351–370. URL: https://www.sciencedirect.com/science/article/pii/S0029801816305571, doi:https://doi.org/10.1016/j.oceaneng.2016.11.058.

Eça, L., Hoekstra, M., 2014. A procedure for the estimation of the numerical uncertainty of cfd calculations based on grid refinement studies. Journal of Computational Physics 262, 104–130. doi:10.1016/j.jcp.2014.01.006.

Hansen, H., Freund, M., 2010. Assistance tools for operational fuel efficiency, in: 9th International Conference on Computer and I.T. Applications in the Maritime Industries. COMPIT 2010, Gubbio, Italy.

Hughes, G., 1954. Friction and Form Resistance in Turbulent Flow, and a Proposed Formulation for Use in Model and Ship Correlation. R. I. N. A. 96.

Hüffmeier, J., Lundman, J., von Elern, F., 2020. Trim and Ballast Optimisation for a Tanker Based on Machine Learning. Technical Report WP3. Research Institutes of Sweden.

IMO, 2011. Annex 19: Resolution MEPC.203(62) .

IMO, 2021. Fourth IMO GHG Study 2020. International Maritime Organisation, 4 Albert Embankment, London SE1 7SR.

IMO, 2022a. 2022 guidelines on operational carbon intensity indicators and the calculation methods (CII guidelines, G1). Annex 14: Resolution MEPC.352(78) .

IMO, 2022b. 2022 guidelines on the method of calculation of the attained energy efficiency existing ship index (EEXI). Annex 12: Resolution MEPC.350(78) .

IMO, 2023. Definitions of maturity levels according to uptake across the maritime industry, and degree of proven technology/principle. URL: https://greenvoyage2050.imo.org/technology-groups/.

Insel, M., 2008. Uncertainty in the analysis of speed and powering trials. Ocean Engineering 35, 1183 – 1193. URL: http://www.sciencedirect.com/science/article/pii/S0029801808000929, doi:https://doi.org/10.1016/j.oceaneng.2008.04.009.

Islam, H., Guedes Soares, C., 2019. Effect of trim on container ship resistance at different ship speeds and drafts. Ocean Engineering 183, 106–115. URL: https://www.sciencedirect.com/science/article/pii/S0029801819301477, doi:https://doi.org/10.1016/j.oceaneng.2019.03.058.

ITTC, 1957. Subjects 2 and 4 Skin Friction and Turbulence Stimulation .

ITTC, 2014. General guideline for uncertainty analysis in resistance tests. ITTC – Recommended Procedures and Guidelines 7.5-02-02-02.

ITTC, 2021a. 1978 ittc performance prediction method. ITTC – Recommended Procedures and Guidelines 7.5-02-03-01.4.

ITTC, 2021b. General guideline for uncertainty analysis in resistance tests. ITTC - Quality System Manual Recommended Procedures and Guidelines 7.5-02-02-02.

ITTC, 2021c. Open water test. ITTC – Recommended Procedures and Guidelines 7.5-02-03-01.

ITTC, 2021d. Practical guidelines for ship resistance cfd. ITTC – Recommended Procedures and Guidelines 7.5–03–02–04.

ITTC, 2021e. Quality assurance in ship cfd application. ITTC – Recommended Procedures and Guidelines 7.5–03-01–02.

ITTC, 2021f. Quality assurance in ship CFD application. ITTC – Recommended Procedures and Guidelines 7.5-03-01-02.

ITTC, 2021g. Resistance test. ITTC – Recommended Procedures and Guidelines 7.5-02-02-01.

ITTC, 2021h. Uncertainty analysis in cfd verification and validation methodology and procedures. ITTC - Quality System Manual Recommended Procedures and Guidelines 7.5-03-01-01.

Kanninen, P., Peltonen, P., Vuorinen, V., 2022. Full-scale ship stern wave with the modelled and resolved turbulence including the hull roughness effect. Ocean Engineering 245, 110434. URL: https://www.sciencedirect.com/science/article/pii/S0029801821017194, doi:https://doi.org/10.1016/j.oceaneng.2021.110434.

Kjellberg, M., Gerhardt, F.C., Werner, S., 2022. Sailing in waves: A numerical method for analysis of seakeeping performance and dynamic behavior of a wind powered ship, in: The 24th Chesapeake Sailing Yacht Symposium, Annapolis, Maryland.

Korkmaz, K.B., Werner, S., Bensow, R., 2019. Investigations for CFD based form factor methods, in: Numerical Towing Tank Symposium (NuTTS 2019).

Korkmaz, K.B., Werner, S., Bensow, R., 2021a. Verification and validation of CFD based form factors as a combined CFD/EFD method. Journal of Marine Science and Engineering 9. URL: https://www.mdpi.com/2077-1312/9/1/75, doi:10.3390/jmse9010075.

Korkmaz, K.B., Werner, S., Bensow, R., 2022. Scaling of wetted-transom resistance for improved full-scale ship performance predictions. Ocean Engineering 266, 112590. URL: https://linkinghub.elsevier.com/retrieve/pii/S002980182201873X, doi:10.1016/j.oceaneng.2022.112590.

Korkmaz, K.B., Werner, S., Sakamoto, N., Queutey, P., Deng, G., Yuling, G., Guoxiang, D., Maki, K., Ye, H., Akinturk, A., Sayeed, T., Hino, T., Zhao, F., Tezdogan, T., Demirel, Y.K., Bensow, R., 2021b. CFD based form factor determination method. Ocean Engineering 220, 108451. URL: https://www.sciencedirect.com/science/article/pii/S0029801820313585, doi:https://doi.org/10.1016/j.oceaneng.2020.108451.

Larsson, L., Raven, H.C., 2010. Ship Resistance and Flow. The Society of Naval Architects and Marine Engineers, Jersey City, New Jersey.

Lemb Larsen, N., Simonsen, C.D., Nielsen, C.K., Holm, C.R., 2012. Understanding the physics of trim, in: 9th Annual Green Ship Technology (GST) Conference, Copenhagen, Denmark.

Mahmoodi, H., Ghamari, I., Hajivand, A., Mansoori, M., 2023. A cfd investigation of the propulsion performance of a low-speed vlcc tanker at different initial trim angles. Ocean Engineering 275, 114148. URL: https://www.sciencedirect.com/science/article/pii/S0029801823005322, doi:https://doi.org/10.1016/j.oceaneng.2023.114148.

Mahmoodi, H., Hajivand, A., 2022. Numerical trim and draft optimization of a twin-screw modern surface combatant with inverted bow. Applied Ocean Research 123, 103186. URL: https://www.sciencedirect.com/science/article/pii/S0141118722001298, doi:https://doi.org/10.1016/j.apor.2022.103186.

Menter, F.R., 1993. Zonal two-equations $k-\omega$ turbulence models for aerodynamic flows, in: 23rd Fluid Dynamics, Plasmadynamics, and Lasers Conference, Orlando,FL,U.S.A. pp. 93–290. URL: https://doi.org/10.2514/6.1993-2906, doi:10.2514/6.1993-2906.

Menter, F.R., 1994. Two-equation eddy-viscosity turbulence models for engineering applications. AIAA Journal 32, 1598–1605. URL: https://doi.org/10.2514/3.12149, doi:10.2514/3.12149, arXiv:https://doi.org/10.2514/3.12149.

Prohaska, C.W., 1966. A Simple Method for the Evaluation of the Form Factor and Low Speed Wave Resistance. Proceeding of 11th ITTC .

Queutey, P., Visonneau, M., 2007. An interface capturing method for free-surface hydrodynamic flows. Computers and Fluids 36, 1481–1510.

Raven, H.C., 2019. Shallow-water effects in ship model testing and at full scale. Ocean Engineering 189, 106343. URL: https://www.sciencedirect.com/science/article/pii/S0029801819305062, doi:https://doi.org/10.1016/j.oceaneng.2019.106343.

Regnström, B., 2008. Introduction to Overlapping Grids in SHIPFLOW. FLOWTECH International AB, Gothenburg, Sweden.

Reichel, M., Minchev, A., Larsen, N.L., 2014. Trim optimisation - theory and practice. TransNav, the International Journal on Marine Navigation and Safety of Sea Transportation 8, 387–392. doi:10.12716/1001.08.03.09.

Roache, P., 2009. Fundamentals of verification and validation. Hermosa Publishers.

Sames, P.C., Köpke, M., 2012. CO2 Emissions of the Container World Fleet. Procedia - Social and Behavioral Sciences 48, 1–11. URL: https://linkinghub.elsevier.com/retrieve/pii/S1877042812027188.

Schultz, M.P., 2007. Effects of coating roughness and biofouling on ship resistance and powering. Biofouling 23, 331–341. URL: https://doi.org/10.1080/08927010701461974, doi:10.1080/08927010701461974, arXiv:https://doi.org/10.1080/08927010701461974. pMID: 17852068.

Shivachev, E., Khorasanchi, M., Day, A.H., 2017. Trim Influence on Kriso Container Ship (KCS): An Experimental and Numerical Study, in: Volume 7A: Ocean Engineering, American Society of Mechanical Engineers, Trondheim, Norway. doi:10.1115/OMAE2017-61860.

Starke, B., Raven, H., van der Ploeg, A., 2007. Computation of transom-stern flows using a steady free-surface fitting RANS method. 9th International Conference on Numerical Ship Hydrodynamics , 18.

Sun, J., Tu, H., Chen, Y., Xie, D., Zhou, J., 2016. A Study on Trim Optimization for a Container Ship Based on Effects due to Resistance. Journal of Ship Research 60, 30–47. URL: https://doi.org/10.5957/jsr.2016.60.1.30, doi:10.5957/jsr.2016.60.1.30.

Tezdogan, T., Incecik, A., Turan, O., 2016. A numerical investigation of the squat and resistance of ships advancing through a canal using CFD. Journal of Marine Science and Technology 21, 86–101. doi:10.1007/s00773-015-0334-1.

Wackers, J., Deng, G., Guilmineau, E., Leroyer, A., Queutey, P., Visonneau, M., 2014. Combined refinement criteria for anisotropic grid refinement in free-surface flow simulation. Computers & Fluids 92, 209–222. URL: https://www.sciencedirect.com/science/article/pii/S0045793013005112, doi:https://doi.org/10.1016/j.compfluid.2013.12.019.

Wackers, J., Deng, G., Guilmineau, E., Leroyer, A., Queutey, P., Visonneau, M., Palmieri, A., Liverani, A., 2017. Can adaptive grid refinement produce grid-independent solutions for incompressible flows? Journal of Computational Physics 344, 364–380. URL: https://linkinghub.elsevier.com/retrieve/pii/S0021999117303650, doi:10.1016/j.jcp.2017.04.077.

Wackers, J., Koren, B., Raven, H.C., van der Ploeg, A., Starke, A.R., Deng, G.B., Queutey, P., Visonneau, M., Hino, T., Ohashi, K., 2011. Free-Surface Viscous Flow Solution Methods for Ship Hydrodynamics. Archives of Computational Methods in Engineering 18, 1–41. URL: http://link.springer.com/10.1007/s11831-011-9059-4, doi:10.1007/s11831-011-9059-4.

Paper VII

A Validation Study of Full-Scale CFD Simulation for Sea Trial Performance Prediction of Ships

X International Conference on Computational Methods in Marine Engineering
MARINE 2023
J. García-Espinosa, L. González, J.E. Gutiérrez & B. Serván-Camas (Eds)

A Validation Study of Full-Scale CFD Simulation for Sea Trial Performance Prediction of Ships

Kadir Burak Korkmaz[1*], Keunjae Kim[1], Mattias Liefvendahl[1], Sofia Werner[1] and Michal Orych[†]

[1] RISE-SSPA Sweden AB, 400 22 Gothenburg, Sweden, web page: http://www.ri.se

[†] FLOWTECH International AB, 400 22 Gothenburg, Sweden, web page: http://www.flowtech.se

[*] Corresponding author: Kadir Burak Korkmaz, burak.korkmaz@ri.se

ABSTRACT

Shipping is a critical component of global trade but also accounts for a substantial portion of global greenhouse gas emissions. Recognising this issue, the International Maritime Organisation (IMO) has implemented new measures aimed at determining the energy efficiency of all ships and promoting continuous improvements, such as the Energy Efficiency Existing Ship Index (EEXI). As Computational Fluid Dynamics (CFD) can be used to calculate the EEXI value, RISE-SSPA[1] and Flowtech have developed a CFD-based method for predicting full-scale ship performance with SHIPFLOW v7.0, which meets the new requirements of IMO. The method is validated through an extensive comparison study that examines the delivered power and propeller rotation rate between full-scale CFD predictions and high-quality sea trials using 14 common cargo ships of varying sizes and types. The comparison between the CFD predictions and 59 sea trials shows that both delivered power and RPM can be predicted with satisfactory accuracy, with an average comparison error of about 4% and 2%, respectively. The numerical methods used in this study differ significantly from the majority of the state-of-the-art CFD codes, highlighting their potential for future applications in ship performance prediction. Thorough validation with a large number of sea trials is essential to establish confidence in CFD-based ship performance prediction methods, which is crucial for the credibility of the EEXI framework and its potential to contribute to shipping decarbonisation.

Keywords: CFD; full-scale; quality assurance; ship hydrodynamics; self-propulsion

1. INTRODUCTION

Seaborne transportation mobilises the vast majority of the cargo worldwide by common cargo vessels. However, the crucial role of shipping in global trade is realised while emitting 2.89% of Global Greenhouse Gas (GHG) emissions (IMO, 2021). In addition, the future projections on long-term economic and energy scenarios of the International Maritime Organisation (IMO) indicate that shipping emissions need to be reduced according to the goals set by IMO (2021). In line with this vision, one of the possible paths to reduce shipping emissions is increasing ships' energy efficiency. Therefore, IMO has been introducing regulations to mitigate the GHG emissions from ships. An earlier example is the introduction of the Energy Efficiency Design Index (EEDI) (IMO, 2011), which aims to eliminate

[1]SSPA Sweden AB has become a fully integrated part of the RISE Research Institutes of Sweden since 01-01-2023.

inefficient ships to join the global fleet and to promote higher energy efficiency ship designs. EEDI calculations are now a mandatory step where the applicable ships are pre-verified with towing tank tests during the design phase of a new ship.

IMO introduced a new regulation mandating the calculation of the Energy Efficiency Existing Ship Index (EEXI) for all ships (IMO, 2022). Similar to the previously introduced EEDI, the EEXI calculations aim to obtain energy efficiency indications for existing ships. The new regulation requires that all vessels, including those built before the introduction of the EEDI regulation, undergo the calculation of the Energy Efficiency Existing Ship Index. As stipulated by (IMO, 2022), the calculated EEXI value for each individual ship must be below the required EEXI. Thus, a minimum energy efficiency standard is established for all ships. If towing tank tests are available for the vessel, the EEXI value can be calculated from the extrapolated speed-power relations. However, towing tank tests may not be available for all existing ships. Therefore, IMO (2022) has agreed to accept Computational Fluid Dynamics (CFD) results for calculating the EEXI value.

The requirements for the numerical methods and their usage to produce a speed-power curve for EEXI calculations are described in IACS (2022). According to the IACS guidelines, not only the model scale computations but also the full-scale CFD can be performed. The model scale CFD methodology has been verified and validated for decades and reached an acceptable maturity level in terms of resistance, self-propulsion, and local flow predictions (Hino et al., 2020). However, the verification and validation effort for the full-scale CFD computations is relatively new and lagging behind mainly due to a lack of publicly available full-scale data, i.e. sea trials. Lloyd's Register conducted a full-scale numerical modelling workshop with a blind test case for validation. The results of the workshop, as summarised by Ponkratov (2016), offer valuable insights into the performance of various numerical modelling techniques. Upon closer analysis of the published results, it was found that the mean comparison error for the predicted power was 13% for all submissions, indicating a certain degree of variability in the accuracy of the models. Nevertheless, it is worth noting that three out of the twenty-seven participants achieved highly accurate results, with errors below 3% for all considered speeds. In addition, recent publications such as Orych et al. (2021); Sun et al. (2020); Mikulec and Piehl (2023); Mikkelsen and Steffensen (2016); Niklas and Pruszko (2019); Schouten et al. (2022) demonstrated good accuracy of predicting sea trial conditions with full-scale CFD. However, most of the full-scale validation studies in the literature are performed on a ship with one or a limited number of sea trials. As discussed in Korkmaz et al. (2021), a large number of sea trials are required for full-scale validations since the uncertainty of each trial is large.

The three steps listed in the IACS guidelines for the applicability of the CFD method are the demonstration of qualification, validation/calibration and calculation. This study focuses on the demonstration of qualification (Step 1) following the procedure recommended by ITTC (2021b). Therefore, the computational methods and the development of the Best Practice Guidelines (BPG) are discussed in Section 2. In addition, the results of an extensive comparison study performed with fourteen vessels and 59 sea trials between the full-scale CFD predictions and sea trials are discussed in Section 4.

The numerical techniques employed in the current study for full-scale computations considerably differ from many state-of-the-art CFD codes. Specifically, the study employs structured and overlapping grids, no-slip wall treatment, free-surface treatment, and propeller modelling. As a result, the current research could offer crucial insights and experiences into these techniques. Additionally, the study highlights the importance of meticulous validation work in establishing quality assurance and confidence, which is imperative for ensuring the credibility of the Energy Efficiency Existing Ship Index (EEXI) framework and its potential to facilitate the decolonisation of the shipping industry.

2. COMPUTATIONAL METHODS

This study utilises the SHIPFLOW version 7.0 CFD solver for its simulations, employing the potential flow solver XPAN to compute heave and pitch Janson (1997) and the steady-state RANS solver XCHAP for full-scale self-propulsion simulations (Broberg et al., 2022).

Featuring higher-order panels and singularity distributions, XPAN is a nonlinear Rankine source panel method (Janson, 1997). The iterative process for the nonlinear free surface boundary condition, which applies nonlinear boundary conditions to the free surface, calculates dynamic sinkage and trim. During each iteration, the ship's position is adjusted, and the panelization of the hull and free surface is updated. The heave and pitch obtained are then used to position the hull in the RANS simulations through one-way coupling.

The steady, incompressible Reynolds Averaged Navier-Stokes (RANS) equations are solved by XCHAP using a finite volume method. The Explicit Algebraic Stress Turbulence Model (EASM) is implemented in this paper Deng et al. (2005). Wall functions are not used, and the equations are integrated up to the wall. The Roe scheme discretises the convection (Roe, 1981), while a central scheme is employed for the diffusive fluxes. Explicit flux correction is applied to achieve second-order accuracy (Dick and Linden, 1992), (Chakravarthy and Osher, 1985). The Volume of Fluid Method (VOF) is used to handle the water-air interface.

By modifying the boundary conditions for the specific dissipation of turbulent kinetic energy, ω, and turbulent kinetic energy, k (Orych et al., 2022a), the hull roughness effect is modelled. The equivalent sand grain roughness height, k_S, is employed for quantifying roughness.

Structured grids are utilised in XCHAP. For a bare hull case, a single block grid is typically generated, while multi-block structured or overlapping grids are used for more complex geometries, such as hulls with appendages and local grid refinements.

To account for the propeller's effect, body forces are introduced. As the flow traverses the propeller swept volume, its linear and angular momentum increase as if interacting with a propeller with an infinite number of blades. The forces, spatially varying but time-independent, produce a propeller-induced steady flow. A built-in lifting line propeller analysis program calculates the body forces (Zhang, 1990). Furthermore, a friction resistance component is considered, which contributes to the propeller torque. This simplified modelling approach also addresses blade roughness.

An iterative procedure is used for body force computation. Initially, the current velocity field approximation is extracted at a representative propeller plane. The induced propeller wake is subtracted to obtain the effective wake, which is determined by the circulation from the previous iteration in the lifting line method. New circulation and forces are computed within the effective wake. These forces are then distributed across the volume cells in the cylindrical grid. The body forces are incorporated into the flow equations' right-hand side, resulting in a new velocity field after solving the equations. Body forces are updated with each iteration. Upon convergence, the total wake calculated by the RANS solver and the lifting line method should correspond in the chosen propeller plane.

For self-propulsion simulation, the program automatically adjusts the propeller rotational speed to achieve equilibrium between resistance and thrust (ITTC, 2017).

The development of the best practice guidelines with SHIPFLOW for full-scale self-propulsion free-surface RANS computations has been initiated from the model-scale investigations that span over decades (Liefvendahl, 2023). The computation of the resistance with the double-body RANS approach

has been extensively verified, and validated, and best practice guidelines have been developed in Korkmaz et al. (2021). The self-propulsion capabilities of the SHIPFLOW code have been successfully demonstrated by Kim and Li (2010) and Korkmaz et al. (2015). Additionally, verification, validation, and in-depth investigations have been performed on the lifting line model for open water and in behind conditions (Korkmaz, 2015). The free-surface RANS capabilities of SHIPFLOW in model scale have been demonstrated by an extensive validation study where a wide range of transom shapes and Froude numbers have been covered in Orych and Larsson (2015). A Verification and Validation (V&V) study has been carried out for self-propulsion simulations using free-surface RANS (Orych and Regnström, 2023). The surface roughness modelling for full-scale computations has been investigated, and the implementation of different models is discussed in Orych et al. (2022b). In Orych et al. (2021), a V&V study has been performed in full scale. It was demonstrated that the full-scale delivered power comparison error between the CFD prediction and sea trials is significantly smaller than the validation uncertainty, indicating numerical and modelling errors are well within acceptable levels in full scale. Based on both published and internal studies, a best practice guideline for full-scale self-propulsion free-surface RANS computations. The SHIPFLOW best-practice guidelines fulfil the requirements of IACS guidelines (IACS, 2022).

3. TEST CASES AND COMPUTATIONAL CONDITIONS

The test cases comprise fourteen common cargo vessels which were towing tank tested at RISE-SSPA earlier. As the speed trials of some vessels were performed at more than one loading condition, the total number of test cases is nineteen. The L_{PP} of the vessels range from approximately 175 m to 350 m, block coefficients (C_B) vary between 0.52 and 0.84, and the Froude numbers (the achieved speed at 75% MCR) are covering the range of 0.14 to 0.23.

Eleven of the fourteen vessels were built in series, and speed trials were performed for each sister ship. For three vessels, one speed trial is available per vessel. The data set consists of 59 sea trials in total. The trial measurements were conducted by the yards and analysed by RISE-SSPA with in-house software according to ITTC Recommended Procedures and Guidelines for Preparation, Conduct and Analysis of Speed/Power Trials (ITTC, 2017b) and ISO Ships and marine technology—Guidelines for the assessment of speed and power performance by analysis of speed trial data (ISO, 2015). The trials fulfil the ISO 15016/ITTC limits on weather conditions. The corresponding model tests were conducted at RISE-SSPA.

The hull, propeller and appendage geometries used in the full-scale computations were identical to the earlier towing tank tests. Similarly, the computational conditions replicate the same conditions as the full-scale predictions from the towing tank tests, such as calm and deep waters with seawater properties corresponding to 15°C. The geometry of the superstructure is not included in the computations; therefore, the air resistance is included as an external force in the computations. The air resistance is calculated from the air resistance coefficient as described in ITTC (2021d) using the transversal projected area of the ship above the waterline.

As most hulls have more than one speed trial and the speed attained at each trial differs between the sister ships, it is not practical to simulate the sea trial speeds directly. Instead, at least three ship speeds were computed for each test case. The speeds used for the full-scale computations are adopted from the Froude numbers tested earlier in the towing tank tests.

4. RESULTS

This section presents an extensive validation study between the sea trial measurements and CFD predictions, as required in the demonstration of the quality step of the ITTC Quality Assurance (QA) Procedure (ITTC, 2021c). Each CFD computation has been performed according to the best practice guideline developed for full-scale self-propulsion free-surface RANS computations. It means that in addition to the computational setup, the grid resolution of each hull is highly similar, thanks to the parametric nature of the structured grid generation in SHIPFLOW. An example of the grid distribution on the no-slip surfaces (i.e. hull and the appendages), the wave elevation and the effective wake generated by the lifting line model is presented in Fig. 1.

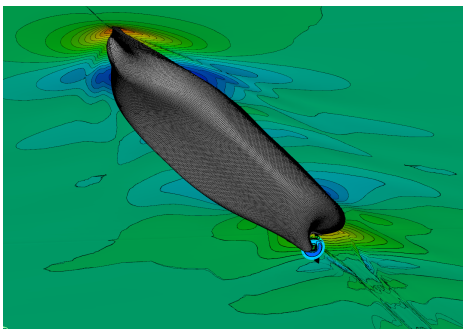

(a) Perspective view from the bow

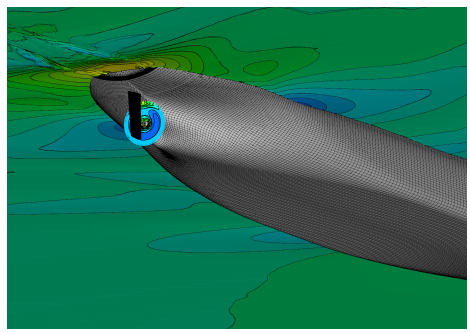

(b) Perspective view from the stern

Figure 1: Free surface wave elevation, effective wake and the grid distribution on the appended hull

4.1 Sea Trial Analysis

The combination of the precision and bias limits of single speed trial result is approximately 10% of total uncertainty as indicated by Werner and Gustafsson (2020) and Insel (2008). Therefore, comparing the CFD predictions and a limited number of speed trials will likely be inconclusive. Instead, a large number of sea trials are required for a statistically meaningful comparison between the trials and CFD predictions since the uncertainty of each trial is substantial.

As explained in Section 3, the full-scale computations were not performed at speed attained at each speed trial. Instead, as seen in Fig. 2, three speeds were computed for one of the test cases and a polynomial curve is fitted to the computed values for the delivered power (P_{DT}) and propeller turning rate (rps). The computed power and rps values are then obtained from the speed-power and speed-rps curves at the same speed as the attained speed at the sea trial.

The comparison between the speed trial measurement and the computations were quantified similarly to the correlation factors ($C_P - C_N$) (ITTC, 2017a) in the 1978 Power Prediction method (ITTC, 2021a). The correlation of each individual speed trial, C'_P and C'_N, are calculated as

$$C'_{\mathrm{P}} = \frac{P_{\mathrm{D}\ trial}}{P_{\mathrm{D}\ CFD}} \quad \text{and} \quad C'_{\mathrm{N}} = \frac{n_{trial}}{n_{CFD}} \tag{1}$$

where the $P_{\mathrm{D}\ trial}$ and n_{trial} are the power and propeller turning rate from a speed trial, while $P_{\mathrm{D}\ CFD}$ and n_{CFD} represent the corresponding predictions based on the model test. Note that in IACS

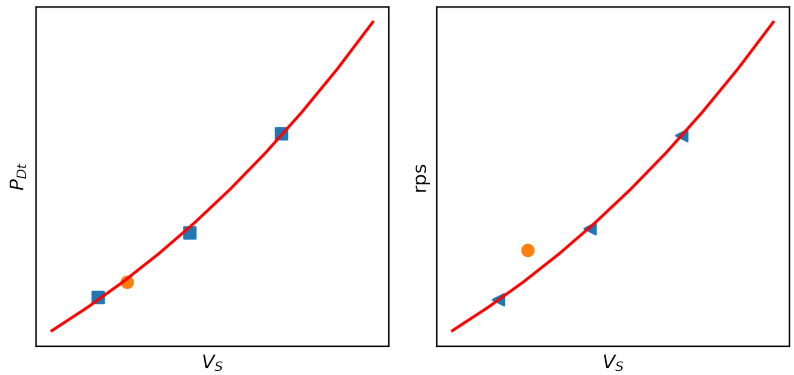

Figure 2: Power and propeller turning rate versus ship speed for computed (blue square markers) and measured (orange circle markers) values

guidelines (IACS, 2022), C'_P and C'_N are named as calibration factors which is the ratio between the sea trial power and the numerical calculation found power.

After C'_P and C'_N are calculated for each sea trial, an assembled correlation factor for C_P and C_N are determined by taking the median of C'_P and C'_N of all trials of sufficient quality (Werner and Gustafsson, 2020). The assembled correlation factors are used in towing tank testing practice as "correction for any systematic errors in model test and powering prediction procedure, including any facility bias" (ITTC, 2017a). In this study, C_P and C_N will be used to correct the CFD results, which corresponds to the current CFD setup, i.e. best practice guidelines. The Probability Density Functions (PDFs) and histograms of C'_P and C'_N are presented by shifting the median of PDFs to 1, i.e. multiplication of individual correlation factors with the assembled C_P and C_N, respectively.

4.2 Comparison between the CFD predictions and speed trials

The histograms and the probability density functions of the normalised correlation factors, $C_P(CFD)$ and $C_N(CFD)$, are calculated for each speed trial. In addition to the normalised PDF curve, the probability density function of the correlation factors before the correction is also displayed together with the standard deviation (σ) and the mean of $C_P(CFD)$ and $C_N(CFD)$ in Fig. 5. The mean of PDF are 0.96 and 1.02 for C'_P and C'_N. This indicates that the mean comparison error between the CFD predictions and the sea trials is 4% and 2% for delivered power and propeller turning rate, respectively. In addition, the mean absolute comparison error (before C_P and C_N correction) is 5.6% and 3.3% for the delivered power and propeller turning rate.

After assembled C_P and C_N corrections, the histogram and the probability density function derived from the normal distribution are highly similar for both the power and propeller turning rates. Thus, the comparison error, e.g. $C_P(CFD)$-1, is also normally distributed, and no significant bias exists between the predictions and trial measurements.

Comparing the standard deviations for the power and RPM predictions indicates that the scatter is significantly lower for the propeller turning rate. In other words, the propeller turning rate prediction is more accurate ($\sigma = 0.036$) than the delivered power prediction ($\sigma = 0.060$). Assuming normal

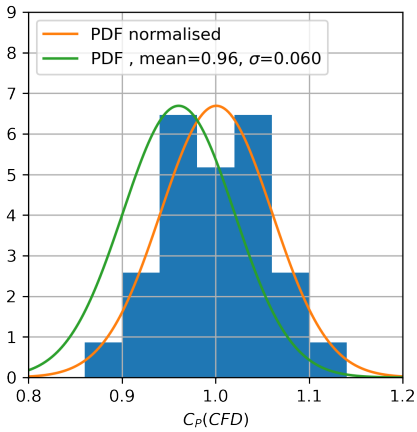

(a) Delivered power

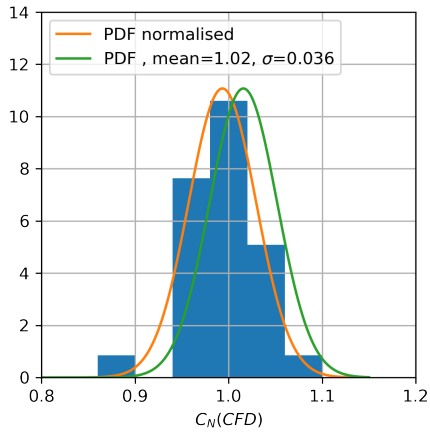

(b) Propeller turning rate

Figure 3: Histogram and probability density functions of the $C_P(CFD)$ and $C_N(CFD)$

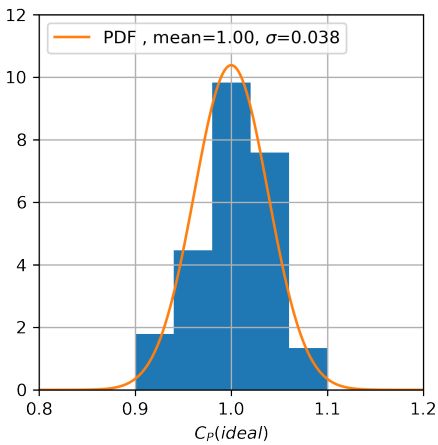

(a) Delivered power

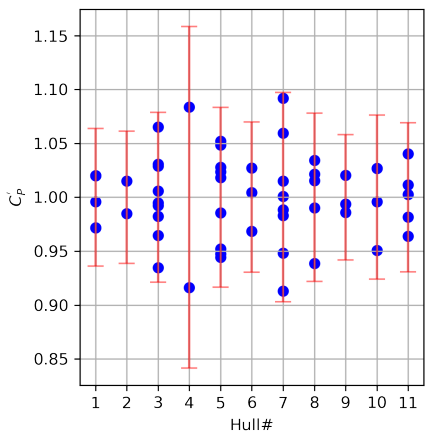

(b) Scatter among the sister vessels for the delivered power

Figure 4: Histogram and probability density function of the delivered from the ideal case and individual trials for each hull

distribution is valid, the standard deviations indicate that 95% of the speed trials were predicted by CFD within ±12% and ±7% accuracy for power and RPM, respectively.

At first glance, the accuracy of the CFD predictions may not look too impressive; however, a considerable part of the standard deviation is caused by the scatter in the speed trials of the sister ships as argued by Korkmaz et al. (2021). To illustrate this, an ideal prediction scenario has been prepared using cases with more than one speed trial. The ideal case means the CFD prediction is identical to

the speed trial measurement. However, since the speed trial measurements between the sister ships vary, the ideal case would be that the mean C_P' of a series of sisters would be 1. The resulting C_P' values for the vessels with more than one speed trial are presented in Fig. 4b as blue markers. In order to indicate the uncertainty of the speed trials for each vessel, the standard deviation of the C_P' values for a given hull is combined with the bias limit (U_{bias}) of 4% as estimated by Insel (2008). The resulting total uncertainty estimations ($\sqrt{\sigma^2 + U_{bias}^2}$) are indicated in Fig. 4b as error bars for each hull. As seen in Fig. 4b, the scatter among the sister ships varies significantly vessel by vessel, and the measured power at the trial can vary up to 18% between the sister ships.

Similar to the earlier plots, the histogram and the probability density function of the ideal prediction case (including hulls with one speed trial) are presented in Fig. 4a. The comparison between the predictions and the ideal case shows that more than half of the scatter indeed originates from the scatter among the sister ships. The standard deviation from the ideal prediction case is 0.038, meaning that 95% of the speed trials can be predicted within ±7.6% accuracy in the best-case scenario, while the CFD predictions were within ±12% accuracy. This comparison indicates that the accuracy of the CFD is within acceptable levels considering the bulk of the scatter originates from the differences between the sister ships.

4.3 Prediction of the delivered power and propeller turning rate

The prediction accuracy of the delivered power and propeller turning rate have been discussed individually through statistical analysis. However, a successful full-scale performance prediction requires both power and RPM to be predicted with reasonable accuracy simultaneously. To visualise if this is the case with the full-scale CFD predictions, the normalised correlation factors for the power and the propeller turning rate are plotted against each other in Fig. 5. The predictions are differentiated with varying colour and marker types in the respective loading conditions. In addition, a light blue uncertainty band extending between ±8% for $C_P(CFD)$ and ±4% for $C_N(CFD)$ is plotted. As observed in Fig. 5, the majority of the predictions are within the marked uncertainty band, indicating that the delivered power and propeller rotation rate are predicted with an acceptable accuracy at the same time.

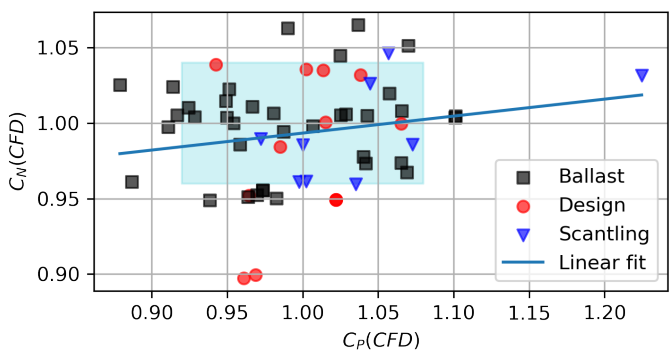

Figure 5: Correlation factors $C_P(CFD)$ versus $C_N(CFD)$

The predictions for different loading conditions are somewhat randomly distributed within the uncertainty band. There are two outliers (more than two standard deviations from 1) for $C_N(CFD)$ belonging to the Hull number 5 (see Fig. 4b), which has 6% variation between trials. The other outlier is in the delivered power prediction of the Hull number 4 (see Fig. 4b), which shows a variation of 18% difference between the trials. It can be concluded that the large scatter between the sister ships may be partially the reason for the outliers. Excluding the exceptions, no distinctive bias can be observed for predicting a particular loading condition. More definitive conclusions regarding bias for the predictions at different loading conditions can be achieved with more speed trial samples at design and scantling loading conditions.

5. CONCLUSIONS

This study presents a CFD-based method for predicting full-scale ship performance, which meets the new requirements of IMO. An extensive comparison study was performed with fourteen vessels and 59 sea trials between the full-scale CFD predictions and sea trials, where the CFD setup and grid generation were consistently according to the best practice guidelines for all test cases.

The comparison between the CFD predictions and the sea trial showed that the mean comparison error is 4% and 2% for delivered power and propeller turning rate, respectively. The histograms of the ratio between a sea trial and corresponding CFD prediction for the delivered power and propeller turning rate, i.e. correlation factor, are distributed similarly to a normal distribution. Therefore, the comparison error after the corrections on delivered power and propeller turning rate can also be assumed normally distributed, and no significant bias can be observed between the predictions and trial measurements.

The relatively large standard deviation of the correlation factors for the delivered power should be considered with care. As illustrated by an ideal prediction scenario, more than half of the standard deviation originates from the scatter among the sea trials of sister ships; hence, highlighting the significance of an extensive validation study.

A successful full-scale performance prediction method requires both power and RPM to be predicted with reasonable accuracy simultaneously, as it is critical for the engine selection. As observed from the analysis of individual correlation factors, the CFD-based method employed in this study can predict the delivered power and propeller rotation rate with acceptable accuracy at the same time. In addition, no distinctive bias was observed in predicting a particular loading condition.

The CFD method used in the current research relies on numerical techniques that differ significantly from many state-of-the-art CFD codes. These techniques provide valuable insights and experiences for future research in this field. Additionally, the study emphasises the importance of meticulous validation work to ensure the quality assurance and confidence needed to establish the credibility of the Energy Efficiency Existing Ship Index (EEXI) framework. Further studies with more test cases are needed, especially where the sea trials are available at design and scantling loading conditions to further enhance the confidence in the CFD method.

ACKNOWLEDGEMENTS

The study was mainly supported by internal strategic funding, which supports development in core competence areas. In addition, this work received funds from the Swedish Transport Agency, project LOVA TRV 2020/92054 and the Swedish Energy Agency, project ITRIM grant 2020/018759.

References

Broberg, L., Regnström, B., and Östberg, M. (2022). *XCHAP – Theoretical Manual*. FLOWTECH International AB, Gothenburg, Sweden.

Chakravarthy, S. and Osher, S. (1985). A new class of high accuracy TVD schemes for hyperbolic conservation laws. *23rd Aerospace Sciences Meeting, Reno, NV, U.S.A., AIAA paper No*, 85-0363.

Deng, G. B., Queutey, P., and Visonneau, M. (2005). Three-dimensional flow computation with Reynolds Stress and Algebraic Stress Models. In *Procedings of the ERCOFTAC International Symposium on Engineering Turbulence Modelling and Measurements; ETMM6, Sardinia, Italy, 23–25 May, 2005*, pages 389–398.

Dick, E. and Linden, J. (1992). A multigrid method for steady incompressible navier-stokes equations based on flux difference splitting. *International Journal for Numerical Methods in Fluids*, 14:1311–1323.

Hino, T., Stern, F., Larsson, L., Visonneau, M., Hirata, N., and Kim, J. (2020). *Numerical Ship Hydrodynamics: An Assessment of the Tokyo 2015 Workshop*. Springer International Publishing.

IACS (2022). Guidelines on numerical calculations for the purpose of deriving the V_{ref} in the framework of the EEXI regulation. *IACS Rec. No. 173*.

IMO (2011). *Annex 19: Resolution MEPC.203(62)*.

IMO (2021). *Fourth IMO GHG Study 2020*. International Maritime Organisation, 4 Albert Embankment, London SE1 7SR.

IMO (2022). 2022 guidelines on the method of calculation of the attained energy efficiency existing ship index (EEXI). *Annex 12: Resolution MEPC.350(78)*.

Insel, M. (2008). Uncertainty in the analysis of speed and powering trials. *Ocean Engineering*, 35(11):1183 – 1193.

ISO (2015). Ships and marine technology – guidelines for the assessment of speed and power performance by analysis of speed trial data. *15016:2015*.

ITTC (2017). *1978 ITTC Performance Prediction Method, ITTC Quality System Manual, Recommended Procedures and Guidelines*. Propulsion Committee of the 28th ITTC.

ITTC (2017a). Guidelines on the determination of model-ship correlation factors. *ITTC – Recommended Procedures and Guidelines*, 7.5-04-05-01.

ITTC (2017b). Preparation, conduct and analysis of speed/power trials. *ITTC – Recommended Procedures and Guidelines*, 7.5-04-01-01.

ITTC (2021a). 1978 ittc performance prediction method. *ITTC – Recommended Procedures and Guidelines*, 7.5-02-03-01.4.

ITTC (2021b). Quality assurance in ship CFD application. *ITTC – Recommended Procedures and Guidelines*, 7.5-03-01-02.

ITTC (2021c). Quality assurance in ship cfd application. *ITTC – Recommended Procedures and Guidelines*, 7.5–03-01–02.

ITTC (2021d). Resistance test. *ITTC – Recommended Procedures and Guidelines*, 7.5-02-02-01.

Janson, C.-E. (1997). *Potential Flow Panel Methods for the Calculation of Free-surface Flows with Lift*. Doctoral dissertation, Department of Naval Architecture and Ocean Engineering, Division of Hydromechanics, Chalmers University of Technology, Gothenburg.

Kim, K. and Li, D.-Q. (2010). Estimation of numerical uncertainty of Shipflow in self-propulsion simulation of KCS. In *Gothenburg 2010 workshop – CFD in ship hydrodynamics*, Gothenburg, Sweden.

Korkmaz, K. B. (2015). CFD predictions of resistance and propulsion for the JAPAN Bulk Carrier (JBC) with and without an energy saving device. Master's thesis, Department of Shipping and Marine Technology, Chalmers University Technology, Gothenburg, Sweden.

Korkmaz, K. B., Orych, M., and Larsson, L. (2015). CFD prediction including verification and validation of resistance, propulsion and local flow for the Japan bulk carrier (JBC) with and without an energy saving device. In *Tokyo 2015 workshop – CFD in ship hydrodynamics*, Tokyo, Japan.

Korkmaz, K. B., Werner, S., and Bensow, R. (2021). Verification and validation of CFD based form factors as a combined CFD/EFD method. *Journal of Marine Science and Engineering*, 9(1).

Liefvendahl, M. (2023). Ship power prediction with cfd in full scale. Technical Report RE71221461-01-00-A, Research Institutes of Sweden.

Mikkelsen, H. and Steffensen, M. L. (2016). Full scale validation of CFD model of self-propelled ship. Master's thesis, Technical University of Denmark, Denmark.

Mikulec, M. and Piehl, H. (2023). Verification and validation of CFD simulations with full-scale ship speed/power trial data. *Brodogradnja*, 74(1):41–62.

Niklas, K. and Pruszko, H. (2019). Full-scale CFD simulations for the determination of ship resistance as a rational, alternative method to towing tank experiments. *Ocean Engineering*, 190:106435.

Orych, M. and Larsson, L. (2015). Hydrodynamic aspects of transom stern optimization. In *5th High Performance Yacht Design Conference*, pages pp.247–256, Auckland , New Zealand.

Orych, M. and Regnström, B. (2023). Verification and validation of volume-of-fluid functionality in Shipflow. *personal communication*.

Orych, M., Werner, S., and Larsson, L. (2021). Validation of full-scale delivered power CFD simulations. *Ocean Engineering*, 238:109654.

Orych, M., Werner, S., and Larsson, L. (2022a). Roughness effect modelling for wall resolved RANS – comparison of methods. *Ocean Engineering*, 266:112778.

Orych, M., Werner, S., and Larsson, L. (2022b). Roughness effect modelling for wall resolved RANS – Comparison of methods for marine hydrodynamics. *Ocean Engineering*, 266:112778.

Ponkratov, D. (2016). 2016 workshop on ship scale hydrodynamic computer simulation. In Ponkratov, D., editor, *loyd's Register workshop on ship scale hydrodynamics*.

Roe, P. L. (1981). Approximate Riemann solvers, parameter vectors, and difference schemes. *Journal of Computational Physics*, 43:357.

Schouten, D. R., Drouet, A., Birvalski, M., and Morand, L. (2022). Full Scale CFD Validation Using Ship Performance and Wave Pattern Measurements of a Mega Cruise Ship. In *Volume 7: CFD and FSI*, page V007T08A041, Hamburg, Germany. American Society of Mechanical Engineers.

Sun, W., Hu, Q., Hu, S., Su, J., Xu, J., Wei, J., and Huang, G. (2020). Numerical Analysis of Full-Scale Ship Self-Propulsion Performance with Direct Comparison to Statistical Sea Trail Results. *Journal of Marine Science and Engineering*, 8(1):24.

Werner, S. and Gustafsson, L. (2020). Uncertainty of Speed Trials. In *5th Hull Performance & Insight Conference*, Hamburg, Germany.

Zhang, D. (1990). *Numerical Computation of Ship Stern/Propeller Flow*. Doctoral dissertation, Department of Shipping and Marine Technology, Chalmers University of Technology, Gothenburg.